Investigation of Wire Structures for Heat Transfer Enhancement in Compact Heat Exchangers

Zur Erlangung des akademischen Grades eines
DOKTORS DER INGENIEURWISSENSCHAFTEN (Dr.-Ing.)

von der KIT-Fakultät für Maschinenbau des
Karlsruher Instituts für Technologie (KIT)
angenommene

DISSERTATION

von

Dipl.-Math. Hannes Fugmann

Tag der mündlichen Prüfung:	27. Mai 2019
Hauptreferentin:	Prof. Dr.-Ing. B. Frohnapfel
Korreferent:	Prof. Dr.-Ing. T. Wetzel

Abstract

Enhanced heat transfer surfaces enable more energy-efficient, compact and lightweight heat exchangers. However, no single surface geometry exists that simultaneously optimizes all of these three objectives. With the presence of trade-offs, many different enhancement designs have been developed and are still being developed. Within this thesis, enhanced heat transfer surfaces based on cylindrically shaped pin fins with wire diameters in the order of 100 µm are analyzed for flat-tube heat exchangers.

Very high convective heat transfer coefficients and material savings can be expected. The objective of this thesis is to estimate the performance potential of these wire structures.

Four steps are taken to allow an estimation. Firstly, a performance evaluation method for comparing different types of enhancements is developed. The method's objectives are defined as the energy, volume, and mass efficiency of the enhancement. Secondly, computational thermal-fluid-dynamic simulations of fluid flow through different wire structure geometries are performed and thermal-hydraulic correlations are developed. Thirdly, the technical feasibility of manufacturing wire structure heat exchangers is analyzed and a selection of samples is tested experimentally for their thermal-hydraulic performance. Lastly, the thermal-hydraulic correlations are used to optimize the energy, volume, and mass efficiency of the wire structure enhancement with respect to specified geometrical and operational constraints.

The evaluation shows benefits for the wire structures when the volume and especially the mass efficiency is taken into consideration. The potential is equivalent or higher when a combination of volume and energy efficiency is considered for air velocities up to approximately 2.5 m/s. For higher velocities

the analyzed wire structure designs appear not to confer any advantages over standard fins when evaluated for energy and volume efficiency.

Kurzfassung

Verbesserte Wärmeübertrageroberflächen ermöglichen energieeffizientere, kompaktere und leichtere Wärmeübertrager. Eine spezifische Oberfläche, die in allen drei Kriterien optimal ist, gibt es nicht. Mit der Existenz dieses Zielkonflikts wurden und werden eine Vielzahl unterschiedlicher verbesserter Oberflächendesigns entwickelt. Innerhalb dieser Arbeit werden Wärmeübertrageroberflächen auf Basis zylindrischer Drähte/Stiftrippen mit Drahtdurchmessern in der Größenordnung von 100 µm für Flachrohranwendungen untersucht. Sehr hohe konvektive Wärmeübergangskoeffizienten und deutliche Materialeinsparungen können erwartet werden. Das Ziel dieser Arbeit ist es, das Potenzial dieser Drahtstrukturen abzuschätzen.

Vier Schritte werden für die Abschätzung durchgeführt. Zunächst wird eine Methode zur Bewertung unterschiedlicher Oberflächenentwicklungen ausgearbeitet. Die Zielgrößen der Methode sind definiert als eine energetische, eine volumenspezifische und eine massenspezifische Effizienz. Im zweiten Schritt wird eine numerische Simulation der Fluidströmung durch verschiedene Drahtstrukturgeometrien durchgeführt und es werden Korrelationen für Kennzahlen der Thermo- und Fluiddynamik entwickelt. Im dritten Schritt wird die Machbarkeit der Herstellung von Drahtstruktur-Wärmeübertragern untersucht und eine Reihe von Wärmeübertragerproben wird experimentell im Hinblick auf ihre thermische und hydraulische Leistung geprüft. Im letzten Schritt werden die neu entwickelten Korrelationen verwendet, um die energetische, volumenspezifische und massenspezifische Effizienz der Drahtstrukturen unter geometrischen und operativen Randbedingungen zu optimieren.

Die Begutachtung zeigt Vorteile der Drahtstrukturen auf für Anwendungen, bei denen Volumen- und insbesondere Masseneffizienz eine wesentliche Rolle

spielen. Wird eine Kombination aus energie- und volumenbezogener Bewertung durchgeführt, sind die Drahtstrukturen bei kleinen und mittleren Luftgeschwindigkeiten unterhalb etwa 2.5 m/s vorteilhaft. Für höhere Geschwindigkeiten sind die untersuchten Drahtstrukturen nicht vorteilhaft im Vergleich zu üblichen Lamellen.

Table of Contents

1 Introduction

1.1 Motivation

For several centuries, efforts have been made to prepare more efficient heat exchangers by employing various methods of heat transfer enhancement. In Roman times, Vitruvius [1] described geometries and materials used to improve a hypocaust, in the early 19th century hot water heating boilers were manufactured and patented in quantity [2], and nowadays, especially savings in materials and energy usage provide strong motivation for the development of improved methods of surface enhancement for a vast number of applications. When designing cooling systems for automotive devices or airplanes, it is imperative that the heat exchangers are particularly lightweight. Further, enhanced devices are necessary for heat exchangers with high effectiveness or low auxiliary power found, e.g., in air-cooled condensers of power plants. Applications with limited space in the building sector profit from more compact heat exchanger designs. These applications, as well as numerous others, have led to the development of various enhanced heat transfer surfaces. In general, enhanced heat transfer surfaces can be used for three purposes [3]:

1. to make heat exchangers more compact in order to reduce their overall volume, mass, and possibly their cost,
2. to reduce the pumping or fan power required for a given heat transfer process, or
3. to increase the product of the overall heat transfer coefficient U_{HX} times the surface area A_{HTS} of the heat exchanger.

The product of U_{HX} times A_{HTS} is based on the thermal resistances of each fluid side of a heat exchanger. These resistances are connected in series such that the fluid side with the lowest heat transfer coefficient h times surface area A limits the entire series.

The heat transfer surface enhancements within this thesis are realized on the gas side of a gas-to-liquid (or gas-to-gas) heat exchanger, as heat transfer is generally limited there (primarily due to the low thermal conductivity of the gas). There are three basic ways to achieve a higher hA [3, 4]:

Approach 1 "Increase the effective heat transfer surface area (A) per unit volume without appreciably changing the heat transfer coefficient (h). Plain fin surfaces enhance heat transfer in this manner" [3].

Approach 2 "Increase h without appreciably changing A. This is accomplished by using a special channel shape, such as a wavy or corrugated channel, which provides mixing due to secondary flows and boundary-layer separation within the channel" [3].

Approach 3 "Increase both h and A. Interrupted fins (i.e. offset strip and louvered fins [and cellular metal structures]) act in this way. These surfaces increase the effective surface area, and enhance heat transfer through repeated growth and destruction of the boundary layers" [3].

In particular, the development of cellular metal structures as heat transfer surface area enhancements has been intensified in recent years. These structures are interesting for a wide range of applications where heat must be dissipated over relatively small spaces. "These cellular metal structures can be classified into two broad classes, one with a stochastic topology and the other with a periodic structure" [5]. A stochastic topology includes, e.g., metal foams and packed beds. However, these structures generally have very high pressure drops due to their undirected microgeometry [6–8]. Likewise, heat flux through undirected microgeometry is inhibited. "Examples of periodic cellular metal structures include materials made from stacked or corrugated

metal textiles and microtruss concepts (e.g. tetrahedral, pyramidal, or Kagome topologies)" [5, 9].

The focus of this thesis is on periodic cellular metal structures in gas-to-liquid heat exchangers which are based on wire structures. This is due to innovative methods of the technical textile industry to process metal materials in specific arrangements. These technical textiles promise to fulfil the requirements of highly efficient heat exchangers, such as large heat transfer surface areas, low material utilization, and flexible geometries. The wire diameter of the analyzed "structures is in the submillimeter range. The lengths of the wires between two faces, separating the gas side from the liquid side, are in the lower centimeter range" [FLS17]. Similar to heat transfer enhancement with ordinary fins, gas flows around the additional structure. Assuming that the gas is colder than the liquid, heat is transferred from the liquid to the inner tube wall by forced convection, through the tube wall and the wires, by conduction, and finally to the gas, again by convection (see design in Figure 1.1 with air as gas side and water as liquid side).

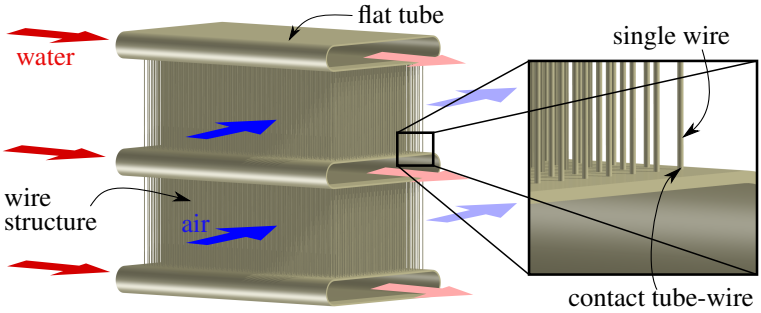

Figure 1.1: Concept of a flat-tube heat exchanger with plate-fin wire structure; based on [FSF19].

"The heat transfer coefficient on the wires increases with decreasing wire diameter, due to a reduction of the thermal boundary layer thickness and, therefore, larger temperature gradients in the gas flow (if the velocity is kept constant). This results in a heat transfer coefficient of approximately

$500\,\mathrm{W/(m^2\,K)}$ for the air flow around a single wire of 0.1 mm in diameter, at an incoming air temperature of 25 °C and a velocity of $2\,\mathrm{m/s}$ [10, ch. Gf] [at atmospheric pressure]. In addition, the material utilization for manufacturing wires is less than that for metal sheets with the same heat transfer surface. Assuming that the diameter of a wire is the same as the thickness of a metal sheet, the mass-specific surface area [of the wires] is twice the metal sheet. These positive effects have to outweigh possible drawbacks, which are related to high pressure drop due to very dense wire structures and low volume-specific heat transfer surfaces for very open wire structures" [FLS17].

In the following section, specific questions regarding the positive effects and the drawbacks are proposed.

1.2 Objectives and Procedure

The objective of this thesis is to estimate the thermal-hydraulic performance potential of wire structures in flat-tube heat exchangers. Therefore, three major questions arise:

1. Which performance evaluation criteria are suitable to enable a fair comparison of wire structure heat exchangers with other types of heat exchangers?
2. How can a large variety of different wire structure geometries be fundamentally evaluated for performance?
3. Is it feasible to manufacture wire structure sample heat exchangers and can their performance be accurately measured?

Question 1 is answered by a review of existing thermal-hydraulic evaluation methods, a rating of their benefits and drawbacks, and the development of coherent and fair evaluation criteria based on the rating. The criteria can be easily illustrated in performance charts, such that a fast comparison to other types of heat exchangers is possible.

For answering Question 2, performance correlations in the literature for flow around wire structures and similar geometries are reviewed and evaluated for their suitability. Additional 2-dimensional (2D) and 3-dimensional (3D) simulations of fluid flow and heat transfer around wire structures as part of a flat-tube heat exchanger are performed. The simulations allow a more detailed performance evaluation for a variety of geometries and they allow the development of performance correlations for these geometries. Hence, a fundamental performance evaluation for wire structure heat exchangers based on the method developed within Question 1 is presented to the reader.

Lastly, for answering Question 3, a review on existing wire structure heat exchangers with wire dimensions in the order of 100 µm is performed. The heat exchangers are analyzed for usage in flat-tube heat exchangers. Thereupon a variety of different wire structure sample heat exchangers, manufactured within different projects, are presented. The size of the samples is chosen such that (i) their manufacturing effort is small, (ii) the uncertainties in performance measurements are small, and (iii) the manufacturing feasibility of real-size heat exchangers is proven. Two test facilities for heat transfer and pressure drop measurements ensure these requirements: one test facility for air-side surface enhancements of small-scale heat exchanger samples with air-side cross-sections in the order of 10 cm^2 and a second test facility for real-size air-to-water heat exchangers of air-side cross sections in the order of 500 cm^2.

A combination of simulation results (Question 2) and experimental results (Question 3) with means of the developed evaluation criteria (Question 1) finally allows a classification of flat-tube wire structure heat exchangers in terms of thermal-hydraulic performance.

1.3 Outline

The thesis continues in Chapter 2 with the description of thermodynamics and fluid dynamics within compact heat exchangers, with a focus on wire structure

heat exchangers. Essential quantities describing the fluid flow are defined. A classification of wire structures based on available designs in the literature is done and an idealized wire structure design idea for flat-tube heat exchangers is defined. The design idea is based on an elementary, but generic, geometry of parallel wires. The generic design idea will be used in simulations, and the manufacture of samples is oriented towards it. The design idea comprises the essential characteristics of available and envisaged wire structure heat exchangers.

In Chapter 3, available performance evaluation criteria in the literature are presented and extended such that different types of surface enhancements can be compared to each other. The purpose of the extension is to define objectives that represent a beneficial heat transfer versus energetic, mass-specific, and volume-specific costs, adequately and consistently.

Chapter 4 deals with the thermal-hydraulic 2D and 3D simulations of the wire structure design idea and with the development of correlations for thermodynamic and fluid dynamic performance parameters. Further, an analytical expression of fin efficiency is presented that takes into account a non-uniform fluid temperature distribution along the wires. The development of the correlations in combination with the new fin efficiency calculation allows a very accurate and fast optimization of geometrical and operational quantities within this thesis, and for engineers who dimension and design wire structure heat exchangers and need simplified tools for performance calculations.

In Chapter 5 different samples of wire structure heat exchangers are tested experimentally for thermal-hydraulic performance. The essential objectives of this chapter are to validate the simulation model, to show feasible manufacturing processes and to analyze limitations in manufacturing.

Chapter 6 condenses the work done in the previous chapters. The performance evaluation method developed in Chapter 3 is applied to the generic design idea from Chapter 2. This is done by calculating the performance and optimizing the geometry with the correlations developed in Chapter 4. As a consequence,

an estimation of the thermal-hydraulic performance potential of wire structures can be given in terms of (i) differences from an optimum of the manufactured and feasible geometries, (ii) essential geometric characteristics that are preferable for wire structure heat exchangers, and (iii) differences between optimized wires structures and other types of surface enhancements.

The conclusions of the thesis are summarized in Chapter 7 and appropriate and inappropriate applications of wire structures in heat exchangers are discussed.

2 Foundations

Within this chapter, a classification of wire structure heat exchangers, based on available designs in the literature, is presented. Thereafter, an idealized wire structure design idea for flat-tube heat exchangers is defined. The generic design idea is based on an elementary geometry of parallel wires. The design idea comprises the essential characteristics of available and envisaged wire structure heat exchangers. It is the basis for later simulation and experimental analysis of the performance potential. The chapter continues with the description of thermodynamics and fluid dynamics within compact heat exchangers; with a focus on wire structure heat exchangers. Essential quantities describing the fluid flow are defined.

2.1 Heat Transfer Surface Area Enhancement

2.1.1 Types of Surface Enhancement

The objectives of a surface enhancement are given in Approach 1 to Approach 3 very precisely. However, the execution of designing and manufacturing surface enhancements is very diverse. Concentrating on the first objective in Approach 1, an enhanced heat exchanger should have a large heat transfer surface area per unit volume of the exchanger. The ”classification according to surface compactness” follows this objective. Shah and Sekulić [11] define a compact gas-to-fluid exchanger if it incorporates a heat transfer surface having a surface area density β greater than about $700\,\mathrm{m}^2/\mathrm{m}^3$. Examples of compact gas-to-fluid exchangers are plate-fin, tube-fin, and rotary regenerators. Table 2.1 gives a detailed view of surface enhancements and their surface area

densities used for heat exchangers with gas flow on one or both fluid sides. The list starts with flow interruptions (wavy, offset strip, multilouver, perforated) which increase the heat transfer coefficient to two to four times that for the corresponding plain fin surface [11, p. 37]. Common values for surface area density range up to $1900\,\mathrm{m}^2/\mathrm{m}^3$. Higher values can be achieved with lattice truss or metal foams. Common pin fin geometries for electronic cooling do not allow high surface area densities; however, a huge increase can be achieved when considering micro pin fins. Similarly wire screens used in heat exchangers show small values of surface area density however, smaller wire diameters can yield much higher values. Figure 2.1 shows some examples of surface enhancements.

Enhancement	Common values of β in $\mathrm{m}^2/\mathrm{m}^3$	Source
Wavy, offset strip, multilouver, perforated fins	up to 1500	[11, p. 41]
	up to 1900	internal
Pin fin	500	[12]
Micro pin fin	up to 17000	[13, p. 3618]
Wire screen	1000	[14, p. 1146]
Lattice truss	up to 3400	[15, p. 300]
Metal foams	up to 3200	[7, p. 48]
	up to 6000	[16, p. 2197]
Human lungs	17500	[11, p. 11]

Table 2.1: Selection of surface enhancements for heat exchangers.

Plate-fin and tube-fin geometries with wavy, offset strip, multilouver, or perforated fins are the two most common types of extended surface heat exchangers [11, p. 37].

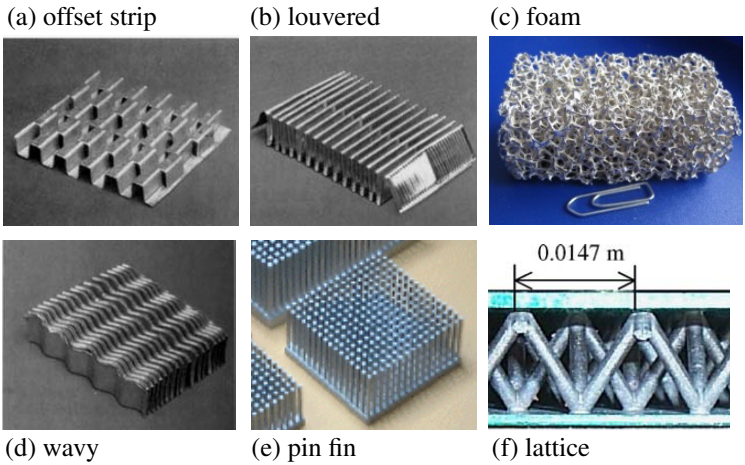

Figure 2.1: Different types of heat exchanger surface enhancements: (a), (b), and (d) from [11], (c) from [17], (e) from [12], and (f) from [18].

2.1.2 Classification of Wire Structure Heat Exchangers

Wire structure heat exchangers can be assigned to different categories of heat exchangers. Referring to the "classification according to construction" in Shah and Sekulić [11, p. 2] wire structure heat exchangers can be found in plate-fin and tube-fin exchangers and in regenerators. Figure 2.2 shows a variety of wire structures assigned to these categories; Figure 2.3 shows examples of these structures in the literature.

Plate-Fin Exchanger Surface

The plate-fin exchanger surfaces are commonly used in gas-to-gas, gas-to-phase change or gas-to-fluid exchangers where either the heat transfer coefficients are low or a high exchanger effectiveness is desired. This construction allows high surface area densities up to $6000\,\mathrm{m}^2/\mathrm{m}^3$ and a considerable amount of flexibility [11, p. 694].

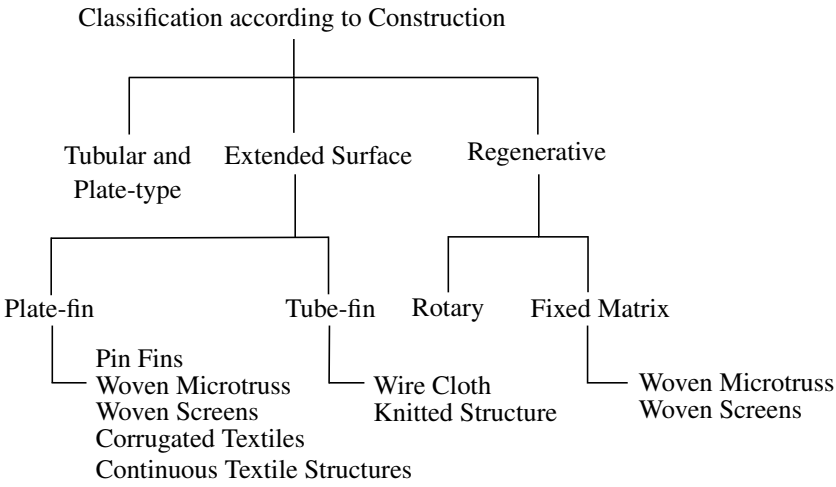

Figure 2.2: Classification of wire structure heat exchangers according to construction.

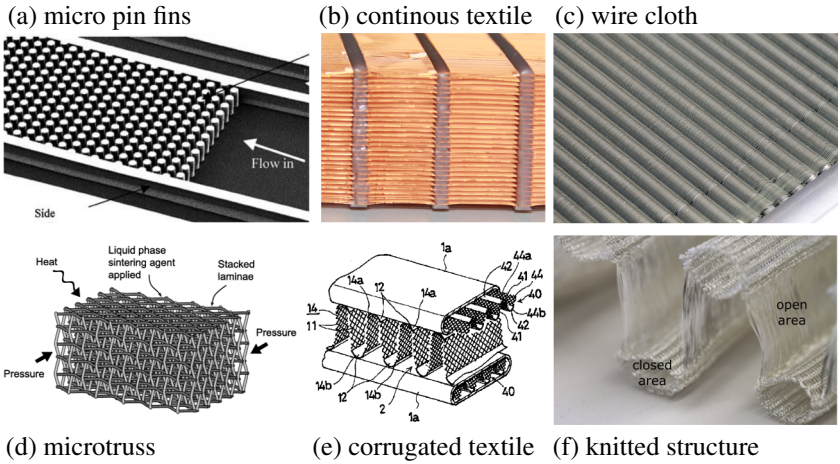

Figure 2.3: Different types of wire structure heat exchangers: (a) from [13], (b) from [19], (c) from [BFS17] (d) from [9], (e) from [20], (f) from [FLS17].

Pin Fins Classical pin fins can be manufactured by casting, metal injection molding [21] or at very high speed continuously from a wire of proper dia-

meter [11, p. 697]. Common pin diameters d_{wire} are in the millimetre range [22], common streamwise spacing ratios $l_{\text{longitudinal}}/d_{\text{wire}}$ are in the range of 2, and common transverse spacing ratios $l_{\text{lateral}}/d_{\text{wire}}$ range from 2 to 7 [22]. Pin length ratios $H_{\text{st}}/d_{\text{wire}}$ are analyzed for values around 10 [23], but are more common between 0.5 and 8 [13]. Classic pin fins are used in electronic cooling devices with free convection [11, p. 697] or forced convection [13]. A large number of studies on forced convection evaluate the thermal-hydraulic performance of pin fins numerically [24, 25] and experimentally [26]. Smaller pin diameters are used in micro pin fins heat exchangers. Heat transfer coefficients for microscale pins with wire diameters below 1 mm are very large [13]. However, heat conduction through the fins can limit the overall heat transfer.

Textile Structures Enhancements in plate-fin exchangers can be based on metallic woven-wire mesh structures [14, 27–29], also referred to as microtruss or screen-fin structures. Periodic metal microtruss laminates based on wire weave [9] make use of the wire orientation and allow fluids to easily pass the structure for efficient cross flow exchange. The woven mesh is contacted to a flat primary surface. A wire structure with continuous non-woven wires is manufactured by Vision4Energy. The market-available air-to-air heat exchanger with a separating plastic wall is patented within [30]. An evaluation of its performance is done numerically by Bonestroo [31]. Corrugated wire structures are described in various patents [20, 32, 33]. However, a public documentation on manufacturing and/or performance could not be found, besides own publications [SLF+14, FLS17, Fug18].

Tube-Fin Exchanger Surface

Textile Structures Wire-on-tube type heat exchangers [34, 35] have to enable contact on rounded surfaces. Some design ideas are specified in patents [36, 37]. The wire diameter in both types of heat exchanger primarily ranges from 0.1 mm to 1 mm.

Wire structure design concepts have been developed for tube-fin heat exchangers in [FLS17]. An advanced manufacturing process is presented therein to "fabricate complex 3-dimensional wire structures that serve as gas-side heat exchanger surface. A combination of knitting and weaving takes place to form the final product with dense domains and coarse domains. The coarse domains serve as heat exchanger surface enhancement where gas flows around the wires. The dense domains are soldered to a primary structure" [FLS17].

A third design is a wire cloth micro heat exchanger. The micro tubes are arranged in one direction and are perpendicularly interlaced with a large number of fine wires by means of a weaving process. Thus, the wire cloth gains a high stability and a high heat transfer surface area [BFS17] and [Tah15, Rin17].

Regenerator

The regenerator is a storage-type heat exchanger. The heat transfer surface or elements are usually referred to as a matrix [11, p. 47ff]. Many fin configurations of plate-fin exchangers and any porous or fibrous material (high specific heat preferred) that provides high surface area density may be used as matrix. Randomly packed woven wire screens and knitted wire structures are frequently used as a matrices. Wire diameters are usually in the order of submillimeters and manufactured from copper, bronze, aluminum and stainless steel. As part of a stirling engine, a wire screen regenerator is one of the most expensive components thereof.

2.1.3 Design Idea

The design idea for a flat-tube wire structure heat exchanger, being analyzed in this thesis, is related to a standard flat tube fin design. The wires are arranged primarily perpendicular to the flat tubes (see Figure 1.1). The design idea is elementary, but generic in (i) the distances of the wires to each other, (ii) height, position and diameter of the wires (see Figure 2.4), (iii) nuber of

wires in flow direction, and (iv) velocities through the wire structure. The generic design idea is used in simulations and is the basis for manufacturing. The design idea comprises the essential characteristics of available and envisaged wire structure heat exchangers. The elementary definition of the design is motivated by the main objective of this thesis on a general estimation of performance of wire structure heat exchangers.

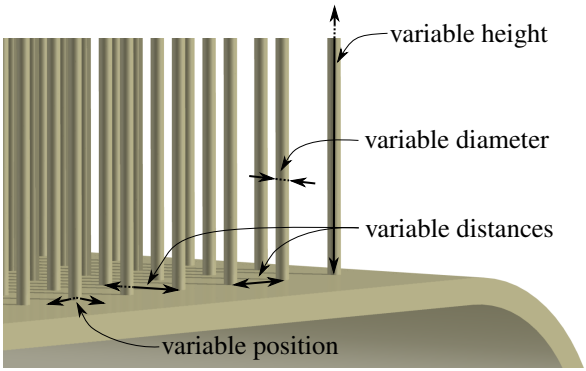

Figure 2.4: Variable geometrical parameters for generic design idea.

The manufacturing can be based on 2D corrugated textile fabrics or single wires cut to length. The bonding of the wires to the tubes can be done by welding or soldering. In each case, the thermal resistance of contact can be a limiting factor. The arrangement of wires is dependent on the manufacturing process and either in-line, staggered, or differently patterned. Different arrangements will change the thermal-hydraulic behaviour of the heat exchanger and thus allow an adoption to a specific application. This study concentrates on air to water heat exchangers. However, due to the use of non-dimensional numbers, results can be transferred to other combinations.

The design specifications for this thesis are related to applications with air cooled condensers, air cooled evaporators, and coolant radiators. Thus, geometric dimensions and operating conditions can be restricted to the values given in Table 2.2.

Parameter	Range	Comment
air frontal velocity	$0.2\,\mathrm{m/s}$ to $10\,\mathrm{m/s}$	lower velocities e.g. for HVAC systems, higher velocities e.g for automotive
air inlet temperatures	$-10\,^{\circ}\mathrm{C}$ to $40\,^{\circ}\mathrm{C}$	winter and summer conditions for ambient air
mean air to fluid temperature difference	$> 2\,^{\circ}\mathrm{C}$	very low heat flux applications excluded
wire diameter	$50\,\mu\mathrm{m}$ to $500\,\mu\mathrm{m}$	strong increase in prices for smaller diameters, insufficient surface area densities for larger diameters
wire length	$5\,\mathrm{mm}$ to $30\,\mathrm{mm}$	too small structure volume (small wire length) yields a relatively high tube volume, too long wires limit thermal conduction
material	aluminum or copper alloys	wire manufacturing and processing well known; thermal conductivity sufficient

Table 2.2: Restrictions of geometric dimensions and operating conditions.

2.2 Fluid Dynamics of Fluid Flow through a Heat Exchanger

2.2.1 Fundamental Equations

The motion of a steady state incompressible fluid can be described by the continuity and Navier-Stokes equations. They are given by

$$\nabla \cdot (\rho \mathbf{u}) = 0, \tag{2.1}$$

$$\rho(\mathbf{u} \cdot \nabla)\mathbf{u} - \mu \Delta \mathbf{u} + \nabla p = 0. \tag{2.2}$$

Therein the fluid velocity is given as the vector $\mathbf{u}$. The density, the dynamic viscosity, and the pressure are represented by ρ, μ, and p, respectively.

In a non-dimensional form the velocity is expressed in terms of the Reynolds number. It is defined as

$$\mathrm{Re} = \frac{vd}{\nu}, \tag{2.3}$$

with ν being the kinematic viscosity (do not mistake the viscosity ν for the velocity v). For the water side of an air-to-water heat exchanger the Reynolds number $\mathrm{Re}_{\mathrm{water}}$ will be based on the characteristic length d_{water} and the mean velocity v_{water} within the tube. For the air-side the central Reynolds number is defined as

$$\mathrm{Re}_{\mathrm{st}} = \frac{v_{\mathrm{st}} d_{\mathrm{st}}}{\nu_{\mathrm{air,st}}}, \tag{2.4}$$

with the mean superficial air velocity in main flow direction within the structure v_{st}, the characteristic length of the air-side structure d_{st}, and the mean kinematic air viscosity $\nu_{\mathrm{air,st}}$. The superficial air velocity v_{st} is a hypothetical flow velocity calculated as if the fluid were the only one present in the given cross sectional area $A_{\mathrm{in,st}}$. The solid part of the structure is disregarded.

The velocity field $\mathbf{u}$ and the pressure scalar p are dependent on the boundary conditions and on the geometry within the fluid domain. Fine geometries, such as porous or wire structures yield a pressure drop within a fluid flowing through the structure. The share related to the structure itself and the share related to inflow and outflow geometry of a heat exchanger shall be discussed next.

2.2.2 Pressure Drop

The pressure drop associated with a heat exchanger Δp_{HX} is considered as a sum of two major contributions [11, Equation 6.28]: Pressure drop associated with the core or matrix, and pressure drop associated with fluid distribution devices such as inlet/outlet headers, manifolds, tanks, nozzles, ducting, and so on. The core pressure drop consists of one or more of the following contributions, depending on the exchanger construction: (i) frictional losses associated with fluid flow over the heat transfer surface, (ii) momentum effect (pressure drop or rise due to the fluid density changes in the core), (iii) pressure drop associated with sudden contraction and expansion at the core inlet and outlet.

The pressure drop Δp_{HX} is split into three parts. Δp_{in} is the pressure drop at the core entrance due to sudden contraction, Δp_{st} the pressure drop within the core structure, and Δp_{out} the pressure rise at the core exit. Usually, Δp_{st} is the largest contribution to the total pressure drop of the heat exchanger:

$$\Delta p_{\mathrm{HX}} = \Delta p_{\mathrm{st}} + \Delta p_{\mathrm{in}} - \Delta p_{\mathrm{out}}. \tag{2.5}$$

The pressure drop within the core structure Δp_{st} consists of two contributions: (i) the pressure change due to the momentum rate change in the core structure, and (ii) the pressure loss caused by fluid friction:

$$\Delta p_{\mathrm{st}} = \frac{G_{\mathrm{st}}^2}{2\rho_{\mathrm{air,in}}} \left[\underbrace{2\left(\frac{\rho_{\mathrm{air,in}}}{\rho_{\mathrm{air,out}}} - 1\right)}_{\text{momentum effect}} + \underbrace{f_{\mathrm{st}} \frac{4L_{\mathrm{st}}}{d_{\mathrm{st}}} \frac{\rho_{\mathrm{air,in}}}{\rho_{\mathrm{air,st}}}}_{\text{core friction}} \right], \tag{2.6}$$

with the core structure mass velocity

$$G_{\mathrm{st}} = \rho_{\mathrm{air,st}} v_{\mathrm{st}} = \frac{\dot{m}_{\mathrm{air}}}{A_{\mathrm{in,st}}}, \tag{2.7}$$

the Fanning friction factor f_{st}, and the structure length L_{st} (see Figure 4.1).

The core entrance pressure drop Δp_{in} consists of two contributions: (i) the pressure drop due to the flow area change, and (ii) the pressure losses associated with free expansion that follow sudden contraction.

$$\Delta p_{\mathrm{in}} = \frac{G_{\mathrm{st}}^2}{2\rho_{\mathrm{air,in}}} \left[1 - \sigma^2 + K_c\right] \tag{2.8}$$

Pressure drop due to (i) is based on the ratio of core minimum free-flow area to heat exchanger inlet area, defined as

$$\sigma = \frac{A_{\mathrm{in,st}}}{A_{\mathrm{in,HX}}}. \tag{2.9}$$

Pressure drop due to (ii) is taken into account by the contraction loss coefficient K_c.

The core exit pressure rise Δp_{out} consists of two contributions: (i) the pressure rise due to the deceleration associated with an area increase, and (ii) pres-

sure losses associated with the irreversible free expansion and momentum rate changes following an abrupt expansion.

$$\Delta p_{\text{out}} = \frac{G_{\text{st}}^2}{2\rho_{\text{air,out}}} \left[1 - \sigma^2 - K_e\right] \tag{2.10}$$

Pressure drop due to (ii) is taken into account by the exit loss coefficient K_e.

Within this study values for K_c and K_e are based on data from Kays and London [11, p. 386].

Equation (2.5) was reduced for simulation to obtain the Fanning friction factor f_{st}. Air is treated as an incompressible fluid, and the density of air $\rho_{\text{air,st}}$ is treated as constant according to an average air temperature. The simplified equation is [38]:

$$f_{\text{st}} = \frac{d_{\text{st}}}{4L_{\text{st}}} \left[\frac{2\Delta p_{\text{HX}}}{\rho_{\text{air,st}} v_{\text{st}}^2} - (K_c + K_e)\right]. \tag{2.11}$$

The sum of K_c and K_e can be linearly approximated for $0.5 < \sigma < 1$ (for laminar flow) by [11, Page 386]:

$$K_c + K_e = 1.52(1 - \sigma) \tag{2.12}$$

2.3 Thermodynamics of Fluid Flow through a Heat Exchanger

The heat transfer is determined predominately by two processes: (i) The convection on both fluid sides, strongly related to the velocity field and (ii) the conduction within the tube walls and the heat transfer surface enhancement.

2.3.1 Convection

The temperature distribution within the fluid is described by the heat equation

$$\rho c_p \mathbf{u} \cdot \nabla T + \nabla \cdot (k \nabla T) = 0. \tag{2.13}$$

Based on the air-side and water-side temperature field, the heat transfer rate $\dot{Q}_{\mathrm{HX}}$ of a air-to-water heat exchanger required for calculation of air-side performance characteristics can be determined with three different (but coupled) equations.

$$\dot{Q}_{\mathrm{HX}} = \dot{m}_{\mathrm{air}} c_{p,\mathrm{air}} \Delta T_{\mathrm{air}}, \tag{2.14}$$

$$\dot{Q}_{\mathrm{HX}} = \dot{m}_{\mathrm{water}} c_{p,\mathrm{water}} \Delta T_{\mathrm{water}}, \tag{2.15}$$

$$\dot{Q}_{\mathrm{HX}} = U_{\mathrm{HX}} A_{\mathrm{HTS}} \Delta T_{\mathrm{m}}. \tag{2.16}$$

Experimentally or simulatively determined data comprises in general the mass flow rates on the air-side $\dot{m}_{\mathrm{air}}$, resp. water side $\dot{m}_{\mathrm{water}}$, the specific heat capacities $c_{p,\mathrm{air}}$ and $c_{p,\mathrm{water}}$, and the temperature differences within the fluids ΔT_{air} and $\Delta T_{\mathrm{water}}$. Thus, Equations (2.14) or (2.15) provide the heat transfer rate $\dot{Q}_{\mathrm{HX}}$. The overall heat transfer coefficient U_{HX} is related to the heat transfer

surface area A_{HTS} on the air-side and the true (or effective) mean temperature difference ΔT_{m} [11] between the fluids:

$$\Delta T_{\mathrm{m}} = \Delta T_{\log} F \tag{2.17}$$

The correction factor F can be determined based on the flow configuration and the operating conditions. The data for $\Delta T_{\log}$ and A_{HTS} can be determined experimentally or simulatively. Based on the inlet/outlet temperatures of the two fluids, the parameter $\Delta T_{\log}$ is calculated by

$$\Delta T_{\log} = \frac{(T_{\mathrm{air,in}} - T_{\mathrm{water,out}}) - (T_{\mathrm{air,out}} - T_{\mathrm{water,in}})}{\log \frac{T_{\mathrm{air,in}} - T_{\mathrm{water,out}}}{T_{\mathrm{air,out}} - T_{\mathrm{water,in}}}}. \tag{2.18}$$

Thus, a combination of Equation (2.14) or (2.15) with Equation (2.16) results in U_{HX}.

The air-side convection heat transfer coefficient h_{air} can be obtained from

$$\frac{1}{U_{\mathrm{air,eff}} A_{\mathrm{HTS}}} = \frac{1}{\eta_0 h_{\mathrm{air}} A_{\mathrm{HTS}}} = \frac{1}{U_{\mathrm{HX}} A_{\mathrm{HTS}}} - \frac{1}{h_{\mathrm{water}} A_{\mathrm{HTS,water}}} - \frac{\delta_{\mathrm{wall}}}{k_{\mathrm{wall}} A_{\mathrm{wall}}}. \tag{2.19}$$

The second term on the right-hand-side of Equation (2.19) indicates the water side thermal resistance; the third term indicates the tube wall thermal resistance. Again, for experimental work or simulation the right hand side of (2.19) is known. The extended surface efficiency η_0 is given in [11] for e.g. louvered and pin fins and expresses the reduction in heat transfer due to limitation in heat conduction through the heat transfer surface area enhancement. Since the extended surface efficiency η_0 is a function of convection heat transfer coefficient h_{air}, the value for h_{air} can be obtained only iteratively. If a separation of convection (h_{air}) and conduction (η_0) is not possible or not necessary, an effective parameter $U_{\mathrm{air,eff}}$ combines these two resistances.

The convection heat transfer coefficient h_{air} describes a mean air-side heat transfer on the primary surface A_p (tube outer wall) and on the structure surface A_{st}, with $A_{\text{HTS}} = A_p + A_{\text{st}}$. Based on simulations or correlations it is possible to split the convection heat transfer coefficient h_{air} into two parts: (i) On the primary surface the convective heat transfer coefficient is defined as h_{p} and (ii) on the secondary (structure) surface it is defined as h_{st}. It holds

$$U_{\text{air,eff}} A_{\text{HTS}} = \eta_{\text{fin}} h_{\text{st}} A_{\text{st}} + h_{\text{p}} A_{\text{p}} = \eta_0 h_{\text{air}} A_{\text{HTS}}. \tag{2.20}$$

In this study two cases are considered:

Case 1 The primary heat transfer coefficient h_{p} is negligibly small and/or the primary surface A_{p} is negligibly small. Then it holds

$$A_{\text{HTS}} = A_{\text{st}},$$
$$h_{\text{air}} = h_{\text{st}},$$
$$\eta_0 = \eta_{\text{fin}}.$$

Case 2 The primary heat transfer coefficient h_{p} is in the same order as h_{st} and/or the primary surface A_{p} is negligibly small. Then it holds

$$A_{\text{HTS}} = A_{\text{st}} + A_{\text{p}},$$
$$h_{\text{air}} = h_{\text{st}} = h_{\text{p}},$$
$$\eta_0 = 1 - \tfrac{A_{\text{st}}}{A_{\text{HTS}}}(1 - \eta_{\text{fin}}) \text{ (cf Eq. (2.30))}.$$

The situation for Case 1 can be found for geometries with high wire lengths and/or very dense wire arrangement. The situation for Case 2 can be found for shorter wire lengths and/or more open wire arrangement.

Based on the dimensional convection heat transfer coefficient a non-dimensional quantity can be defined: The Nusselt number. It expresses the convective heat transfer versus the conductive heat transfer. In this study it is defined on the water side as

$$\text{Nu}_{\text{water}} = \frac{h_{\text{water}} d_{\text{water}}}{k_{\text{water}}}, \tag{2.21}$$

and on the air-side as

$$\mathrm{Nu}_{\mathrm{air}} = \frac{h_{\mathrm{air}} d_{\mathrm{st}}}{k_{\mathrm{air,st}}}. \tag{2.22}$$

For calculation of heat transfer rates the number of transfer units $\mathrm{ntu}_{\mathrm{air}}$ and the effectiveness ϵ_{air} are helpful quantities. For the air-side they are defined as:

$$\mathrm{ntu}_{\mathrm{air}} = \frac{h_{\mathrm{air}} A_{\mathrm{HTS}}}{\dot{m}_{\mathrm{air}} c_{p,\mathrm{air}}} = \frac{\mathrm{Nu}_{\mathrm{air}}}{\mathrm{Re}_{\mathrm{st}} \mathrm{Pr}_{\mathrm{air}}} \frac{A_{\mathrm{HTS}}}{A_{\mathrm{in,st}}}, \tag{2.23}$$

$$\epsilon_{\mathrm{air}} = \frac{T_{\mathrm{air,in}} - T_{\mathrm{air,out}}}{T_{\mathrm{air,in}} - T_{\mathrm{water,in}}}. \tag{2.24}$$

2.3.2 Conduction

The heat transfer rate into the fins can be presented by the concept of fin efficiency η_{fin}, comparing actual heat transfer rate with an idealized heat transfer rate with non-limiting conduction. The fin efficiency is described by Shah and Sekulić [11, p. 283] for pin fin structures and is adopted here for the wires:

$$\eta_{\mathrm{fin}} = \frac{\tanh(ml)}{ml}, \tag{2.25}$$

with

$$l = \frac{H_{\mathrm{st}}}{2}, \tag{2.26}$$

$$m = \left(\frac{4 h_{\mathrm{st}}}{k_{\mathrm{st}} d_{\mathrm{st}}} \right)^{0.5}, \tag{2.27}$$

whereas d_{st} is the wire diameter and H_{st} is the wire height from the upper to the lower tube (see Figure 4.1). The product of m and l determine the

fin efficiency. The product will be defined as κ. Its dependency on non-dimensional parameter ratios is given by:

$$\kappa = ml = \frac{H_{st}}{d_{st}} \left(\frac{k_{air,st}}{k_{st}} \frac{h_{st} d_{st}}{k_{air,st}} \right)^{0.5}. \tag{2.28}$$

Thus, η_{fin} is based on (i) the non-dimensional geometric parameter $c = {H_{st}}/{d_{st}}$; (ii) the non-dimensional ratio of thermal conductivities $\chi_{st,air} = {k_{st}}/{k_{air,st}}$; and (iii) the non-dimensional Nusselt number $\mathrm{Nu}_{st} = {h_{st} d_{st}}/{k_{air}}$.

In most tube-fin designs, there is also a primary surface exposed to the fluid along with the fins (secondary surface). The heat transfer performance of this extended surface is measured by an extended (or overall) surface efficiency η_0, defined as

$$\eta_0 = \frac{\dot{Q}_{total}}{\dot{Q}_{max}}. \tag{2.29}$$

Here $\dot{Q}_{max}$ is associated with a perfect fin having (i) the same geometry as the actual fin; (ii) the same operating conditions; and (iii) infinite thermal conductivity k_{st} of the fin material. Under these circumstances, the perfect fin is at the uniform base temperature T_{wall} and heat transfer rate is higher than with real thermal conductivity k_{st}.

Combining Equation (2.25) and (2.29) results in [11, p. 289]

$$\eta_0 = 1 - \frac{A_{st}}{A_{HTS}} (1 - \eta_{fin}). \tag{2.30}$$

Limitations related to the simplified definition of heat conduction in terms of a fin efficiency will be discussed later in Section 4.5.

2.4 Fluid- and Thermodynamics of Laminar Flow around Parallel Wires

The flow around the wires is considered to be laminar for the analyzed geometry and operating conditions specified in Table 2.2 [39, 40]. The geometry of parallel wires can be described as well as pin fins, circular cylinders or bank of tubes. However, care has to be taken with the dimensions.

The flow around a singular wire is described in [41, ch. Gf, p. 521] and [40, 42, 43]. For singular wires and Reynolds numbers $\mathrm{Re}_{\mathrm{st}}$ beyond 5 and up to 48, measurement data [44] show that "the flow separates on the cylinder surface and the wake behind the cylinder consists of a pair of symmetric contra-rotating vortices on either side of the wake centreline. Further it was observed that as the flow Reynolds number increases, the length of the closed wake L_{wake} increases" [40]. The ratio of closed wake length and cylinder diameter is shown in Figure 2.5.

For a flow through a wire structure the distances between the wires in flow direction might be smaller than the specified closed wake length in Figure 2.5 and the wire distance normal to flow direction influences the flow behaviour additionally. Thus, the fluid flow through the wire structure differs from the flow across a singular wire. The two extreme cases of wire structure arrangement are (i) an in-line and (ii) a staggered arrangement of the wires. "Fluid flow across the first row of pins resembles the flow across a singular fin for both in-line and staggered pin arrangements. For the second and subsequent rows, the flow patterns are specific for each arrangement. For the staggered arrangement, the nature of the flow over the inner rows differs only slightly from that over the first row [...]. [For the in-line arrangement] a substantial part of the fluid flows through the longitudinal passage between the pins" [45].

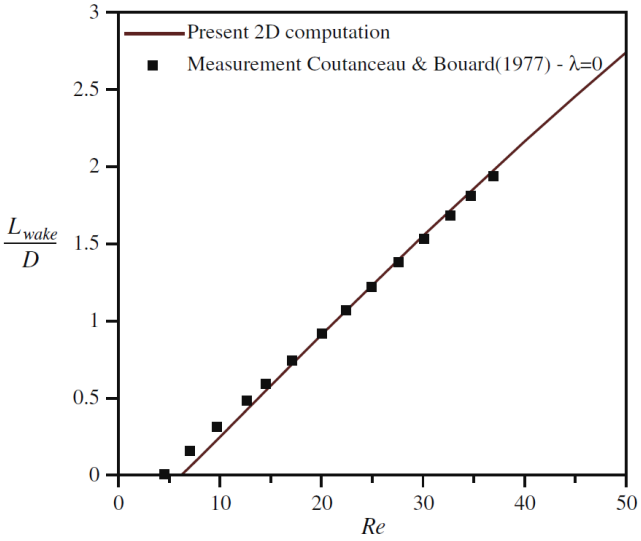

Figure 2.5: Simulation data with 2D computation from [44] and experimental measurement data from [40] for the ratio of closed wake length L_{wake} and wire diameter D as a function of Reynolds number Re_{st}; based on [40].

2.4.1 Correlations in the Literature

Correlations for flow around a single wire can be found in [42]. The impact on neighbouring wires can not be neglected for the wire structure heat exchanger. Thus, these correlations can only be used for validation of simulations of flow around single wires.

"Within the VDI-Wärmeatlas [41] correlations for Nusselt number based on Reynolds numbers below 100 and non-dimensional wire distances below 4 can be found from various authors. However, according to the source of the correlation [46, 47], the corresponding measurements were taken at Reynolds numbers above 1000 for a Prandtl number in the required range of 1 (gas). Thus, the correlation does not include the" [FSF19] targeted operation range

of Reynolds number between 3 and 100 for wire structure heat exchangers in this study.

Bacellar et al. [48] shows a comparison of CFD-Simulation and existing correlations for the airside friction and heat transfer characteristics for staggered tube bundle in crossflow configuration with diameters from 0.5 mm to 2 mm. Similar configurations are presented in [49–51]. A transformation to operating and geometry conditions for wire structure heat exchanger is not possible, due to geometrical dimension much larger than for the wire structures (factor 10).

Due to the insufficient availability of correlations for thermal-hydraulic performance within a wire structure for the specified operating and geometry conditions, own correlations will be developed within this study in Section 4.4.

3 Performance Evaluation Criteria for Surface Area Enlargement

This chapter is based on the publication *Multi-Dimensional Performance Evaluation of Heat Exchangers* [FLS19]. Within the chapter "a method for comparing different types of enhancement and different geometries with multiple objectives is developed in order to evaluate new and existing enhancement designs. The method's objectives are defined as energy, volume, and mass efficiency of the enhancement. They are given in dimensional and non-dimensional form and include limitations due to thermal conductivity within the enhancement. The transformation to an explicit heat transfer rate per dissipated power, volume, or mass is described in detail. The objectives are visualized for different Reynolds numbers to locate beneficial operating conditions" [FLS19]. As a result, a performance evaluation method is available to compare wire structure heat exchanger geometries among themselves and with other surface enhancements.

3.1 Discussion on Performance Evaluation Criteria in the Literature

"Several different methods are described in the literature on the evaluation of heat exchanger performance. As the benefits and drawbacks of a surface change can be very complex and multidimensional, a simple method of performance evaluation will not be comprehensive. The focus of this discussion shall be on different evaluation methods in the literature and the integration of (i) a heat transfer limitation due to low thermal conductivity through the fins

and (ii) variable objectives within the method. The former information (i) is necessary for a broader study of geometry variation of surface area enhancements; the enhancement yields, at some geometrical design point, always a limitation of the heat transfer due to low thermal conductivity of the fins. If this is not represented in an evaluation method, the feasible set of possible geometries must be specified very restrictively.

Stone [3] gives a comprehensive review of existing methods, simple as well as more complex ones. The method of 'j and f vs. curves' is among them. It shows curves of the Colburn factor j and the friction factor f, plotted versus the Reynolds number or the reciprocal of an equivalent diameter. The values tend to vary over a wide range [52] or have a large scattering, such that the method is applicable with restrictions [3]. The fin efficiency or an equivalent description of conductivity through the fins is not part of the method.

A second method describes the goodness criteria [53]. In the area goodness factor method, the ratio of the Colburn factor and the Fanning friction factor is plotted versus the Reynolds number. The consequence of this definition is that 'a surface having a higher j/f factor is good because it will require a lower free-flow area and hence a lower frontal area for the exchanger' [11, p. 705]. However, 'no significant variation is found in the j/f ratio' [11, p. 705], such that the free-flow area is hardly changing for various surfaces. But the volume of a heat exchanger is very sensitive to a surface change. The volume goodness factor for surfaces with different characteristic lengths expresses the capability to transfer heat ($\eta_0 h_{\mathrm{std}} \beta$) versus the dissipated power per volume ($E_{\mathrm{std}} \beta$). The same fluid flow rate is required for comparison. Then, 'for constant $E_{\mathrm{std}} \beta$, a surface having a high plot of $\eta_0 h_{\mathrm{std}} \beta$ vs. $E_{\mathrm{std}} \beta$ is characterized as the best from the viewpoint of heat exchanger volume' [11, p. 707]. A screening method is presented by Webb and Kim [54] with a collection of performance evaluation criteria (PEC). They are partitioned into fixed geometry (FG), fixed flow area (FN), and variable geometry (VG) criteria. The idea is to replace a plain

surface by an enhanced surface, while keeping some boundary conditions constant and, thereafter, to compare the thermal-hydraulic characteristics.

Two dimensionless performance parameters are defined by LaHaye et al. [52] referring to the j and f vs. Curves method. The two parameters are the heat transfer performance factor $J = j\mathrm{Re}$ and the pumping power factor $F = f\mathrm{Re}^3$. The parameters are plotted versus each other. The effects of fin thickness (and thermal conductivity through the fin) have not been accounted for in that method.

The extension of this method by Soland [55] with reference to more general dimensions of the heat exchanger (plate-fin) also lacks inclusion of the fin efficiency. The benefit of the method is that a 'comparison of many surfaces to a single common smooth plate nominal diameter permits a relative comparison between surfaces having different nominal diameters' [55, p. 38]. Several different types of plate-fin surfaces can be considered with this method.

The general comparison methods developed by Cowell [56] show 'how measures for the relative value of required hydraulic diameter, frontal area, total volume, pumping power, and number of transfer units for different surfaces can be derived and displayed' [56]. Two or three of these parameters are kept constant, while the others can be varied and calculated based on the formulas given by Cowell. The effects of the fin efficiency are ignored.

Sahiti et al. [57] suggest to show the quotient of the heat transfer rate and the heat exchanger volume versus the quotient of the required power input and the heat exchanger volume. This method resembles the ranking performance method [55] and uses the number of transfer units to continue calculation of the heat transfer rate. Wherever possible, Sahiti et al. recommends to take into account the additional thermal resistances (fins, second fluid) in the calculation of the number of transfer units.

A comparison of enhancements with some of the methods above is given in [58] for a variety of enhancements. Marthinuss [59] compares five different enhancements given in [11], including volume and mass efficiency.

Table 3.1 shows a summary of the main assets and the integration of thermal conductivity through the fins of the methods presented above.

Method	**Sources**	**Assets**	**Inclusion of conductivity**
j and f vs. curves	[3, 52]	simple visualization of the thermal-hydraulic performance	no
Area goodness factor	[3, 11]	identification of feasible surfaces with low free-flow area	no
Volume goodness factor	[11]	identification of feasible surfaces with low volume	yes
Performance evaluation criteria (PEC)	[54]	designer-specific choice of evaluation criteria	(yes)*
Performance parameters	[3, 52]	convenient method for comparing various heat transfer geometries in one figure	no
Ranking performance	[55]	comparison of very different fin types with respect to different designer conditions	no
General comparison method	[56]	designer-specific choice of evaluation criteria	no
Energetic comparison	[57]	no volume or surface geometry constraints	yes

Table 3.1: Methods for performance evaluation retrieved from the literature, with the main assets and information on whether thermal conductivity of the fins is integrated in the method or not; based on [FLS19]. *The general formulation includes thermal conductivity of the fins.

From the literature review, a lack in performance evaluation methods including thermal conductivity within the fins can be seen. However, the two methods of volume goodness factor [11] and energetic comparison [57] consider the thermal conductivity. Although they have drawbacks in the choice of the objectives, the fundamental concepts of the methods shall be taken and extended in the following analysis. The extension includes an evaluation of the dissipated power, volume, and mass with respect to the heat transferred." [FLS19].

3.2 Multi-dimensional Performance Evaluation Criteria

"Multi-dimensional performance evaluation criteria would allow a many-faceted view on heat exchangers. However, a too broad view on a subject prevents a clear understanding of coherences. Thus, a multi-dimensional approach requires restrictions. In this study, the focus is on one fluid side (fluid 1) and several restrictions are set on the heat exchanger comparison. When two or more heat exchangers are compared, they should have the same thermal-hydraulic scale, defined as restriction R1 to R5:

R1 the same heat transfer fluids,

R2 the same inlet temperatures T_{in} and pressures p_{in},

R3 the same mass flow rates $\dot{m}$,

R4 the same heat transfer rates $\dot{Q}$,

R5 the same small thermal resistances on the second fluid side.

The values above can be chosen arbitrarily, but must then be fixed. The compared heat exchangers might differ in the actual design costs, defined as

- dissipated power P_{diss},
- structure volume V_{st},
- structure mass m_{st}.

The development of the method will be based on air as fluid 1, but can be transferred to other fluids. The dissipated power $P_{\mathrm{diss}} = \Delta p_{\mathrm{st}} \dot{V}_{\mathrm{air,st}}$ is the product of the pressure drop within the core structure Δp_{st} (cf. Eq. 2.6) and the volume flow rate through the structure $\dot{V}_{\mathrm{air,st}}$. The relation to the electric power consumption P_{el} is given by $P_{\mathrm{diss}} = \eta_{\mathrm{fan,system}} P_{\mathrm{el}}$. The fan system efficiency $\eta_{\mathrm{fan,system}}$ includes the aerodynamic, mechanical, and motor losses. The structure volume V_{st} is equal to the product of the structure frontal area $A_{\mathrm{in,st}}$ and the structure length L_{st}. In this study, the focus is on the comparison of heat exchangers with equal $A_{\mathrm{in,st}}$ (and thus equal velocities through the structure), but is not limited to this. Both parameters $A_{\mathrm{in,st}}$ and L_{st} can vary.

With the above restrictions, the mean fluid properties for the compared heat exchangers are equal and the heat transfer rate $\dot{Q}$ can be expressed according to Equation (2.16) by

$$\dot{Q} = \eta_0 h A_{\mathrm{HTS}} \Delta T_{\mathrm{m}}, \tag{3.1}$$

with the extended surface efficiency η_0 (Equation (2.30)), the heat transfer coefficient h, the heat transfer surface area A_{HTS}, and the mean temperature difference between the fluids ΔT_{m}.

Simplification allows comparing the heat exchangers at equal $\eta_0 h A_{\mathrm{HTS}}$, instead of equal heat transfer rate $\dot{Q}$, as long as ΔT_{m} in Equation (3.1) is constant (which is ensured by restrictions R1 to R5). The product $\eta_0 h A_{\mathrm{HTS}}$ is defined as benefit of the heat transfer process and it is related to different costs in (i) a dimensional straightforward way and in (ii) a non-dimensional way allowing more general statements." [FLS19].

3.2.1 Definition of Dimensional Evaluation Criteria

"The dimensional criteria shall relate the benefit to different types of costs, which are linked to operational costs (e.g. driven by the dissipated power or

mass) and investment costs (e.g. driven by the volume or mass). Details are given in Table 3.2.

Cost	**Key Figure**	**Def.**	**Altern. Def.**	**Dim.**
Dissipated power on the air-side $\Delta p_{\mathrm{st}} \dot{V}_{\mathrm{air,st}}$ in W, which is proportional to the electric power consumption of the fans	Energy efficiency ϵ_{E}	$\frac{\eta_0 h_{\mathrm{air}} A_{\mathrm{HTS}}}{\Delta p_{\mathrm{st}} \dot{V}_{\mathrm{air,st}}}$	$\frac{\dot{Q}}{P_{\mathrm{diss}}} \frac{1}{\Delta T_{\mathrm{m}}}$	$1/\mathrm{K}$
Available volume for heat transfer enhancement V_{st} in m^3 (excluding fluid guidance volume and header/distributor)	Volume efficiency ϵ_{V}	$\frac{\eta_0 h_{\mathrm{air}} A_{\mathrm{HTS}}}{V_{\mathrm{st}}}$	$\frac{\dot{Q}}{\dot{V}_{\mathrm{st}}} \frac{1}{\Delta T_{\mathrm{m}}}$	$\mathrm{W}/(\mathrm{m}^3\,\mathrm{K})$
Material usage for the wire or fin structure m_{st} in kg (excluding fluid guidance, solder material and header/distributor)	Mass efficiency ϵ_{M}	$\frac{\eta_0 h_{\mathrm{air}} A_{\mathrm{HTS}}}{m_{\mathrm{st}}}$	$\frac{\dot{Q}}{m_{\mathrm{st}}} \frac{1}{\Delta T_{\mathrm{m}}}$	$\mathrm{W}/(\mathrm{kg}\,\mathrm{K})$

Table 3.2: Key figures for extended performance evaluation; defined as benefit $\eta_0 h_{\mathrm{air}} A_{\mathrm{HTS}}$ per cost. The main definition and the alternative definition are equivalent, but differ in the input parameters; based on [FLS19].

These key figures can be presented based on performance measurement data or correlations found in the literature. However, a comparison with the restrictions R1 to R5 requires equal temperature and pressure conditions, which are difficult to achieve during measurement. Thus, a non-dimensioning of the defined key figures could allow a more easy implementation of data, with the drawback of a less accessible output." [FLS19].

3.2.2 Definition of Non-Dimensional Evaluation Criteria

"The transformation from dimensional into non-dimensional evaluation criteria requires parameters such as the Reynolds number, the Nusselt number, and the Fanning friction factor (cf. Equations (2.4), (2.22), and (2.11), respectively), as well as the surface area density

$$\beta = \frac{A_{\mathrm{HTS}}}{V_{\mathrm{st}}}, \tag{3.2}$$

and the structure porosity

$$\varphi_{\mathrm{st}} = \frac{V_{\mathrm{st}} - V_{\mathrm{st,mat}}}{V_{\mathrm{st}}}. \tag{3.3}$$

The dependencies of the non-dimensional parameters $\mathrm{Nu}_{\mathrm{air}}$, f_{st}, and η_0 on each other and on additional parameters are given in Appendix A.3.1.

The non-dimensional energy efficiency $\epsilon_{\mathrm{E}}^{*}$ will now be defined. It is a novel combination of area and volume goodness factor [11] and the dimensional energy efficiency ϵ_{E}:

$$\epsilon_{\mathrm{E}}^{*} = \frac{\dot{Q}}{P_{\mathrm{diss}}}\mathrm{Br}, \tag{3.4}$$

with Brinkman number

$$\mathrm{Br} = \frac{\mu_{\mathrm{air,st}} v_{\mathrm{st}}^2}{k_{\mathrm{air,st}} \Delta T_{\mathrm{m}}}. \tag{3.5}$$

The Brinkman number expresses the ratio between the viscous dissipation power and the heat transported by molecular conduction. Based on restrictions R1 to R5, the Brinkman number is equal for the comparison of different heat exchangers with equal structure frontal area $A_{\mathrm{in,st}}$. From the right-hand side term in Eq. (3.4), the idea of $\epsilon_{\mathrm{E}}^{*}$ should become clearer: The benefit versus cost ratio of $\dot{Q}$ and P_{diss} is reduced by each driving force, which is $k_{\mathrm{air,st}} \Delta T_{\mathrm{m}}$ on

the thermal side and $\mu_{\text{air,st}} v_{\text{st}}^2$ on the dynamic side. The higher the parameter ϵ_{E}^*, the less power is dissipated.

The value of ϵ_{E}^* has no evident upper limit. For a fully developed laminar flow through a smooth circular duct, ϵ_{E}^* equals 0.46, and for the turbulent flow, ϵ_{E}^* is bounded by 0.81. The thermal-hydraulic correlations used to calculate these values are given in [11, p. 476,p. 482]: $\text{Nu}_T = 3.657$ and $f\text{Re} = 16$ for the laminar case and the Bhatti-Shah and Gnielinski correlations for the turbulent case. The curves are shown in Figure 3.1 (b) for a Reynolds number based on a duct diameter in the range of $10 \leq \text{Re}_{\text{st}} \leq 10^6$. The value of ϵ_{E}^* for the laminar case is constant; the value for the turbulent case increases first, with a maximum at $\text{Re}_{\text{st}} = 6 \times 10^4$, and slowly decreases thereafter. The transition regime in the range of $2000 \leq \text{Re}_{\text{st}} \leq 4000$ is not shown due to strong differences within different correlations in this regime. A comparison between heat exchangers takes place at constant (or similar) Reynolds numbers (cf. restrictions R1 to R5). Thus, Figure 3.1 (b) should not misdirect to a statement on whether turbulent flow is more energy efficient than laminar flow. In order to emphasize this point, Figure 3.1 (a) shows the dimensional energy efficiency defined in Table 3.2.

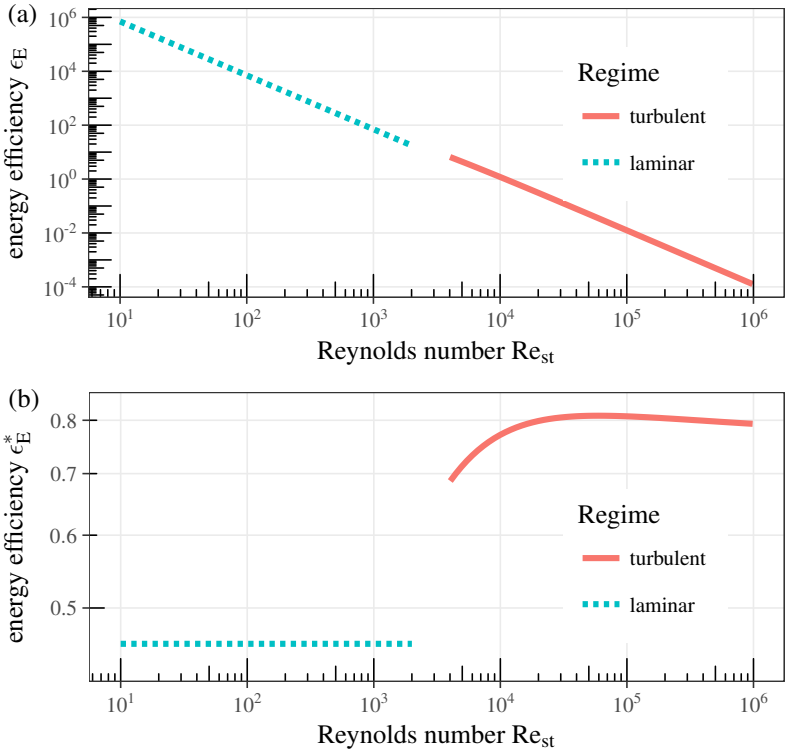

Figure 3.1: Dimensional (a) and non-dimensional (b) energy efficiency ϵ_E and ϵ^*_E, respectively, versus Reynolds number Re_{st} for a fully developed laminar and turbulent flow in a smooth circular duct; air is used in (a) as fluid at 25 °C and 1 atm with a duct diameter of 5 mm; the transition flow is not shown. Data is based on [11] and [FLS19].

The non-dimensional way of accounting for energetic performance is given in Table 3.3 with additional calculation formulas for ϵ^*_E. The volume and mass efficiencies are included as well. Their derivation is given in Appendix A.1.1. Similar to the definition of ϵ^*_E, the non-dimensional volume efficiency ϵ^*_V is the product of $\dot{Q}/\dot{V}_{st}$ and a driving parameter; and the non-dimensional mass efficiency ϵ^*_M is the product of $\dot{Q}/\dot{m}_{st}$ and another driving parameter." [FLS19].

Key figure	Definition	Relation to dimensional parameter	Reduced expression
ϵ^*_{E}	$\frac{\dot{Q}}{P_{\mathrm{diss}}}\mathrm{Br}$	$\epsilon_{\mathrm{E}}\ \mathrm{Br}\Delta T_{m,\mathrm{HX}}$	$\frac{\mathrm{Nu}_{\mathrm{air}}}{2\mathrm{f}_{\mathrm{st}}}\eta_0\frac{d_{\mathrm{st}}\beta}{\mathrm{Re}_{\mathrm{st}}}$
ϵ^*_{V}	$\frac{\dot{Q}}{\dot{V}_{\mathrm{st}}}\frac{\nu^2_{\mathrm{air,st}}}{v^2_{\mathrm{st}}k_{\mathrm{air,st}}\Delta T_{\mathrm{m,HX}}}$	$\epsilon_{\mathrm{V}}\ \frac{\nu^2_{\mathrm{air,st}}}{v^2_{\mathrm{st}}k_{\mathrm{air,st}}}$	$\frac{\mathrm{Nu}_{\mathrm{air}}}{\mathrm{Re}_{\mathrm{st}}}\eta_0\frac{d_{\mathrm{st}}\beta}{\mathrm{Re}_{\mathrm{st}}}$
ϵ^*_{M}	$\frac{\dot{Q}}{\dot{m}_{\mathrm{st}}}\frac{\rho_{\mathrm{air,st}}\nu^2_{\mathrm{air,st}}}{v^2_{\mathrm{st}}k_{\mathrm{air,st}}\Delta T_{\mathrm{m,HX}}}$	$\epsilon_{\mathrm{M}}\ \frac{\rho_{\mathrm{air,st}}\nu^2_{\mathrm{air,st}}}{v^2_{\mathrm{st}}k_{\mathrm{air,st}}}$	$\frac{\mathrm{Nu}_{\mathrm{air}}}{\mathrm{Re}_{\mathrm{st}}}\eta_0\frac{d_{\mathrm{st}}\beta}{\mathrm{Re}_{\mathrm{st}}}\frac{\rho_{\mathrm{air,st}}}{\rho_{\mathrm{st}}(1-\varphi_{\mathrm{st}})}$

Table 3.3: Non-dimensional key figures for extended performance evaluation; based on [FLS19].

"From the 'reduced expression' in Table 3.3, Section 2.3.2 and Appendix A.3.1, it can be seen, that all three efficiencies ϵ^* are solely dependent on the Reynolds number $\mathrm{Re}_{\mathrm{st}}$, on the ratio of the thermal conductivities $k_{\mathrm{air,st}}/k_{\mathrm{st}}$, on the Prandtl number, and on the non-dimensional geometry. The key figure ϵ^*_{M} is, in addition, dependent on the ratio of the densities $\rho_{\mathrm{air,st}}/\rho_{\mathrm{st}}$.

Further inspection of ϵ^* shows that they are defined such that they are independent of the choice of the characteristic length. Thus, for a fixed geometry, fixed values according to restrictions R1 to R5, and for any choice of characteristic length d_{st}, the values of ϵ^* are equal.

A thermal-hydraulic performance evaluation of different heat exchangers must take place on the same thermal-hydraulic scale (restrictions R1 to R5). Thus, at equal $A_{\mathrm{in,st}}$, the comparison is made at equal superficial air velocities v_{st}. However, in the non-dimensional expressions this does not coincide with equal Reynolds numbers $\mathrm{Re}_{\mathrm{st}}$, due to possibly different values for the choice of characteristic length. For later comparisons, a common diameter must be defined for the Reynolds number, such that a comparison is straightforward. As stated by Soland [55, p. 38], a single common smooth plate nominal diameter could be chosen, representing the distance of the tubes. This recommendation is followed in this study. In general, it is allowed for each comparison to define a new common diameter. In order to distinguish between the diameters, we refer to d_{mi} as a diameter on the micro-level, usually related to the per-

formance correlations and specific for each heat exchanger structure. d_{ma} is referred to as a diameter on the macro-level, usually related to the specific task for comparison, with a stronger relation to the overall dimension of the heat exchanger, and equal for all compared heat exchangers. The different diameters d_{mi} and d_{ma} can be used as characteristic lengths in the Reynolds number. The index of $\mathrm{Re}_{\mathrm{st}}$ will be extended to $\mathrm{Re}_{\mathrm{st,mi}}$ and $\mathrm{Re}_{\mathrm{st,ma}}$, respectively. Figure 3.2 shows three different heat exchangers and the method of comparison. The individual performance visualizations are matched by relating the efficiency to the modified Reynolds number

$$\mathrm{Re}_{\mathrm{st,ma}} = \mathrm{Re}_{\mathrm{st,mi}} \frac{d_{\mathrm{ma}}}{d_{\mathrm{mi}}}. \tag{3.6}$$

The efficiency curves of the heat exchangers show the efficiency ϵ^* in terms of these modified Reynolds numbers. A comparison of curves at equal $\mathrm{Re}_{\mathrm{st,ma}}$ allows the evaluation of performance differences. The higher the values of ϵ^*, the lower is the cost in terms of energy, volume, or mass (at equal heat transfer rate $\dot{Q}$).

Up to now the assumption of an equal frontal structure area $A_{\mathrm{in,st}}$ was used for developing the performance figures. Its relationship with the structure velocity v_{st} and the Reynolds number $\mathrm{Re}_{\mathrm{st,ma}}$ is

$$A_{\mathrm{in,st}} = \frac{\dot{m}_{\mathrm{st}}}{v_{\mathrm{st}}} = \frac{\dot{m}_{\mathrm{st}} d_{\mathrm{ma}}}{\nu_{\mathrm{air,st}}} \frac{1}{\mathrm{Re}_{\mathrm{st,ma}}}. \tag{3.7}$$

The first term on the right side of Equation (3.7) is constant due to restrictions R1 to R5. Thus, a decrease in the Reynolds number yields a reciprocally proportional increase in the frontal structure area.

If two heat exchangers with different frontal structure areas $A_{\mathrm{in,st}}$ are to be compared to each other and restrictions R1 to R5 are still valid, then the Reynolds number $\mathrm{Re}_{\mathrm{st,ma}}$ differs. The method in Table 3.3 and Figure 3.2 allows this comparison for different frontal structure areas and thus modi-

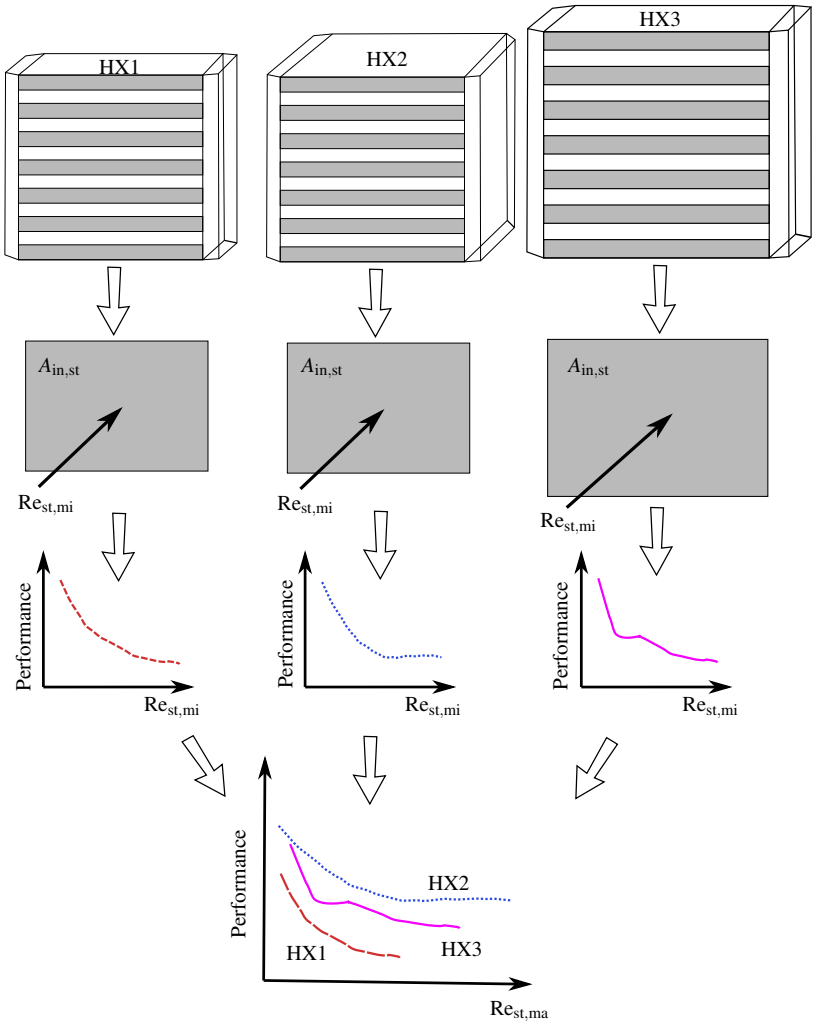

Figure 3.2: Scheme of a performance visualization generation for different types of heat transfer enhancements in differently sized heat exchangers; based on [FLS19].

fied Reynolds numbers $Re_{st,ma}$. Two heat exchangers, HX1 and HX2, have

the same energy-, volume-, or mass-specific heat transfer rate, if and only if the efficiencies ϵ^* show the following relationship with the Reynolds number $\mathrm{Re}_{\mathrm{st,ma}}$:

$$\left(\frac{\dot{Q}}{P_{\mathrm{diss}}}\right)_{\mathrm{HX1}} = \left(\frac{\dot{Q}}{P_{\mathrm{diss}}}\right)_{\mathrm{HX2}} \quad \Leftrightarrow \quad \epsilon^*_{\mathrm{E,HX1}} = \frac{\left(\frac{\epsilon^*_{\mathrm{E}}}{\mathrm{Re}^2_{\mathrm{st,ma}}}\right)_{\mathrm{HX2}}}{\mathrm{Re}^2_{\mathrm{st,ma,HX1}}} \tag{3.8}$$

$$\left(\frac{\dot{Q}}{V_{\mathrm{st}}}\right)_{\mathrm{HX1}} = \left(\frac{\dot{Q}}{V_{\mathrm{st}}}\right)_{\mathrm{HX2}} \quad \Leftrightarrow \quad \epsilon^*_{\mathrm{V,HX1}} = \frac{\left(\epsilon^*_{\mathrm{V}}\mathrm{Re}^2_{\mathrm{st,ma}}\right)_{\mathrm{HX2}}}{\mathrm{Re}^2_{\mathrm{st,ma,HX1}}} \tag{3.9}$$

$$\left(\frac{\dot{Q}}{m_{\mathrm{st}}}\right)_{\mathrm{HX1}} = \left(\frac{\dot{Q}}{m_{\mathrm{st}}}\right)_{\mathrm{HX2}} \quad \Leftrightarrow \quad \epsilon^*_{\mathrm{M,HX1}} = \frac{\left(\epsilon^*_{\mathrm{M}}\mathrm{Re}^2_{\mathrm{st,ma}}\right)_{\mathrm{HX2}}}{\mathrm{Re}^2_{\mathrm{st,ma,HX1}}} \tag{3.10}$$

The Reynolds number is related to the structure velocity through the structure frontal area $A_{\mathrm{in,st}}$ by Equation (3.7). Some consequences of this definition are:

- Two equal heat exchangers arranged either in parallel or in-line are on the same efficiency curve as only one of these heat exchangers.
- When the geometric dimension of a heat exchanger is scaled (e.g. from large to small) the efficiency curve keeps its shape but experiences a stretching (e.g. to the right) along the x-axis.

The presented method makes use of the three key figures ϵ^*_{E}, ϵ^*_{V}, and ϵ^*_{M}, which can be optimized by means of changing the geometry of the enhancement. Dependent on the change of the geometry, beneficial or unfavorable changes in the key figures can be seen for different Reynolds numbers

If the Reynolds number is specified, two out of the three key figures can be compared by means of a Pareto front. Including the third efficiency, a three-objective problem must be solved for a Pareto optimal set. 3D surface maps or decision maps [60, p. 225 ff] for each Reynolds number could be used for

visualization. A decision maker could then decide, based on their preference information, as to which elements of the Pareto optimal set are best suited.

When comparing enhancements more generally, a decision maker cannot explicitly articulate any preference information. Thus, it is helpful to define possible preferences by including weighting factors for the objectives. Thereby, the problem is transformed into a single-objective optimization problem. This transformation is called scalarizing of multi-objective optimization problems [61]" [FLS19]. It is discussed in Appendix A.1.3, together with the definition of a combined non-dimensional efficiency ϵ_C^*.

3.2.3 Graphical Visualization

“The efficiencies in Table 3.3 are shown exemplarily for three different flat-tube heat exchangers. The enhancements of the heat exchangers are realized by (i) louvered fins, (ii) offset strip fins, and (iii) a wire structure pin fin design. The geometries of the enhancements are shown in Figure 3.3. The choice of geometry was based on common dimension ranges. Within these ranges, the sizes are related to available correlation and simulation data from the literature and in-house, respectively. The dimensions are given in Table 3.4. The heat exchangers have the same macro-geometry (same tube distance d_{ma}), but differ in compactness. The louvered fin enhancement shows, in this example, the lowest value of the heat transfer surface area density with $1083\,\mathrm{m^2/m^3}$; the wire structure shows the highest value with $2024\,\mathrm{m^2/m^3}$. The geometries, including the parameters, are shown in Appendix A.1.2.

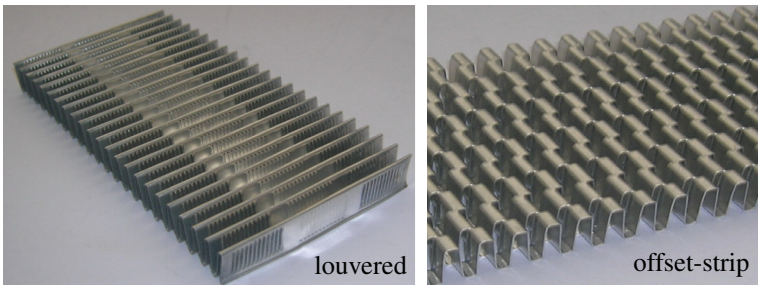

Figure 3.3: Geometry examples of the louvered fin [64] and offset strip fin [38] enhancements used for visualization method; based on [FLS19].

The first comparison is based on the area goodness factor $j_{\mathrm{st}}/f_{\mathrm{st}}$ [11, p. 705] and it is shown in Figure 3.4. The louvered fins and the offset strip fins show slightly higher values for lower Reynolds numbers and much higher values for higher Reynolds numbers than the pin fins. The benefit of a high convective heat transfer in relation to viscous dissipation shrinks due to limitations in heat conduction through the fins (wire structure) and low surface area density

Parameter	**Dimension**	**Louvered Fin**	**Offset Strip Fin**	**Wire Structure**
Source	-	[62]	[63]	[FSF19, FDSS18]
Thermal conductivity structure, k_{st}	$\mathrm{W/(mK)}$	385	385	385
Fin pitch, l_{lateral}	mm	2.3	1.9	1.2
Substructure length, $l_{\mathrm{longitudinal}}$	mm	4.76	1.01	0.35
Structure thickness, d_{st}	µm	152	152	250
Structure length, L_{st}	mm	48	-	10
Structure height, H_{st}	mm	10	10	10
Heat transfer surface area density, β	$\mathrm{m^2/m^3}$	1083	1403	2024
Porosity, φ_{st}	-	0.93	0.91	0.88
Micro-diameter, d_{mi}	mm	4.76	2.58	0.25
Macro-diameter, d_{ma}	mm	10	10	10

Table 3.4: Dimensions of exemplary heat transfer enhancements; based on [FLS19].

(louvered fins, offset strip fins). These drawbacks cannot be accounted for, with the area goodness factor show in Figure 3.4, but will be addressed next.

Figure 3.5 shows the energy efficiency $\epsilon_{\mathrm{E}}^{*}$ (cf. Table 3.3) for the three heat exchangers. The evaluation contains the limitation due to heat conduction through the fins and the surface area density. Thus, the offset strip fins and the pin fins show a better performance than in Figure 3.4. The energy efficiency is not necessarily increasing with Reynolds number. A decreasing fin efficiency and a flattening of the Nusselt number curve with increasing Reynolds number dampens the gradient. Especially the wire structure shows this behaviour. The surface efficiency η_0 of the wire structures ranges from 0.72 for higher veloc-

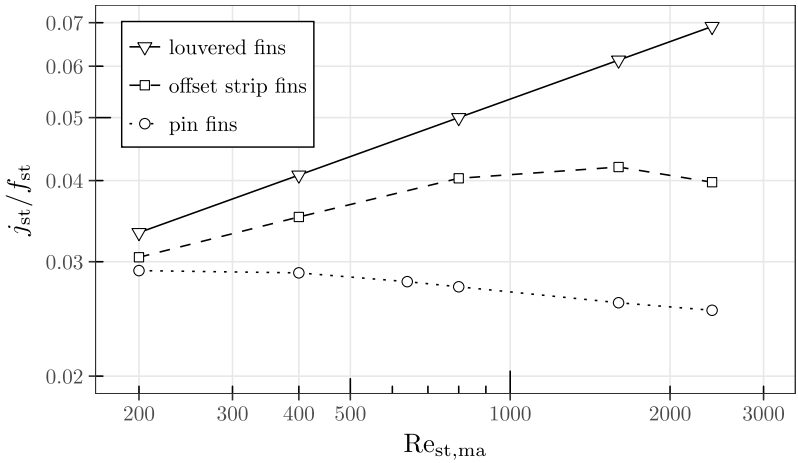

Figure 3.4: Ratio of Colburn factor j_{st} and Fanning friction factor f_{st} versus Reynolds number for different enhancements; based on [FLS19].

ities to 0.8 for lower velocities. Thus, heat conduction through the structure already limits overall heat transfer considerably. For larger Reynolds numbers, the energy efficiency decreases for the offset strip and louvered fins (not visible) with respect to the Reynolds number as well. For lower Reynolds numbers, the wire structures show a superior performance. From $Re_{st,ma} = 550$ onwards, the louvered fins show the best performance.

A huge advantage of this depiction is the well-defined range of energy efficiency values between 0.15 and 0.45 (in this example evaluation). A comparison at equal Reynolds numbers (and thus, equal structure free-flow areas as described in Equation (3.7)) is very clear. Exemplarily, a comparison at $Re_{st,ma} = 1600$ is shown by a vertical grey line in Figure 3.5. The louvered fins (marked with 1) show an efficiency 1.3 times higher than that of offset strip fins (2), and 1.5 times higher than that of pin fins (3). By implication, the pin fins will cause 1.5 times more dissipated power P_{diss} than the louvered fins for the same heat transfer rate $\dot{Q}$.

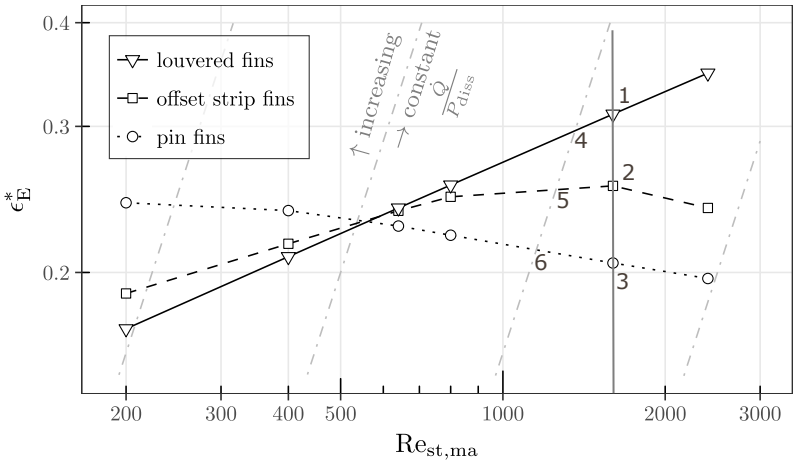

Figure 3.5: Non-dimensional energy efficiency ϵ^*_E versus Reynolds number $Re_{st,ma}$ for different enhancements; standard comparison is at equal Reynolds numbers; grey dash-dot lines represent combinations of ϵ^*_E and $Re_{st,ma}$ with equal $\dot{Q}/P_{diss}$; based on [FLS19].

A comparison of the enhancement performance at different Reynolds numbers (cf. Equation (3.8)) has to consider the lines of equal heat transfer rate per dissipated power (grey dash-dot lines). A lower Reynolds number allows a lower energy efficiency. Thus, the louvered fins, operated at a Reynolds number shown by Point 4 in Figure 3.5 have the same ratio of $\dot{Q}/P_{diss}$ as the offset strip fins operated at point 5 and the pin fins operated at point 6. One drawback is the need of a higher frontal structure area for lower Reynolds numbers (cf. Equation (3.7)). Another drawback will become clear when considering the volume or mass efficiency later on for lower Reynolds numbers. From the perspective of energy efficiency, lower velocities are preferable. Higher values of $\dot{Q}/P_{diss}$ can be achieved for lower Reynolds numbers and/or higher non-dimensional energy efficiency ϵ^*_E (top left corner).

As a hypothesis on the mechanism of heat transfer and shear stress, the Reynolds Analogy (see e.g. [65]) supports reducing the velocity for higher values of $\dot{Q}/P_{diss}$. The Analogy states that the Stanton number ($Nu/RePr$) equals

half the skin friction coefficient ($c_f/2$) at a Prandtl number of unity. Simplifications, such as neglecting form drag within the heat exchanger and extending the range of Prandtl numbers to values below, but close to unity (cf. [66]), yield a proportionality between the Nusselt number and the friction factor: $\mathrm{Nu} \propto f\mathrm{Re}$ (for constant Prandtl number). Thus, the energy efficiency ϵ_{E}^* is approximately constant for varying Reynolds numbers and $\dot{Q}/P_{\mathrm{diss}}$ is proportional to $1/v_{\mathrm{st}}^2$ (more precise to $1/\mathrm{Br}$). Thus, an increase in $\dot{Q}/P_{\mathrm{diss}}$ for lower $\mathrm{Re}_{\mathrm{st,ma}}$ is not necessarily a consequence of a good enhancement structure and should not be misjudged.

Figure 3.6 shows a performance evaluation based on the volume needed for the enhancement structure. The wire structure shows a high potential. Along all Reynolds numbers, it shows more than twice the volume efficiency ϵ_{V}^*. All curves have a negative slope. This is related to the definition of ϵ_{V}^* with the square of velocity v_{st}^2 in the denominator in order to achieve a non-dimensional parameter independent of the hydraulic length. A comparison at equal Reynolds numbers is as straightforward as in Figure 3.5. A comparison at different Reynolds numbers needs a depiction of lines of equal $\dot{Q}/V_{\mathrm{st}}$. These lines have a negative slope as well. However, the gradient is steeper than that of the performance curves. Thus, higher Reynolds numbers allow higher values of $\dot{Q}/V_{\mathrm{st}}$ for the same enhancement structure.

Lastly, Figure 3.7 shows the mass efficiency ϵ_{M}^*. The basic behaviour is similar to that in Figure 3.6 due to the same structure material density ρ_{st} and similar porosity φ_{st}.

In Figure 3.8 the energy and the volume efficiencies are combined in one diagram. It shows the Pareto optimal sets [61] (or Pareto frontiers) at three different Reynolds numbers. For each of these Reynolds numbers none of the three enhancements is superior to the others in both ϵ_{E}^* and ϵ_{V}^*; with an increase in energy efficiency, a decrease in volume efficiency follows. The pin fins show, in each set, the highest volume efficiency; the louvered fins show the highest energy efficiency. However, the feasible set Θ, the set of all possible points

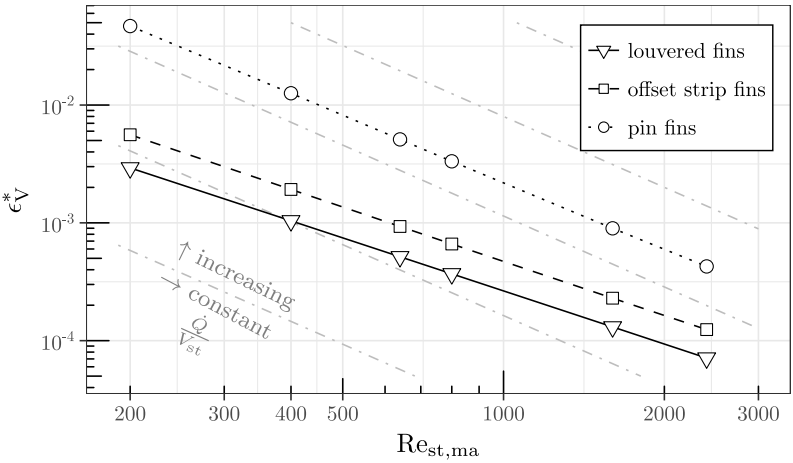

Figure 3.6: Non-dimensional volume efficiency ϵ^*_V versus Reynolds number $\mathrm{Re}_{st,ma}$ for different enhancements; standard comparison is at equal Reynolds number; grey dash-dot lines represent combinations of ϵ^*_V and $\mathrm{Re}_{st,ma}$ with equal $\dot{Q}/v_{st}$; based on [FLS19].

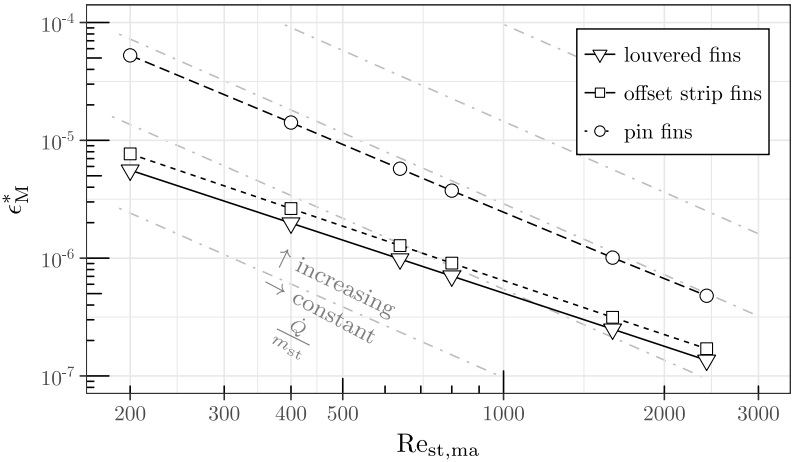

Figure 3.7: Non-dimensional mass efficiency ϵ^*_M versus Reynolds number $\mathrm{Re}_{st,ma}$ for different enhancements; standard comparison is at equal Reynolds numbers; grey dash-dot lines represent combinations of ϵ^*_M and $\mathrm{Re}_{st,ma}$ with equal $\dot{Q}/m_{st}$; based on [FLS19].

of the optimization problem, consists in this example solely of three feasible decision θ (three geometrically specified enhancements). In general, a larger feasible set with different enhancements and their geometric variations would be considered. A posteriori methods, such as evolutionary algorithms [61], could then be used to generate a new Pareto optimal set." [FLS19]

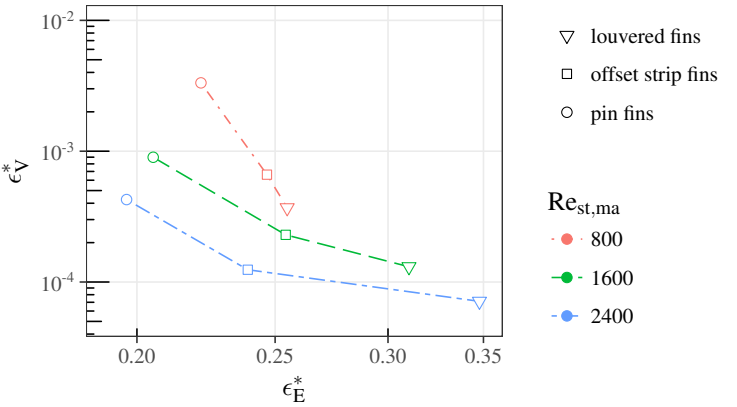

Figure 3.8: Pareto front of the bi-objective problem to optimize energy and volume efficiency. Fronts are given for three Reynolds numbers with three different enhancements in the feasible set Θ; based on [FLS19].

3.3 Discussion

"The introduction of the dimensional performance figures in Table 3.2, representing the ratio of the driving-force-specific heat transfer rate $\dot{Q}/\Delta T_m$ to the dissipated power P_{diss}, volume V_{st}, and mass m_{st} is straightforward. The method uses the definition of efficiency in terms of benefit versus cost for all three types of costs analogously. The comprehensibility should be high; however, the drawback of a dependency on material properties is inevitable. For measurement, simulation, or correlation data for a specific application, this method can be sufficient for comparing different enhancements. A transfer to other operating conditions should be done with caution.

The transformation from the dimensional performance figures into non-dimensional figures considers driving parameters such as the Brinkman number for the energy efficiency. The driving parameters are expected to be equal for a comparison of different enhancements. This limitation of the comparison method is non-restrictive as long as the comparison is based on equal fluid free-flow areas $A_{in,st}$ (and equal heat transfer rates).

When allowing different $A_{in,st}$, relationships between $Re_{st,ma}$ and ϵ^* are developed. These relationships can be integrated into the graphical visualization of the performance figures in a simple way. Thus, the restrictions are less strong (cf. restrictions R1 to R5). An increase in $A_{in,st}$ is usually needed in order to obtain the required fluid flow rate without an increase in the pressure drop and without a change in the heat exchanger volume [57]. It yields a reduced heat exchanger flow length. The shape is characteristic of heat exchangers in automotive and air conditioning applications. However, further increases in frontal areas are limited in these applications also by space availability. Thus, the need for more compact and lightweight heat exchangers remains valid.

The advantage of the proposed performance evaluation method is that different requirements can be considered separately with ϵ^*_E, ϵ^*_V, and ϵ^*_M, as well as combined with ϵ^*_C. The curves of ϵ^*_E in Figure 3.5 show distinct differ-

ences in performance with respect to the Reynolds number. The wire structures profit from high heat transfer coefficients, but yield high fluid friction. For higher Reynolds numbers, the fluid friction outweighs the beneficial heat transfer characteristics, such that $\epsilon_{\mathrm{E}}^{*}$ shows lower values for the wire structure than for the louvered and strip fins. The effect of different Reynolds numbers on the volume and mass efficiency is less pronounced. The performance curves in Figure 3.6 and Figure 3.7 run approximately parallel to each other and with slightly less decrease than the lines of constant $\dot{Q}/V_{\mathrm{st}}$ and $\dot{Q}/m_{\mathrm{st}}$. Thus, the graphical visualization gives a clear indication of the performance with the wire structure, which has more than twice the volume and mass efficiency compared to the other two enhancements.

The method allows finding solutions to the multi-objective optimization problem $\max\left(\epsilon_{\mathrm{E}}^{*}\left(\theta\right), \epsilon_{\mathrm{V}}^{*}\left(\theta\right), \epsilon_{\mathrm{M}}^{*}\left(\theta\right)\right)$ with $\theta \in \Theta$. Therein, the set Θ is the feasible set of decision vectors. In the exemplary enhancement comparison, Θ is composed of the louvered fins, the offset strip fins, and the wire structure. In a more general comparison, the feasible set should allow different geometrical parameters for each enhancement, such that the Pareto fronts in Figure 3.8 are shifted further to the top right corner for each enhancement type" [FLS19]. This is part of the analysis in Chapter 6.

4 Simulation of Laminar Flow within Wire Structures

This chapter deals with the thermal-hydraulic 2D and 3D simulations of the wire structure design idea and with the development of correlations for thermodynamic and fluid dynamic performance parameters based on several geometric and operational degrees of freedom. Further, an analytical expression of fin efficiency is presented which takes into account a non-uniform fluid temperature distribution along the wires. The development of the correlations in combination with the new fin efficiency calculation allows a very accurate and fast optimization of geometrical and operational quantities.

4.1 Simulation Foundations

The design idea for the flat-tube wire structure heat exchanger is considered in the simulation model. The wires are arranged perpendicular to the flat tubes (see Figure 1.1). The arrangement is either in-line, staggered (see Figure 4.1) or differently patterned. Different arrangements will change the thermal hydraulic behaviour of the heat exchanger. Air flow is in y-direction; water flow is in x-direction. The volume between two flat tubes is defined as the structure volume V_{st} with the wires and air as solid respectively fluid fraction.

The material parameters for the air and the solid structure domains are defined independently of temperature and absolute pressure, if not otherwise stated. In Table 4.1 the standard values are defined; they are based on a fixed air temperature of 20 °C and an atmospheric pressure of 1 atm.

Symbol	Description	Unit	Value
$\rho_{\mathrm{air,st}}$	density of air	$\mathrm{kg/m^3}$	1.205
$\mu_{\mathrm{air,st}}$	dynamic viscosity of air	Pa s	1.82E-5
$k_{\mathrm{air,st}}$	thermal conductivity of air	$\mathrm{W/(m\,K)}$	0.0257
$c_{p,\mathrm{air}}$	specific heat of air	$\mathrm{W/(m\,K)}$	1007
k_{st}	thermal conductivity of wire	$\mathrm{W/(m\,K)}$	300

Table 4.1: Definition of material parameters for the simulation model.

4.2 2D Simulation Model

This section is based on the publication *Heat Transfer and Pressure Drop Correlations for Laminar Flow in an In-line and Staggered Array of Circular Cylinders* [FSF19].

4.2.1 Model Description

"Steadystate fluid flow and heat transfer was simulated using the finite element method (FEM), implemented in COMSOL Multiphysics (Version 5.3). The continuity equation (2.1), Navier Stokes equation (2.2) and energy (heat) equation (2.13) describe the system on the air-side [...]. Several simplifications are related to the energy equation (2.13). Firstly, the work related to a thermal expansion is neglected. Secondly, the influence of varying viscosity between the boundary layer and the bulk flow during heating or cooling is neglected [67, Ch. 3]. Both simplifications are motivated by the small impact on the performance as long as temperature differences within the fluid are moderate. Thirdly, the viscous dissipation is neglected. Viscous dissipation could contribute significantly to heat generation, especially for fluids with small wall-to-fluid temperature differences [68, p. 53]. A possible evaluation criterion is given by the ratio of viscous heat generation to external heating, expressed with the Brinkman number $\mathrm{Br_{air}}$ [in Equation (3.5)] [68, p. 54]

[...][The choice of neglecting the viscous dissipation in this study is motivated

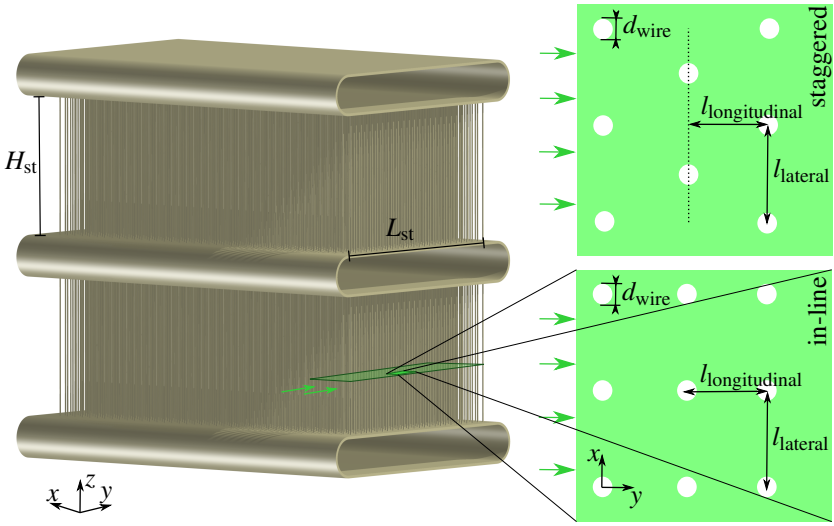

Figure 4.1: Length scales in wire structure heat exchanger; based on [FSF19].

by the fact that] the Brinkman number is small ($|\mathrm{Br}_{\mathrm{air}}| < 10^{-3}$) for applications with moderate velocities v_{st} below 10 m/s and temperature differences [ΔT_{m} between the wall T_{wall} and the air $T_{\mathrm{air,m}}$] above 2 K (for air temperatures from 0 °C to 100 °C and atmospheric pressure 1 atm). For a wide variety of applications [(cf. Table 2.2)] this holds true.The scope of this study is on these applications. A cross section through a wire structure heat exchanger in direction of air fluid flow is shown in Figure 4.1. In the cross section the wires appear as circular obstacles.

Simulating flow and heat transfer around the wires in the 2D cross section can give a first estimate on the thermal-hydraulic behaviour of the heat exchanger. The following assumptions AS1 to AS5 are taken for the heat exchanger geometry and the operating condition:

AS1 Gradients in z-direction of velocity, pressure and temperature field are negligibly small

AS2 Air velocity z-component is negligibly small (e.g. caused by reduction of free-flow area due to blocking tubes)

AS3 Pressure drop associated with sudden contraction and expansion at the core structure inlet and outlet (due to the blocking tubes) is negligibly small or is known

AS4 Heat flux through the tube wall in direct contact to air is negligibly small or is known

AS5 Operation is steady state with uniform temperature and velocity profiles at the heat exchanger inlet

In this study the wires are arranged symmetrically in x-direction, meaning that one characteristic in-line or staggered element represents the entire geometry.

The characteristic element and the boundary conditions for temperature, pressure and velocity for the steady state laminar flow are shown for the in-line and staggered 2D cross section in Figure 4.2. The symmetry conditions ensure that the influence of neighbouring wires in x-direction on the flow is considered. Assumptions AS1 and AS2 are only valid if the height of the structure H_{st} is

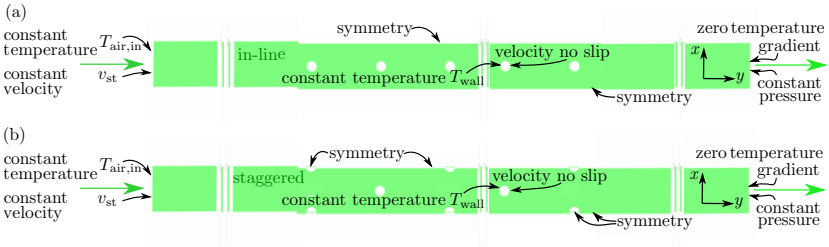

Figure 4.2: Boundary conditions of the in-line (a) and staggered (b) cross section model [FDS16].

at least 5 times higher than the lateral wire distance $l_{lateral}$ (see geometry in Figure 4.1). Based on several 3D simulations [FGS19] [and section 4.5], the influence on the pressure drop and heat transfer coefficient was within $\pm 5\%$ above the ratio threshold of $H_{st}/l_{lateral} > 5$. Assumption AS3 can in general be reduced to an estimation of the pressure losses associated with free expan-

sion that follow sudden contraction and pressure losses associated with the irreversible free expansion and momentum rate changes following an abrupt expansion. The related contraction and exit loss coefficient can be determined based on literature values [11, p. 385-389]. Assumption AS4 is particularly fulfilled if the (tube wall) primary surface area A_p is small in comparison to the structure surface area A_st. In the case of the wire structure it holds ${}^{A_\mathrm{p}}/_{A_\mathrm{st}} < 20\%$ if ${}^{H_\mathrm{st}}/_{l_\mathrm{lateral}} > 5$ and ${}^{l_\mathrm{longitudinal}}/_{d_\mathrm{wire}} < 1.5$. Additionally the heat flux through the wall in direct contact to air is reduced due to a larger thermal boundary layer near the wall in comparison to the wires, expressed by high convection heat transfer coefficients for the wires.

The characteristic element is determined by the wire diameter $d_\mathrm{st} = d_\mathrm{wire}$, the lateral and longitudinal distance of the wires l_lateral and $l_\mathrm{longitudinal}$, respectively, and the total length of the structure L_st or the number of wire rows n_wires (see Figure 4.1). The air velocity field is determined by the structure velocity v_st [...]. The non-dimensional input parameters of the model are given in Table 4.2. The choice of parameter ranges is related to available manufacturing possibilities and typical applications of air-side heat transfer enhancement [cf. Table 2.2].

Symbol	Definition	Description	Min	Max
a	$\frac{l_\mathrm{lateral}}{d_\mathrm{wire}}$	Non-dimensional lateral distance of the wires	2	12
b	$\frac{l_\mathrm{longitudinal}}{d_\mathrm{wire}}$	Non-dimensional longitudinal distance of the wires	1.3	8
Re_st	$\frac{v_\mathrm{st} d_\mathrm{wire}}{\nu_\mathrm{air,st}}$	Air-side Reynolds number	3	60
n_wires	$\frac{L_\mathrm{st}}{l_\mathrm{longitudinal}}$	Number of wire rows in flow direction	2	200
Pr_air	$\frac{\nu_\mathrm{air,st} c_{p,\mathrm{air}} \rho_\mathrm{air,st}}{k_\mathrm{air,st}}$	Prandtl number	0.71	0.71

Table 4.2: Definition of non-dimensional input parameters to simulation model with minimal and maximal values in parametric study; based on [FSF19].

Neighbouring wires in y-direction (main flow direction) affect fluid flow and temperature fields around a wire. Thus, a simulation run with a specific number of wire rows did not allow a distinct definition of thermal-hydraulic characteristics of a geometry with fewer wires. The number of wire rows had to be changed in each simulation run.

The meshing of the domain was separated into a triangular mesh next to the wires and a quadrilateral mesh further on (see Figure 4.3). The triangular and quadrilateral meshes were refined in order to obtain a mesh independent solution. The Richardson method (cf. [69]) was used to determine the order of accuracy of the mesh refinement" [FSF19]. A detailed analysis is given in the following section.

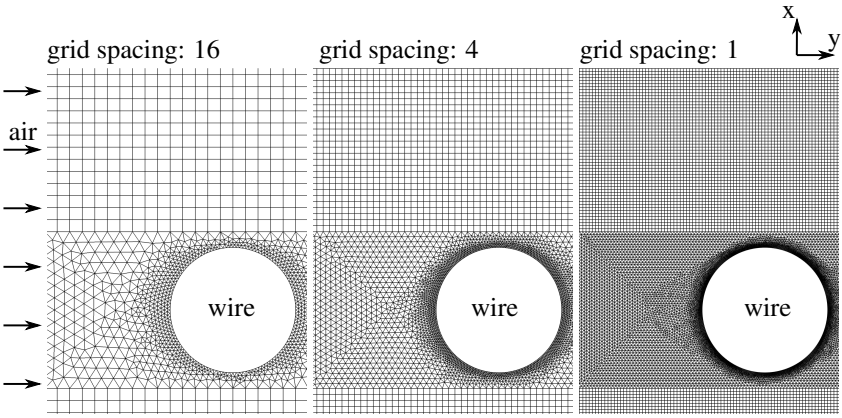

Figure 4.3: Meshing of 2D cross section; based on [FSF19].

4.2.2 Mesh Quality

"The normalized grid spacing was defined as the surface area of a quadrilateral element normalized with the surface area of the quadrilateral element of the finest mesh. The quadrilateral element of the finest mesh was equal to $2.5\,\mu m \times 2.5\,\mu m$. The length of one quadrilateral mesh element ranged from

2.5 µm to 25 µm in a geometry of 100 µm wire diameter. A direct evaluation of the order of convergence p_{mesh} could be obtained from three solutions using a constant grid refinement ratio r_{mesh}. The Grid Convergence Index based on the procedure for estimation of uncertainty due to discretization [69] is shown in Table 4.3" [FSF19]. Uncertainty due to discretization is thus lower than 0.05%

Solution	r_{mesh}	p_{mesh}	GCI_{12} in %	GCI_{23} in %
Nu_{st}	4	0.245	0.032	0.045
f_{st}	4	1.013	0.009	0.038

Table 4.3: Grid Convergence Index (GCI) based on Richardson method [69] for Nusselt number and friction factor. Geometry consists of five wires in row ($a = 8, b = 3$) at $\text{Re}_{\text{st}} = 11.25$. Index 1 represents finer mesh, index 3 coarser mesh; based on [FSF19].

for grids with normalized grid spacing 1 or 4. In this study a normalized grid spacing of 4 will be used from now on.

Based on the normalized grid spacing the Nusselt number Nu_{st} and friction factor f_{st} are plotted in Figure 4.4 and 4.5. "Similar Grid Convergence Index

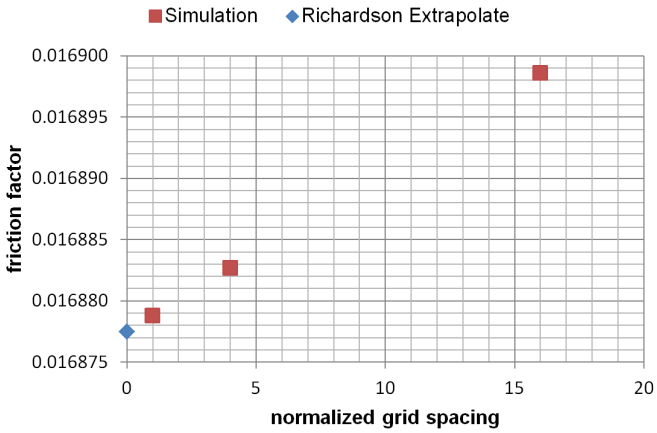

Figure 4.4: Variation of friction factor f_{st} due to mesh refinement in 2D-model. With Richardson Extrapolate for normalized grid spacing equal to zero.

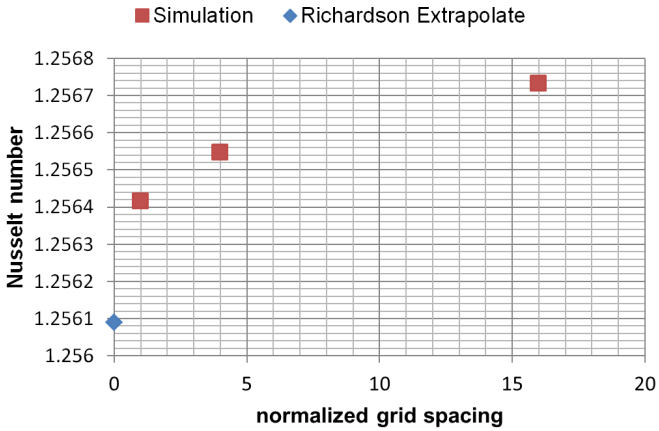

Figure 4.5: Variation of Nusselt number Nu_{st} due to mesh refinement in 2D-model. With Richardson Extrapolate for normalized grid spacing equal to zero.

as in Table 4.3 could be achieved with number of wire rows equal to 30 and Reynolds numbers equal to 5.6, 11.2 and 22.5; all other parameters were kept constant. Grid Convergence Indeces GCI_{12} and GCI_{23} were below 0.05%" [FSF19].

4.2.3 Local and Global Definitions

"The Nusselt number Nu_{st} [...] was simulated and calculated for different number of wire rows. As the number of wire rows differed within different simulations, the number of wire rows is added to the Nusselt number as an index for reasons of clarity. The global Nusselt number Nu_{st} is a mean of all wires within the domain. The local Nusselt number or thermal entrance Nusselt number $Nu_{st,local}$ (cf. [11, p. 502]) for each wire is related to the global definition according to:

$$Nu_{st,i} = \frac{1}{i-1} \int_1^i Nu_{st,local}(y)\, dy \tag{4.1}$$

such that $\mathrm{Nu}_{\mathrm{st},1} = \mathrm{Nu}_{\mathrm{st,local},1}$. When the number of wire rows increases, the global and local Nusselt numbers converge towards the same limit value. This limit value represents the Nusselt number in a thermally developed flow. The limit value is defined as

$$\mathrm{Nu}_{\mathrm{st},\infty} = \mathrm{Nu}_{\mathrm{st,local},\infty}. \tag{4.2}$$

The flow direction through the heat exchanger is non-dimensionalized as

$$y^* = \frac{y}{d_{\mathrm{wire}} b}, \tag{4.3}$$

with $y = 0$ representing the entrance of the heat exchanger structure. Thus, the non-dimensional flow direction y^* at the outlet of the heat exchanger structure is equal to the number of wire rows in the heat exchanger.

The global Nusselt number $\mathrm{Nu}_{\mathrm{st}}$ can be represented by a power law ansatz with a decrease of Nusselt number for increasing length of the heat exchanger. The continuous decrease can be approximated by

$$\mathrm{Nu}_{\mathrm{st},y^*} = \mathrm{Nu}_{\mathrm{st},\infty} + \frac{C_{1,\mathrm{Nu}}}{C_{2,\mathrm{Nu}}(y^* - 1)}\left(1 - y^{*-C_{2,\mathrm{Nu}}}\right) \tag{4.4}$$

The second term on the right hand side of Equation (4.4) decreases with respect to y^* toward 0. Based on Equations (4.1) and (4.4) the continuous local Nusselt number can be written as

$$\mathrm{Nu}_{\mathrm{st,local},y^*} = \mathrm{Nu}_{\mathrm{st},\infty} + C_{1,\mathrm{Nu}} y^{*\left(-C_{2,\mathrm{Nu}}+1\right)} \tag{4.5}$$

The Nusselt number $\mathrm{Nu}_{\mathrm{st},\infty}$ and the coefficients $C_{1,\mathrm{Nu}}$ and $C_{2,\mathrm{Nu}}$ are fitted, by means of a weighted least square error method, based on at least 9 simulation points with different number of wire rows.

For several applications, it is helpful to know the thermal entrance length L_{th} of a flow through a structure beyond which the flow is thermally developed. This

knowledge allows an estimation whether the entrance region has to be considered in performance evaluation or could be neglected. Following the definition in Equation (4.3) the thermal entrance length L_{th} is non-dimensionalized as

$$L_{\mathrm{th}}^{*} = \frac{L_{\mathrm{th}}}{d_{\mathrm{wire}} b}. \tag{4.6}$$

The existence of the non-dimensional thermal entrance length L_{th}^{*} [70, Eq. 4.87] is assumed, such that for all $y^{*} \geq L_{\mathrm{th}}^{*}$ it holds (i) the relative difference of $\mathrm{Nu}_{\mathrm{st,local},\infty}$ and $\mathrm{Nu}_{\mathrm{st,local}}(y^{*})$ is small and (ii) the relative difference of simulated values $\mathrm{Nu}_{\mathrm{st},y^{*}}$ and interpolated values is small. Both requirements are expressed in terms of $\epsilon = 0.05$, such that:

$$\left| \frac{\mathrm{Nu}_{\mathrm{st,local},\infty} - \mathrm{Nu}_{\mathrm{st,local},y^{*}}}{\mathrm{Nu}_{\mathrm{st,local},y^{*}}} \right| < \epsilon \quad \text{for all } y^{*} > L_{\mathrm{th}}^{*} \tag{4.7}$$

and

$$\left| \frac{\mathrm{Nu}_{\mathrm{st,local,corr}} - \mathrm{Nu}_{\mathrm{st,local,sim}}}{\mathrm{Nu}_{\mathrm{st,local,sim}}} \right| < \epsilon \quad \text{for all } y^{*} > L_{\mathrm{th}}^{*} \tag{4.8}$$

Equation (4.8) hast to be checked individually, Equation (4.7) can be expressed as

$$L_{\mathrm{th}}^{*} = \left(\frac{\mathrm{Nu}_{\mathrm{st},\infty}\, \epsilon}{C_{1,\mathrm{Nu}}(1-\epsilon)} \right)^{\frac{-1}{C_{2,\mathrm{Nu}}+1}} \tag{4.9}$$

Downstream of L_{th}^{*} the flow is declared as thermally developed.

For the friction factor the same procedure is chosen. The non-dimensional hydraulic entrance length L_{hy}^{*}, the global, local, and developed flow friction factors f_{st}, $f_{\mathrm{st,local}}$, and $f_{\mathrm{st},\infty}$, respectively, and the coefficients $C_{1,f}$ and $C_{2,f}$ result from this analysis. The corresponding definitions can be found in the Appendix A.3.2" [FSF19].

4.2.4 Flow around Single Wire

The arrangement of wires in the heat exchanger is such that the flow around a single wire can be affected by neighbouring wires. This effect decreases with increasing distance of the wires and vanishes for a single wire in a channel with infinite distance to the boundaries. The flow around such a single wire is described shortly in section 2.4 based on [40–43]. “Steady laminar flow exists at a Reynolds number between 5 and 40. [...] Beyond a critical value of Reynolds number a transverse oscillation sets in with loss of flow symmmetry and vortices are shed from the cylinder surface” [40]. Thus, for Reynolds numbers above 40 a simulation with transient conditions might be necessary. However, a comparison of the present stationary simulation model with the literature results shows good accordance for Reynolds numbers between 1 and 60. Moreover, the present model has been extended to transient conditions and the Nusselt number as well as the drag coefficient have been calculated. Figure 4.6 shows the comparison. The non-dimensional channel width is $a = 60$ and on the channel wall a slip boundary condition is set.

The Nusselt number matches with the literature data within $\pm 2\%$ for the stationary simulation model and $\mathrm{Re_{st}} \leq 50$. The relative difference increases to 7 % for $\mathrm{Re_{st}} \leq 100$. The transient simulation model shows a slightly higher value of the Nusselt number than the stationary simulation model for $60 \leq \mathrm{Re_{st}} \leq 100$. The transient Nusselt number corresponds to the literature data within +/-2%. The difference in Nusselt number between transient and stationary simulation model at $\mathrm{Re_{st}} \leq 60$ is in the order of 0.1%.

Flow through an array of cylinders can be seen as an internal flow through a certain geometry. Thus, the friction factor (see Eq. 2.11) is the appropriate quantity to express the losses in the flow field. These losses are due to the dissipation of mechanical energy [71]. However, flow around a single wire can be seen as an external flow around a certain geometry. Although the losses

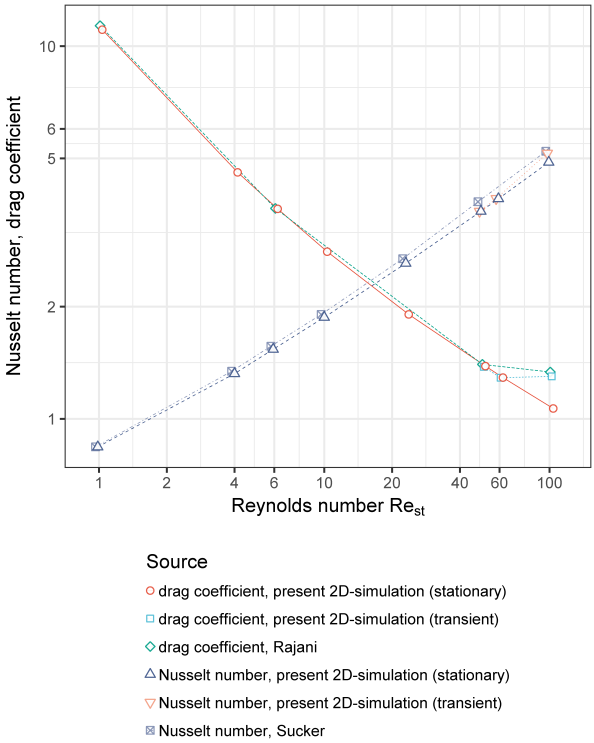

Figure 4.6: Comparison of present stationary and transient simulation model for a flow around a single wire (lateral channel distance $a = 60$) with literature data. The Nusselt number $\mathrm{Nu_{st}}$ and the drag coefficient c_d are related to the Reynolds number $\mathrm{Re_{st}}$. Literature data is based on numerical data from Rajani et al. [40] and Sucker and Brauer [42].

are again due to the dissipation of mechanical energy, they are expressed by the drag coefficient c_d

$$c_\mathrm{d} = \frac{F_\mathrm{d}}{\frac{1}{2}\rho_{\mathrm{air,st}} v_\mathrm{st}^2 A}, \tag{4.10}$$

with the drag force F_d.

Following the idea of Herwig and Schmandt the "entropy generation in the flow field is the volumetric expression of the losses, an integration of this quantity over the flow field will end up with the information about the losses in the flow around or through a certain geometry" [71]. Thus, the drag coefficient can be transferred via the idea of entropy generation to a head loss coefficient $K_p = {}^{2\Delta p_{\mathrm{st}}}/_{\rho_{\mathrm{air,st}} v_{\mathrm{st}}^2}$ [72] and a friction factor $f_{\mathrm{st}} = {}^{d_{\mathrm{wire}} K_p}/_{4L_{\mathrm{st}}}$ to be consistent with the concept of showing hydraulic performance in terms of a friction factor. However, the transformation [71]

$$f_{\mathrm{st}} = c_{\mathrm{d}} \frac{1}{4ab} \tag{4.11}$$

requires a non-dimensional channel width $a = {}^{l_{\mathrm{lateral}}}/_{d_{\mathrm{wire}}}$ and channel length $b = {}^{l_{\mathrm{longitudinal}}}/_{d_{\mathrm{wire}}}$. For a singular wire this is not meaningful. Thus, the simulative drag coefficient is compared to literature values.

The drag coefficient c_{d} matches with data from Rajani [40] within $\pm 3\%$ for the stationary simulation model and $\mathrm{Re}_{\mathrm{st}} \leq 50$. The relative difference increases to 25% for $\mathrm{Re}_{\mathrm{st}} \leq 100$. The transient simulation model shows a much higher value of the drag coefficient than the stationary simulation model for $\mathrm{Re}_{\mathrm{st}} = 100$. The transient drag coefficient corresponds to the data of Rajani within $\pm 2\%$. The difference in drag coefficient between transient and stationary simulation model at $\mathrm{Re}_{\mathrm{st}} \leq 60$ is in the order of 0.2%.

Thus, the assumption of stationary conditions for $3 \leq \mathrm{Re}_{\mathrm{st}} \leq 60$ for the simulation model is still valid, as the error with respect to a transient simulation is very small.

On the basis of this validation, the simulation model is assumed to be sufficiently exact. It will be used for multiple wires in flow direction without additional validation to literature, as no adequate data could be found for the specific geometry and operating conditions used in this thesis for in-line and staggered arrays.

4.3 3D Simulation Model

This section is based on the publication *Efficiency of Micro Pin Fin Heat Exchangers with Non-Uniform Temperature Profile of Ambient Fluid* [FGS19].

4.3.1 Model Description

The continuity equation (2.1), Navier Stokes equation (2.2) and energy (heat) equation (2.13) describe the system on the air-side. The material parameters are fixed based on Table 4.1. The velocity field $\mathbf{u} = (u, v, w)$ and the pressure scalar p are dependent on the boundary conditions and on the geometry within the fluid domain.

"The wire structure heat exchanger geometry consists of repetitive elements. By properties of symmetry a characteristic element can be specified. This element is shown in Figure 4.7 as part of a pin fin heat exchanger and in Figure 4.8 in detail.

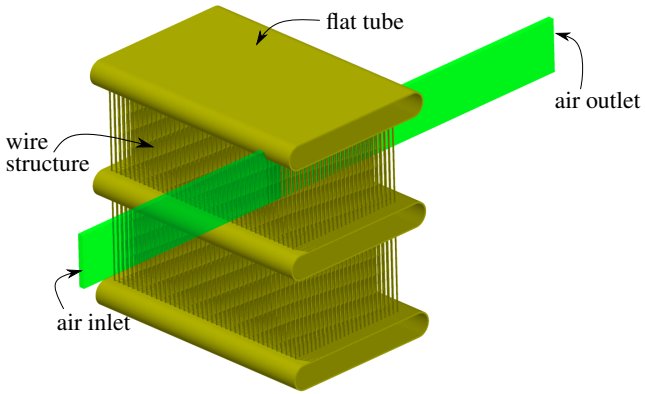

Figure 4.7: Concept of an in-line plate-fin wire structure heat exchanger with pin fins and characteristic element (green) for 3D simulation.

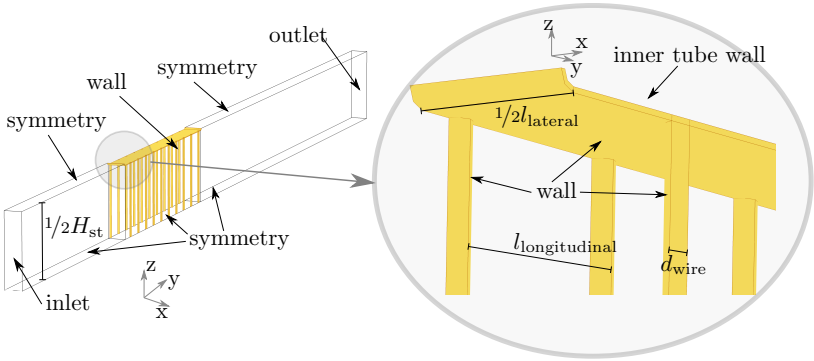

Figure 4.8: Boundary conditions and geometry parameters of the staggered 3D-Model. Based on [FGS19].

Parameter	Description	Min	Max
a	non-dimensional lateral distance of the wires	3	12
b	non-dimensional longitudinal distance of the wires	1.3	8
c	non-dimensional height of structure	10	100
Re_{st}	Reynolds number	3	60
n_{wires}	number of wire rows in flow direction	2	300
Pr	Prandtl number	0.71	0.71
σ	free-flow ratio	0.88	0.99
$\chi_{wall,wire}$	ratio of thermal conductivity of tube wall versus wires	10^{-7}	1
$\chi_{wire,air}$	ratio of thermal conductivity of wires versus air	10^{-7}	10^{-2}

Table 4.4: Definition of necessary non-dimensional input parameters to 3D simulation model with minimum and maximum values in parametric study. Based on [FGS19].

The characteristic element is determined by the wire diameter d_{wire}, the lateral and longitudinal distance of the wires, $l_{lateral}$ and $l_{longitudinal}$, respectively, the height of the structure (distance between the tubes) H_{st}, and the total length of the structure L_{st} or the number of wire rows n_{wires} (Figure 4.8). The air velocity field is determined by the structure velocity v_{st} and the inlet tempera-

ture $T_{\text{air,in}}$. For a variety of parameters a parametric study was performed. The non-dimensional input parameters of the model and the minimum/maximum values of parametric study are given in Table 4.4. The boundary conditions for the temperature, pressure and velocity for the steady state laminar flow are shown for the staggered 3D cross section in Figure 4.8 and Table 4.5. The in-line arrangement has the same boundary conditions" [FGS19].

Boundary	Velocity $\mathbf{u}$ and pressure p	Temperature T
inlet	$\mathbf{u} = v_{\text{air,in}}\mathbf{n}$	$T = T_{\text{air,in}}$
outlet	$\left[-p\mathbf{I} + \mu_{\text{air}}\left(\nabla\mathbf{u} + (\nabla\mathbf{u})^{\text{T}}\right)\right]\mathbf{n} = p_0\mathbf{n}$	$-k_{\text{air}}\nabla T \cdot \mathbf{n} = 0$
symmetry	$\mathbf{u}\cdot\mathbf{n} = 0$, $\left[-p\mathbf{I} + \mu_{\text{air}}\left(\nabla\mathbf{u} + (\nabla\mathbf{u})^{\text{T}}\right)\right]\mathbf{n} = 0$	$-k_{\text{air}}\nabla T \cdot \mathbf{n} = 0$
wall	$\mathbf{u} = 0$	-
inner tube wall	-	$T = T_{\text{wall}}$

Table 4.5: Boundary conditions; the normal $\mathbf{n}$ is outward-pointing. Based on [FGS19].

Based on the inlet boundary condition it holds $v_{\text{air,in}} = \sigma v_{\text{st}}$. For the outlet the absolute pressure p_{A} is set to 1 atm. The outlet pressure is related to the pressure p in the Navier Stokes equation (2.2) by $p_{\text{A}} = p + p_{\text{ref}}$ with $p_{\text{ref}} = 1\,\text{atm}$. Thus, it holds $p_0 = 0\,\text{atm}$ in Table 4.5. The tangential stress component is set to zero. At the symmetry boundaries no penetration and vanishing shear stresses are assumed. At the wall the no slip condition is assumed for the velocity field.

4.3.2 Mesh Quality

The triangular mesh was refined in order to get a mesh independent solution. The Richardson method [69] was used to get the order of accuracy of mesh refinement. The normalized grid spacing was defined as the reciprocal of the number of degrees of freedom normalized with the number of degrees of freedom of the finest mesh. The number of degrees of freedom for the finest mesh was equal to 1.3×10^7 for a geometry with 60 wires. Exemplarily three

meshes for $a = 8$, $b = 2$, $c = 100$ are shown in Figure 4.9. The mean volume of one element differed from $120\,000\,\mu m^3$ (coarse mesh) to $4000\,\mu m^3$ (fine mesh). A direct evaluation of the order of convergence p_{mesh} could be obtained from three solutions using a constant grid refinement ratio r_{mesh}. Grid Convergence Index based on the procedure for estimation of uncertainty due to discretization [69] is shown in Table 4.6.

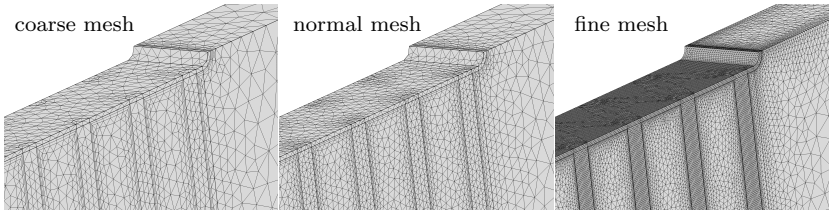

Figure 4.9: Mesh of a staggered 3D-Model ($a = 8$, $b = 2$, $c = 100$). The normal mesh is used for the parametric analysis. Based on [FGS19].

Re_{st}	a	b	c	n_{wires}	Solution	r_{mesh}	p_{mesh}	GCI_{12}	GCI_{23}
11.25	8	2	100	60	Nu_{st}	3.7	0.86	0.65	0.18
					f_{st}		1.04	0.56	2.16
60	3	1.3	10	10	Nu_{st}	1.8	0.87	6.18	8.16
					f_{st}		1.42	2.13	4.94

Table 4.6: Grid Convergence Index (GCI) in % based on Richardson method [69] for Nusselt number and friction factor for two different operating and geometric conditions with staggered wire arrangement. Index 1 represents finer mesh, index 3 coarser mesh.

Uncertainty due to discretization is thus lower than 6.2% for grids with normalized grid spacing 1. In this study a normalized grid spacing of 1 will be used from now on. Based on the normalized grid spacing the Nusselt number Nu_{st} and friction factor f_{st} are plotted in Figure 4.10 and 4.11.

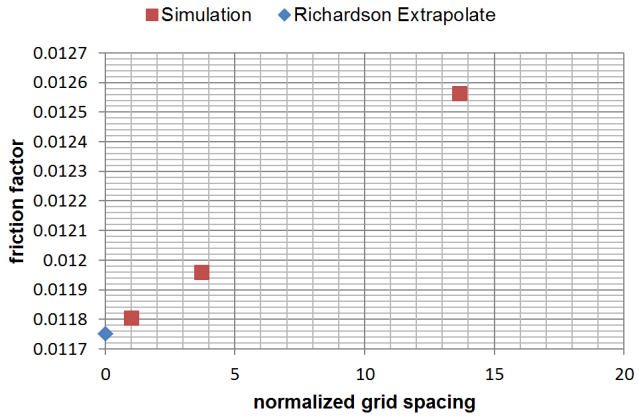

Figure 4.10: Variation of friction factor f_{st} due to mesh refinement in 3D model. With Richardson Extrapolate for normalized grid spacing equal to zero ($Re_{st} = 11.25$,$a = 8$, $b = 2$, $c = 100$, $n_{wires} = 60$).

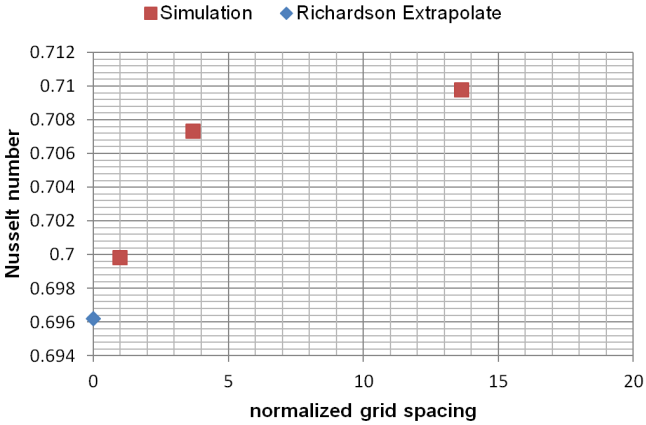

Figure 4.11: Variation of Nusselt number Nu due to mesh refinement in 3D model. With Richardson Extrapolate for normalized grid spacing equal to zero ($Re_{st} = 11.25$,$a = 8$, $b = 2$, $c = 100$, $n_{wires} = 60$).

4.4 Correlations based on 2D Simulation

This section is based on the publication *Heat Transfer and Pressure Drop Correlations for Laminar Flow in an In-line and Staggered Array of Circular Cylinders* [FSF19].

4.4.1 Simulation Results

"The pressure difference, velocity, and temperature profiles of an in-line wire structure geometry with lateral and longitudinal wire distance $a = 10$ and $b = 3$, respectively, and $\mathrm{Re}_{\mathrm{st}} = 20$ are given exemplarily in Figure 4.12. The

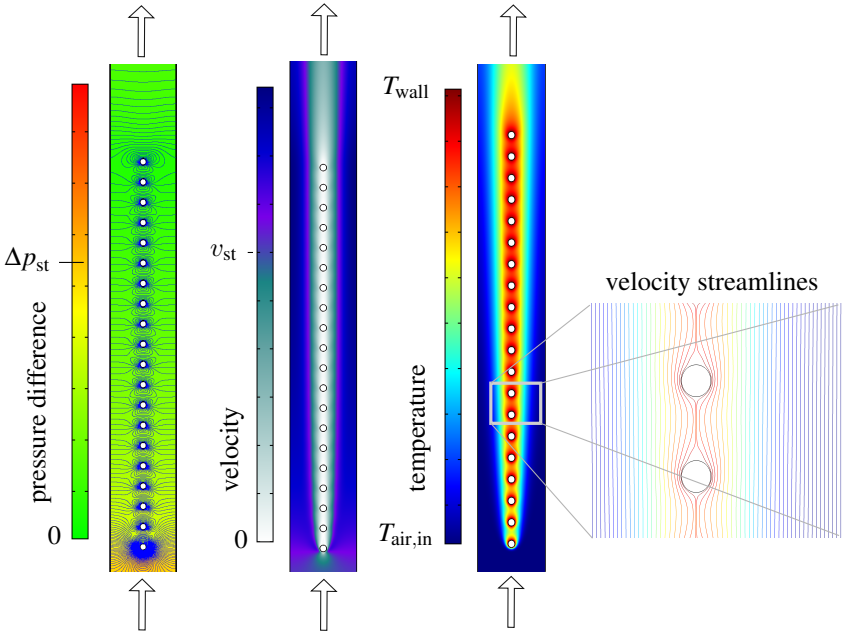

Figure 4.12: Pressure difference, velocity and temperature of a 2D in-line wire structure simulation with $a = 10$, $b = 3$, $\mathrm{Re}_{\mathrm{st}} = 20$, and $n_{\mathrm{wires}} = 20$. Contour lines for pressure difference are equally distributed. Velocity streamlines are colored based on the temperature scale [FSF19].

contour lines of pressure difference next to the first few wires are very dense. In the middle part of the structure the contour lines resemble each other and are less dense. Similar behaviour can be seen for the velocity: A strongly changing velocity profile for the first wires and an almost unchanged profile in the middle. Both plots show the evolution of a hydraulically developed flow. The temperature profile shows no convergent behaviour. This is due to the fact that a thermally developed flow is not defined by a non-varying temperature profile in flow direction, but by a steady relation of local heat transfer rate to driving temperature difference between fluid and wall. The staggered arrangement shows in principle the same behaviour" [FSF19]

A parameter variation was performed based on the parameter inputs in Table 4.2. The parameter ranges are shown there as well. Their definition was related to available manufacturing possibilities and typical applications described in Table 2.2. "Nusselt numbers and Fanning friction factors for the developed flow are shown as functions of Reynolds number in Figure 4.13. Decreasing values of lateral distance a yield higher Nusselt numbers and higher friction factors. Higher Nusselt numbers can be achieved with higher values of longitudinal distance b and higher Reynolds number. The friction factor shows a linear relation with the Reynolds number in the logarithmic scale of Figure 4.13 for fixed geometry parameters. Each simulation point in Figure 4.13 is based on a parameter sweep of the number of wire rows from 2 up to 300 wires in flow direction (cf. Table 4.2)" [FSF19].

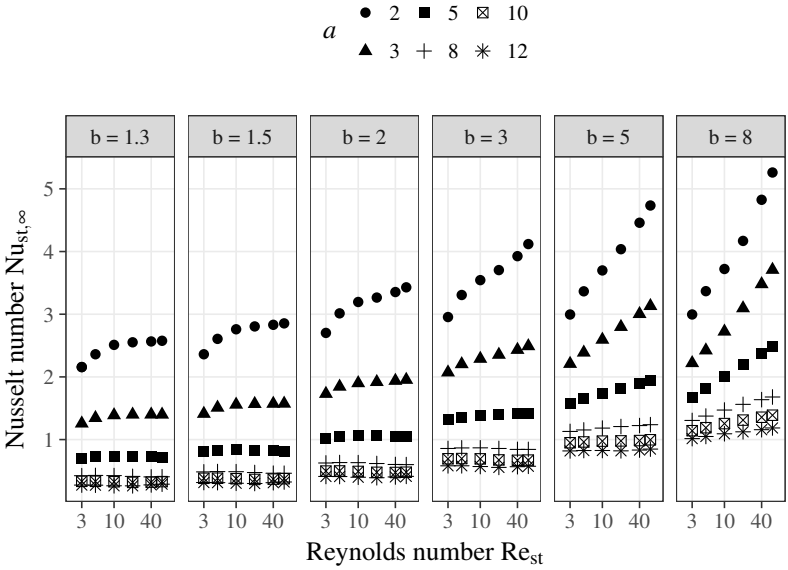

(a) Nusselt number

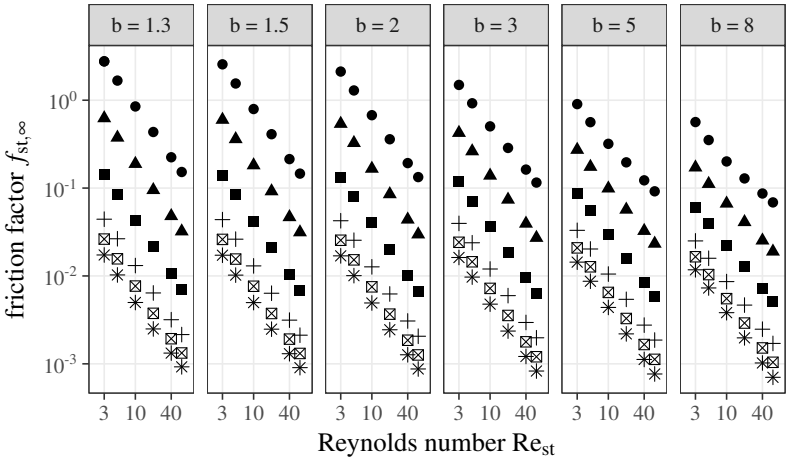

(b) Friction factor

Figure 4.13: Thermal-hydraulic performance for developed flow in an in-line wire arrangement, based on 2D-simulation [FSF19].

4.4.2 Determination of Correlation

The Prandtl number was not a test variable, but the two-thirds power of the Prandtl number could be included as an approximation over a moderate range of Prandtl numbers and shall be at least adequate for all gases [73].

The Effect of the Number of Wire Rows

"A set of results for one of the parameter sweeps defined in Table 4.2 is given in Figure 4.14 for the Nusselt number. It shows the results for the global Nusselt number $\mathrm{Nu}_{\mathrm{st}}$ from 9 CFD-simulations with fixed a, b, and $\mathrm{Re}_{\mathrm{st}}$ and varying number of wire rows. Based on Equation (4.4) the Nusselt number $\mathrm{Nu}_{\mathrm{st},\infty}$ and the coefficients $C_{1,\mathrm{Nu}}$ and $C_{2,\mathrm{Nu}}$ were determined with a weighted least square error method. The weighting factor was chosen as the number of wire rows to the power of 3 to force good agreement of interpolation with the simulation for larger number of wire rows. The coefficients were used to express the local Nusselt number $\mathrm{Nu}_{\mathrm{st,local}}$ and the non-dimensional thermal entrance length L^*_{th} in terms of Equation (4.5) and (4.9), respectively, both shown in Figure 4.14. The same procedure is followed for the friction factor. An exemplary result is shown in Figure 4.14 (b).

The differences of the predicted values $\mathrm{Nu}_{\mathrm{st},y^*,\mathrm{corr}}$ and $f_{\mathrm{st},y^*,\mathrm{corr}}$ versus the simulated values $\mathrm{Nu}_{\mathrm{st},y^*,\mathrm{sim}}$ and $f_{\mathrm{st},y^*,\mathrm{sim}}$ based on Equation (4.4) are shown in Figure (4.15). The correlation shows errors of up to 20 % for a low number of wire rows and equal to or less than 1% for a number of wire rows higher than 5. [More than] 98% of the data are below a 10% relative residual error. A similar agreement is found for the correlation-based prediction of the friction factor.

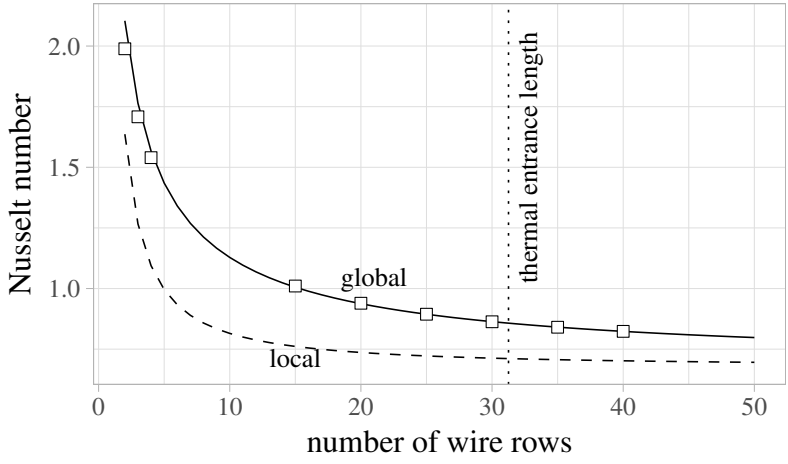

(a) Nu_{st} and $Nu_{st,local}$

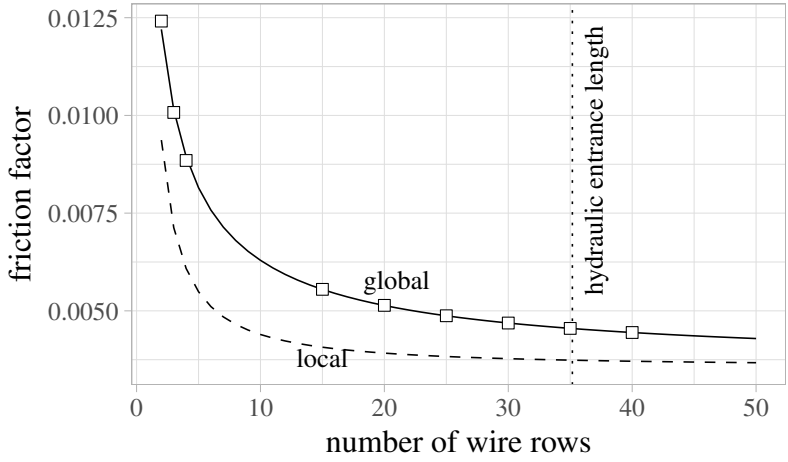

(b) f_{st} and $f_{st,local}$

Figure 4.14: Correlated global (solid lines) and local (dashed lines) performance parameter for an in-line arrangement as functions of the number of wire rows. Curves are based on the simulated global data points (squares) and fixed values for $a = 10$, $b = 3$, and $Re_{st} = 20$. Downstream of the entrance lengths (dotted lines) the flow is declared as developed; based on [FSF19].

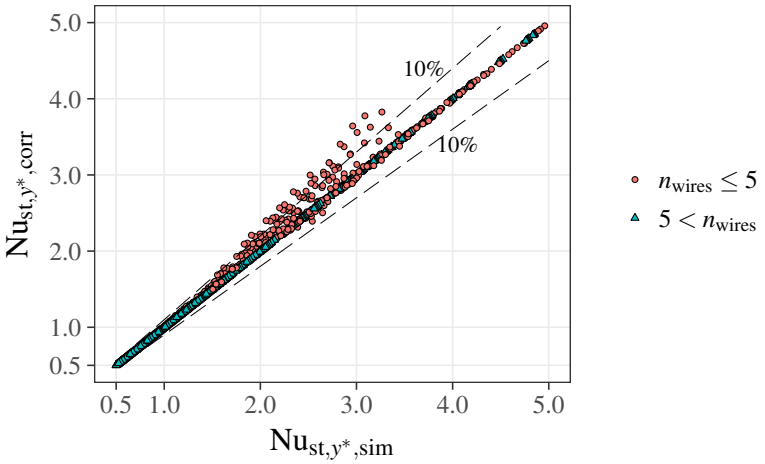

(a) Nusselt number

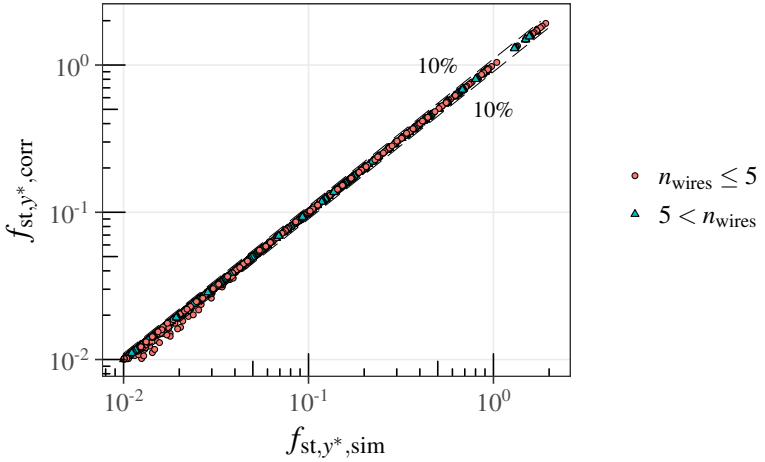

(b) Fanning friction factor

Figure 4.15: Predicted (correlated) values versus simulated values for the Nusselt number and the Fanning friction factor. Data is based on Equation (4.4) and (A.23). The predicted values are correlated via the number of wire rows n_{wires} (see Table 4.2) for specific Reynolds numbers $\mathrm{Re}_{\mathrm{st}}$ and geometry parameters a and b for an in-line arrangement, based on [FSF19].

The effect of Reynolds number and wire distances

The Nusselt number $\mathrm{Nu}_{\mathrm{st},\infty}$, Fanning friction factor $f_{\mathrm{st},\infty}$, and the coefficients $C_{1,\mathrm{Nu}}$, $C_{2,\mathrm{Nu}}$, $C_{1,f}$ and $C_{2,f}$ were determined based on 216 different operating and geometry conditions ($\mathrm{Re}_{\mathrm{st}}$, a, b). Each coefficient is correlated to these conditions by means of a weighted least square error with the software Eureqa. The weighting factor is chosen as the reciprocal of the coefficient itself. Table 4.7 and Table 4.8 give an overview of the derived correlations. Those correlations are chosen to be as accurate as possible, but with a limited number of correlation coefficients.

The Nusselt number $\mathrm{Nu}_{\mathrm{st},\infty}$ is related to the Reynolds number by a power law ansatz. The exponent varies between 0.1 and 1.25 mainly dependent on the lateral wire distance a. Figure 4.16(a) and (b) show the shape of curve for $\tilde{A}_{\mathrm{Nu}}$ and for the exponent $\tilde{B}_{\mathrm{Nu}}$ based on both geometry parameters. The friction factor $f_{\mathrm{st},\infty}$ is related to the logarithm of the Reynolds number by an exponential

Coefficients	Equations
$\mathrm{Nu}_{\mathrm{st},\infty}$	$\mathrm{Nu}_{\mathrm{st},\infty} = \tilde{A}_{\mathrm{Nu}} + 0.021\mathrm{Re}_{\mathrm{st}}^{\tilde{B}_{\mathrm{Nu}}}$
	$\tilde{A}_{\mathrm{Nu}} = \dfrac{2.16b}{a+b-\left(\frac{7.68b}{(3.56+b)^{0.5}}\right)^{0.5}}$
	$\tilde{B}_{\mathrm{Nu}} = \dfrac{b^{0.345}}{\exp(0.25a)}$
$f_{\mathrm{st},\infty}$	$f_{\mathrm{st},\infty} = \exp(\tilde{A}_f + \tilde{B}_f \log(\mathrm{Re}_{\mathrm{st}}))$
	$\tilde{A}_f = 0.005531ab + 0.005751a^2 + \dfrac{8.6054 - 0.2222b}{a + 0.1311ab}$
	$\quad - 0.9024 - 0.2985a - 0.008528b^2$
	$\tilde{B}_f = 0.07776b + 0.01624a + 0.0001427ab^2$
	$\quad - 0.06345\log(a) - 0.03442b\log(a) - 1.02134$

Table 4.7: Derived correlations for $\mathrm{Nu}_{\mathrm{st},\infty}$ and $f_{\mathrm{st},\infty}$ for in-line wire structure; based on [FSF19].

Coefficients	Equations
$C_{1,\mathrm{Nu}}$	$C_{1,\mathrm{Nu}} = \begin{cases} \tilde{A}_{1,\mathrm{Nu}} & \text{if } \mathrm{Re}_{\mathrm{st}}^{0.8} a^{2.0} b^{-1.1} > 24 \\ 0 & \text{if } \mathrm{Re}_{\mathrm{st}}^{0.8} a^{2.0} b^{-1.1} \leq 24 \end{cases}$
	$\tilde{A}_{1,\mathrm{Nu}} = 1.6896 + 0.03636b + 0.02745\mathrm{Re}_{\mathrm{st}} + \frac{0.5171a\mathrm{Nu}_{\mathrm{st},\infty}}{b} + \frac{-4.4822}{2.0963 + 0.1266\mathrm{Re}_{\mathrm{st}}} - 0.6369\mathrm{Nu}_{\mathrm{st},\infty}$
$C_{1,f}$	$C_{1,f} = \begin{cases} \tilde{A}_{1,f} & \text{if } \mathrm{Re}_{\mathrm{st}}^{0.8} a^{1.8} b^{-1.0} > 12 \\ 0 & \text{if } \mathrm{Re}_{\mathrm{st}}^{0.8} a^{1.8} b^{-1.0} \leq 12 \end{cases}$
	$\tilde{A}_{1,f} = 2.9 \times 10^{-5} - 0.428 f_{\mathrm{st},\infty} + \frac{f_{\mathrm{st},\infty}^{0.5}}{\tilde{B}_{1,f}}$
	$\tilde{B}_{1,f} = 1.631b + 0.064a\log(\mathrm{Re}_{\mathrm{st}}) - 0.62 - 0.0562ab^{0.5} - 0.155b\log(\mathrm{Re}_{\mathrm{st}})$
C_2	$C_2 = C_{2,f} = C_{2,\mathrm{Nu}} = \frac{1}{1+\tilde{A}_2}$
	$\tilde{A}_2 = 3.77 \times 10^{-6}\ \mathrm{Re}_{\mathrm{st}}^{1.95} a^{3.81} b^{-0.68}$

Table 4.8: Derived correlations for coefficients of $\mathrm{Nu}_{\mathrm{st}}$ and f_{st} for in-line wire structure based on Equation (4.4) and (A.23); based on [FSF19].

ansatz. The auxiliary coefficients $\tilde{A}_f$, and $\tilde{B}_f$ are shown in Figure 4.16(c) and (d), respectively. Both approaches, the power law ansatz and the exponential ansatz, are widely used to correlate the Nusselt number and the Fanning friction factor to the Reynolds number, respectively [11]. The coefficients $C_{1,\mathrm{Nu}}$ and $C_{1,f}$ are set to zero in case the global Nusselt number and friction factor, respectively, depend only weakly on the number of wire rows. Otherwise they are related to the operating and geometry conditions, as well as to $\mathrm{Nu}_{\mathrm{st},\infty}$ and $f_{\mathrm{st},\infty}$. Lastly, the coefficient C_2 as a representative of the decay of Nusselt number and friction factor with respect to the number of wire rows was chosen equal for both, the thermal and the hydraulic decay.

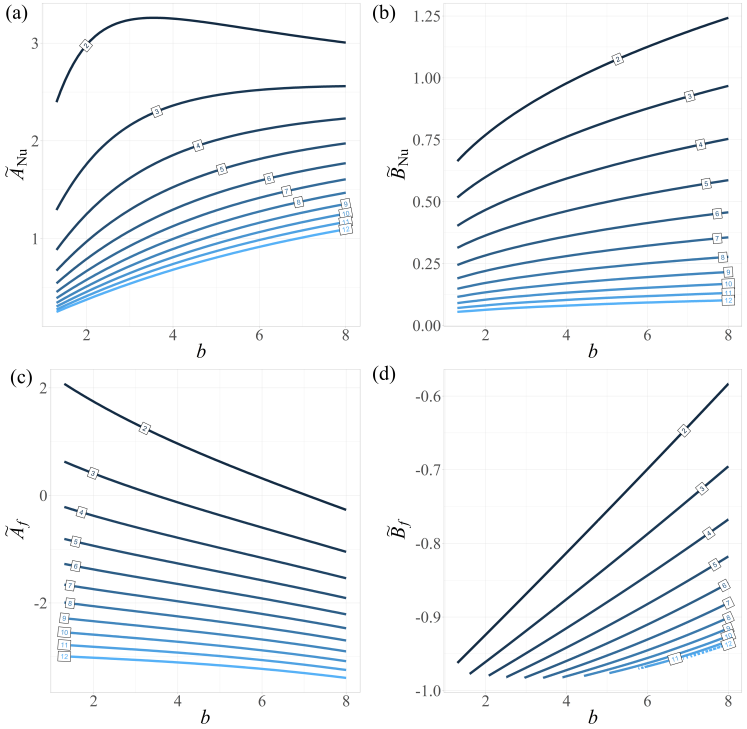

Figure 4.16: Auxiliary coefficients $\tilde{A}_{Nu}$ (a), $\tilde{B}_{Nu}$ (b), $\tilde{A}_f$ (c), and $\tilde{B}_f$ (d) needed for calculation of correlated Nusselt number and friction factor for an in-line arrangement based on Table 4.7. Geometry parameter a is shown on the contour lines [FSF19].

In Figure 4.17 the non-dimensional thermal and hydraulic entrance length is shown. Increasing Reynolds number, increasing lateral wire distance a, and decreasing longitudinal wire distance b yields a higher thermal entrance length. The entrance lengths range from 1 wire up to 200 wires.

The correlations in Table 4.7 and Table 4.8 can be used to calculate the entrance lengths L^*_{th} and L^*_{hy} based on Equation (4.9) and (A.25), respectively.

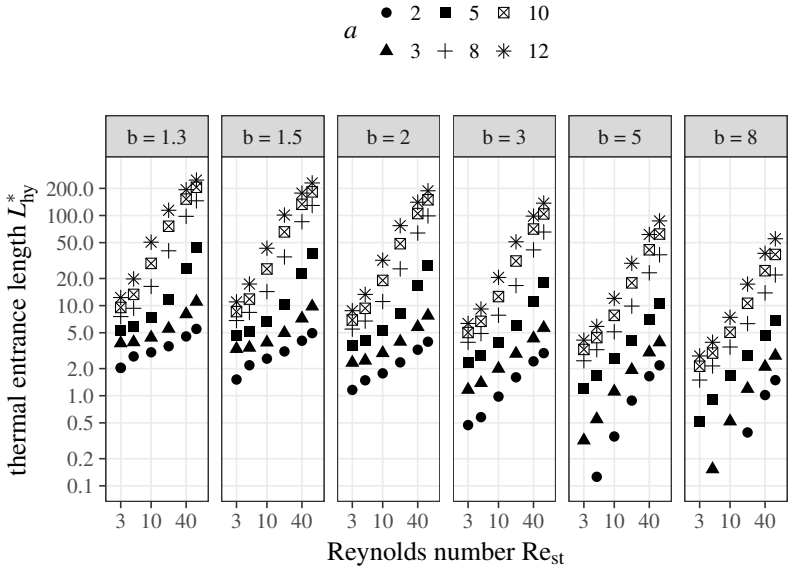

(a) Thermal entrance length L^*_{th}

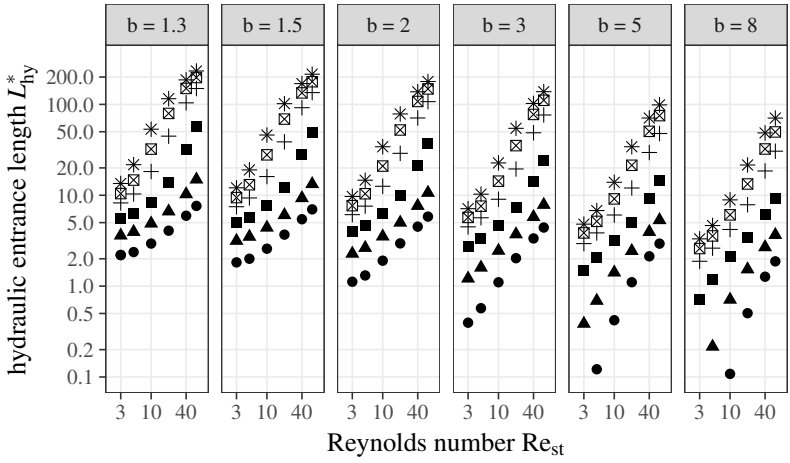

(b) Hydraulic entrance length L^*_{hy}

Figure 4.17: Non-dimensional entrance lengths for an in-line wire structure based on the Reynolds number Re_{st} and geometry parameters a and b. Entrances lengths below 0.1 are not shown [FSF19].

Correlation Errors

The correlations show good agreement for all investigated parameters a, b and $\mathrm{Re_{st}}$. The corresponding differences are summarized in Figure (4.18) and Figure (4.19) for $\mathrm{Nu_{st,\infty}}$,$f_{\mathrm{st},\infty}$ and for $\mathrm{Nu_{st,y^*}}$, f_{st,y^*}, respectively. It can be seen that the relative differences of predicted (correlated) Nusselt numbers versus simulated Nusselt numbers are below 25% and similarly for friction factors. The correlation predicts 94% and 99% of the simulated data for $\mathrm{Nu_{st,\infty}}$ and $f_{\mathrm{st},\infty}$ within $\pm 10\%$, respectively. Therefore, a thermally and hydraulically developed flow is well predicted with the correlation. The developing flows have an additional dependency on the number of wire rows. The correlation for the developing flow predicts 93% and 97% of the simulated data for $\mathrm{Nu_{st,y^*}}$and f_{st,y^*} within $\pm 10\%$, respectively. Table 4.9 shows details of the relative residual errors for different intervals and number of wire rows.

		relative residual error	
		$< 5\%$	$< 10\%$
$\mathrm{Nu_{st,\infty}}$	$n_{\mathrm{wires}} > L^*_{\mathrm{th}}$	81	94
$f_{\mathrm{st},\infty}$	$n_{\mathrm{wires}} > L^*_{\mathrm{hy}}$	94	99
$\mathrm{Nu_{st,y^*}}$	$n_{\mathrm{wires}} > 2$	76	93
$\mathrm{Nu_{st,y^*}}$	$n_{\mathrm{wires}} > 5$	79	95
f_{st,y^*}	$n_{\mathrm{wires}} > 2$	89	97
f_{st,y^*}	$n_{\mathrm{wires}} > 5$	92	99

Table 4.9: Percentage of correlated data which satisfy a relative residual error below 5% and 10% for $\mathrm{Nu_{st,\infty}}$, $f_{\mathrm{st},\infty}$, $\mathrm{Nu_{st,y^*}}$, and f_{st,y^*}. The percentage is specified for different number of wire rows in an in-line wire arrangement; based on [FSF19].

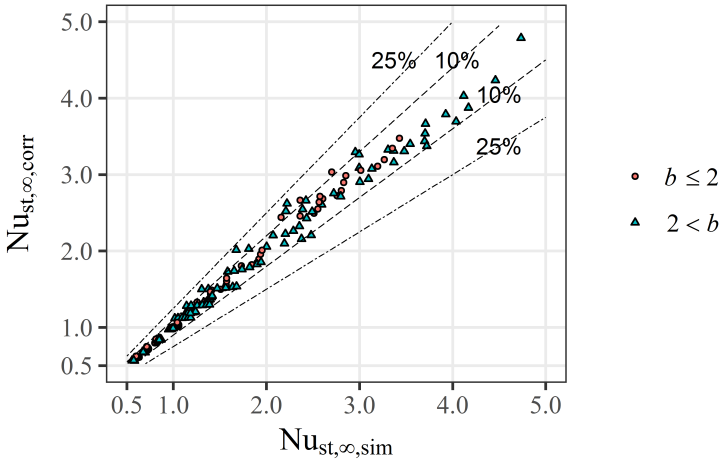

(a) Nusselt number

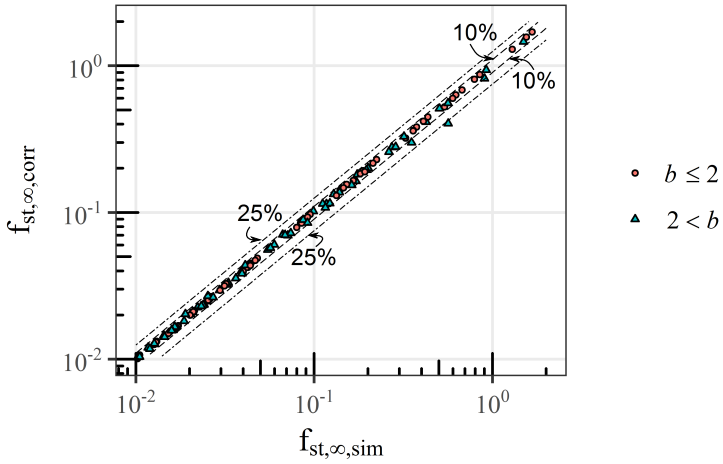

(b) Fanning friction factor

Figure 4.18: Predicted (correlated) values versus simulated performance parameters for a developed flow. Data is based on Table 4.7. The predicted values are correlated via the Reynolds number Re_{st} and geometry parameters a and b for an in-line arrangement; based on [FSF19].

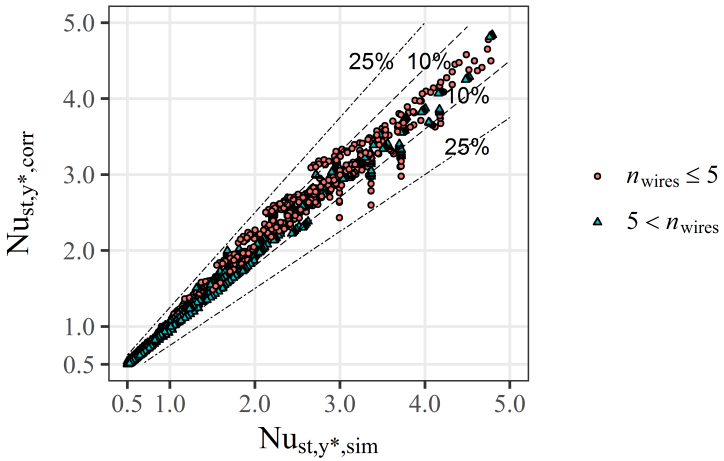

(a) Nusselt number

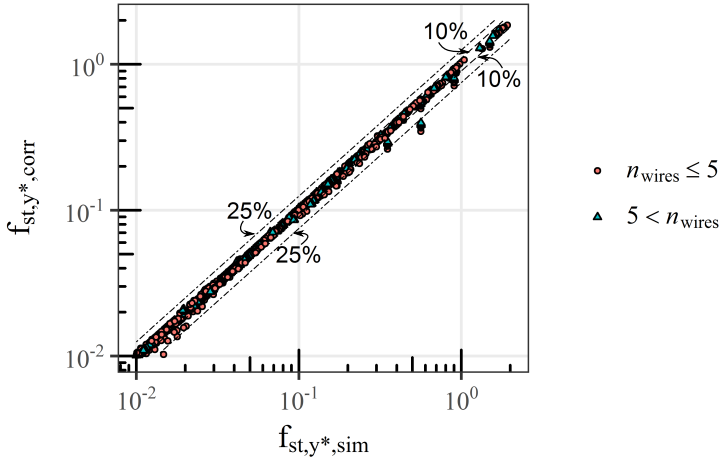

(b) Fanning friction factor

Figure 4.19: Predicted (correlated) values versus simulated performance parameters for a developing flow. Data is based on Equation (4.4) and (A.23), Table 4.7 and Table 4.8. The predicted values are correlated via the Reynolds number Re_{st}, geometry parameters a and b, and the number of wire rows n_{wires} for an in-line arrangement; based on [FSF19].

Discussion

The decrease in Nusselt number and friction factor for the in-line arrangement with respect to the number of wire rows can be well represented by the power law ansatz in Equations (4.4) and (A.23) for each combination of geometry parameters a and b, and the operation parameter Reynolds number (cf. Figure 4.14). The derived correlation for the developing flow predicts 93% and 97% of the simulated data for $\mathrm{Nu}_{\mathrm{st},y^*}$ and f_{st,y^*} within $\pm 10\%$. For the fully developed flow the correlation predicts 94% and 99% of the simulated data for $\mathrm{Nu}_{\mathrm{st},\infty}$ and $f_{\mathrm{st},\infty}$ within $\pm 10\%$. Further, the power law ansatz allows a description of the hydraulic and thermal entrance lengths related to a, b, and $\mathrm{Re}_{\mathrm{st}}$. The strong increase in non-dimensional entrance lengths with decreasing b can be explained by a shadowing effect for serried rows of wires in flow direction. A change in Reynolds numbers and lateral wire distances yields, similar to laminar fluid flow through a pipe, a proportional change in non-dimensional entrance lengths [70]. Figure 4.17 affirms this statement. Table 4.8 shows a simplified relation among a, b, and $\mathrm{Re}_{\mathrm{st}}$ for which the entrance region can be neglected for performance evaluation. For this combination of parameters it is sufficient to use the Nusselt number $\mathrm{Nu}_{\mathrm{st},\infty}$ and friction factor $f_{\mathrm{st},\infty}$ based on Table 4.7, independently of the number of wire rows in the application. However, apart from this combination of parameters, it is necessary to include the entrance region in the performance evaluation. The global Nusselt number for a specific heat exchanger can vary significantly from the Nusselt number $\mathrm{Nu}_{\mathrm{st},\infty}$ derived for the developed flow. Especially for compact heat exchangers with dimensions in the submillimeter range, the structure length in flow direction L_{st} is small, as heat transfer coefficients are high. Thus, the number of wire rows in flow direction can be very low and differ strongly from the non-dimensionalized entrance lengths. Exemplarily Figure 4.14(a) shows the difference of global Nusselt number $\mathrm{Nu}_{\mathrm{st},10}$ for a number of wire rows $n_{\mathrm{wires}} = 10$ to the Nusselt number $\mathrm{Nu}_{\mathrm{st},\infty}$ derived for the developed flow. $\mathrm{Nu}_{\mathrm{st},10}$ is 1.7 times higher than $\mathrm{Nu}_{\mathrm{st},\infty}$. The correlation predicts the relevant

parameters for a number of wire rows in the range of 2 to 5 more inexactly than higher number of wire rows. This decline in predictability is due to an error-prone estimation for low number of wire rows based on the method of interpolation. Therefore, it is recommended using the correlation for a number of wire rows less than 5 with caution. However, this restriction is minor, as a wire structure heat exchanger will probably be manufactured with more than 5 wires in flow direction in order to achieve a sufficiently high heat transfer surface. The performance upscaling to a 3D wire structure heat exchanger needs in addition information on wire material (particularly thermal conductivity) and wire length. Based on this information the fin efficiency (Section 4.5 or [11]) can be calculated and combined with the heat transfer coefficient, calculated from the correlation given in this study. Assuming the wire structure surface area dominates the total heat transfer surface area (cf. Case 1), the thermal resistance on the air-side can then be calculated. This procedure is valid as long as the influence of the tube wall is negligibly small (cf. model assumptions AS1 to AS5). Thus, very open structures (large a and b) or structures with short wire lengths need information on heat transfer on the outer tube wall. The staggered arrangement (with correlations shown in the Appendix A.3.2) shows higher Nusselt numbers and friction factors compared to the in-line arrangement for the same Reynolds number and geometry parameters a and b. This is not surprising, as the blockage of flow in the staggered arrangement is obvious. Thus, a staggered arrangement allows an even more compact design than the in-line arrangement. However, the related increase in pressure drop has to be considered" [FSF19].

The correlations are used in Chapter 6 for optimization of the wire structure geometry.

4.5 Fin Efficiency

"The common method of calculating the fin efficiency is based on a uniform (constant) temperature of the ambient fluid along the fin. The fin efficiency η_{fin} of plate-fin and tube-fin geometries of uniform fin thickness and adiabatic tip is given in Section 2.3 based on [11]. [...] The thin fin theory has several restrictions; pin fin heat exchangers might not confirm with two of them:

- The heat transfer coefficient h_{air} for the fin surface is uniform over the surface
- The temperature of the ambient fluid is uniform

Especially the second restriction is not valid for flows with lower fin efficiencies and several pin fins in flow direction: The fluid passes first a pin with non-constant temperature, thus reaching all following pins in flow direction with a non-constant fluid temperature. The fin efficiency with uniform ambient fluid temperature will be defined as $\eta_{\text{fin,uT}}$." [FGS19]

4.5.1 Method based on Non-Uniform Temperature

"The developed method of calculating the fin efficiency is based on a non-uniform temperature of the ambient fluid along the fin. The general one-dimensional ordinary differential equation describing heat conduction within a fin can be taken from [11] and is given as:

$$\frac{\partial^2 T_{\text{fin}}}{\partial z^2} - m^2 (T_{\text{fin}} - T_{\text{fluid},\infty}) = 0 \tag{4.12}$$

$$T_{\text{fin}}(0) = T_{\text{base}} \tag{4.13}$$

$$\frac{\partial T_{\text{fin}}}{\partial z}(l) = 0 \tag{4.14}$$

We consider $T_{\text{fluid},\infty}$ to be a function of z and thus the ordinary differential equation system (4.12)-(4.14) has to be solved differently from [11]. The

solution shall allow an analytic description of the fin efficiency η_{fin} analogously to Equation (2.25). Two steps have to be taken therefore. Firstly, the far field temperature $T_{\text{fluid},\infty}$ has to be defined reasonably; Secondly, the solution of temperature field T_{fin} has to be determined. The far field temperature $T_{\text{fluid},\infty}$ should have

- close to the wall a temperature (fin base) equal to the wall temperature:

  $T_{\text{fluid},\infty}(0) = T_{\text{wall}}$
- a vanishing derivative at half the wire length (fin tip):

  $\frac{\partial T_{\text{fluid},\infty}}{\partial z}(l) = 0$
- a mean value specified by the user:

  $T_{\text{fluid},\infty,\text{mean}}$
- a coefficient representing the curve slope of the far field temperature:

  K_1

A possible functional expression of $T_{\text{fluid},\infty}$ can be of the following form:

$$T_{\text{fluid},\infty} = K_3 \left(\exp\left(-\frac{K_1 z}{l} \right) + \frac{K_1 z}{l} \exp\left(-K_1\right) - K_2 \right) \tag{4.15}$$

with

$$K_2 = \frac{T_{\text{fluid},\infty,\text{mean}} - 0.5 K_1 T_{\text{wall}} \exp(-K_1) - \frac{T_{\text{wall}}}{K_1} + \frac{T_{\text{wall}}}{K_1} \exp(-K_1)}{T_{\text{fluid},\infty,\text{mean}} - T_{\text{wall}}} \tag{4.16}$$

$$K_3 = \frac{T_{\text{wall}}}{1 - K_2} \tag{4.17}$$

and K_1 ranging from 0 to infinity. K_1 to K_3 are auxiliary values. Figure 4.20 shows the fluid temperature courses for a variety of values of K_1 along the wire length l ranging from $z = 0\,\text{m}$ to $0.005\,\text{m}$. The temperature has a strong non-linear profile. [The coefficient K_1 is an artificial quantity to express a variety of reasonable far field fluid temperature curves. It is later related to physical quantities.]

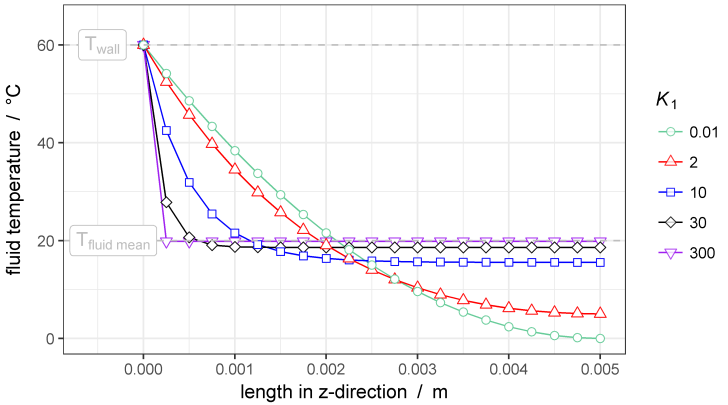

Figure 4.20: Different fluid temperature courses $T_{\text{fluid},\infty}$ (based on Equation (4.15)) along the length l of the fin in z-direction for an exemplaric wall temperature $T_{\text{wall}} = 60\,°\text{C}$ and mean fluid temperature $T_{\text{fluid},\infty,\text{mean}} = 20\,°\text{C}$; $K_1 = 300$ resembles constant fluid temperature; based on [FGS19].

The differential equation system (4.12)-(4.14) together with Equation (4.15) are solved analytically in the Appendix A.2.1. The solution yields a fin efficiency with a non-uniform temperature (nuT) profile:

$$\eta_{\text{fin,nuT}} = -\frac{1}{\kappa^2}\frac{K_1 e^{-K_1} - \frac{K_1\kappa^2}{\kappa^2 - K_1^2} - \alpha_1\kappa + \alpha_2\kappa}{1 - e^{-K_1}\left(\frac{K_1}{2} - \frac{1}{K_1}\right) - \frac{1}{K_1})} \tag{4.18}$$

with the parameters α_1 and α_2 specified in Equation (A.13) and $\kappa = ml$ specified in Equation (2.28). The fin efficiency courses are shown in Figure 4.21.

For $\kappa \leq 1$ the differences of fin efficiency based on the non-uniform and uniform temperature method are rather small. However, for larger values of κ the fin efficiency calculation based on the uniform temperature method could yield high errors compared to the expected value." [FGS19]

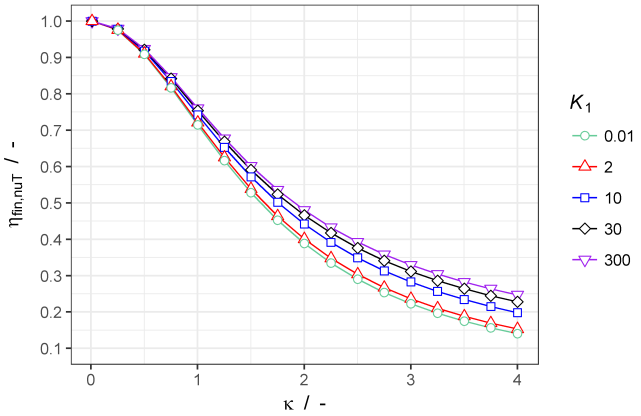

Figure 4.21: Fin efficiency courses (based on Equation (4.18)) related to κ for different values of K_1; $K_1 = 300$ resembles constant fluid temperature with $\eta_{\text{fin,nuT}} = \eta_{\text{fin,uT}}$; based on [FGS19].

4.5.2 Verification of Methods

"The combination of the 2D simulation correlations of convective heat transfer with the analytic solutions for conductive heat transfer through the pin fins ($\eta_{\text{fin,uT}}$,$\eta_{\text{fin,nuT}}$) shall be analyzed here. The combination of the convective method with the conductive method will be compared to the 3D model results. Further the 2D simulation correlations for friction factor shall be compared to the 3D results. The friction factor of the 3D simulation and the 2D simulation [correlations] differ slightly from each other. The 3D simulation shows a higher value for friction factor compared to the 2D simulation; however, the relative difference is below 10% for more than 90% of the data points. Thus, the friction factor is assumed to be simulated with sufficient accuracy with the 2D simulation and no correction is necessary. Several options are available for expressing the heat transfer performance of a heat exchanger. Equations (2.16), (2.19), and (2.22) show the effective heat transfer coefficient $U_{\text{air,eff}}$, the convective heat transfer coefficient h_{air}, and the Nusselt number Nu_{air}.

Figure 4.22 shows schematically the linkages among themselves and with the fin efficiencies defined above." [FGS19]

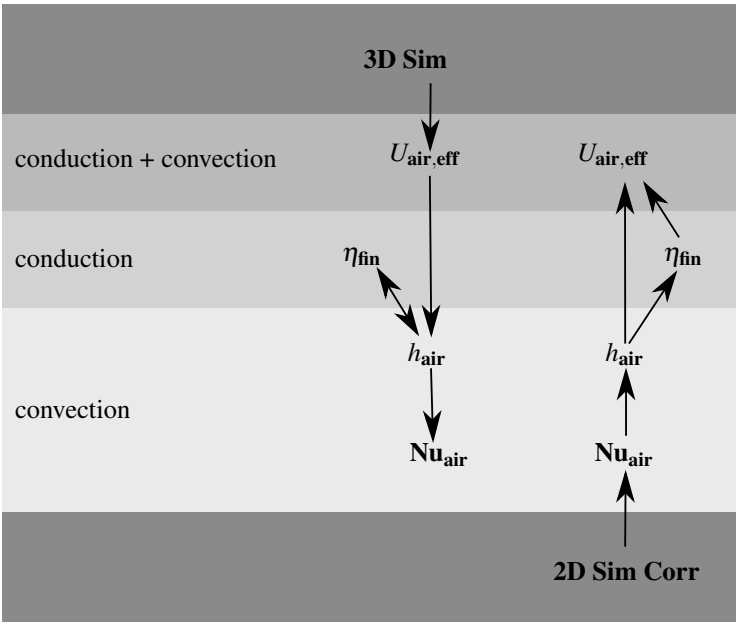

Figure 4.22: Scheme of the heat transfer quantities used for comparison and their linkages; based on [FGS19].

Example-Based Comparison of Fin Efficiency Methods

"As an example a simulation with $\mathrm{Re_{st}} = 20$, $a = 3$, and $b = 2$ is shown in Figure 4.23. The mean fluid temperature is taken to be the mean of the thermodynamic fluid temperature in the flow before (cross section 1) and after (cross section 2) the wire. Due to differences in velocity in the cross section, this thermodynamic mean temperature differs from a non-weighted temperature mean. The simulated fluid temperature shown in Figure 4.24 is the far field temperature on the edge of cross section 2 shown in Figure 4.23. It shows a

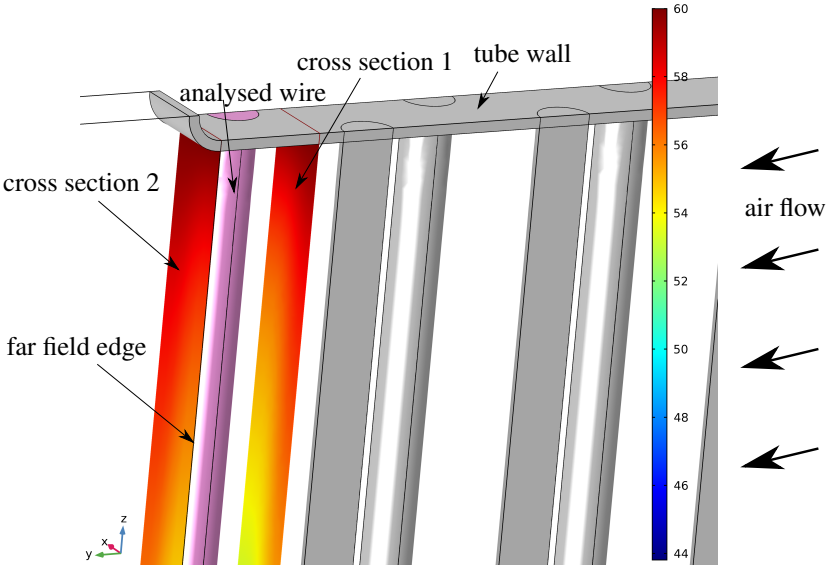

Figure 4.23: Domains and sections of a wire structure heat exchanger analyzed for fin efficiency of the last wire in flow direction; based on [FGS19].

non-uniform profile (circles) which is in good agreement with the temperature $T_{\text{fluid},\infty}$ based on Equation (4.15) with $K_1 = 1$ (triangles). Based on the choice of K_1 the ordinary differential equation system (4.12)-(4.14) has been solved analytically. The non-uniform temperature solution yields the fin (wire) temperature T_{fin} (V shaped triangles). This temperature is again in good agreement with the simulated wire temperature (diamonds). The common method of solving (4.12)-(4.14) with a uniformly constant ambient temperature (squares) yields a third wire temperature (crosses) in Figure 4.24. The wire temperature is higher for the uniform temperature method, especially in the second half of the fin compared to the simulated wire temperature. Thus, the uniform temperature method does not allow a sufficient description of fin temperature (and fin efficiency) for these geometric and operational conditions. The differences in fin efficiency and effective heat transfer coefficient of the non-uniform and the

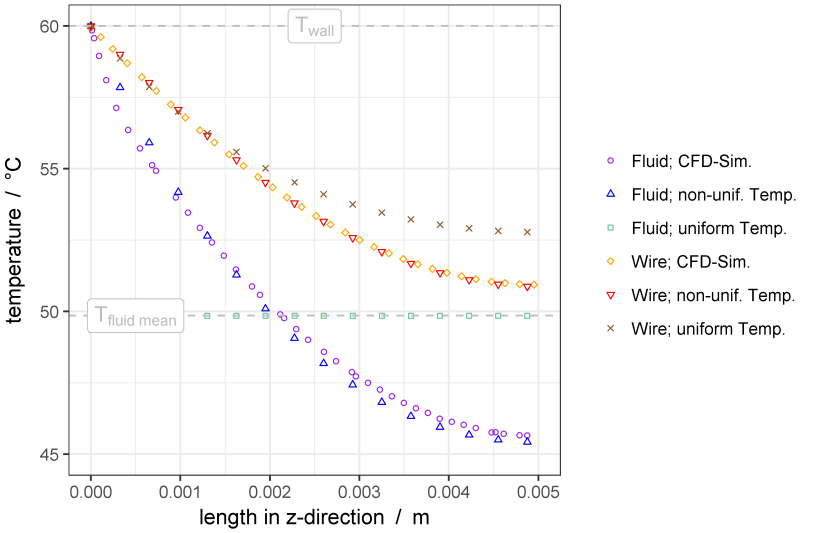

Figure 4.24: Comparison of the temperatures of the fluid and the wire for the outlet region (cf. Figure 4.23) of a wire structure with $\mathrm{Re}_{\mathrm{st}} = 20$, $a = 3$, $b = 2$ for a non-uniform and uniform fluid temperature distribution; $T_{\mathrm{fluid},\infty,\mathrm{mean}}$ is equal to the thermodynamic temperature, $K_1 = 1$; length in z-direction; based on [FGS19].

uniform temperature method is shown in Table 4.10. Data for h_{air} are based on the 2D-simulation [correlation]. This example shows the necessity to use adequate fluid temperatures for calculation of fin efficiency and thus effective heat transfer coefficients $U_{\mathrm{air,eff}}$ from given heat transfer coefficients h_{air} (e.g. from 2D Simulation) or conversely (e.g. from measurements)." [FGS19]

Evaluation of Convection Method

"The effective heat transfer coefficient for 3D and 2D simulations is shown in Figure 4.25. The 3D data represents high fin conductivity. In the results the solid part of the structure (wires) and the tube wall is not included in the heat transfer simulation. The contact area between solid and fluid is set as outer boundary for the fluid side. With a temperature boundary condition on

Parameter	Dimension	Analytic 1 (uniform temperature)	Analytic 2 (non-uniform temperature)	CFD (3D simulation)
K_1	-	Inf	1.0	-
h_{air}	$W/(m^2\,K)$	1099	1099	-
κ	-	1.86	1.86	-
η_{fin}	-	0.500	0.415	-
$U_{air,eff}$	$W/(m^2\,K)$	549	456	456

Table 4.10: Thermodynamic characteristics of wire No. 10 from Figure 4.23 for analytic solutions and the 3D-CFD simulation; based on [FGS19].

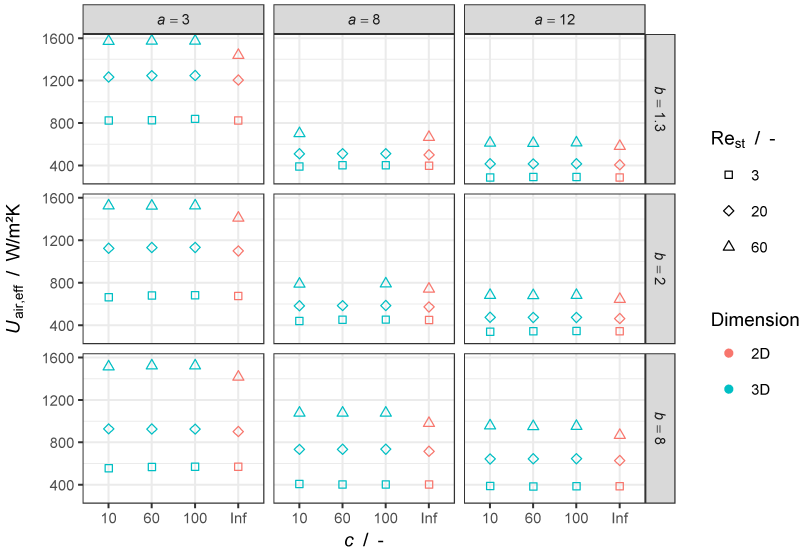

Figure 4.25: Effective heat transfer coefficient $U_{air,eff}$ as a function of non-dimensional wire length c for 3D simulations ($k_{st} = \infty$, $k_{wall} = 0$) and 2D simulations ($k_{st} = \infty$); based on [FGS19].

the wires and a zero temperature gradient boundary condition on the outer tube wall. Thus, the heat transfer surface area is based on the wire surface area only and the specific wall conductivity can be assumed to be $\chi_{\text{wall,st}} = 0$ (3D). The non-dimensional wire length is given by $10 \leq c \leq 100$ (3D) and the number of wire rows is equal to 10. Missing data points are related to simulations which did not converge for the normalized grid spacing 1 (cf. Table 4.6) and for different solving methods.

Higher values for Reynolds number Re_{st} show higher effective heat transfer coefficients, as the limitation due to convection is reduced. Smaller values of c show slightly larger values of $U_{\text{air,eff}}$. However, the maximum relative difference between $U_{\text{air,eff}}$ for $c = 100$ and for $c = 10$ is 3.5%. The slope of $U_{\text{air,eff}}$ with respect to c is either horizontal or slightly positively inclined, such that $U_{\text{air,eff}}$ is converging against a fixed value for specific a, b, and Re_{st}. The 3D simulation shows slightly higher values for $U_{\text{air,eff}}$ compared to the 2D simulation due to different flow characteristics in the tube-wire-geometry and due to the higher uncertainty in 3D-discretization (cf. Table 4.6). The relative differences range from 0.1% to 9.7%. Low values of non-dimensional lateral wire distance a allow the highest values of $U_{\text{air,eff}}$, whereas a trend for b is not obvious.

Evaluation of the Conduction Method

The dependency of $U_{\text{air,eff}}$ on the Reynolds number is shown in Figure 4.26. Higher values of k_{st} and Re_{st} show higher effective heat transfer coefficients, as the limitation due to conduction and convection is reduced, respectively. Low values of a allow the largest values of $U_{\text{air,eff}}$.

Figure 4.27 shows the Nusselt number, calculated with Equation (2.22). The fin efficiency and surface efficiency is based on the uniform temperature method in Equation (2.25) and (2.30), respectively. The Nusselt number increases with increasing Reynolds number. For small values of b and large values of a the differences in Nusselt number due to the thermal conductiv-

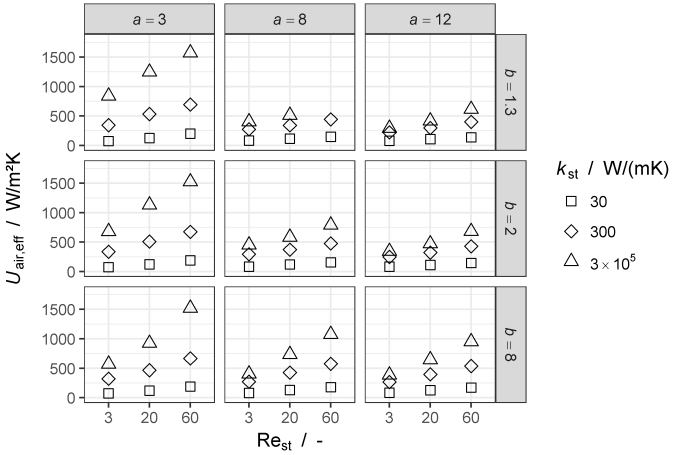

Figure 4.26: Effective heat transfer coefficient for 3D simulation results ($k_{st} = 3$, 300 and $3 \times 10^5 \mathrm{W}/(\mathrm{m\,K})$); non-dimensional wire length is given by $c = 100$; based on [FGS19].

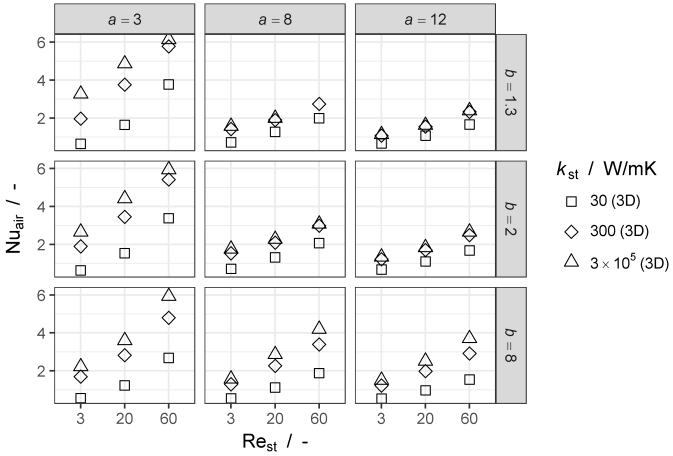

Figure 4.27: Nusselt number for 3D simulation results ($k_{st} = 3$, 300 and $3 \times 10^5 \mathrm{W}/(\mathrm{m\,K})$); Calculation of fin efficiency based on uniform temperature method from Equation (2.25); based on [FGS19].

ity k_{st} diminish. Conversely the Nusselt number shows strong differences for large values of b and small values of a. As the convective heat transfer and thus the Nusselt number should be independent of the parameter k_{st}, the underlying calculation of the conductive heat transfer with the uniform temperature method must be insufficient. Otherwise all data points for a specific set of a and b should lie on one curve.

Assuming the Nusselt number (and h_{air}) for $k_{st} = 3 \times 10^5 \mathrm{W}/(\mathrm{m\,K})$ has no dependency on conduction and is thus representing the convective heat transfer adequately, a corrected fin efficiency for the parameter sweep with lower thermal conductivity of the wire can be calculated with Equation (2.20). This fin efficiency is denoted $\eta_{fin,sim}$ and it is given by the quotient of $U_{air,eff}$ (with lower thermal conductivity) and h_{air} (with $k_{st} = 3 \times 10^5 \mathrm{W}/(\mathrm{m\,K})$). In the simulation, the heat conduction is limiting the heat transfer more than expected from the analytical solution by the uniform temperature method. This underestimation is more noticeable for lower Reynolds numbers represented by a higher number of transfer units ntu_{fluid} (cf. Equation (2.23)). Figure 4.28 (left) shows the overestimation of the fin efficiency by a factor of up to 4 based on the common method with a uniform temperature profile. The usage of the non-uniform temperature method could decrease this overestimation. However, the value of K_1 must be estimated in order to calculate the fin efficiency with Equation (4.18). In the Appendix A.2.2 it is shown, that the fin efficiency is solely dependent on κ and ntu_{fluid}. However, based on Appendix A.2.1 the fin efficiency is given explicitly by the two parameters κ and K_1 Thus, the value of K_1 is solely dependent on κ and ntu_{fluid}. An approximation of correlation is given by

$$K_1 = \frac{31.1}{\mathrm{ntu}_{fluid}} + \frac{8.6 + 3.4\kappa}{\mathrm{ntu}_{fluid}} \tag{4.19}$$

based on a parametric sweep of the model in Appendix A.2.2. The system (A.18) was solved with Comsol Multiphysics for $0.1 < \mathrm{ntu}_{fluid} < 4$ and

$0.1 < \kappa < 8$. The fin efficiency was thereafter calculated based on Equation (4.18) and (4.19) and the 3D simulation data. Small values of $\mathrm{ntu_{fluid}}$ and/or κ yield a more homogeneous fluid temperature and thus a higher value of K_1. Figure 4.28 (right) shows the fin efficiency with uniform temperature profile $\eta_{\mathrm{fin,nuT}}$ in comparison to the expected value $\eta_{\mathrm{fin,sim}}$." [FGS19]

4.5.3 Discussion

" The 3D simulation model allows simulation of several different geometrical and operational conditions of a pin fin heat exchanger; however, due to high computational costs a broad parametric study is not suitable: A single simulation run (geometry and air inlet velocity fixed; see Table 4.2) has been simulated within at least 1 hour on a simulation server (KDE SC 4; 2 Intel Xeon E5-2690; each 6 cores, 2.9 GHz; 128 GB RAM). The minimum degrees of freedom for the geometry and the operating conditions have been defined by 7 parameters ($\mathrm{Re_{st}}$, a, b, n_{wires}, c, σ, and $\chi_{\mathrm{st,air}}$). Thus, a reasonable parametric study with 5 values for each parameter would consist of 7^5 simulation runs,

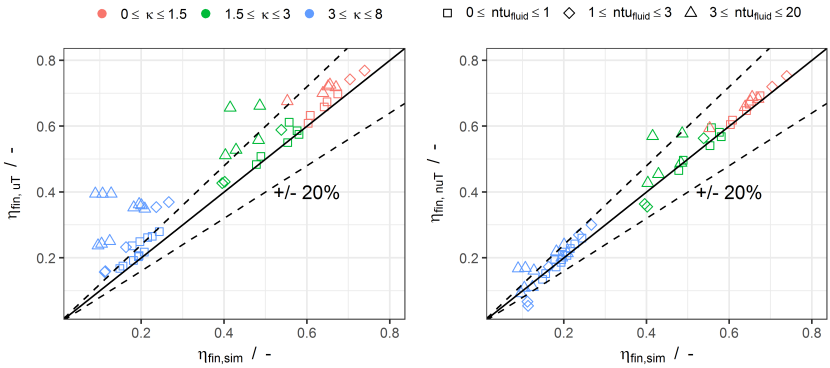

Figure 4.28: Fin efficiency for 3D simulation results; Calculation of fin efficiency based on common method from Equation (2.25) (left) with uniform temperature profile and on developed method from Equation (4.18)-(4.19) (right) with non-uniform temperature profile; based on [FGS19].

which corresponds to more than 700 days. However, the 3D simulation has been used for validation of a more simple determination of thermal-hydraulic performance based on the 2D simulation of convection heat transfer and an analytic solution of conductive heat transfer with non-uniform temperature profile. The agreement of 2D and 3D simulation results for pressure drop (friction factor) is sufficient, with more than 90% of the data points showing a relative difference below 10%. Thus, the correlations developed in Section 4.4.2 based on $\mathrm{Re}_{\mathrm{st}}$, a, b, and n_{wires} can be used straight away including the free-flow ratio σ in Equations (2.11) and (2.12). The effective heat transfer coefficient for 3D simulations with reduced limitation by conduction ($k_{\mathrm{st}} = \infty$) shows reasonable agreement with the 2D simulation correlations (see Figure 4.25). 90% of the data have a relative difference of less than 8%. A correction, due to the different inflow conditions with the tubes blocking the flow, can be considered; however, uncertainties due to an inadequate description of conduction predominate and have been focused on. Even for smaller fin heights (order $c = 10$) the 2D simulation results are adequately representing the convection heat transfer, although wall effects are occurring.

The Nusselt number of the 3D simulation with reasonable thermal conductivity ($k_{\mathrm{st}} = 30$ and $300\ \mathrm{W/(mK)}$) is much smaller than the non-limiting case ($k_{\mathrm{st}} = \infty$), when using the common uniform temperature method of fin efficiency calculation for the 3D data. Conversely, a direct adoption of the common fin efficiency in combination with the Nusselt number from Section 4.4.2 yields for a wide range of parameters a strong overestimation (of up to 400%) of the total heat transfer of a pin fin heat exchanger (see Figure 4.28). The example application shows one important reason for the inadequate description of conduction with the uniform temperature method: A non-uniform temperature profile of the ambient fluid. The equation of state, describing the fin and air temperature, allows two approaches to find an adequate description of conduction through the pin fins. Firstly, the ambient fluid temperature is set to a well-defined value or function and the system is solved for the fin temperature

(Equations (4.12)-(4.14)); secondly the ambient temperature and the fin temperature are numerically solved at the same time (Equations (A.18)). For the first approach a suitable function for non-uniform temperature profiles could be defined in Equation (4.15); however, the rate of temperature change must be indicated by a parameter K_1. The value of K_1 is based on the geometrical and operational conditions, such that K_1 cannot be fixed to a special value. Information on the temperature profiles could be taken from simulations or measurements; however, the effort would be too large to justify this approach. Thus, a compromise of an analytical solution and a numerical solution for the fin efficiency has been tackled. The parameter K_1 is related to the number of transfer units $\mathrm{ntu}_{\mathrm{fluid}}$ and to the parameter κ, based on solving the 2D fin and air temperature Equations (A.18). The developed correlation (4.19) was chosen such that the complexity was reasonable and the accuracy for the considered range of η_{fin} data (based on Equation (4.18) and (A.21)) was below 2% relative difference. Equations (4.12)-(4.14) could then be solved analytically (Appendix A.2.1) for a non-constant ambient temperature. The reduction in fin efficiency due to the non-uniform temperature profile can be seen in Figure 4.21. The fin efficiency shows deviations of up to 100% for fixed values of κ, but different types of ambient temperature profiles.

The non-uniform temperature method for fin efficiency calculation is more complex than the uniform temperature method. Besides the parameter κ the number of transfer units $\mathrm{ntu}_{\mathrm{fluid}}$ is needed. Differently to [74] the fin efficiency is based strongly on an analytical solution. The benefit can be seen in Figure 4.28. The fin efficiency based on the non-uniform temperature method shows much smaller differences to the expected fin efficiency $\eta_{\mathrm{fin,sim}}$. More than 87% of the data lies within a $\pm 20\%$ bandwidth; for the uniform temperature method only 56% lies within this bandwidth. The fin efficiencies $\eta_{\mathrm{fin,nuT}} > 0.6$ show a very small difference of less than 5% towards $\eta_{\mathrm{fin,sim}}$. Especially these fin efficiencies will occur within a heat exchanger. The fin efficiencies $\eta_{\mathrm{fin,uT}}$ show in this range still differences of up to 10% compared

to $\eta_{\text{fin,sim}}$. However, for a wide range of reasonable operating conditions (e.g.: $\kappa \leq 1$, $\text{ntu}_{\text{fluid}} \leq 4$) the difference of $\eta_{\text{fin,uT}}$ and $\eta_{\text{fin,nuT}}$ is below 3%. Thus, in general it is not necessary to use the non-uniform temperature method for rough performance estimation. Care has to be taken when designing fins with lower common fin efficiency, or when uncertainties will be very low. The limitation due to convection will be more pronounced than in the design case.

The developed fin efficiency can be used for an in-line arrangement of pin fins and for a wall conductivity which is in the same dimension as the wire conductivity ($\chi_{\text{wall,st}} \approx 1$, Case 2). The basic profile of ambient temperature could be the same as for the staggered arrangement with reduced wall conductivity. The simplification ($\chi_{\text{wall,st}} \ll 1$) allowed a clear definition of the comparable heat transfer coefficients of 2D and 3D simulations. The 2D correlation should be used with caution, when the heat transfer surface area is not determined by the wires, but by the wall. The method of non-uniform temperature profiles can be applied for other types of fins as well. Equation (4.18) holds independently of the fin type. Care has to be taken with the parameters m and K_1. Whereas the definition of m can be looked up in [11] for a variety of fin types, the correlation in Equation (4.19) for K_1 holds only for fins with approximately zero heat conduction in flow direction of the air. The pins, as separated from each other, fulfil this requirement. Other types of fins, such as corrugated fins, have additional thermal conductivity in air flow direction. The energy equations (A.18) have to be solved again with an additional term representing the thermal conductivity of the fin in air flow direction. ” [FGS19] The definition of fin efficiency in Equation (4.18) will be used for performance evaluation of wire structures in Chapter 6.

5 Experimental Analysis of Wire Structure Heat Exchangers

The simulation results show high heat transfer coefficients with the use of wire structures in a heat exchanger. However, the simulation is limited to parallel wires with (1) no contact resistance between wires and plate, (2) in-line and staggered arrangement of wires without manufacturing inaccuracy and (3) steady-state laminar flow. This limitation might be invalid for some types of wire structures. The experimental analysis shall show performance data which can be compared later to simulation. The limitations can be checked thereafter. Moreover, the experimental analysis shall show the feasibility of manufacturing wire structure heat exchangers based on two technologies. The first technology is based on corrugation of woven fabrics with a low number of impeding wires and subsequent welding to plates/tubes. The second technology is based on the pin fin manufacturing process however, with much longer and thinner wires than commonly used .

The size of the wire structure heat exchanger has to meet two important requirements. Firstly, manufacturing effort should be kept small. Secondly, uncertainties in performance measurement shall be kept small. In simplified terms, the former requirement can be realized with small dimensions of heat exchangers, the latter with large dimensions. Thus, dependant on the manufacturing effort, small samples as well as large samples have been manufactured and tested for performance at two different test rigs.

5.1 Description of Testing Facilities

5.1.1 Test Rig for Heat Exchangers

“The test samples are characterized for heat transfer and fluid dynamics at a test rig at Fraunhofer ISE. Air and water are used for characterizing the gas-to-liquid heat exchangers. The test rig is described in [FTS15] and has been adapted. In front of the test section containing the sample (see Figure 5.1), a flow conditioning section is installed on the air-side (not shown). It comprises of a chiller, an electric heater, a humidifier, a controllable fan, and the respective sensors for air temperature, humidity, and volume flow (orifice plate). It can deliver temperatures in the range of 5-40 °C and volume flow rates of 150-1000 m^3/h.

In order to be able to measure heat exchangers at lower air volume flows, a bypass valve is installed in the upper part of the setup, with an ultrasonic flow

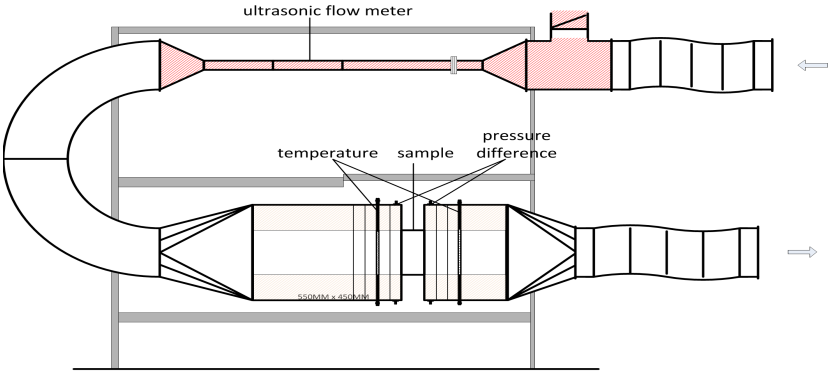

Figure 5.1: Scheme of the air-side of the heat exchanger test rig at Fraunhofer ISE; the air flow conditioning section is connected at the right side of the test rig; based on [FLS17].

meter in a DN50 duct section (highlighted in Figure 5.1). This way, air volume flows as low as $10\,m^3/h$ can be measured. For volume flows of $150\,m^3/h$ and above, this section is replaced by a straight DN280 tube. Following the bend (DN280), there is a 510-mm straight, rectangular channel of 185 mm × 231 mm. In the test section, fast-reacting thin chip Pt100 temperature sensors are used (calibrated to a standard uncertainty of 0.05 K). Four sensors are installed at the inlet channel, followed by two metal screens, which ensure a uniform velocity profile. In the outlet channel, 12 sensors record the temperature. All sensors are installed in the center of squares of equal area adopted from DIN EN 306 [75]. The pressure drop across the sample is measured with two differential pressure transmitters (PU/PI; halstrup-walcher GmbH, Kirchzarten, Germany) with a measuring range of 0-50 Pa (for good accuracy at low pressure drops; standard uncertainty: 0.1 Pa) and 0-250 Pa (for high pressure drops; standard uncertainty: 1 Pa). The entire testing section is leakage tested and thermally insulated. On the water side, the temperature and volume flow rate can be controlled by a chiller/heater (Unichiller 017Tw-H, Huber Kältemaschinenbau AG, Offenburg, Germany) and measured with Pt100 resistance temperature sensors (Omnigrad T TST310, Endress+Hauser, Reinach, Switzerland; calibrated to a standard uncertainty of 0.05 K) and an electromagnetic flow sensor (Optiflux 1000, Krohne, Duisburg, Germany; standard uncertainty: 0.4% of the measured value). Pressure drop is measured via a differential pressure transmitter (idm331, 0-0.6 bar; ICS Schneider Messtechnik GmbH, Hohen Neuendorf, Germany; standard uncertainty: 3 mbar). During measurements, the inlet air temperature $T_{air,in}$ is fixed at ambient temperature in order to avoid losses, while the water enters the heat exchanger [in standard tests] at $T_{water,in} = 60\,°C$. The water flow rate is set to approximately $1\,m^3/h$ to avoid heat transfer limitation on the water side; therefore, the change in water temperature across the heat exchanger is very small ($< 1\,K$). For the characterization of the heat exchangers, the air volume flow rate is increased stepwise from $30\,m^3/h$ to $800\,m^3/h$. The heat

domain	measured variable	technolgy	range	standard uncertainty
air	temperature	thin Pt100	5-90 °C	0.05 K
air	volume flow rate	ultrasonic flow meter	10-270 m^3/h	2% of meas. value
air	volume flow rate	orifice plate	150-1000 m^3/h	2% of meas. value
air	pressure drop	differential pressure transmitter	0-50 Pa	0.1 Pa
air	pressure drop	differential pressure transmitter	0-250 Pa	1 Pa
air	absolute pressure	barometric pressure sensor	500-1100 hPa	0.3 hPa
water	temperature	Pt100 rod sensor	5-90 °C	0.05 K
water	volume flow rate	electromagnetic flow sensor	0-7.2 m^3/h	0.4% of meas. value
water	pressure drop	differential pressure transmitter	0-0.6 bar	3 mbar

Table 5.1: Major sensor technology installed at test rig for heat exchangers.

exchanged is then determined through the air-side energy balance" [FLS17]. The installed sensor technology is summarized in Table 5.1.

5.1.2 Test Rig for Heat Exchanger Surface Area Enhancement

"As the manufacturing of [...] new structures is demanding and a variation of geometry is often necessary, manufacturing of real-size heat exchangers is costly in terms of labour and investment. Thus, an experimental setup for small-scale samples (with air channel heights in the centimeter range) is

favoured over a setup for large-scale samples. Smaller test rigs are accompanied with higher relative uncertainties, due to e.g., lower mass flow rates and lower heat transfer rates. This results in limitations for performance evaluation of the heat transfer enhancement structures [...]. A number of authors have constructed test facilities for small-scale samples and show some limitations of performance analysis. Petroski [76] describes the test rig for measurement of confined, saw-tooth shaped wire-on-tube condensers with a height of channel equal to 50.8 mm and the width of the test section fixed at 762 mm. Prasad et al. [28] show measurements for a packed bed solar absorber (wire screen matrices) with a channel height of 25 mm. Tian et al. [5] reduce the channel height further to 10 mm for measurements of cellular copper structures. They vary the mean inlet air velocity from 1.0 to 10 m/s and work out a comparison of different heat transfer surface area enhancements with an uncertainty in Nusselt number of 5%. Kim et al. [18] examine triangulated, lightweight, aluminum lattice-frame materials (LFMs) with a channel height of 12 mm. A non-rectangular cross section test rig is described in [8], with a 7 mm diameter round tube and a porous media foam inside the tube. For the applied thermocouples an accuracy of 0.5°C is assumed. A collection of test facility characteristics is given in Table 5.2." [FDSS18]

In the context of several master's theses [Car18, Saw16] and [77] a test facility for surface area enhancements has been built and operated. The concept is based on the test facilities described in Table 5.2. However, some extensions have been added. "A schematic diagram of the test rig for pressure drop and heat transfer measurements is shown in Figure 5.2. The main components are: air flow conditioning section, test section, test sample, test core, and data acquisition. The air flow conditioning section is installed prior to the test section. It comprises of a chiller, an electric heater, a humidifier, a controllable fan and the respective sensors for air temperature, humidity and volume flow (orifice plate). It can deliver temperatures in the range of -10 to $40\,^{\circ}\mathrm{C}$ and volume flow rates between $80\,\mathrm{m}^3/\mathrm{h}$ and $300\,\mathrm{m}^3/\mathrm{h}$. Preconditioned air, as

	present study	Petroski [76]	Prasad [28]	Tian [5]	Kim [18]	Hutter [8]
sample height (mm)	8.15-10	50.8-152	25	10	12	7
sample length (mm)	10-30	622	750	60	127	200
sample geometry	micro pin fin	saw-tooth	wire screen	square, diamond cells	LFM	metal foams, porous media
temp. measm. method	Pt100, Pt106	thermo-couple (type T)	thermo-couple (type T)	thermo-couple (type T)	thermo-couple (type T)	thermo-couple (type K)
heating method	electric heating pad	water	solar radiation	electric heating pad	electric heating pad	wrap-around heating cord
uncer-tainty	6.6 %	6.4-8.7%	6.0%	5.4%	8.3%	-

Table 5.2: Characteristics of test facilities in the literature for small-scale heat exchanger samples; air as flow medium; uncertainty for heat transfer related to Nusselt number deviation; based on [FDSS18].

coolant, is drawn from the conditioning section to the test section. A bypass can optionally be used for lower air velocities at the beginning of the test section. Air passes a humidity sensor (HMT120; Vaisala, Vantaa, Finland; standard uncertainty of $\pm 3\%$ relative humidity) and thereafter a mass flow sensor. Two options are available for the mass flow sensor; Option 1 is suited for low flow rates up to $50\,l/min$ (Red-y; Vögtlin Instruments GmbH, Aesch, Switzerland; standard uncertainty of 0.5% of measured value + $0.15\,l/min$); Option 2 is suited for flow rates from 50 to 190 $190\,l/min$ (TA Di 16 GE; Höntzsch GmbH, Waiblingen-Hegnach, Germany; standard uncertainty of 2% of measured value $+0.24\,l/min$). The channel enlarges after the mass flow

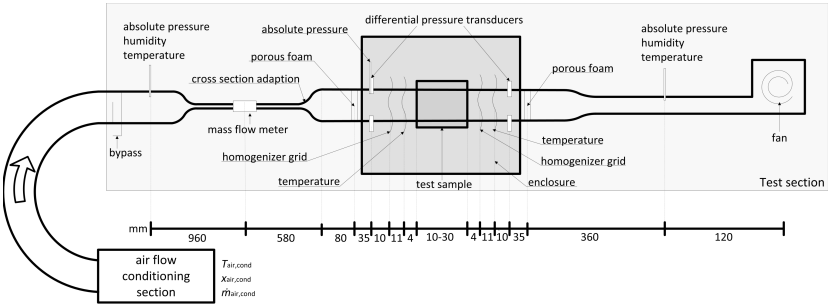

(a) Forced air convection test section for small-scale heat exchanger samples

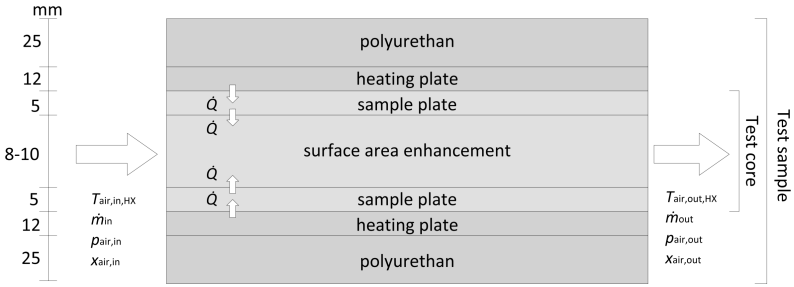

(b) Test sample with test core, heating plates and sensor information

Figure 5.2: Experimental test set-up scheme; based on [FDSS18].

meter and before the test sample. The ratio of channel length to channel height for this section is $L_{\text{channel,in}}/H_{\text{channel,in}} = 14$. The channel itself has a cross section of $10\,\text{mm} \times 100\,\text{mm}$.

Within the enclosure and before reaching the test sample, efforts were made to ensure the coolant flow velocity was constant (uniform) all over the cross section. To achieve this, the coolant first flows through a porous foam, then 10 mm and 5 mm before the sample core through a homogenizer grid based on a polyamide mesh with a mesh size of 0.5 mm. After the air passed the sample, two homogenizer grids were positioned 5 mm and 10 mm behind the sample to ensure uniform velocity for temperature measurement. Air passes

a second humidity sensor (HMT120) and finally a fan (G1G126-AB13-13; ebm-papst, Mulfingen, Germany). The fan is installed to control the volume flow of air in more detail and to run preliminary [tests] without the air flow conditioning section.

For pressure drop measurements, a differential pressure sensor for a measurement range from 0 to 60 Pa (CXLdp; ICS Schneider, Neuendorf, Germany; standard uncertainty 0.54 Pa) and for 50 to 250 Pa (Druckaufnehmer PI-Sensor; halstrup-walcher GmbH, Kirchzarten, Germany; standard uncertainty 2.8 Pa) were positioned at the inlet and outlet of the test sample, respectively. The absolute pressure can be measured (331113; Feingeräte Fischer, Drebach, Germany; 90 to 105 kPa, standard uncertainty 0.1 kPa) at the beginning and the end of the test section and 25 mm before the test sample.

For heat transfer measurement, a constant wall temperature boundary condition was imposed on the bottom and top face of the test core by two heating cartridges ($^{24\,volt}/_{100\,watt}$, $\varnothing 25\,mm \times 100\,mm$; Friedr. Freek GmbH, Menden, Germany) installed in the heating plates. A heat conducting foil (thermal pad 1 mm; 3 M, Maplewood, MN, USA), was inserted between the heating plates and the sample plates to ensure the uniformity of the temperature. 12 thin PT-100 temperature sensors (RTD Platinum Sensor, IST AG, Ebnat-Kappel, Switzerland, calibrated standard uncertainty 0.1 K) with $1.6\,mm \times 1.2\,mm \times 0.6\,mm$ outer dimensions were mounted in the heating plates. 12 additional PT-100 temperature sensors were mounted in the sample plates (see Figure 5.10 and Figure 5.11). Two self-built meandering platinum wire temperature sensors (each 0.5 m long, 0.025 mm diameter platinum wire, threaded in polyamide mesh, ca $100\,\Omega$ at $0\,^{\circ}C$; calibrated standard uncertainty 0.1 K) were positioned within the homogenizer grids at the inlet and outlet of the test sample to measure the coolant temperature at the cross section. Thus, an integrative value for air temperature for the channel cross section can be determined. To minimize heat losses to the ambient a test sample enclosure was installed. It consists of a polyurethane box which is lined from the inside with

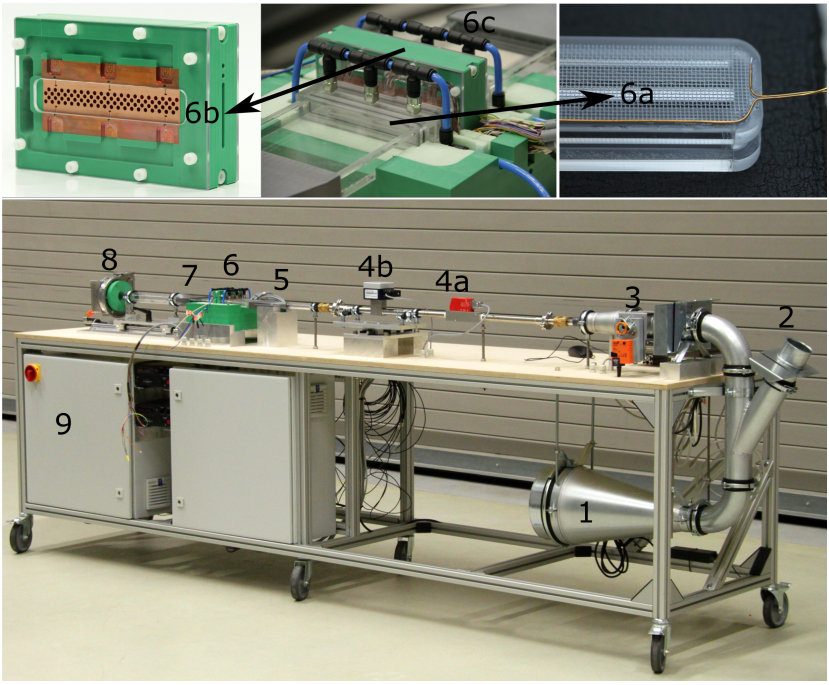

Figure 5.3: View of the test section and additional components; 1: preconditioned air inlet; 2: bypass; 3: throttle valve; 4a and b: mass flow rate sensors; 5: cross section adaption; 6: test sample enclosure; 6a: platinum wire temperature sensor threaded in polyamide mesh; 6b: test sample; 6c: differential pressure probes; 7: contraction duct; 8: fan; 9: electric cabinet; based on [FDSS18].

the insulation material Styrodur. The test core and heating plate is closed at top and bottom by panels of polyurethane which are screwed together to hold the heating plate, test core, and the temperature sensors in position.

All measurements were performed under steady-state conditions and repeated until significant data repetition was ensured. The usual time to reach steady state was less than 10 min; however, the boundary conditions have been kept constant for 30 min. The measurements were taken at several different air velocities ranging from 0.25 to 4 m/s. The heating power was chosen such

domain	measured variable	technolgy	range	standard uncertainty
air	temperature	meandering platinum wire	5-70 °C	0.1 K
air	mass flow rate	thermal mass flow meter	0-50 l/min	0.5% of meas. value + 0.15 l/min
air	volume flow rate	thermal measuring tube	50-290 l/min	2% of meas. value + 0.24 l/min
air	pressure drop	differential pressure transmitter	0-60 Pa	0.54 Pa
air	pressure drop	differential pressure transmitter	50-250 Pa	2.8 Pa
air	absolute pressure	barometric pressure sensor	90-105 kPa	0.1 kPa
heater	temperature	thin Pt100	5-70 °C	0.1 K

Table 5.3: Primary sensor technology installed at the test rig for heat exchanger surface area enhancements.

that the maximum heating plate temperature was below 68 °C to prevent deformation or melting of test section parts. Details of the test rig are given in Figure 5.3" [FDSS18]. The installed sensor technology is summarized in Table 5.3.

5.2 Description of Samples

An ideal geometry of parallel wires could be achieved by different manufacturing processes. This Section shall introduce some of these processes and evaluate their feasibility based on small-scale and large-scale samples for

- mechanical stability analysis,
- thermo-hydraulic performance analysis,
- manufacturing on an industrial scale,
- validation of simulation results.

5.2.1 Small-Scale Samples

The small-scale samples analyzed are limited to plate-fin wire structure exchangers and plate-fin reference exchangers. Five different manufacturing processes of wire structures have been analysed. These are:

- 3D printing,
- knitting and corrugating,
- weaving and corrugating,
- continuous wire layering,
- wire pinning

3D Print

The use of 3D printing for sample manufacturing is an obvious step in order to achieve homogeneous structures for comparison of measured with simulated performance. Together with Fraunhofer IFAM Bremen a pin fin structure was designed and printed for first tests. The steel sample is shown in Figure 5.4. The pin fin diameter was chosen to be 500 µm for reasons of mechanical stability. Thus, the diameter already exceeds an intended diameter of 100 µm by a factor of 5. Nonetheless the sample showed strong deformations after fin-

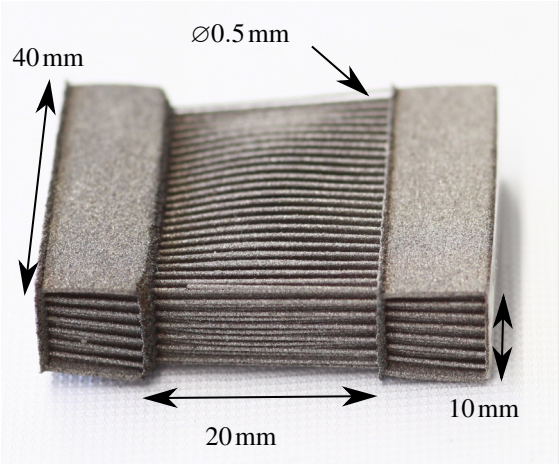

Figure 5.4: 3D printed pin fin structure; manufacturing by Thorsten Müller, Fraunhofer IFAM Bremen within the Harvest Project.

ishing the printing. Two major problems arise when thinking of 3D printing of micro pin fin structures. Firstly, the particles of the metal powder limit the minimum detail resolution. Particles in the range of 5 µm are available, reaching minimum detail resolution of 20 µm [78]. However, more common are detail resolutions of 100 µm and more. Secondly, the high aspect ratio (pin fin length to diameter) yields a mechanical instability and the risk of deformation. As other manufacturing methods of wire structure heat exchangers based on prefabricated wires have been available, no further analysis of suitability of 3D printing has taken place. Similar types of heat exchanger geometries have been printed by Rezaey et al. [79].

Knitted Textile Structures

One of these techniques using prefabricated wires is knitting. The process is well known, not only for using natural or synthetic fibres, but as well for using metallic wires. In the Effimet project [80] several knitted fabrics have been

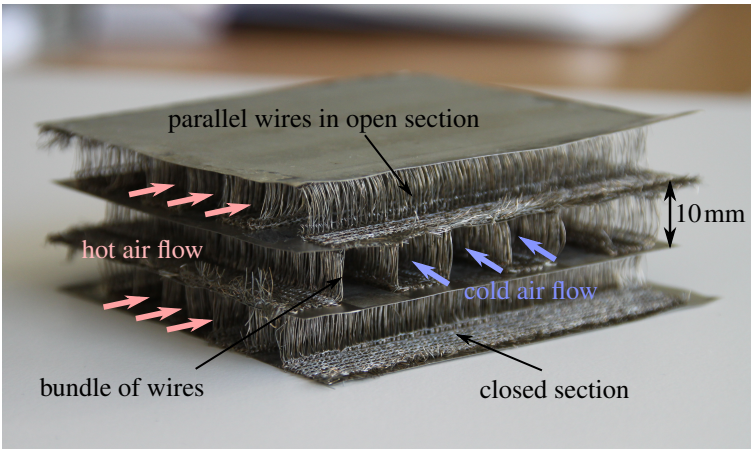

Figure 5.5: Knitted wire fabric arranged such that channels for air flow emerge; manufacturing by Visiotex and Fraunhofer IFAM Dresden within the Effimet Project [80].

tested for suitability as heat transfer surface area enhancement. A small-scale sample is shown in Figure 5.5 in an air-to-air heat exchanger concept. The knitted fabric was corrugated manually and thereafter soldered to the metal sheets. The wire material was Cu-HCP/385 with a wire diameter of 100 µm. The processing of the knitted fabric towards a heating surface structure was possible; however, due to mechanical instability during the knitting process 4 wires have been packed as a bundle. Less wires in a bundle could have caused a wire break during manufacturing and thus a possible disruption of the knitting process. Thus, the parallel wires are not symmetrically arranged and the flow of air through the structure will not flow around the wires in an ideal way. Further the stitches need to have a specific distance. For stability reasons several stitches are used to switch from the more open section (parallel wires) to the more closed section. This closed section is contacted to top and bottom plates (or tubes). Due to the distance and number of stitches the contact region is unnecessary large, causes high material consumption, and prevents smaller lateral distances of the parallel wires. This would be necessary to have

sufficient heat transfer surface area density. The suitability of knitted metal fabrics as heat transfer surface area enhancement is thus limited however, not precluded. The following changes could be done:

- the number of wires in a bundle could be reduced to a single wire when the material is less fragile or the tensile force could be kept in specific limits
- the closed region could be reduced to 2 stitches, allowing an adequate lateral wire distance of the parallel wires
- some stability wires could consist of a different material than metal and could be burnt during the welding process, thus reducing the mass

These adaptations have been discussed with the textile manufacturer Visiotex and their feasibility is estimated positively. A further analysis of knitted fabrics has been done on a large-scale heat exchanger in Section 5.2.2.

Woven Textile Structures

Woven textile fabrics are promising base materials for forming heat transfer structures. One possible step towards the transformation from a 2D fabric to a 3D structure is corrugating the fabric mechanically. Usually corrugation takes place with thin metal sheets forming structures for plate-fin exchangers. However, some textile fabrics are suitable for mechanical corrugation as well. They need to have (i) a low tendency for fraying when cutting to size, (ii) a high mechanical stability for the corrugation process in order to allow easy handling of the fabrics, and (iii) a high mechanical stability after deformation in order to allow compression force when contacting to top and bottom plates. The testing of corrugation and welding was done with woven metal textiles available on the market. Table 5.4 gives an overview. Limitations in welding are given by requirements of the furnace. The furnace available had to be operated with fins based on Al99.5. Thus, welding tests could be done only with one of the fabrics.

#	supplier	material	d_{wire} in mm	$l_{lateral}$ in mm	comment
TS2	Spörl OhG	Al99.5	0.200	0.200	every 2.5mm stabilizing wires, stability sufficient
TS3	Haver & Böcker	aluminum alloy	0.180	0.250	aluminum not suitable for furnace
TS4	Haver & Böcker	aluminum alloy	0.315	1.400	aluminum not suitable for furnace
TS5	Spörl OhG	Cu DIN CW024A	0.280	1.130 and 1.310	copper not suitable for furnace
TS7	Spörl OhG	AlMg5	0.100	0.112	stability good, aluminum not suitable for furnace

Table 5.4: Selection of woven metal textiles used for corrugation testing; Short name given by testing structure (TS) numbering; based on [Fug18].

The selection of testing structures in Table 5.4 is shown in Figure 5.6 at different levels of feasibility analysis.

The feasibility of corrugation and calibration of the tested structures could be confirmed. It can be assumed: the less compact the structure, the more difficult to corrugate and calibrate to an even fin strip. The testing structure TS2 in Table 5.4 could be seen as the softest possible structure to be corrugated and calibrated in the testing process [Fug18]. Based on the feasibility analyzes and the material requirements, a selection of different woven textile fabrics has been defined and manufactured by textile industry partners. These fabrics have than been used to construct the large-scale heat exchangers described in Section 5.2.2.

Continuous Textile Structures

Final design of parallel wire plate-fin exchanger “resembled the geometry of a market available heat exchanger from Vision4Energy [19]. The Dutch company produces a gas to gas heat exchanger used in ventilation systems.

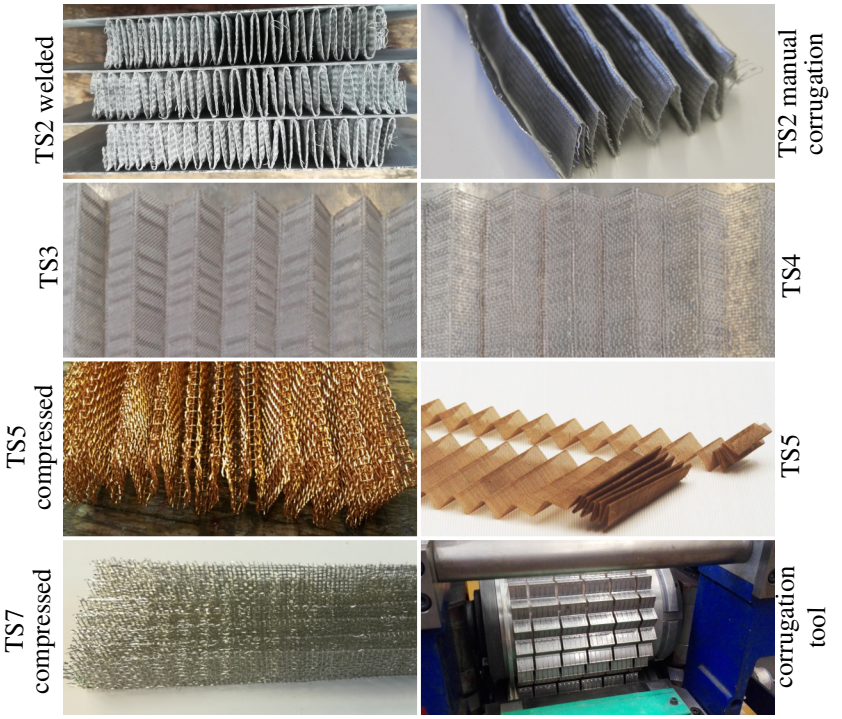

Figure 5.6: Selection of corrugated woven wire structures and the corrugation tool used to reform the woven fabrics.

The gases flow primarily in counter-flow arrangement, separated by a dividing wall. Header and distributer are such that the both air flows are angled with respect to the wire structure block (see Figure 5.7 left side)" [FOS17]. The manufacturing process is based on two steps: (i) spanning one layer of several wires in a parallel plane to the working surface; (ii) printing several lines of an adhesive plastic perpendicular to the wire direction with the height of the longitudinal wire distance. By repetition of these steps layer by layer a wire structure is formed with parallel wires and plastic walls forming sepa-

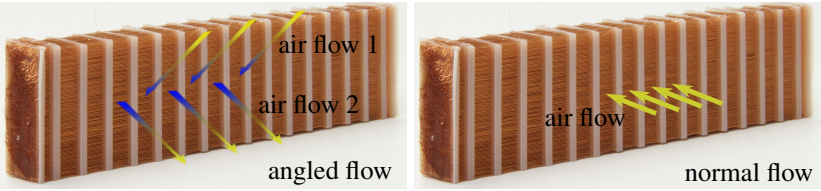

Figure 5.7: Section of a gas to gas heat exchanger with continuous horizontal wires. Vertical separation wall formed by adhesive plastic; left: angled flow with two fluids in a combined counter-flow and cross-flow arrangement ; right: normal flow with one fluid; based on [FOS17].

rated channels. A transfer of this technique for manufacturing plate-fin wire structures is not straightforward. However, some possible steps are

- the plastic printing could be replaced by metal printing; the whole structure could be cut to separated packages of parallel wires fixed by the metal printing top and bottom layer. these layers could either be contacted to tubes or form tubes by themselves
- the plastic wall could be cut; the separated packages of parallel wires could be stacked between tubes with a soldering layer; during soldering the plastic burns, but the wires are fixed by the soldered wall contact

The second step has been tested. However, contacting (soldering) the wires to a plate with the plastic wall being still present and necessary to keep the wires in position, was challenging: Due to the heat of the soldering, the plastic melts too fast and the geometry gets deformed. Figure 5.8 (b) shows a cut of the structure in the x-y-plane next to a separating plastic wall.

In order to make use of the continuous textile structures two sections of the Vision4Energy heat exchanger have been cut for tests at the test facility for (i) large-scale heat exchangers (see Figure 5.16) and for (ii) heat transfer surface enhancements (see Figure 5.8 (a)), with the geometric parameters given in Table 5.8. As the wires have not been contacted to a metal sheet or tube, the thermodynamic performance has not been addressed, but the hydraulic performance. The arrangement of the wires in the test samples is neither in-

line nor staggered. Figure 5.8 (a) shows the shift of wires in x-direction from an in-line arrangement. The mean shift is in the order of one wire diameter.

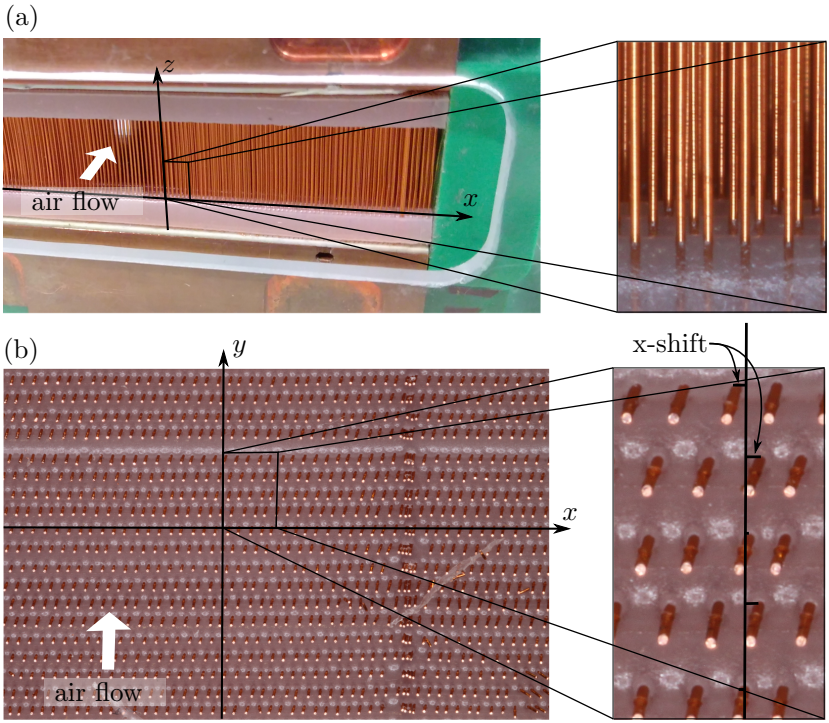

Figure 5.8: A package of parallel wires based on the gas to gas heat exchanger in Figure 5.7, cut on two sides at the plastic wall. (a) heat transfer surface enhancement installed in the test facility. (b) topview on one cut plane (Dimensions compare Table 5.8).

Louvered Fin Reference

"Louvered fins were chosen to represent a market available geometry for an enhancement. The louvered fins serve as a reference. The copper fins in the test sample (Figure 5.9) have 16 louvers within a flow length of 32 mm. With a fin pitch of 2 mm and a fin thickness of 0.04 mm, this geometry reaches

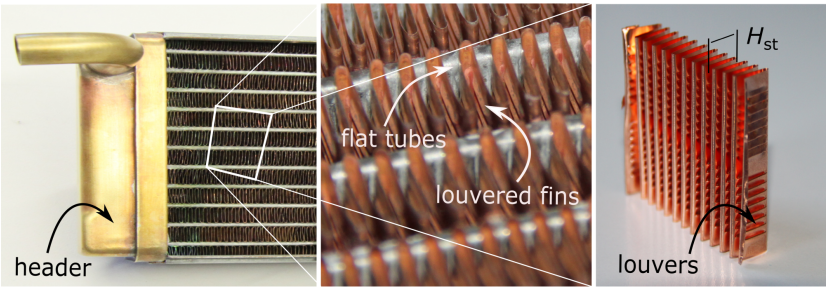

Figure 5.9: Air-to-water flat-tube heat exchanger (left) with louvered fins between the tubes (middle); Details of a louvered fin package used between top and bottom sample plates (right); based on [FDSS18, FOS17].

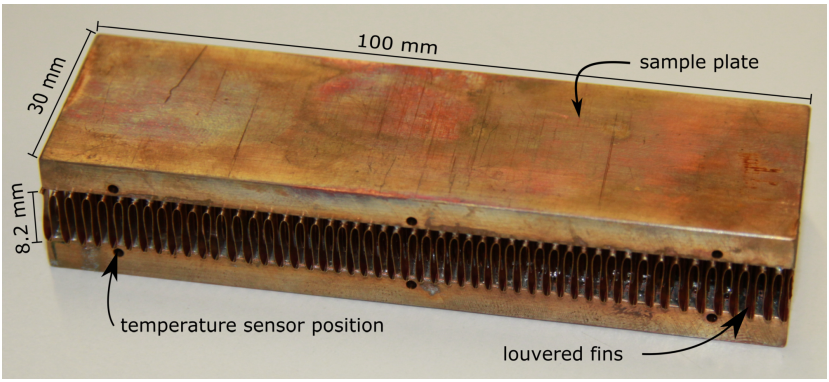

Figure 5.10: Louvered fin test core with top and bottom sample plate for experimental performance analysis; based on [FDSS18].

volume specific surface areas above 2100 m^2/m^3. Further morphological information is given in Table 5.5. The louvered fin package (Figure 5.10) is contacted to two copper (Cu-ETP) sample plates each 5 mm thick. Contacting is done with a soft solder paste based on alloy Sn97Cu3 with the flux material colophony. The sample plates have drilled holes (⌀1.4 mm) for temperature sensor positioning" [FDSS18]. The sample is tested for thermal-hydraulic performance in the test rig for surface area enhancements.

	Unit	Parameter	Wire Structure	Louvered Fin
wire diameter/fin thickness	mm	$d_{\text{wire}}/d_{\text{fin}}$	0.25	0.04
channel height	mm	H_{channel}	10	8.15
sample length	mm	L_{st}	10	32
number of wire rows/fins	-	$n_{\text{wires}}/n_{\text{fins}}$	2296	50
heat transfer surface area	m^2	A_{HTS}	0.0198	0.058
volume of structure	m^2	V_{st}	1×10^{-5}	2.6×10^{-5}
material	-	-	Cu-ETP	Cu-ETP
thermal conductivity of wire/fin material	$\text{W}/(\text{mK})$	k_{st}	385	385
lateral wire/fin distance	mm	l_{lat}	1.21	2
longitudinal wire distance	mm	l_{long}	0.35	-
mass specific surface area	m^2/kg	-	1.95	6.21
porosity	%	φ_{st}	88.4	96.0
volume specific weight	kg/m^3	-	1009	361
volume specific surface area	m^2/m^3	β_{st}	1970	2240

Table 5.5: Morphological parameters for wire structure and louvered fin samples; heat transfer surface area includes top and bottom sample plate; based on [FDSS18].

Micro Pin Fins

A pin fin structure with wires of 250 µm diameter has been manufactured at Fraunhofer ISE for comparison to the louvered fins. This "sample wire structure is in a staggered arrangement. The manufacturing of the sample consists of (i) cutting of the copper wires to equal length, (ii) forming a wire bundle, (iii) positioning of the wires on a perforated metal plate, (iv) soldering of the wires to the bottom sample plate, and (v) soldering the wires to the top sample plate. The test core (Figure 5.11) has geometrical irregularities due to this manual manufacturing process. Mean morphological properties are given in Table 5.5. The test core was designed, such that thermal-hydraulic perfor-

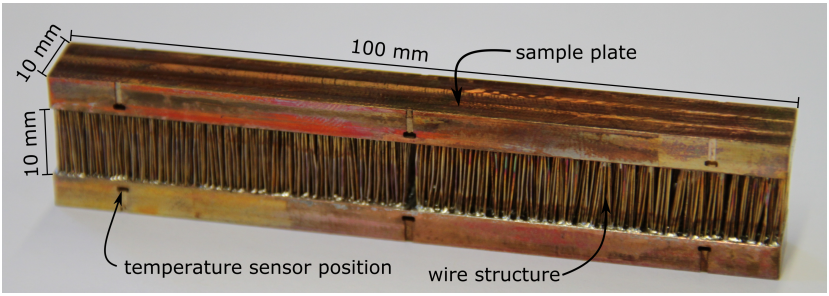

Figure 5.11: Micro pin fin test core with 2296 parallel copper wires (diameter 250 µm) soldered to bottom and top copper plates for experimental performance analysis; based on [FDSS18].

mance for velocities of 2 to 2.5 m/s could be determined" [FDSS18] at the available test rig.

5.2.2 Large-Scale Samples

The large-scale samples analyzed are limited to plate-fin wire structure exchangers and plate-fin reference exchangers. Three different manufacturing processes from the small-scale sample analysis of wire structures have been used. These are:

- knitting and corrugating,
- weaving and corrugating,
- continuous wire layering,

Knitted Textile Structures

Knitted fabrics have been used for manufacturing a large-scale sample to show further aspects of feasibility of manufacturing. Details on the heat exchanger are shown in Figure 5.12. "Flat copper tubes (Eugen Geyer GmbH, Königsbach-Stein, Germany) are first brazed into headers. After electroplating, the [corrugated] wire structure (Figure 5.12, left) is inserted into the frame

and heat-treated for soldering. The wire structure is a flat-knitted fabric and consists of several narrow stitches followed by one wide stitch. Air will flow through the more open area of the wide stitch. The wire material is copper. The structure is folded at the edges between the narrow and wide sections so that the narrow region can be connected to the tubes. The droplets on the headers result from excess solder on the surface areas not in contact with the wire structure. The utilization of additional polytetrafluoroethylene counterparts to keep the folded structure in its form before soldering has been tested. However, it was found that the structure is self-supporting, so that the counterparts could be omitted (see Figure 5.12 middle)" [FLS17]. For a homogeneous flow distribution in the flat tubes, the cross-section of the headers was designed very large. The morphological parameters of the flat tube heat exchanger are given in Table 5.6. Performance characterisation of the heat exchanger has taken place. However, as the purpose was on the manufacturing side the design was not such that an adequate size of surface area could be achieved. Thus, the results will not be part of further analysis in this thesis.

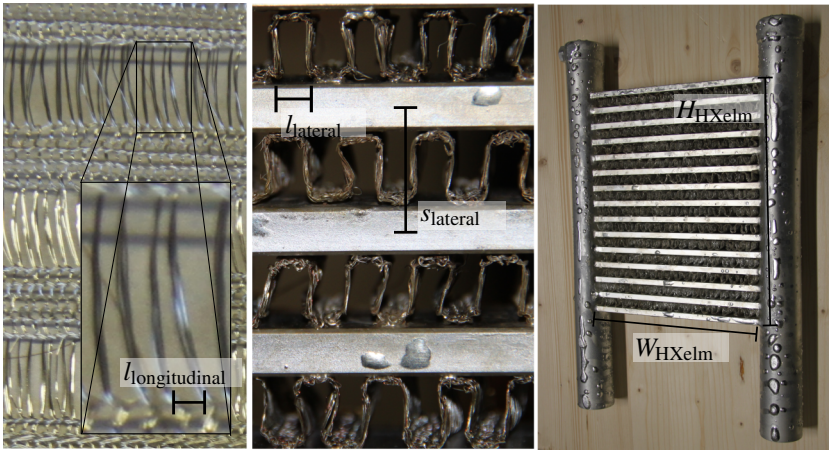

Figure 5.12: Flat tube wire heat exchanger based on a knitted wire fabric; manufacturing by Visiotex and Fraunhofer IFAM Dresden within the Effimet Project; based on [FLS17].

Specification	Parameter	Unit	Knitted Structure
number of tubes	n_{tubes}	-	15
tubes outer dimensions × wall thickness	-	mm	$30 \times 6.5 \times 1.5$
tube pitch perpendicular to flow direction	s_{lateral}	mm	16.4
tube length with contact to air-side	W_{HXelm}	mm	195
wire diameter	d_{wire}	mm	0.1
material / thermal conductivity		W/mK	Cu-HCP/385
wire pitch perpendicular to flow direction (bundles of 4 wires)	l_{lateral}	mm	5.4
wire pitch in flow direction (bundles of 4 wires)	$l_{\text{longitudinal}}$	mm	1
heat exchanger outer dimension (without headers)	$W_{\text{HXelm}} \times H_{\text{HXelm}} \times L_{\text{HXelm}}$	mm^3	$195 \times 231 \times 30$
header outer dimensions × wall thickness	-	mm × mm	$\varnothing 43 \times 1.7$
wire structure mass	m_{st}	kg	0.18
heat transfer surface area density	β_{st}	m^2/m^3	160

Table 5.6: Morphological parameters for knitted textile structure heat exchanger sample; based on [FLS17].

Further sample production has been ceased, as the effort for the textile manufacturer (for a small number of fabrics with new requirements) was assumed to be too large.

Woven Textile Structures

Four different heat exchangers have been manufactured within the MinWaterCSP Project [Min18]; two heat exchangers based on woven textile structures and two references. The geometrical details are given in Table 5.7. The tube configuration and header/collector was designed such that the water flows in several passes through the heat exchanger. Figure 5.13 shows the design

and one of the manufactured heat exchangers. Details on the structure itself are shown in Figure 5.14.

The main challenge of stacking and brazing the wire structure was to control the stacking force and material expansion during brazing. The stacking force was needed to neutralize structure height deviations from manual calibration. This was needed to allow a homogeneous contact surface between tube and

Parameter	Unit	Common Values			
H_{HXelm}	mm	217			
W_{HXelm}	mm	200			
L_{HXelm}	mm	120			
n_{tubes}	–	8			
$d_{\mathrm{tube,outer}}$	mm	12			
$d_{\mathrm{tube,inner}}$	mm	10			
$A_{\mathrm{HTS,water}}$	m^2	0.35			
L_{st}	mm	96			
H_{st}	mm	19			
V_{st}	m^3	0.0026			
k_{st}	$\mathrm{W}/(\mathrm{m\,K})$	230			
ρ_{st}	kg/m^3	2700			
		Ref Fin	Exp Metal	Wire Structure I	Wire Structure II
l_{lateral}	mm	2.04	2.38	2.21	2.21
$l_{\mathrm{longitudinal}}$	mm	–	0.25	0.25	0.25
l_{vertical}	mm	–	–	0.25	2.60
d_{wire} or d_{fin}	µm	confidential	185	180	250
m_{st}	kg	0.84	0.21	0.35	0.61
A_{HTS}	m^2	2.89	2.23	2.99	4.00
A_{st}	m^2	2.52	1.86	2.62	3.63
β_{st}	$\mathrm{m}^2/\mathrm{m}^3$	1131	873	1169	1567
φ_{st}	$\mathrm{m}^3/\mathrm{m}^3$	0.88	0.97	0.95	0.91

Table 5.7: Morphological parameters for woven textile structure and reference heat exchanger samples; based on [Fug18].

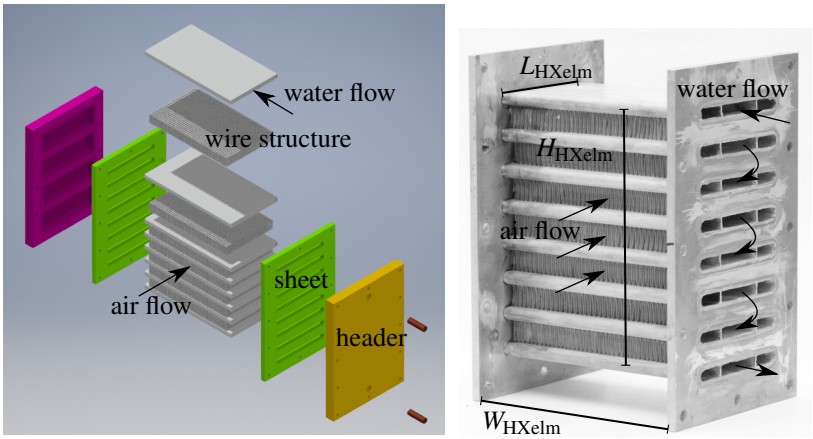

Figure 5.13: Heat exchanger sample; left: CAD drawing; right: manufactured heat exchanger; based on [Min18].

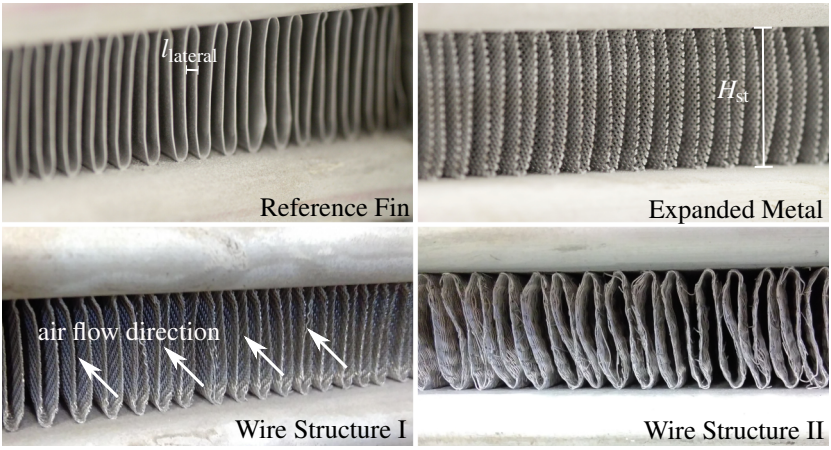

Figure 5.14: Details of structures used in large-scale heat exchangers.

structure and avoid unbrazed fins. When the stacking force, applied by the stacking frame to the structure and tubes, was too high, the structure collapsed during heat up in the furnace later on. This occurred because the material ex-

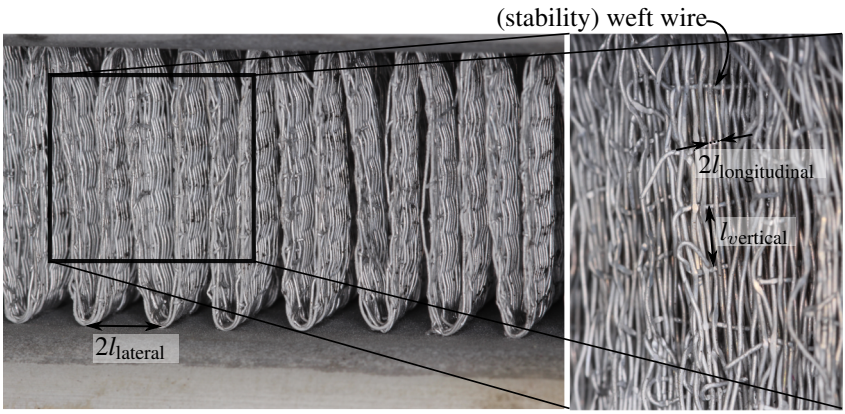

Figure 5.15: Details of wires and wire distances in the woven Wire Structure II heat exchanger.

pansion of the stacking frame is smaller than the material expansion of fins and tubes [Fug18]. The two wire structure heat exchanger show good contacting of tubes and wires, however, a good homogeneity of lateral wire distance could not be achieved. The main reason is the instability of the textile fabric. Wire Structure I and II had a distance of weft wires l_{vertical} of 0.25 mm and 2.60 mm, respectively. Thus, only 9% of the mass is related to stability for Wire Structure II. On one hand repetition of the process could increase accuracy, on the other hand a more stable fabric could be manufactured, by increasing the number of weft wires for the region which needs to be contacted to the tube. Thus, the flow would not be blocked by the stability wires. An impression on (in-)homogeneity of the wires and the wire distances is given in Figure 5.15. Based on the inhomogeneity of the structure, the heat exchangers can represent very well the manufacturing process with corrugated woven textiles. However, for validation of the simulation results the samples are inadequate. The experimental performance results are discussed in Section 5.3 together with the simulation results.

Continuous Textile Structures

The continuous textile structure described as a small-scale sample was available in larger size as well. It was cut to fit in an existing cross section of the heat exchanger test rig and prepared for pressure drop measurement in order to validate the simulation results. The heat exchanger element is shown in Figure 5.16.

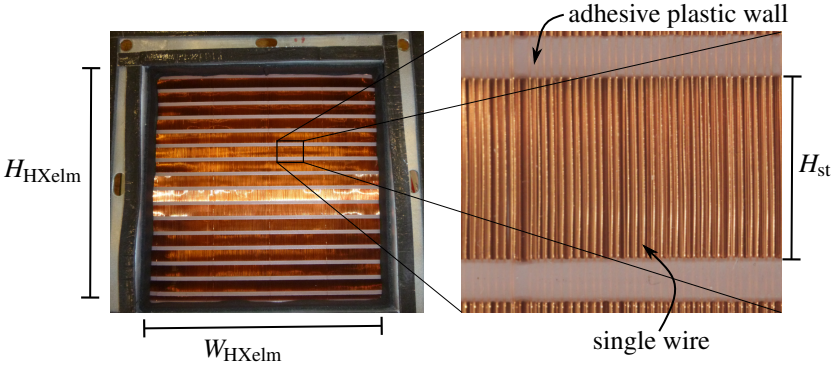

Figure 5.16: Continuous textile structure installed in a testing channel for hydraulic performance measurement; based on [Alt18].

The geometry is described in Table 5.8. It consists of 15 separated wire packages with height 9.8 mm, one wire package with height 2.4 mm, and 16 separating walls with height 2.4 mm.

Parameter	Unit	continuous textile structure
H_{HXelm}	mm	200
W_{HXelm}	mm	200
L_{st}	mm	19
H_{wall}	mm	2.4
H_{st}	mm	9.8
d_{wire}	µm	105
l_{lateral}	µm	445
$l_{\mathrm{longitudinal}}$	µm	704
σ_{HX}	-	0.79

Table 5.8: Morphological parameters for continuous textile structure heat exchanger sample.

5.3 Results

The test samples described above are characterized for thermal-hydraulic performance on either the test rig for heat exchangers or for surface area enhancements. The results are presented in dimensional and non-dimensional numbers and are compared to the simulation results from 2D and 3D models. Partly the results are compared to literature-based or measured references performance.

5.3.1 Micro Pin Fins

The micro pin fins (Section 5.2.1) are compared to the louvered fins (Section 5.2.1) on the test rig for heat exchanger surface area enhancements (cf. [FDSS18] and [Saw16]). Some limitations due to the small-scales shall be discussed in combination with the uncertainties of the measurement.

Uncertainties

"The uncertainties of the temperature sensors given in Section 5.1 are one part of the uncertainty in the test set-up to determine sample plate and air inlet/outlet temperatures. The positioning and number of sensors can influence the uncertainty as well. As the sample plate temperature is a mean value, based on several temperature sensors, a standard deviation can be calculated. This deviation expresses the scattering of temperature within the sample plate around the mean. A large deviation restricts the method of logarithmic mean temperature difference (Equation (2.18)) as the local difference between air outlet temperature and sample plate temperature might differ from the mean difference. Thus, in some areas of the heat exchanger the driving temperature difference (between sample plate and air) might be very low, whereas in other parts it might still be large. As the logarithmic mean temperature is strongly non-linear a mean value will not express the correct driving temperature. Therefore, an additional uncertainty of the mean sample plate temperature has been added to the uncertainty analysis. Figure 5.17 shows the mean

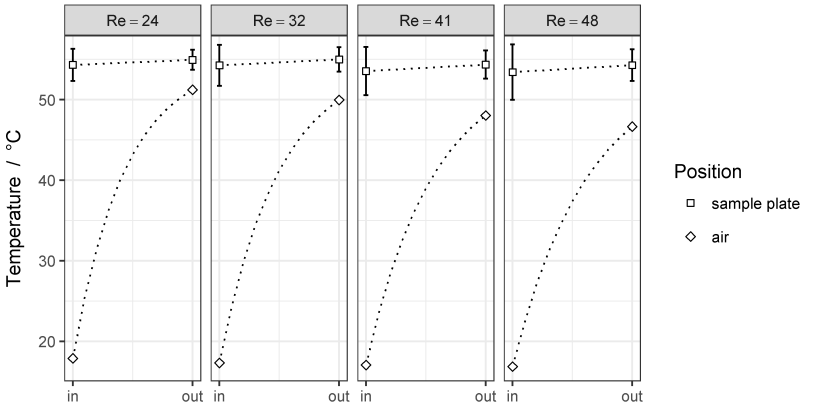

Figure 5.17: Mean inlet and outlet temperatures of the air and sample plate with respect to different Reynolds numbers Re_{st} for the wire structure. Twice the standard deviation of the measured temperature value is given for the sample plates as error bars, representing 95% of the data; based on [FDSS18].

values and the standard deviation of the sample plate temperature of the wire structure. The standard deviation of the temperature values varies from 0.6 to 1.7 K. The standard deviation of the temperature mean is by a factor of $1/\sqrt{6}$ smaller, due to the number of sensors. It will be used as uncertainty for the sample plate mean temperature" [FDSS18].

"The air inlet and outlet temperatures used in Equations (2.14) and (2.19) are integrative values. Exemplarily the definition of $T_{\mathrm{air,in}}$ is given by:

$$T_{\mathrm{air,in}} = \frac{\int_{A_{\mathrm{st,in}}} v_{\mathrm{st}} \rho_{\mathrm{air}} c_{p,\mathrm{air}} T_{\mathrm{air}}}{\int_{A_{\mathrm{st,in}}} v_{\mathrm{st}} \rho_{\mathrm{air}} c_{p,\mathrm{air}}} \tag{5.1}$$

However, the temperature sensor in the air flow measures the temperature:

$$T_{\text{air,in,meas}} = \int_{A_{\text{st,in}}} T_{\text{air}} \tag{5.2}$$

Both temperatures are equal if the velocity v_{st}, the density ρ_{air}, and the heat capacity $c_{p,\text{air}}$ are constant within the air inlet cross section $A_{\text{st,in}}$. This assumption holds for well mixed air flow. In the present test section this is realized by several grids in front of the temperature sensors. However, CFD simulations of the homogenizer grids and air flow through the channel show that a strongly uniform flow cannot be reached. Related to the operating conditions an additional uncertainty of 0.26 K and 0.09 K has been assigned to the air inlet and outlet temperature, respectively. Lastly the pressure drop measurement has additional uncertainty due to the position of the sensors in the channel. However, CFD simulations of the channel air flow show a very low deviation of maximum/minimum pressure in the channel cross section compared to the mean pressure, such that the sensor uncertainty determines the uncertainty. No additional uncertainty has been added. Table 5.9 shows the sensor uncertainties and the additional uncertainties related to position and averaging.

Parameter	Dim	Sensor Uncertainty u_1	Additional Uncertainty u_2	Combined Uncertainty u_c
$T_{\text{air,in}}$	K	0.1	0.26	0.27
$T_{\text{air,out}}$	K	0.1	0.09	0.11
$T_{\text{saplt,in}}$	K	0.1	0.41-0.70	0.41-0.70
$T_{\text{saplt,out}}$	K	0.1	0.25-0.40	0.26-0-40
Δp_{air}	Pa	0.54-2.8	0	0.31-1.62
m_{air}	kg/s	$(4.0-7.7)\times 10^{-5}$	0	$(2.4-4.4)\times 10^{-5}$

Table 5.9: Uncertainties of main parameters for pin fin test sample; sensor uncertainties (Rectangular Distr.) are based on manufacturer information or calibration; additional uncertainties (Normal Distr.) are related to positioning and averaging; combined uncertainty $u_c = \sqrt{(u_1/\sqrt{3})^2 + u_2^2}$ has normal distribution; based on [FDSS18].

The uncertainty of the experimental results is assessed based on measurement uncertainties using the Gaussian uncertainty propagation rule [81]. The level of confidence is expressed in terms of an expanded uncertainty interval. The expanded uncertainty is obtained by multiplying the combined standard uncertainty by a coverage factor of 2. Assuming that the measurement data are normally distributed, 95% of the data lies in this interval" [FDSS18].

Performance

"Several different velocities have been measured with a focus on velocities through the structure in the range of 2 to 2.5 m/s. The heat flow rates ranged from 30 W to 110 W, dependent on the velocity and enhancement structure (see Figure 5.18). As the pin fin test core had a 20% higher channel height, compared to the louvered fins, the air mass flow rate at equal velocities differ. Thus, it was possible to have higher heat flow rates for the pin fins at equal velocities. High heat flow rates are not necessarily related to high thermal

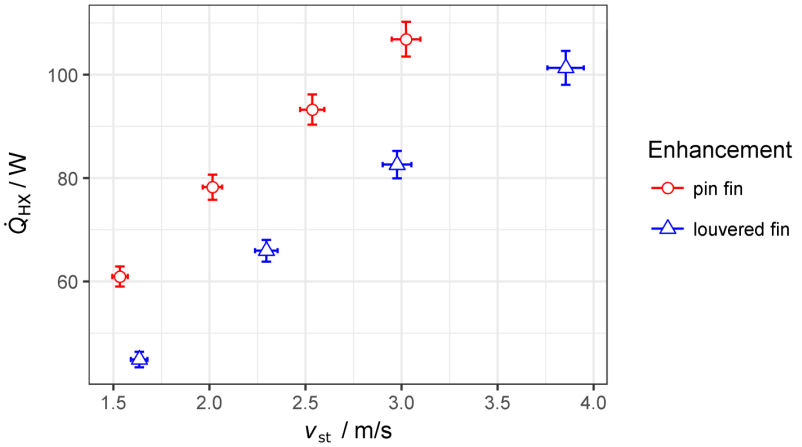

Figure 5.18: Heat flow rate $\dot{Q}_{HX}$ versus air velocity v_{st} for louvered and pin fins; error bars for expanded uncertainty; based on [FDSS18].

performance, but are a consequence of geometric and operational conditions, which differ between pin fin and louvered fin enhancement. The air flow at the outlet reached temperatures close to the sample plate temperature for low velocities. Thus, the uncertainty of the thermal performance key figures is high for those values. An overview of the experimentally determined data points is given in Table 5.10. The air-side effectiveness ϵ_{air} can be considered within

	Parameter	micro pin fin				louvered fin			
		DP1	DP2	DP3	DP4	DP1	DP2	DP3	DP4
input	$T_{\text{air,in}}$ [°C]	17.9	17.3	17.1	16.9	21.2	21.2	21.6	21.5
	v_{st} [m/s]	1.6	2.1	2.7	3.2	1.7	2.4	3.1	4.0
	P_{el} [W]	60	76	90	104	47	67	83	104
output	$\dot{Q}_{\text{HX}}$ [W]	61	78	93	107	45	66	83	101
	$T_{\text{saplt,in}}$ [°C]	54.3	54.3	53.5	53.4	49.0	50.8	50.9	50.1
	$T_{\text{saplt,out}}$ [°C]	54.9	55.0	54.3	54.3	50.2	52.3	52.5	51.8
	$T_{\text{air,out}}$ [°C]	51.2	50.0	48.0	46.7	49.6	51.0	50.4	48.8
	ϵ_{air} [-]	0.90	0.86	0.83	0.79	0.98	0.96	0.93	0.90
	$U_{\text{air,eff}}$ [W/(m^2 K)]	217	250	277	296	110	126	137	154
	η_0 [-]	0.93	0.92	0.91	0.91	0.92	0.91	0.91	0.90

Table 5.10: Selection of experimentally determined data points (DP) for thermal performance evaluation; based on [FDSS18].

the table. With increasing velocity the effectiveness decreases due to a higher increase of the capacity flow rate $\dot{m}c_p$ compared to the increase of the effective heat transfer coefficient $U_{\text{air,eff}}$. Thus, measurements of thermal performance at lower velocities than the depicted could not be performed, as the uncertainty increased too strongly. The energy balances between the heat flow rate into the heat exchanger structure and [into the] air $\dot{Q}_{\text{HX}}$ and the electric power P_{el} matches with a relative difference of a maximum of 4%.

The effective heat transfer coefficient for both enhancements is shown in Figure 5.19. The pin fin enhancement has more than twice the heat transfer coefficient for the considered velocity range of 1.5 m/s to 3 m/s. Both enhance-

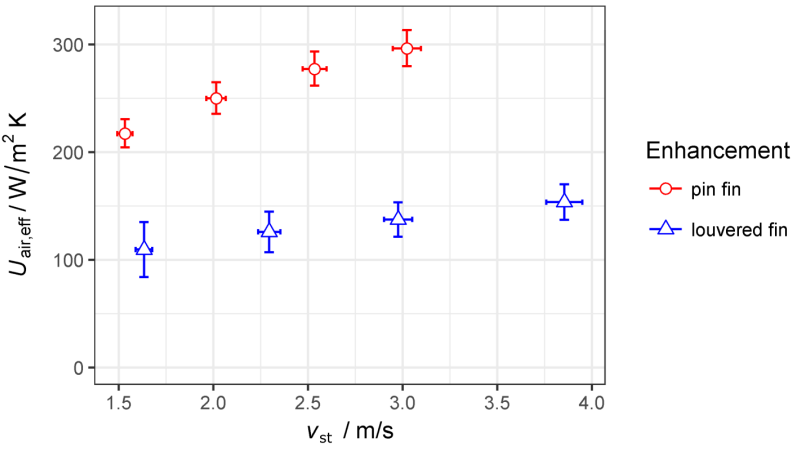

Figure 5.19: Effective heat transfer coefficient $U_{air,eff}$ versus air velocity v_{st} for louvered and pin fins; error bars for expanded uncertainty; based on [FDSS18].

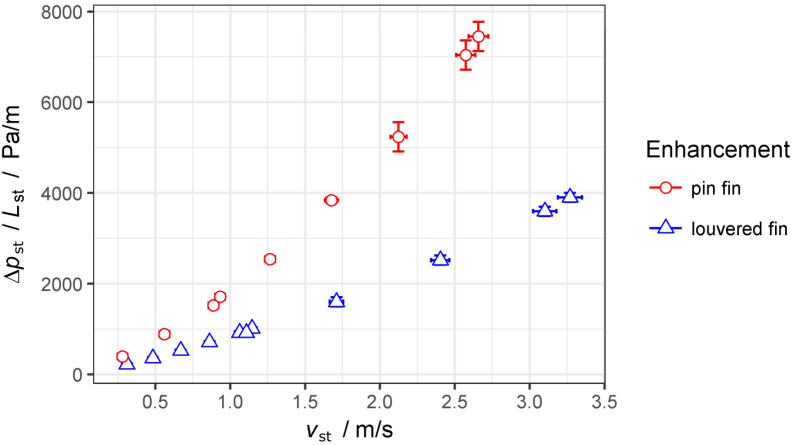

Figure 5.20: Pressure drop Δp_{st} normalized with the length of structure L_{st} versus air velocity v_{st} for louvered and pin fins; error bars for expanded uncertainty; based on [FDSS18].

ments show lower values of heat transfer coefficient for low air velocities. The pressure drop measurements could be extended to lower velocities, thus Figure 5.20 shows the pressure drop per length of structure for velocities from 0.25 m/s to 3.25 m/s. Pressure drop increases with respect to air velocity. The pressure drop of the pin fins is approximately twice as high as the pressure drop of the louvered fins.

The experimental data for thermal-hydraulic performance is shown in non-dimensional form in Figure 5.21. The plots are extended with performance information from correlation [...]. The pin fins are correlated based on the 2D-CFD simulation [in Section 4.4], the louvered fins are correlated versus data from an experimental study [62]. The present measurement and the literature correlation for the louvered fins show a similar slope; the measurements show slightly higher Nusselt numbers and slightly lower Fanning friction factors.

The present measurement and the correlation for the pin fins show a different behavior. Whereas the 2D-CFD simulation data of the Nusselt number shows

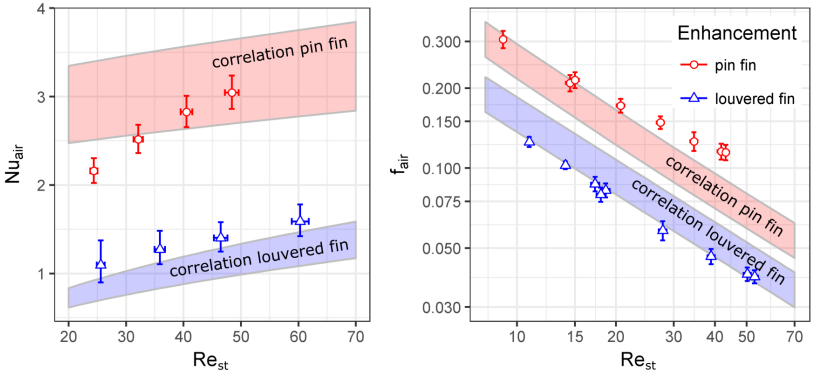

Figure 5.21: Thermal-hydraulic performance in non-dimensional form; Nusselt number Nu_{st} (left) and Fanning friction factor f_{st} (right) versus Reynolds number Re_{st}; Ribbons represent correlated data for pin fins and louvered fins [62], the width of the ribbons is related to the correlation error (see Chapter 4.4.2); error bars for measurement data expressed as expanded uncertainty; based on [FDSS18].

a slope comparable to the louvered fins, the measurement data shows a considerably steeper slope; the measurements show lower Nusselt numbers for low velocities and agree with the simulations for higher velocities. The measured Fanning friction factor for the pin fins shows a flatter slope compared to the simulations. A good agreement of friction factor can be found for lower velocities, for higher velocities the relative difference is in the order of 40%. Similar to Figure 5.19 and Figure 5.20, the pin fin structure shows a clear enlargement of Nusselt numbers, with the drawback of a distinct enlargement of the friction factors" [FDSS18].

Short Discussion

"The test facility allows measurement of heat transfer and pressure drop characteristics for small-scale heat exchanger test samples. The test facility can be operated at a variety of different air velocities. The operational conditions yield different uncertainties. The relative expanded uncertainty of the Nusselt number of the pin fins can be kept lower than 7% for Reynolds numbers between 25 and 50. Data for lower Reynolds numbers show the common phenomenon of a strongly decreasing Nusselt number. A reason for this can be the very small temperature differences of the air outlet and the sample plate temperatures. These mean temperature differences are below 4 °C for velocities lower than 2 m/s. Furthermore, the sample plate temperature at the inlet and outlet differs for the 6 measurement points by 4.5 °C and 3 °C, respectively. Thus, a constant homogeneous heat flux cannot be guaranteed. Data for Reynolds numbers below 30 must be looked at carefully. Similarly, the high uncertainties for the Nusselt number of the louvered fins can be explained. The very high value of effectiveness $\epsilon_{\text{air}} = 0.98$ for low air velocities occurs in conjunction with a small difference of air outlet and sample outlet temperature (0.6 K). Therefore, the expanded uncertainties in Nusselt number range from 12% to 26%. The selection of this louvered fin geometry as a reference geometry was based on available and manufacturable fins. A shortening of the

fin length in air flow length could have been done to decrease the effectiveness and thus the uncertainty. However, uncertainties in fin geometry might have increased the uncertainty again.

The relative expanded uncertainties for pressure drop and thus the relative expanded uncertainties for Fanning friction factor are for all Reynolds numbers ($6 < \mathrm{Re_{st}} < 52$) and both fin types below 8%. The necessity to differentiate between low pressure drops in the range of 5 to 50 Pa and pressure drops in the range of 50 to 250 Pa has proven to be true. The measured pressure drops range from 5 to 90 Pa. The application of two sensors can be recommended if the range of velocities will be large. The measurement of air inlet and outlet temperature with a meandering platinum wire sensor is an unconventional approach for temperature measurement. It allows (i) an integrative measurement of the air temperature in the flow cross section, (ii) a small interference in fluid flow, (iii) a measurement close to the sample with the drawback of (iv) the necessity of equal velocities in the cross section of the sensor, (v) difficulties in the calibration of the sensor due to a non-localized measurement, and (vi) a very time consuming process of threading the platinum wire in the plastic mesh [...].

The louvered fins show the thermal-hydraulic performance expected for the specific geometry based on literature data in [62]. The effective heat transfer coefficients are in the range of $100\,\mathrm{W/(m^2\,K)}$ to $150\,\mathrm{W/(m^2\,K)}$. In combination with the high volume specific surface area of $2240\,\mathrm{m^2/m^3}$and relatively low pressure drops of 2000 to $2800\,\mathrm{Pa/m}$ (for 2-2.5 m/s) the enhancement shows very high performance. Despite the high uncertainties in measurements the Nusselt number follows the shape of curve from literature data.

The micro pin fin wire structure shows a slightly less promising thermal-hydraulic performance compared to the 2D-CFD simulations [in Section 4.4]. There are several possible explanations for this result. First, the 2D simulation neglects influences of the sample plate wall; especially at high inlet velocities the shear stress at the wall influences the pressure, the velocity, and the

temperature field. 2D-CFD simulations show a 30% higher Fanning friction factor for a Reynolds number of $Re_{st} = 70$ for the pin fins compared to the 2D simulation. Second, the pin fin test core (Figure 5.2) has geometrical irregularities due to the manual manufacturing process. As a result, some wires are not contacted, not homogeneously distributed, and there are solder meniscuses on the soldering joints of the wires. A reduction in thermal-hydraulic performance is possible. The large differences in the sample plate temperature provide a first evidence of non-homogeneity. In essence, the effective heat transfer coefficients are twice as high compared to the louvered fins and volume specific surface area is in similar dimension with $1970\,m^2/m^3$. The pressure drop shows significant increase compared to the louvered fins in the order of a factor of 2. Thus, the micro pins fins in a heat exchanger might fail to increase heat transfer significantly with use of less or equal fan power. Nevertheless the pin fins allow a reduction of the heat exchanger size in the order of 2 and thus allow new degrees of freedom in design and a significant material reduction. Furthermore, the tested pin fin wire structures have a wire diameter of 250 µm. A reduction to 100 µm or less might be possible. Heat transfer coefficients can thus be increased further" [FDSS18].

5.3.2 Continuous Textile Structures

Performance

Several different configurations of continuous textile structures have been tested for hydraulic performance. Firstly, one heat exchanger element of length 19 mm in flow direction (cf. [Alt18] and Figure 5.16); secondly, two heat exchanger elements of total length 38 mm (cf. [Mad16]); thirdly, a small-scale sample with only one segment, with width 100 mm and length 19 mm (cf. Figure 5.8 (a)). The hydraulic performance results have been compared to simulation results based on the developed correlation in Sections 4.2 and 4.4. Figure 5.22 shows the pressure drop in terms of friction factor as a function

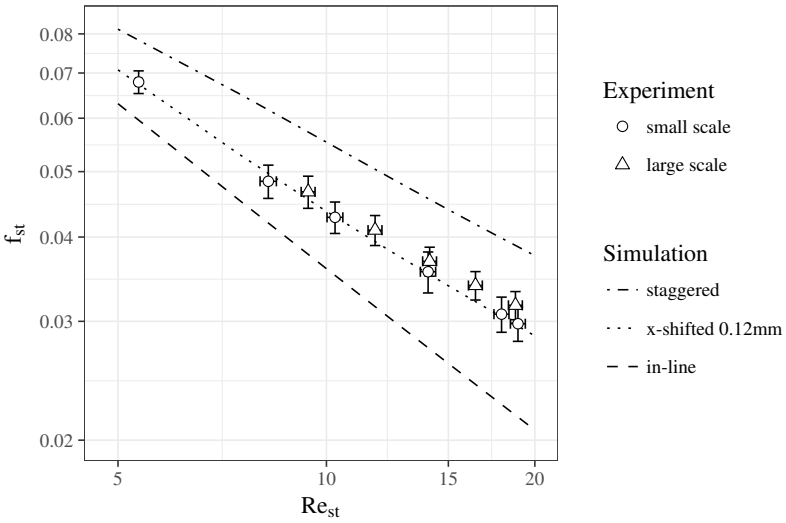

Figure 5.22: Fanning friction factor versus Reynolds number for experimental data and correlation/simulation data based on Sections 4.2 and 4.4.

of Reynolds number for the two configurations with flow length 19 mm. In addition to the in-line and staggered arrangement a 2D simulation with shifted wires in x-direction is presented. Therefore, every second wire in flow direction is shifted from the in-line position normal to the flow by 0.12 mm. The shifting value is in the dimension of the wire diameter.

Short Discussion

The experimentally determined friction factors show appr. 30% higher values than the simulation results for an in-line geometry and appr. 30% lower values than the simulation results for the staggered geometry. The simulation results for the shifted geometry shows good agreement. The two experimental methods (small-scale and large-scale) show good agreement as well. From

Figure 5.8 (b) it is clear, that the wire arrangement is somewhere in between an in-line and staggered arrangement. The shifting of the wires in the simulation is one option to express the irregularity. It reflects the irregularity in a simplified way but is a reasonable estimate of the geometry. Contraction loss and exit loss coefficients (cf. Equation (2.11)) might be underestimated when calculating friction factors based on the pressure drop measurement results.

The comparison shows that the simulation can depict the friction factor sufficiently.

5.3.3 Woven Textile Structures

Performance

The performance for the two woven wire structure heat exchangers is related to the reference fin and expanded metal heat exchanger. The pressure drop of the wire structure is much higher than the reference; from a factor of 1.5 up to a factor of 5. Figure 5.23 shows the shape of the curves for the heat exchanger pressure drop in relation to the heat exchanger frontal air velocity. The data has been generated based on 36 measurement points of steady volume flow rate and steady inlet/outlet temperatures on the air and water side. The water inlet volume flow rate ranged from $0.14\,\mathrm{m^3/h}$ up to $1.10\,\mathrm{m^3/h}$, whereas the air-side inlet volume flow rate ranged from $150\,\mathrm{m^3/h}$ up to $1000\,\mathrm{m^3/h}$. These different operating conditions yield a bandwidth of heat transfer rates shown in Figure 5.24 based on the the different volume flow rates or velocities. For higher water side volume flow rates the thermal resistance on the water side decreases, such that the thermal resistance of the air-side is more pronounced. A slightly higher heat transfer rate can be seen for higher air-side velocities for the wire structures. However, a clearer depiction of the thermal resistance can be given when looking at the product of effective heat transfer coefficient $U_{\mathrm{air,eff}}$ and heat transfer surface area A_{HTS} in Figure 5.25. For higher air-side velocities the wire structures show nearly double the effective heat transfer. At

lower air-side velocities the differences are less distinct. The slope in effective heat transfer with respect to air-side velocity is steeper for the wire structure. The effective heat transfer coefficient $U_{\text{air,eff}}$ is separated into its convective and conductive parts, represented by the heat transfer coefficient h_{air} and the surface efficiency η_0. Figure 5.26 shows that the wire structures have high heat transfer coefficients, with the drawback of a low surface efficiency for the same velocity range of $1 \leq v_{\text{air,in}} \leq 7$.

The comparison to the correlated simulation data for fanning friction factor and Nusselt number is shown in Figure 5.27 and Figure 5.28.

The differences between simulation and measurement are huge. The friction factor is underestimated by the simulation by a factor of 2 to 10. At the same time the Nusselt number is overestimated for Reynolds number above 40 with a factor up to 3.

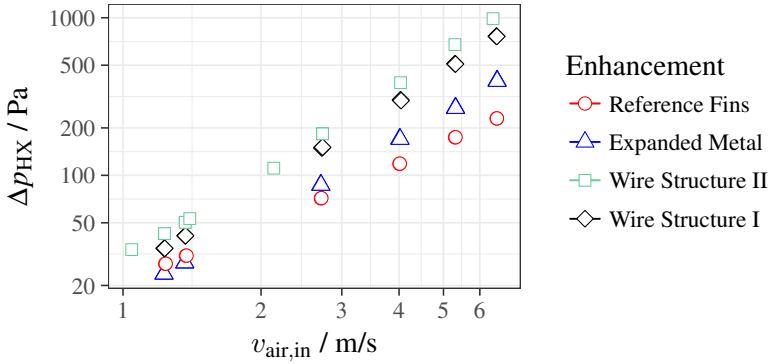

Figure 5.23: pressure drop over the heat exchanger Δp_{HX} as a function of air velocity before the heat exchanger $v_{\text{air,in}}$.

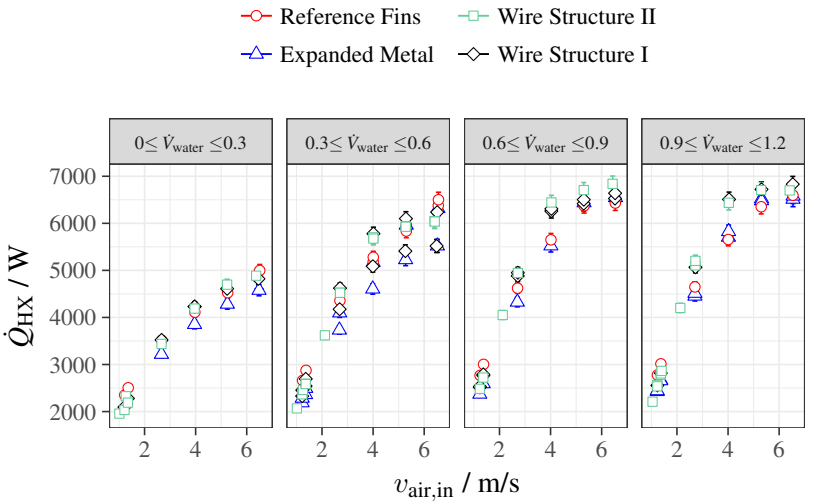

Figure 5.24: Heat transfer rate $\dot{Q}_{\mathrm{HX}}$ as a function of air velocity before the heat exchanger $v_{\mathrm{air,in}}$ and based on different water volume flow rate intervals $\dot{V}_{\mathrm{water}}$ in m^3/h.

Short Discussion

The wire structure heat exchangers show similar and higher heat transfer $U_{\mathrm{air,eff}}A_{\mathrm{HTS}}$, than the reference. However, the increase is less marked than the increase in pressure drop. Figure 5.29 illustrates the performance differences in terms of efficiencies defined in Table 3.3. The energy efficiency $\epsilon_{\mathrm{E}}^{*}$ of the reference heat exchanger is approximately 2 times higher than the efficiency of the wire structure heat exchangers. The benefits of the wire structure are given in the possibility for volume and mass reduction; a factor of up to 2 can be seen for the difference in volume efficiency $\epsilon_{\mathrm{V}}^{*}$ and a factor of up to 4 for the difference in mass efficiency $\epsilon_{\mathrm{M}}^{*}$.

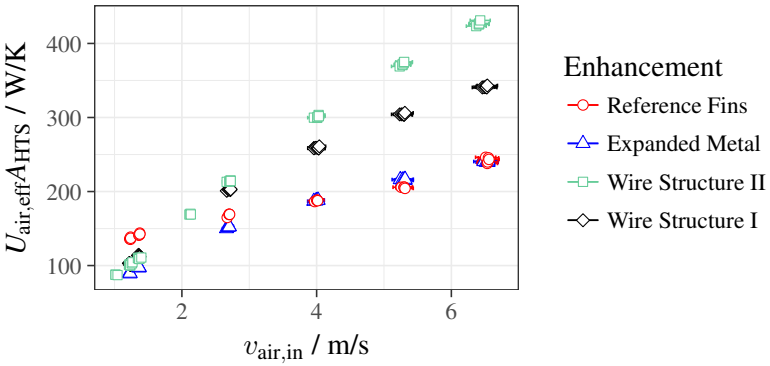

Figure 5.25: Product of effective heat transfer coefficient $U_{\text{air,eff}}$ and heat transfer surface area A_{HTS} as a function of air velocity before the heat exchanger $v_{\text{air,in}}$.

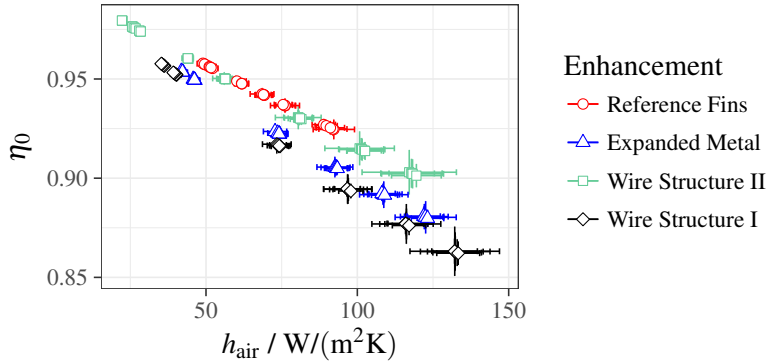

Figure 5.26: Surface efficiency η_0 related to heat transfer coefficient h_{air}.

From the 2D simulation of the wire structure (Figure 5.27 and Figure 5.28) a value for ϵ_{E}^* in the range of 0.4 to 0.5 can be calculated from the definitions of efficiency in Table 3.3. This value is approximately 3 times higher than the measured values shown in Figure 5.29.

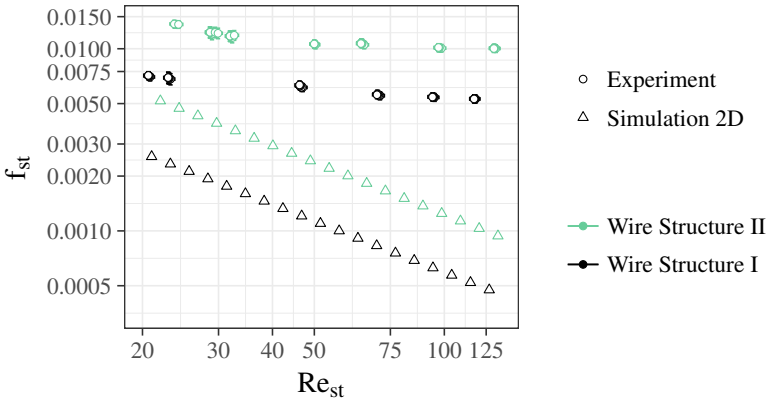

Figure 5.27: Fanning friction factor f_{st} versus Reynolds number Re_{st} for experimental data and simulation data (Section 4.2) of two woven wire structure heat exchangers.

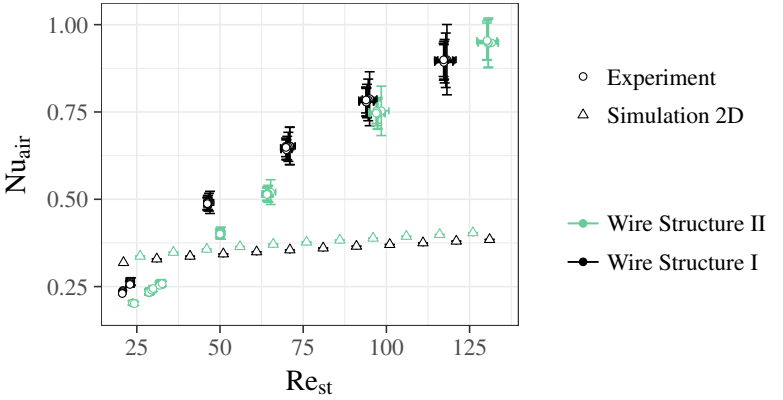

Figure 5.28: Nusselt number Nu_{air} versus Reynolds number Re_{st} for experimental data and simulation data (Section 4.2) of two woven wire structure heat exchangers.

Several possible reasons can be enumerated to explain these differences:

- Contacting a woven wire mesh to tubes via brazing is more challenging, than brazing a corrugated metal sheet to a tube. The latter is a standard process for heat exchanger manufacturing, such that the contacts are done well. However, according to visual inspection the contacts of the wire mesh seem to be good. A performance limitation due to a thermal contact resistance is possible, but with bare possibility.

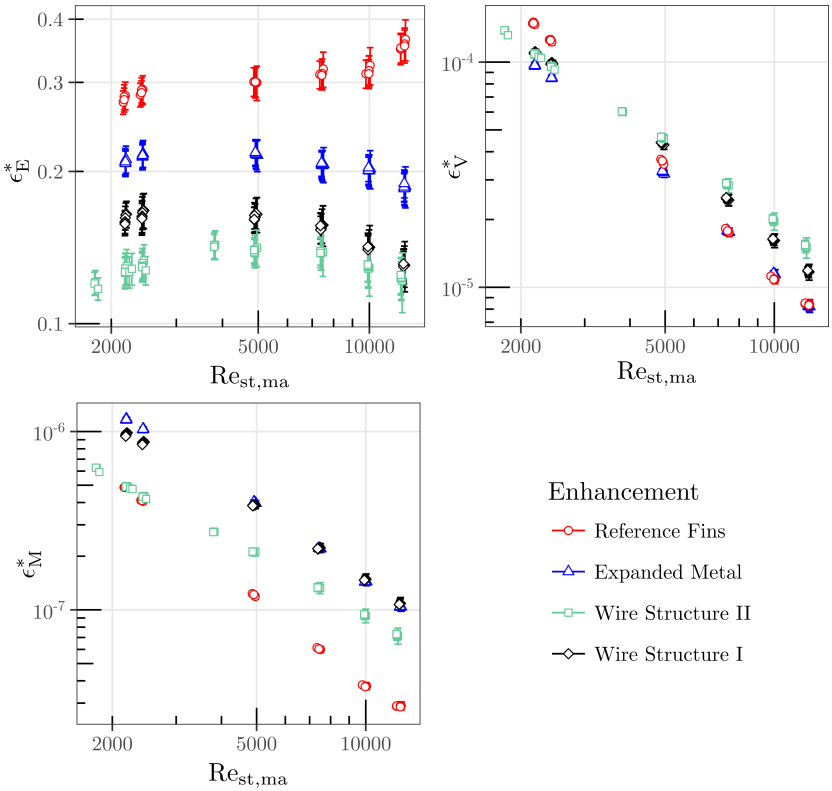

Figure 5.29: Energy, volume and mass efficiency for woven wire structure and reference heat exchangers. Reynolds number is based on a macro diameter of $d_{ma} = 19\,mm (= H_{st})$.

- The corrugation of the structures has been done on a manually operated gearwheel. Thereafter the corrugated structures have been placed in between the flat tubes. During this process the wire structures have been deformed, such that the corrugation is not homogeneous any more. Figure 5.30 shows the inhomogeneity of Wire Structure I. Fin pitches vary strongly and free-flow channels are bent.
- Several additional wires parallel to the tubes have been placed in the woven wire mesh to allow sufficient mechanical stability. However, two negative consequences can be seen from these impeding wires:
  - Pressure drop increases due to an additional blocking of the free channels
  - Heat transfer surface area in good thermal contact with the tube wall is blocked by the stability wires. However, these stability wires are not in good contact with the main wires, such that the heat transfer can be limited
- Heat conduction through the wires is reduced, as less material for surface enhancement is used. The surface efficiency η_0 shows this effect.

In summary the measurements show that the woven wire structure samples are not yet able to perform equal to the idealized simulated structures from the design idea. Geometrical inhomogeneities are assumed to account for a large performance reduction. However, the necessity of (stability) weft wires (see Figure 5.15) yields an arrangement of wires that can not be in-line, thus the blockage of fluid flow in real samples is always underestimated by the in-line simulation. In the following chapter it will become apparent, that the in-line arrangement is favorable for energy efficiency. A deviation of the wire position from an in-line arrangement is inevitable for a woven fabric, due to the weft wires. Therefore, it is not assumed that corrugated woven wire structures will reach the (energetic) performance of an idealized structure.

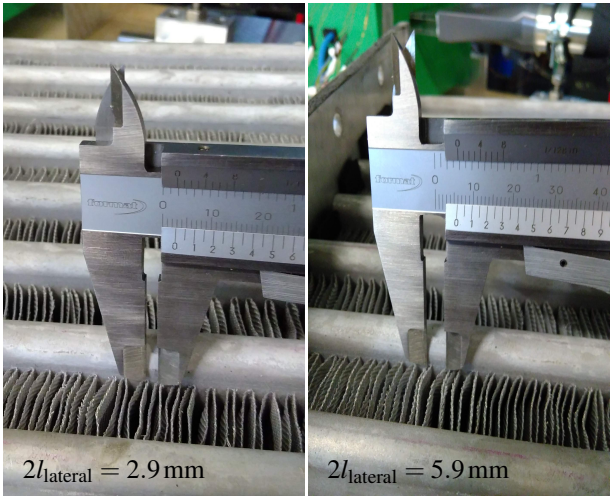

Figure 5.30: Differences in the lateral wire distance l_{lateral} for Wire Structure I. Extreme values for $2l_{\text{lateral}}$ range from 2.9 mm to 5.9 mm. The mean value is 4.4 mm.

6 Potential for Wire Structure Heat Exchangers

Within this chapter, favorable combinations of geometrical parameters of a wire structure heat exchanger are developed, based on optimizing the energy, mass, and volume efficiency. Moreover, optimized wire structure geometries are compared to reference surface enhancements in terms of efficiency. Thus, beneficial and unfavorable operating and geometrical conditions for wire structure heat exchangers can be provided.

6.1 Comparison of Different Geometrical Designs

Different geometric designs of wire structures will now be tested for suitability for efficient heat exchangers. Therefore, geometric feasibility sets Θ are defined representing applicable designs. Two specific feasibility sets represent designs with a specified tube distance of 10 mm (Version 1) and 19 mm (Version 2). This corresponds to the structure heights of the samples in Section 5.3. The performance parameters $\epsilon_{\mathrm{E}}^{*}$, $\epsilon_{\mathrm{V}}^{*}$ and $\epsilon_{\mathrm{M}}^{*}$ are calculated for several geometry points in the feasibility sets based on the 2D simulation correlation in Section 4.4.2 and the extended fin efficiency in Section 4.5.1 for different operating conditions. This analysis allows a statement on preferable and non-preferable geometric designs of wire structures.

6.1.1 Dependency on Geometric Conditions

The choice of a specific combination of geometric parameters d_{wire}, H_{st}, a, b, n_{wires} and staggered or in-line arrangement yields unique efficiencies for

specified $\mathrm{Re}_{\mathrm{st,ma}}$, $k_{\mathrm{st}}/k_{\mathrm{air,st}}$, $\rho_{\mathrm{air,st}}/\rho_{\mathrm{st}}$, and Pr. The definition of a feasibility set Θ limits the choice of possible combinations to a reasonable number.

Two feasibility sets Θ_{V1} and Θ_{V2} are defined in Table 6.1 for the analysis within this section. The definitions are related (i) to the geometric limitations defined in Table 4.2 for the simulation and (ii) to the tested samples in Section 5.3.1 and Section 5.3.3. Thus, the micro pin fin structure, shown in Figure 5.11, is one feasible decision within Θ_{V1}; and the woven wire structure I, shown in Figure 5.14, is one feasible decision within Θ_{V2}.

The analysis makes use of the graphical comparison of the efficiencies ϵ_{E}^*, ϵ_{V}^* and ϵ_{M}^* against each other. The feasible decisions (with superior performance) shape the Pareto front as described in Section 3.2.3 within this comparison plots. For instance, the ϵ_{E}^*-ϵ_{M}^* Pareto optimal set is the subset of a feasible set Θ, which shows a superior performance in an ϵ_{E}^* versus ϵ_{M}^* plot.

The efficiencies of a broad selection of feasible decisions within Θ_{V1} are shown in Figure 6.1 with focus on the wire diameter d_{wire}. The figure shows that high volume and mass efficiencies can be achieved with low wire diam-

Parameter	Θ_{V1}	Θ_{V2}
d_{ma}	10 mm	19 mm
H_{st}	10 mm	19 mm
d_{wire}	$50\,\mu\mathrm{m} \leq d_{\mathrm{wire}} \leq 300\,\mu\mathrm{m}$	$50\,\mu\mathrm{m} \leq d_{\mathrm{wire}} \leq 400\,\mu\mathrm{m}$
a	$4 \leq a \leq 12$	$4 \leq a \leq 12$
b	$1.2 \leq b \leq 4$	$1.2 \leq b \leq 4$
n_{wires}	100	100
$\chi_{\mathrm{st,air}}$	11673	11673
$\rho_{\mathrm{air,st}}/\rho_{\mathrm{st}}$	0.00013	0.00013
Pr	0.71	0.71
Arrangement	in-line or staggered	in-line or staggered

Table 6.1: Feasibility sets Θ_{V1} and Θ_{V2}.

eters. The data shown is based on a Reynolds number $\mathrm{Re}_{\mathrm{st,ma}} = 1600$, which corresponds at standard conditions to a structure velocity v_{st} of 2.4 m/s. The calculation of fin efficiency is based on the non-uniform temperature distribution method (cf. Equation (4.18)). A geometry with a wire diameter below 100 µm is part of the ϵ^*_{E}-ϵ^*_{V} and ϵ^*_{E}-ϵ^*_{M} Pareto optimal set for $\epsilon^*_{\mathrm{E}} < 0.5$. Lower wire diameters than 50 µm could be superior for very high volume and mass efficiency. They are not shown in Figure 6.1 due to the definition of the lower

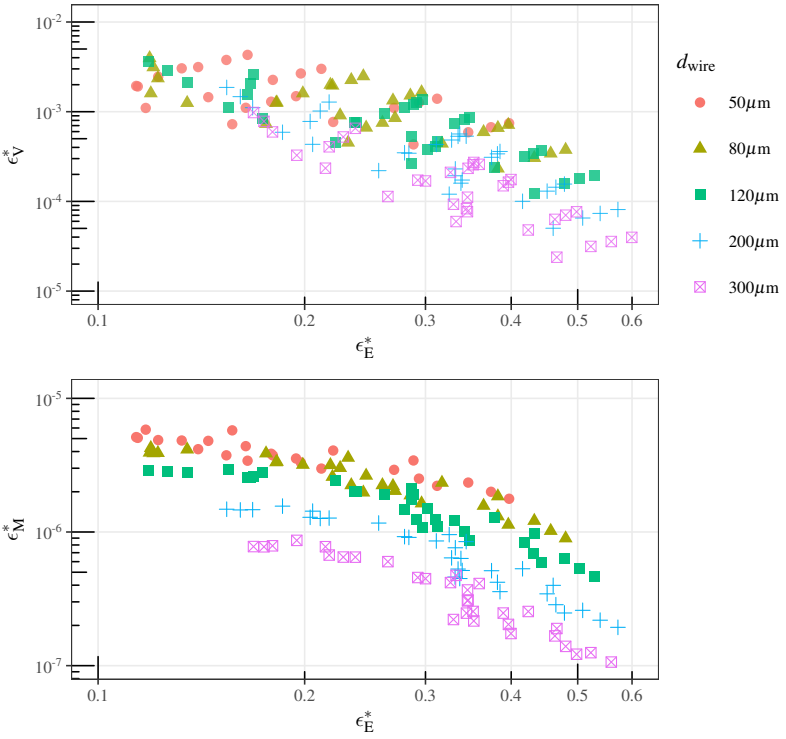

Figure 6.1: Volume and mass efficiency versus energy efficiency for a variety of wire structure heat exchanger with different wire diameters. Data is based on correlations (Chapter 4.4.2) and the feasibility set Θ_{V1} at $\mathrm{Re}_{\mathrm{st,ma}} = 1600$.

boundary for the wire diameter in Θ_{V1}. For applications with a higher demand for energy efficiency, optimal wire diameters rise up to 300 µm. However, the increase in energy efficiency with increasing diameter is not as prominent as the decrease in volume and mass efficiency when considering higher wire diameters.

The same comparison, however, with focus on the arrangement of the wires in an in-line and staggered way is shown in Figure 6.2. The conclusion is

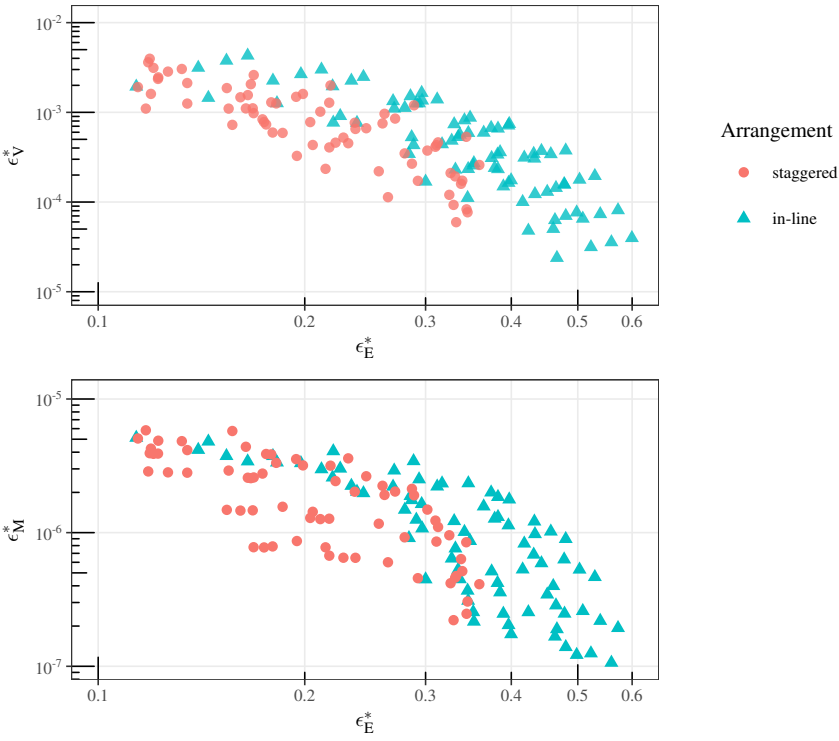

Figure 6.2: Volume and mass efficiency versus energy efficiency for a variety of wire structure heat exchanger with different wire arrangement. Data is based on correlations (Chapter 4.4.2) and the feasibility set Θ_{V1} at $\mathrm{Re}_{\mathrm{st,ma}} = 1600$.

evident: The staggered configuration is only preferable if very high mass efficiency ($\epsilon^*_M > 5 \times 10^{-6}$) is required. For all other cases an in-line configuration should be targeted.

In Figure 6.3 the focus is on the non-dimensional lateral wire distance a. Higher values of energy efficiency can be realized with a wider lateral distance of the wires to each other. Geometries with a lateral wire distance of

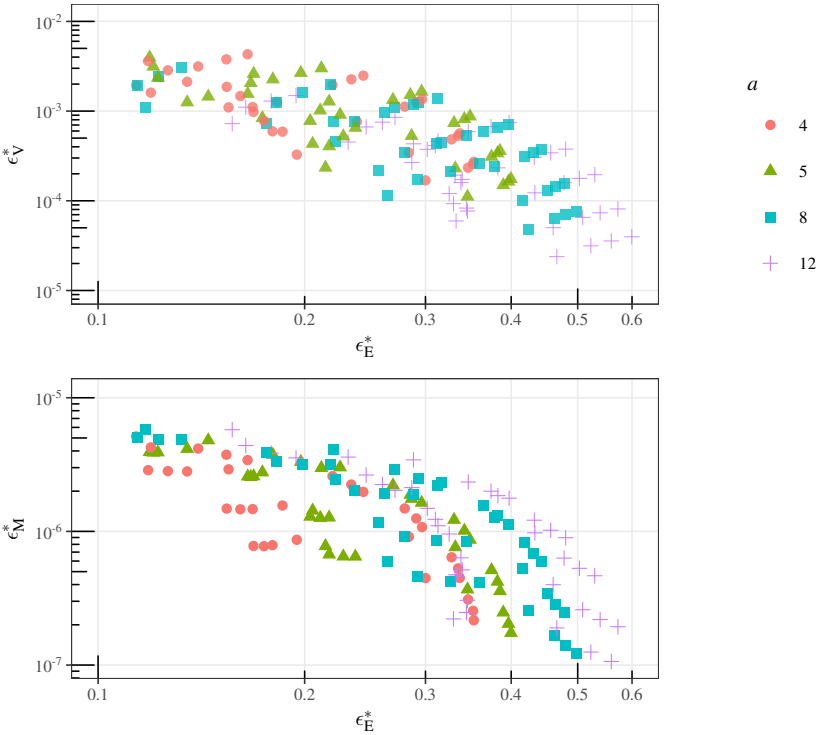

Figure 6.3: Volume and mass efficiency versus energy efficiency for a variety of wire structure heat exchanger with different lateral wire distance a. Data is based on correlations (Chapter 4.4.2) and the feasibility set Θ_{V1} at $\mathrm{Re}_{\mathrm{st,ma}} = 1600$.

$a = 12$ belong to the ϵ_E^*-ϵ_V^* Pareto optimal set as long as $\epsilon_E > 0.4$; and they belong to the ϵ_E^*-ϵ_M^* Pareto optimal set as long as $\epsilon_E > 0.3$.

With decreasing value of a the volume efficiency is increasing. However, the increase is not that strong anymore in the range of $4 \leq a \leq 5$. From this analysis it seems adequate to design wire structures with lateral wire distances in the order of $a = 12$. It seems not to be necessary within the geometric boundary conditions of Θ_{V1} to design wire structures with $a \leq 5$.

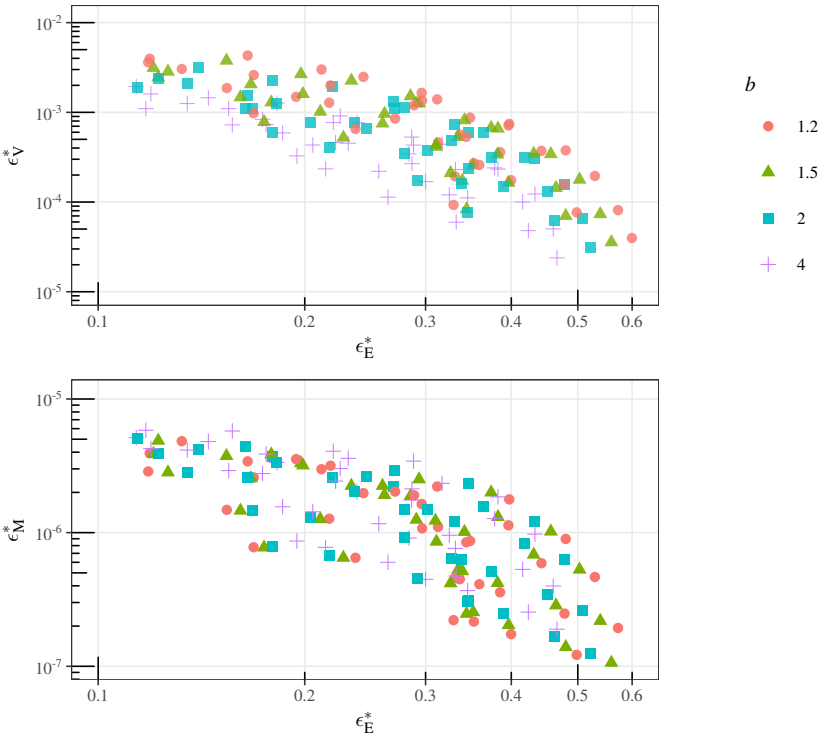

Figure 6.4: Volume and mass efficiency versus energy efficiency for a variety of wire structure heat exchanger with different longitudinal wire distance b. Data is based on correlations (Chapter 4.4.2) and the feasibility set Θ_{V1} at $Re_{st,ma} = 1600$.

The analysis of favorable non-dimensional longitudinal wire distances shows a clear performance benefit for wire structures with small longitudinal distance b (see Figure 6.4). A value of $b = 1.2$ is consistently favorable for an evaluation based on ϵ_{E}^* and ϵ_{V}^*. The benefit of larger distances than $b = 1.2$ is given if mass efficiency requires values above $\epsilon_{\mathrm{M}}^* > 2 \times 10^{-6}$. However, the increase is accompanied with a strong decrease in ϵ_{E}^*. It seems to be reasonable to concentrate on wire distances in the order of $b = 1.2$.

In Appendix A.4 a combined efficiency of the feasible decisions in Θ_{V1} is presented to allow a more detailed analysis for the interested reader.

6.1.2 Comparison to Experimental Data

In Figure 6.5 the Pareto front of the feasibility set Θ_{V1} is shown. It is based on an optimization with a non-dominated sorting genetic algorithm (NSGA) implemented in the programming language R [82]. The Pareto front is the same as the imaginable front in the Figures 6.1 to 6.4, but with variable geometric parameters. Additionally the efficiency of the micro the pin fin sample in Section 5.3.1 is shown together with the simulation-based efficiencies for this specific geometry.

The difference in performance of the measured sample and the simulated geometry is extensively discussed in Section 5.3.1. Likewise, the consistency between the 3D simulation, the 2D simulation, and the correlation is discussed in detail in Section 4.4.

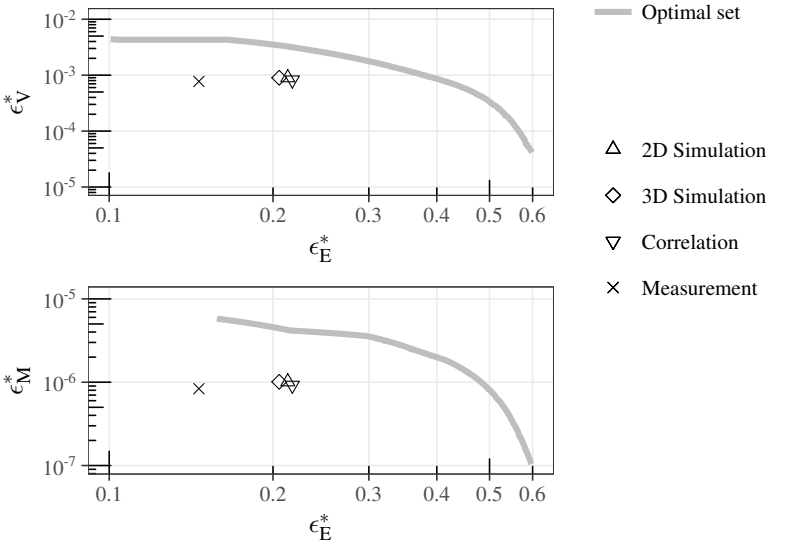

Figure 6.5: ϵ^*_E-ϵ^*_V and ϵ^*_E-ϵ^*_M Pareto optimal sets of Θ_{V1} for wire structure heat exchanger at $Re_{st,ma} = 1600$ in grey. Simulation, correlation and measurement of pin fin structure from Section 5.2.1 for comparison.

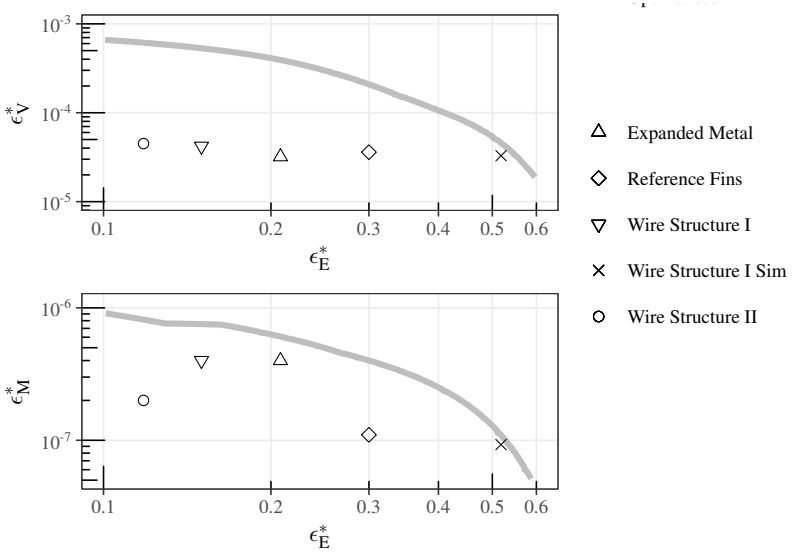

Figure 6.6: ϵ_E^*-ϵ_V^* and ϵ_E^*-ϵ_M^* Pareto optimal sets of Θ_{V2} for wire structure heat exchanger at $Re_{st,ma} = 5000$ in grey. Simulation and measurement of woven wire structure and references from Section 5.3.3 for comparison.

A new aspect is that the wire structure geometry itself is not favorable. For all three efficiencies a higher value could be achieved by changing the geometry.

A slightly different conclusion can be drawn from the woven wire structure design. In Figure 6.6 the Pareto optimal set is shown for the feasibility set Θ_{V2}. The experimental results of the expanded metal, the reference fins and the wire structure I and II samples are included in the figure. Wire Structure I is a feasible decision in Θ_{V2} and the correlated simulation performance is shown as well. Wire Structure II is, due to a longitudinal wire distance of $b = 1$, not an element of Θ_{V2} and is thus not simulated.

Several new insights can be gained from Figure 6.6. Firstly, the geometric design of wire structure I is close to the Pareto front, as can be seen from the simulation result (Wire Structure I Sim). Secondly, the reference fin shows

a clear distance to the Pareto optimal set of the wire structure. Thirdly, the wire structure I and the expanded metal are in the vicinity of the ϵ_E^*-ϵ_M^* Pareto optimal set.

6.1.3 Dependency on Operating Conditions

Three feasible decisions θ_1, θ_2, and θ_3 are selected from the ϵ_E^*-ϵ_V^* Pareto optimal set in Figure 6.5 (based on the feasibility set Θ_{V1}). The selection is shown in Table 6.2.

Decision	d_{wire} / µm	a	b	Arrangement	ϵ_E^*	ϵ_V^*
θ_1	300	12	1.2	in-line	0.60	0.40×10^{-4}
θ_2	120	12	1.2	in-line	0.53	1.97×10^{-4}
θ_3	80	8	1.2	in-line	0.41	7.32×10^{-4}

Table 6.2: Selection of feasible decisions θ_1 to θ_3 as elements of the ϵ_E^*-ϵ_V^* Pareto optimal set of Θ_{V1} at $\text{Re}_{\text{st,ma}} = 1600$.

The feasible decisions are used to show the efficiencies for Reynolds numbers different from $\text{Re}_{\text{st,ma}} = 1600$. Figure 6.7 shows the energy, volume and mass efficiency of the three decisions for Reynolds numbers $700 < \text{Re}_{\text{st,ma}} < 4000$. For $\text{Re}_{\text{st,ma}} = 1600$ none of the decision is favorable over the other. This finding remains true for the range of Reynolds numbers $700 < \text{Re}_{\text{st,ma}} < 4000$. Furthermore, the Pareto optimal sets at the three Reynolds numbers $\text{Re}_{\text{st,ma}} = 700$, $\text{Re}_{\text{st,ma}} = 1600$, and $\text{Re}_{\text{st,ma}} = 4000$ are approximately the same. This indicates that the (geometric) Pareto optimal set is only slightly dependent on the Reynolds number.

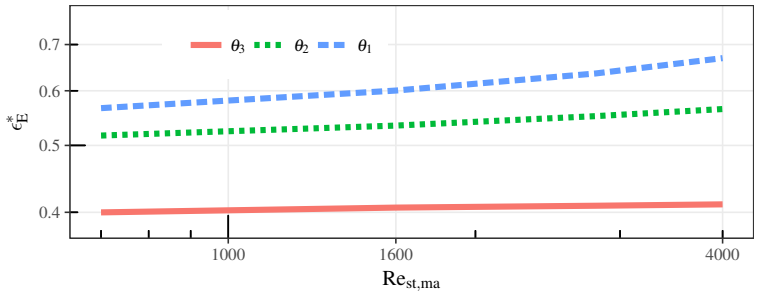

(a) energy efficiency

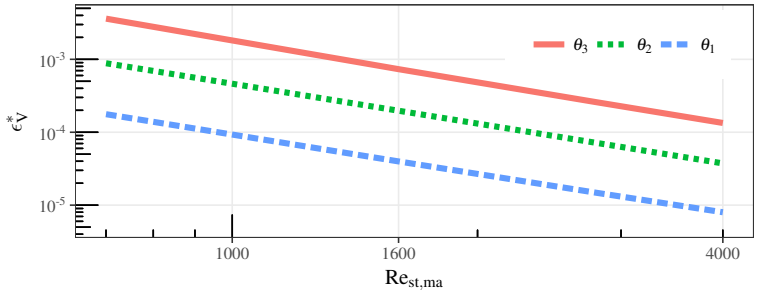

(b) volume efficiency

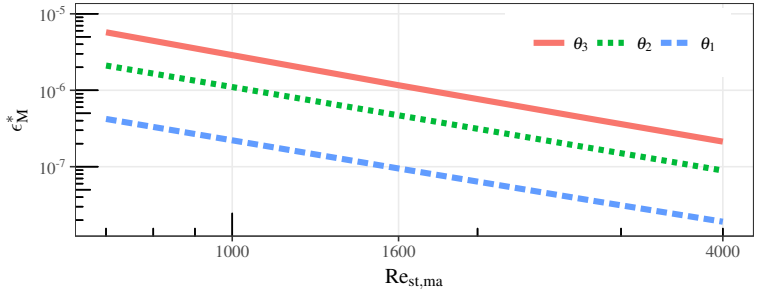

(c) mass efficiency

Figure 6.7: Efficiencies based on the Reynolds number for three feasible decisions θ_1, θ_2, and θ_3 (specific geometries) as elements of the ϵ^*_E-ϵ^*_V Pareto optimal set of the feasibility set Θ_{V1} at $Re_{st,ma} = 1600$.

This assumption is confirmed by the comparison of two new feasibility sets and the relationship of a and d_{wire} within their Pareto optimal subsets. The feasibility sets are defined as Θ_{V3} and Θ_{V4}. They are equal to Θ_{V2}, except the condition for H_{st}: The structure height H_{st} is 4 mm for Θ_{V3} and 30 mm for Θ_{V4}, representing two extreme values for the distance between the flat tubes. The ϵ_{E}^*-ϵ_{V}^* Pareto optimal set is determined for the two feasibility sets at two different structure velocities $v_{\text{st}} = 0.5\,\text{m/s}$ and $v_{\text{st}} = 4\,\text{m/s}$ each. This yields 4 Pareto optimal sets. The feasible decisions within the Pareto optimal set show the same characteristics for b and the arrangement as in Section 6.1.1 (with $b = 1.2$ and in-line configuration). The characteristics for a and d_{wire} is shown in Figure 6.8. The solid and dashed lines are interpolation curves of 300 feasible decisions (in the background) within each Pareto optimal set.

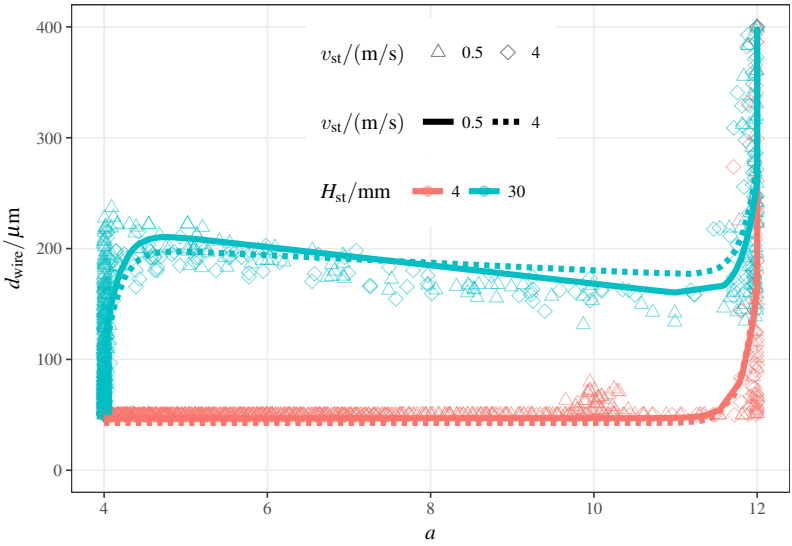

Figure 6.8: Wire diameter d_{wire} related to non-dimensional lateral wire distance a for four ϵ_{E}^*-ϵ_{V}^* Pareto optimal sets of Θ_{V3} ($H_{\text{st}} = 4\,\text{mm}$) and Θ_{V4} ($H_{\text{st}} = 30\,\text{mm}$) at superficial structure velocities $v_{\text{st}} = 0.5\,\text{m/s}$ and $v_{\text{st}} = 4\,\text{m/s}$ each.

Independently of height H_{st} and velocity v_{st}, high energy efficiency is realized with $a = 12$ and $d_{\mathrm{wire}} = 400\,\mu\mathrm{m}$ (top, right corner); high volume efficiency is realized with $a = 4$ and $d_{\mathrm{wire}} = 50\,\mu\mathrm{m}$ (bottom, left corner). These values are the limits of Θ_{V3} and Θ_{V4}. However, the structure with the longer wires favours wire diameters of $d_{\mathrm{wire}} \simeq 180\,\mu\mathrm{m}$ for $4 < a < 12$, whereas the structure with the shorter wires favours wire diameters of $d_{\mathrm{wire}} = 50\,\mu\mathrm{m}$ for $4 < a < 12$. This behaviour is due to the limitation in heat conduction through the wires.

A further insight is that the combination of a and d_{wire} is independent of the velocity v_{st}. This rather counter-intuitive result is related to the relative low increase in the Nusselt number with respect to the Reynolds number (cf. Figure 4.13).

6.1.4 Conclusion on Geometry

The following conclusions can be drawn from the analysis of favorable geometric specifications of the wire structures for a superficial structure velocity of $0.5\,\mathrm{m/s} < v_{\mathrm{st}} < 4\,\mathrm{m/s}$ and a structure height $4\,\mathrm{mm} < H_{\mathrm{st}} < 30\,\mathrm{mm}$:

- The Pareto optimal sets (and thus the optimal geometric specifications) are strongly dependent on the structure height $H_{\mathrm{st}} (= d_{\mathrm{ma}})$ and only slightly dependent on the velocity v_{st}.
- The wire diameter must be in the order of 300 µm to allow the highest energy efficiency. Values above 300 µm do not increase the energy efficiency significantly. A strong increase in volume and mass efficiency can be achieved with a wire diameter in the range of 50 to 180 µm, dependent on H_{st}. The energy efficiency decreases by decreasing the wire diameter. A general decrease of the wire diameter to values around 50 µm can be recommended when volume and mass efficiency is of major importance.
- The in-line arrangement is favorable.

- The lateral wire distance must be in the order of $a = 12$ to achieve high energy efficiencies. Higher volume and mass efficiencies can be achieved with lowering the wire diameter first, keeping the non-dimensional value a in the order of 12. Thereby the dimensional lateral wire distance l_{lateral} decreases proportional to the wire diameter decrease. When the wire diameter reaches a value which allows an acceptable fin efficiency, the distance a can be decreased to reach higher volume and mass efficiencies (with the drawback of lower energy efficiencies)
- The longitudinal wire distance b must be in the order of 1.2 to achieve high energy and volume efficiencies.
- The fin efficiency is in the order of 90% for geometries with high energy efficiency. It drops down to 70% when the wire diameter is reduced in order to increase volume and mass efficiency. The wire diameter is then not reduced further, fin efficiency stays at approximately 70%. The lateral wire distance is reduced down to the minimum allowable value.

6.2 Comparison to Classical Heat Transfer Surface Enhancements

In this section a comparison of the wire structure to classical surface enhancements is performed. The comparison focuses on louvered fins as classical surfaces, as the conceivable applications of louvered fins and wire structures are similar. Moreover, a rectangular channel geometry is used for comparison, representing a plain rectangular fin in a simplified version. Finally, metal foams are analyzed. The comparison is based on the $\epsilon_{\mathrm{E}}^{*}$-$\epsilon_{\mathrm{V}}^{*}$ Pareto optimal sets of each enhancement for a fixed structure height $H_{\mathrm{st}} = 10\,\mathrm{mm}$ and varying velocities between $0.5\,\mathrm{m/s} < v_{\mathrm{st}} < 4\,\mathrm{m/s}$.

6.2.1 Selection of Surface Enhancements

The comparison of the wire structure to classical surface enhancements (see e.g. Figure 2.1) comes with the challenge to find adequate performance descriptions. The following steps were tested for several surface enhancements described in the literature:

- Is the surface enhancement suitable for flat tube configuration?
- Is a thermal-hydraulic correlation (pressure drop and heat transfer) available?
- Are the definitions of geometric parameters (diameters, surfaces, volumes, ..) unambiguous?
- Can the geometry be varied within the correlations and does it fit to the specified structure height?
- Can the velocity be varied within the correlations and does it fit to the specified velocity range?
- Are the correlation uncertainties for the specified parameter range sufficiently small?

- Is an optimization of geometrical parameters with objective functions ϵ_E^*, ϵ_V^*, and ϵ_M^* reasonable?
- Is there a clear accordance in performance with other sources for the same enhancement?

For offset strip fins, the efficiencies vary strongly for several sources [38, 63, 83] with relative differences up to 30% for specific geometries. Thus, offset strip fins are not used for comparison.

Wavy fin correlations in the work of Dong et al. [84, 85] do not allow variation of fin thickness and have a lower limit in fin pitch of 2 mm. The fin pitch limitation is restricting volume efficiency strongly. Khoshvaght [86] is reducing the fin pitch to 1.5 mm, but with insufficient accuracy of correlations for an optimization. Thus, wavy fins are not used for comparison.

Correlations for louvered fins [62, 64] based on experiments show sufficient accordance of efficiencies. Moreover, several geometric parameters are adjustable in an adequate range. Louvered fins are used for comparison.

A clear correlation for plain rectangular fins could not be found in the literature. Therefore, a rectangular channel geometry is used for comparison based on a developed laminar flow [11, p. 476]. The advantage of this ansatz is the possibility to strongly decrease the fin pitch in order to allow high volume efficiencies.

Lastly metal foams are analyzed for availability of adequate correlations. Experimental work with metal foams as surface enhancement is numerous. However, thermal-hydraulic correlations are sparse and in many cases they do not fit (i) the geometric or (ii) velocity boundary conditions specified for the comparison or (iii) the definitions of geometric parameters are ambiguous. Together with L. Cirillo, author of [87] a best guess on metal foam performance has been worked out. A short comparison with the wires is shown at the end of this chapter.

For all three selected surface enhancements, the boundary conditions on the geometry are shown in terms of feasibility sets in the Appendix A.5.

6.2.2 Comparison

Figure 6.9 shows the ϵ_E^*-ϵ_V^* Pareto optimal sets of louvered fins [62], rectangular channels [11, p. 476], and wire structures in terms of ϵ_E^* versus ϵ_V^* and in terms of ϵ_E^* versus ϵ_M^*. The Reynolds number is set to $\mathrm{Re}_{st,ma} = 1600$, which corresponds at standard conditions to a structure velocity v_{st} of $2.4\,\mathrm{m/s}$, e.g. suitable for HVAC systems (cf. Table 2.2).

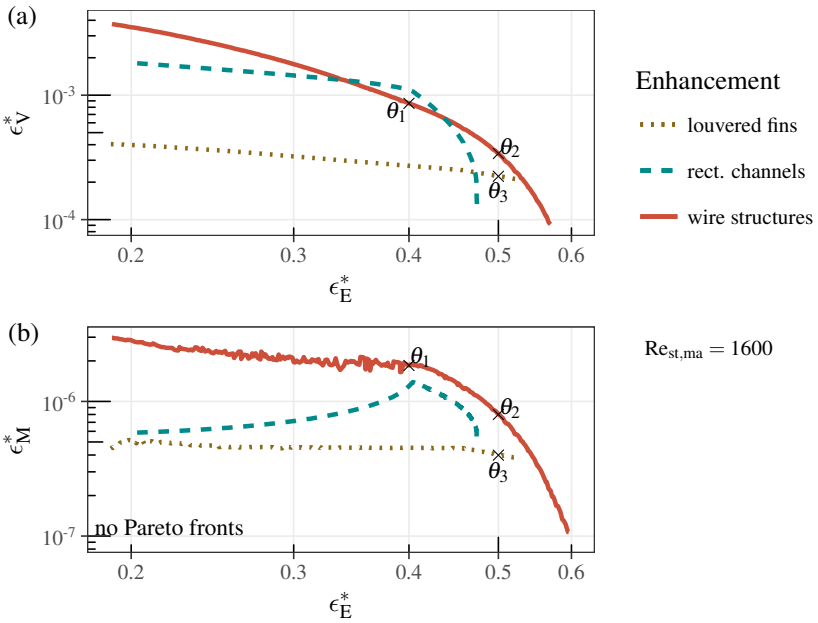

Figure 6.9: Relationship between energy, volume and mass efficiency in terms of ϵ_E^*-ϵ_V^* Pareto optimal sets of louvered fins, rectangular channels, and wire structures based on the feasibility sets $\Theta_{louvers}$, $\Theta_{channels}$, and Θ_{wires}, respectively.

Figure 6.9 (a) shows an increase in volume efficiency ϵ_V^* for decreasing energy efficiency ϵ_E^* for the wire structures. In Section 6.1.1 this behavior is explained by a decrease in wire diameter d_{wire} and lateral wire distance (or more generally fin pitch) $l_{lateral}$.

The rectangular channels show a similar shape of the curve. However, maximum values of ϵ_E^* are 0.47 and thus significantly lower than possible ϵ_E^* of the wire structures with $\epsilon_E^* = 0.6$. Figure 3.1 shows a similar limit of $\epsilon_E^* \leq 0.45$ for a smooth circular duct as the rectangular channels in Figure 6.9 (a).

The rectangular channels are slightly superior to the wire structures for the range $0.34 \leq \epsilon_E^* \leq 0.42$. This is due to a fluid flow through very narrow rectangular channels (small lateral fin distance of 500 µm) and thus high heat transfer coefficients. The rectangular channel volume efficiency is bounded by $\epsilon_V^* \leq 1.2 \times 10^{-3}$. A further increase could be realized with a smaller lateral fin distance than allowed within the feasibility set $\Theta_{channels}$. The fin distance in $\Theta_{channels}$ is bounded by $0.5\,mm \leq l_{lateral} \leq 3\,mm$.

The louvered fins show an inferior performance compared to the wire structure in Figure 6.9 (a). As the correlations are limited to specific geometrical parameters, the Pareto front could be extended for the louvered fins. Especially, the lateral fin distance range ($1\,mm \leq l_{lateral} \leq 1.4\,mm$) limits a higher volume efficiency and a higher energy efficiency. It can be assumed that the louvered fins show similar performance at $\epsilon_E^* = 0.52$ as the wire structures. As the wire structure correlations allow a broader geometrical parameter variation, a comparison of Pareto fronts has to be done with caution.

The mass efficiency shows a more explicit picture. In Figure 6.9 (b) the mass efficiency is plotted versus the energy efficiency. The data is based on the ϵ_E^*-ϵ_V^* Pareto optimal sets from Figure 6.9 (a) and shall not be mistaken with a ϵ_E^*-ϵ_M^* Pareto front; an optimization of all three efficiencies simultaneously would need e.g. weighting factors as described in Section 3.2.3 and is not shown here.

The wire structures are superior in terms of ϵ_E^* and ϵ_M^*. For a fixed value of ϵ_E^*, the wire structures show higher ϵ_M^* by a factor of 1.3 to 5. The louvered fins

show low mass efficiency; among other things due to the lower boundary of fin thickness ($d_{st} > 100\,\mu m$) and fin pitch ($l_{lateral} > 1\,mm$) within $\Theta_{louvered}$.

An exemplification of the difficulty to reach such high values as the wire structure does for mass efficiency is shown in Figure A.9 in the appendix.

The relation of the objective functions ϵ_E^*, ϵ_V^*, and ϵ_M^* to the dimensional quantities P_{diss}, V_{st}, and m_{st} is explained based on the three feasible decisions θ_1, θ_2, and θ_3 shown within Figure 6.9. The decisions θ_1 and θ_2 represent geometrical designs of the wire structure (elements of Θ_{wires}). The decision θ_3 is a specific geometry of the louvered fin design (element of $\Theta_{louvers}$). Based on the restrictions R1 to R5 in chapter 3 the three geometries have the same heat transfer rate $\dot{Q}$.

The geometrical design θ_1 allows a non-dimensional volume efficiency ϵ_V^* that is 3 times higher than the efficiency of θ_2. Thus, the structure volume V_{st} (or length L_{st}) of θ_1 is only one third of the volume of θ_2. Herewith a possible change in tube volume is not considered. At the same time the non-dimensional energy efficiency of θ_1 is 20% less than that of θ_2. This results in a 20% higher dissipated power P_{diss} for θ_1 compared to θ_2. However, a reduction in structure mass m_{st} in the order of 2 for θ_1 compared to θ_2 is possible, due to the difference in ϵ_M^*. A comparison of θ_2 and θ_3 shows an increase in structure volume V_{st} by 50% and an increase in structure mass m_{st} by 100% for the louvered fins at equal dissipated power P_{diss}, according to the same (but reciprocal) changes in efficiencies.

In order to decrease the influence of lateral wire distance $l_{lateral}$, the geometric parameters of the wire structure and the rectangular channels have been adapted to those of the louvered fins. In Figure 6.10 the fin pitch has a lower limit of 1 mm and the wire arrangement is limited to an in-line configuration.

Two reasons can be mentioned for this analysis. Firstly, a small fin pitch (here: below 1 mm) is more difficult to manufacture than a wider lateral fin distance. Secondly, fouling is highly dependent on the width of the free-flow channels. Blocking of channels increases with decreasing fin pitch and can

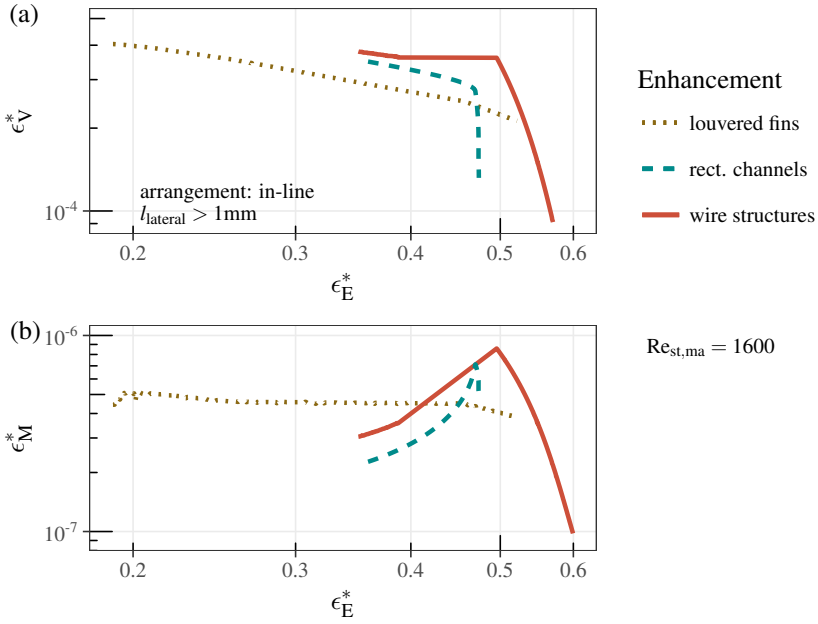

Figure 6.10: Relationship between energy, volume and mass efficiency in terms of ϵ^*_E-ϵ^*_V Pareto optimal sets of louvered fins, rectangular channels, and wire structures based on the feasibility sets Θ_{louvers}, Θ_{channels}, and Θ_{wires}, respectively; with an additional limitation on lateral fin distance $l_{\text{lateral}} > 1\,\text{mm}$.

yield strong performance reduction. Louvered fins and wire structures do not differ in that point [Alt18].

For a range of $0.5 \leq \epsilon^*_E \leq 0.6$, Figure 6.9 (a) and Figure 6.10 (a) show the same performance for the wire structures. For smaller values of ϵ^*_E (in Figure 6.10) the lateral wire distance is constant at $l_{\text{lateral}} = 1\,\text{mm}$. Thus, only an increase in wire diameter yields some benefit in terms of volume efficiency due to less limitation in heat conduction through the wires. This can be seen by the decrease in mass efficiency from $\epsilon^*_M = 9 \times 10^{-7}$ to $\epsilon^*_M = 5 \times 10^{-7}$ for $\epsilon^*_E < 0.5$. Two important aspects can be considered. Firstly, the difference between

the Pareto fronts of all three surface enhancements become small between $0.34 \leq \epsilon_E^* \leq 0.48$. Secondly, the rectangular channels are not superior any more (cf. Figure 6.9 (a)).

Up to now the analysis was limited to a constant Reynolds number of $Re_{st,ma} = 1600$. Now, the Reynolds number is varied from $Re_{st,ma} = 500$ to $Re_{st,ma} = 4500$ in order to see a performance change of the wire structures compared to the reference structures dependent on the operating condition. The analysis based on the reduced Reynolds number is shown in Figure 6.11. The louvered fins show very low energy efficiency. This is due to a stronger de-

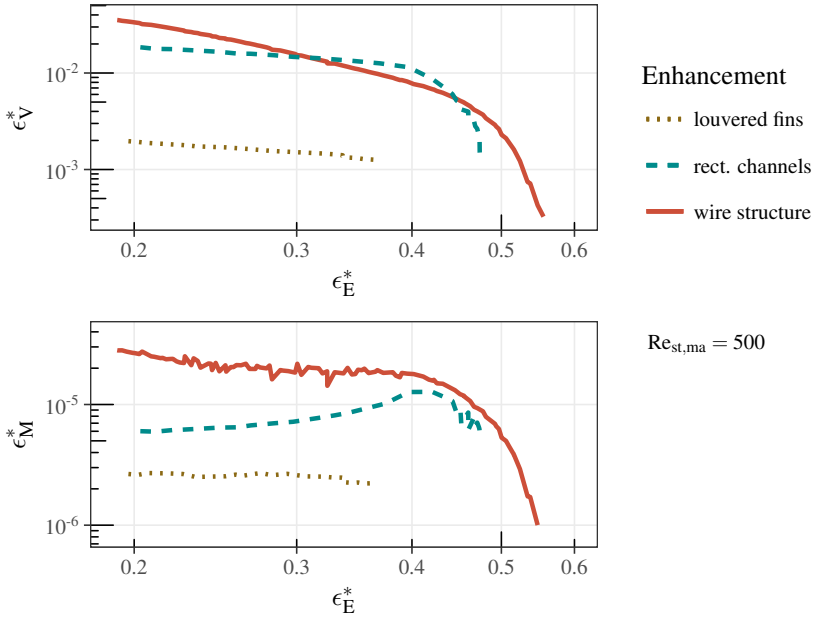

Figure 6.11: Relationship between energy, volume and mass efficiency in terms of ϵ_E^*-ϵ_V^* Pareto optimal sets of louvered fins, rectangular channels, and wire structures based on the feasibility sets $\Theta_{louvers}$, $\Theta_{channels}$, and Θ_{wires}, respectively; with reduced Reynolds number.

crease in Colburn factor than in friction factor for decreasing Reynolds numbers [62]. The rectangular channels and the wire structures show a similar behavior as in Figure 6.9.

Figure 6.12 shows a clear advantage for the louvered fins at higher Reynolds numbers in terms of high energy efficiency. Values up to 0.6 can be reached at higher volume efficiency as the wire structure. Moreover, the wire structure is superior or equal to the rectangular channel for the entire range of data.

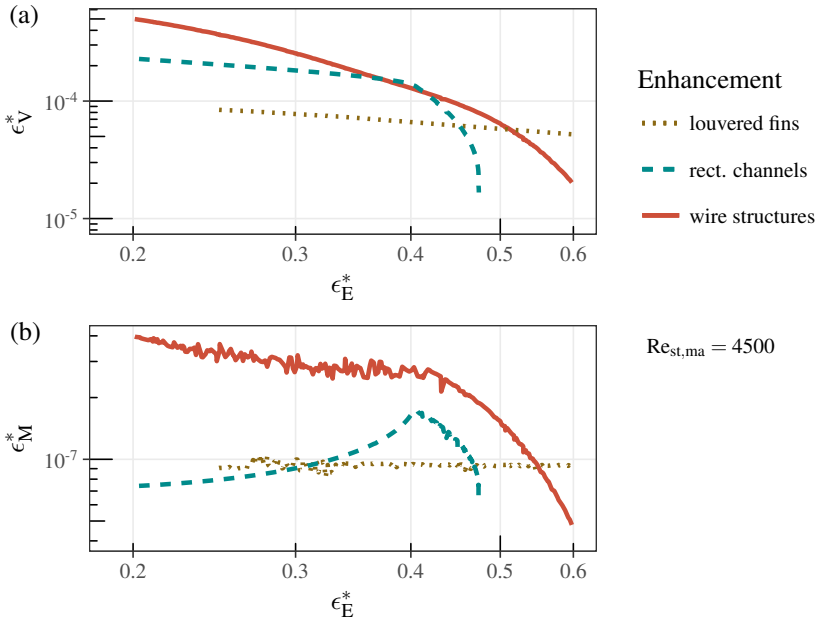

Figure 6.12: Relationship between energy, volume and mass efficiency in terms of ϵ^*_E-ϵ^*_V Pareto optimal sets of louvered fins, rectangular channels, and wire structures based on the feasibility sets $\Theta_{louvers}$, $\Theta_{channels}$, and Θ_{wires}, respectively; with increased Reynolds number.

Lastly, the efficiencies of metal foams shall be discussed. Based on [87], the energy and volume efficiencies of the analyzed metal foams do not exceed

$\epsilon_E^* = 0.1$ at a Reynolds number of $Re_{st,ma} = 85$ and $d_{ma} = 10\,mm$. Pores per inch (ppi) are varied from 10 to 30. Data for higher Reynolds numbers is not available. Details are given in Appendix A.5. The wire structure ($a = 4$, $b = 1.2$, $d_{wire} = 0.35\,mm$, in-line) allows for the same Reynolds number values of $\epsilon_E^* = 0.3$ at similar ϵ_V and ϵ_M. Thus, the energy efficiency is three times higher for the wire structure. For the staggered wire structure arrangement the energy efficiency reduces to $\epsilon_E^* = 0.2$. This result confirms the hypothesis that a well arranged structure allows more heat transfer rate per dissipated power.

6.2.3 Conclusion

The wire structures show throughout all comparisons a superior or equivalent performance in terms of energy and mass efficiency compared to the two references. The wire structures show in parts a superior performance in terms of energy and volume efficiency.

Beneficial operating conditions are in the low to medium velocity range of $0.75\,m/s \leq v_{st} \leq 2.4\,m/s$ (correspond to $500 \leq Re_{st,ma} \leq 1600$) and with the requirement of medium to high energy efficiency $0.4 \leq \epsilon_E^* \leq 0.6$.

Very similar energy and volume efficiencies can be reached by the wire structures and the rectangular channels for the entire range of operating conditions ($500 \leq Re_{st,ma} \leq 5000$) and with the requirement of medium to high volume efficiency; and thus medium to low energy efficiencies $0.4 \geq \epsilon_E^* \geq 0.2$.

The restriction in lateral fin distance to $l_{lateral} > 1\,mm$ in Figure 6.10 shows the limitation of the wire structures in applications with the requirement of sufficiently large free-flow areas.

7 Conclusion and Outlook

The overall objective of this thesis is to estimate the thermal-hydraulic performance potential of wire structures in flat-tube heat exchangers. Therefore, three major questions (see Section 1.2) have been defined in order to establish the necessary foundation to do the performance estimation:

1. Which performance evaluation criteria are suitable to enable a fair comparison of wire structure heat exchangers with other types of heat exchangers?
2. How can a large variety of different wire structure geometries be fundamentally evaluated for performance?
3. Is it feasible to manufacture wire structure sample heat exchangers and can their performance be accurately measured?

The three questions are answered briefly. Thereafter, the overall objective is addressed, followed by an outlook.

Within the chapter on performance evaluation criteria (Chapter 3), a dimensional performance evaluation method including energy, volume, and mass is developed to address the first question. The method allows a straightforward transfer to important quantities for real dimensioning. The dimensional performance evaluation quantities are transferred to non-dimensional efficiencies based on comparable driving parameters. These three efficiencies are the key elements for a fair comparison of wire structure heat exchangers with other types of heat exchangers. With the method, the energy, volume, and mass use can be controlled for an optimization/comparison by setting the efficiencies as objective functions.

Within the chapters on fundamental performance evaluation (Chapters 2 and 4), an elementary, but generic design idea of a flat-tube wire structure heat exchanger is analyzed to address the second question. The design idea has several geometric parameters, that can be varied within reasonable boundaries to allow different wire structure geometries. The fluid flow and heat transfer within the geometry is simulated using a finite-element 2D and 3D method. The simulation model is used to develop correlations for thermodynamic and fluid dynamic performance parameters. Further, an analytical expression of fin efficiency is presented which takes into account a non-uniform fluid temperature distribution along the wires. The development of the correlations in combination with the new fin efficiency calculation allows a very accurate and fast optimization of geometrical and operational quantities.

Several different wire structure heat exchangers were manufactured to address the third question. The focus in the chapter on manufacturing feasibility and performance measurement (Chapter 5) is on the three categories of micro-pin fins, continuous textile structures, and woven textile structures. For all samples, close cooperation with textile and heat exchanger manufacturers took place. Their assessment of the manufacturing feasibility is positive. The main limitation is the mechanical stability of the wire structures. The performance testing took place on two test facilities, one for heat exchanger surface area enhancements, the other one for water-to-air heat exchangers. A sufficiently accurate performance measurement could be realized on both facilities.

The overall question remains: What is the thermal-hydraulic performance potential of wire structures in flat-tube heat exchangers? Chapter 6 condenses the work done in the previous chapters. As a result, an estimation of the thermal-hydraulic performance potential of wire structures is given in terms of (i) essential geometric characteristics that are advantageous for wire structure heat exchangers, (ii) differences from that optimum of the manufactured geometries, and (iii) differences between the optimized wires structures and other types of surface enhancement.

Regarding the essential geometric characteristics (i), a specified value or a range of values for the geometric parameters is acquired in Section 6.1 to allow high efficiencies. The optimal geometric specifications are strongly dependent on the structure height H_{st}. An in-line arrangement is favorable and a longitudinal wire distance b should be in the order of 1.2 to achieve high energy and volume efficiencies. Both, the wire diameter and the lateral wire distance can not be limited to one specific value. They form dependent on the structure height, preferable combinations for high energy and volume efficiencies and other preferable combinations for high energy and mass efficiencies. The range of preferable wire diameters is $50\,\mu\mathrm{m} \leq d_{\mathrm{wire}} \leq 300\,\mu\mathrm{m}$. The lateral wire distance a should be in the order 12 to achieve high energy efficiencies and decreases to the lower boundary of 4 (specified in the feasibility sets) for high volume and mass efficiency.

Regarding the differences from simulated optimum to measurement (ii), the manufactured wire structure heat exchangers do not show the performance expected from the simulation. One possible explanation for this result is the inhomogeneity of the structure. A second explanation is the difference of the manufactured sample to the design idea in terms of wire arrangement. Especially the corrugated woven wire structures do not fulfill an in-line wire configuration due to auxiliary stability wires. A more accurate manufacturing is feasible; a reduction in the number of stability wires is challenging. The geometric parameters chosen for some samples already comply with the requirement for an optimal wire structure as part of a Pareto optimal set. Thus, an infeasibility of the optimal wire structure geometries is not given. The thermal-hydraulic performance potential is not limited by the manufacturing techniques.

Regarding lastly the differences between the optimized wires structures and other types of surface enhancement (iii), the wire structures have been compared to louvered fins and rectangular channels. The main statement is: The thermal-hydraulic performance potential for wire structures is higher than for

the reference surface enhancements when mass reduction plays a key role. The potential is equivalent or higher when a combination of volume and energy efficiency is considered for air velocities up to approximately 2.5 m/s. For higher velocities, the analyzed wire structure designs are not favorable.

As an outlook of this thesis, four more aspects of wire structure heat exchangers are considered, regarding costs, fouling, design, and alternative applications. A fifth aspect addresses the performance evaluation method.

Firstly, the cost is considered. Metal wire drawing (manufacturing of wires) is expensive. The factor in cost per kilogram between the wire and the raw material is equal to 3.6 for copper and a wire diameter of 100 µm. The factor increases strongly to a value of 40 when using aluminum. However, the factors decrease strongly for increasing wire diameters. In Appendix A.6, more details are given regarding the cost analysis. It can be assumed that possible material savings (high mass efficiency) will not compensate for the high costs of the material (and additional manufacturing).

Secondly, the concern that wire structures might be prone to particle fouling is addressed. Measurements of particle fouling on wire structures can relieve these concerns in part (see Appendix A.7). The main parameter influencing particle fouling is the fin pitch. For equal fin pitches, wire structures and louvered fins are expected to have similar tendencies for particle fouling. However, the analysis in Figure 6.10 showed that, for equal fin pitches, the benefits of the wire structure in terms of high energy and volume efficiency nearly vanish. Thus, applications with less risk of particle injection are preferable for wire structure heat exchangers, but wire structures are not limited to those applications.

Thirdly, the arrangement design of the wires in this thesis is basically limited to in-line and staggered arrangements, though additional work has been done on more flexible configurations. Especially for heat exchangers with non-symmetric in-flow and/or out-flow conditions, a more flexible configuration could be beneficial. Standard plate-fin heat exchangers with corrugated

metal sheets do not have this degree of freedom to allow a strong variation of geometry in flow direction.

Fourthly, the usage of the manufactured wire structures is not limited to applications with forced convection through the structure. Several alternative applications require large heat transfer surface areas per volume and mass. In the closed adsorption technology, coated heat exchangers ad- and desorb e.g. water in a cyclic operation. In the process the heat exchangers (thermal) mass is cycled as well, without a benefit. Wire structures might allow on the one hand large surface areas for possible coating and on the other hand low mass of the structure. Other applications which require a cycling of the heat exchanger between different temperatures, such as thermal storages (cf. [Asa19]) or open sorption (cf. [UGF+18]), could profit from wire structures as well. A further application is related to the usage of the surface area for evaporation or condensation.

Lastly, the dimensional and non-dimensional energy, volume, and mass efficiencies defined in Chapter 3 allow an extended evaluation of the surface enhancement. Dependent on the application, an estimation of the requirements regarding energy, volume, and mass savings could be developed in future. A combination of the efficiency plots with the application requirements could then allow a more precise statement on performance potential of a specific surface enhancement for a certain application. Such a combination has to take into account the limitation of the developed performance method on the surface enhancement structure. The energy, volume, and mass savings with respect to the heat exchanger itself are additionally dependent on the tube and manifold design. An extension of the performance method would be necessary.

Bibliography

[1] Vitruvius, *The Ten Books on Architecture: translated by Morris Hicky Morgan*. Cambridge: Harvard University Press, 1914. [Online]. Available: https://archive.org/stream/vitruviustenbook00vitruoft/vitruviustenbook00vitruoft_djvu.txt (visted on 2019-02-18).

[2] B. Roberts, "Heating & Ventilation," The Chartered Institution of Building Services Engineers, 2008. [Online]. Available: https://content.historicengland.org.uk/images-books/publications/heating-ventilation/heatingventilation.pdf/ (visited on 22.12.2018).

[3] K. M. Stone, "Review of Literature on Heat Transfer Enhancement in Compact Heat Exchangers," Air Conditioning & Refrigeration Center, Urbana, IL, U.S., 1996. [Online]. Available: https://www.ideals.illinois.edu/bitstream/2142/11540/2/TR105.pdf (visited on 05.11.2019).

[4] R. L. Webb, "Enhancement of Single-Phase Heat Transfer," in *Handbook of single-phase convective heat transfer*, S. Kakac, R. K. Shah, and W. Aung, Eds. New York, NY, U.S.: John Wiley and Sons Inc, 1987, pp. 17–1–62.

[5] J. Tian, T. Kim, T. J. Lu, H. P. Hodson, D. T. Queheillalt, D. J. Sypeck, and H. Wadley, "The effects of topology upon fluid-flow and heat-transfer within cellular copper structures," *International Journal of Heat and Mass Transfer*, vol. 47, no. 14-16, pp. 3171–3186, 2004, http://dx.doi.org/10.1016/j.ijheatmasstransfer.2004.02.010.

[6] K. Boomsma, D. Poulikakos, and F. Zwick, “Metal foams as compact high performance heat exchangers,” *Mechanics of Materials*, vol. 35, no. 12, pp. 1161–1176, 2003, http://dx.doi.org/10.1016/j.mechmat.2003.02.001.

[7] D. Girlich, “Grundsatzuntersuchungen zum Einsatz offenporiger Metallschäume in der Luft-, Kälte- und Wärmetechnik: Abschlussbericht,” M-Pore GmbH, Lindenberg, Germany, 2006, https://doi.org/10.2314/GBV:510544541.

[8] C. Hutter, D. Büchi, V. Zuber, and P. Rudolf von Rohr, “Heat transfer in metal foams and designed porous media,” *Chemical Engineering Science*, vol. 66, no. 17, pp. 3806–3814, 2011, http://dx.doi.org/10.1016/j.ces.2011.05.005.

[9] D. J. Sypeck and H. N. G. Wadley, “Multifunctional microtruss laminates: Textile synthesis and properties,” *Journal of Materials Research*, vol. 16, no. 03, pp. 890–897, 2001, http://dx.doi.org/10.1557/JMR.2001.0117.

[10] Verein Deutscher Ingenieure, *VDI-Wärmeatlas*, 11th ed. Berlin & Heidelberg, Germany: Springer Verlag, 2013.

[11] R. K. Shah and D. P. Sekulić, *Fundamentals of Heat Exchanger Design*, 1st ed. Hoboken, New Jersey, U.S.: John Wiley & Sons, 2003.

[12] ALPHA Company, “Heat Sink,” 2016. [Online]. Available: https://www.alphanovatech.com/en/index.html (visited on 05.11.2019).

[13] Y. Peles, A. Koşar, C. Mishra, C.-J. Kuo, and B. Schneider, “Forced convective heat transfer across a pin fin micro heat sink,” *International Journal of Heat and Mass Transfer*, vol. 48, no. 17, pp. 3615–3627, 2005, http://dx.doi.org/10.1016/j.ijheatmasstransfer.2005.03.017.

[14] J. Xu, J. Tian, T. J. Lu, and H. P. Hodson, "On the thermal performance of wire-screen meshes as heat exchanger material," *International Journal of Heat and Mass Transfer*, vol. 50, no. 5-6, pp. 1141–1154, 2007, http://dx.doi.org/10.1016/j.ijheatmasstransfer.2006.05.044.

[15] L. Zhao, S. M. Ryan, J. K. Ortega, S. Ha, K. W. Sharp, J. K. Guest, K. J. Hemker, and T. P. Weihs, "Experimental investigation of 3D woven Cu lattices for heat exchanger applications," *International Journal of Heat and Mass Transfer*, vol. 96, pp. 296–311, 2016, http://dx.doi.org/10.1016/j.ijheatmasstransfer.2015.12.059.

[16] J. Vicente, F. Topin, and J.-V. Daurelle, "Open Celled Material Structural Properties Measurement: From Morphology To Transport Properties," *Material Transactions*, vol. 47, no. 9, 2006, https://doi.org/10.2320/matertrans.47.2195.

[17] A. August, J. Ettrich, M. Rölle, S. Schmid, M. Berghoff, M. Selzer, and B. Nestler, "Prediction of heat conduction in open-cell foams via the diffuse interface representation of the phase-field method," *International Journal of Heat and Mass Transfer*, vol. 84, pp. 800–808, 2015, http://dx.doi.org/10.1016/j.ijheatmasstransfer.2015.01.052.

[18] T. Kim, C. Y. Zhao, T. J. Lu, and H. P. Hodson, "Convective heat dissipation with lattice-frame materials," *Mechanics of Materials*, vol. 36, no. 8, pp. 767–780, 2004, http://dx.doi.org/10.1016/j.mechmat.2003.07.001.

[19] Vision4Energy, "Wärmetauscher," 2016. [Online]. Available: http://www.vision4energy.com (visited on 05.10.2016).

[20] T. Yasutake and M. Watanabe, "Corrugated fin for heat exchanger," Japanese Patent JP7 324 884 A2, 1994.

[21] J. L. Johnson, “Metal Injection Molding Of Heat Sinks,” 2004. [Online]. Available: https://www.electronics-cooling.com/2004/11/metal-injection-molding-of-heat-sinks/ (visited on 05.11.2019).

[22] B. E. Short, P. E. Raad, and D. C. Price, “Performance of Pin Fin Cast Aluminum Coldwalls, Part 1: Friction Factor Correlations,” *Journal of thermophysics and heat transfer*, vol. 16, no. 3, pp. 389–396, 2002, http://dx.doi.org/10.2514/2.6692.

[23] G. Theoclitus, “Heat-Transfer and Flow-Friction Characteristics of Nine Pin-Fin Surfaces,” *Journal of Heat Transfer*, vol. 88, no. 4, p. 383, 1966, http://dx.doi.org/10.1115/1.3691583.

[24] H. Nabati, *Optimal pin fin heat exchanger surface*, ser. Mälardalen University Press Licentiate Theses. Västerås, Sveden: School of Sustainable development of Society and Technology, Mälardalen University, 2008, vol. 88.

[25] N. Sahiti, *Pin fin heat transfer surfaces: Thermal and fluid dynamic performance*. Saarbrücken, Germany: VDM Verlag Dr. Müller, 2008. [Online]. Available: https://fim.uni-pr.edu/Personeli/Personeli-akademik/Dr-sc--Naser-Sahiti.aspx (visited on 05.11.2019).

[26] M. Tahat, Z. Kodah, B. Jarrah, and S. Probert, “Heat transfers from pin-fin arrays experiencing forced convection,” *Applied Energy*, vol. 67, no. 4, p. 419 to 442, 2000, http://dx.doi.org/10.1016/S0306-2619(00)00032-5.

[27] Y. Liu, G. Xu, X. Luo, H. Li, and J. Ma, “An experimental investigation on fluid flow and heat transfer characteristics of sintered woven wire mesh structures,” *Applied Thermal Engineering*, vol. 80, pp. 118–126, 2015, http://dx.doi.org/10.1016/j.applthermaleng.2015.01.050.

[28] S. B. Prasad, J. S. Saini, and K. M. Singh, “Investigation of heat transfer and friction characteristics of packed bed solar air heater using wire

mesh as packing material," *Solar Energy*, vol. 83, no. 5, pp. 773–783, 2009, http://dx.doi.org/10.1016/j.solener.2008.11.011.

[29] C. Li and R. A. Wirtz, "High Performance Woven Mesh Heat Exchange," University of Nevada, Reno, Nevada, 2003. [Online]. Available: http://www.dtic.mil/dtic/tr/fulltext/u2/a414464.pdf (visited on 20.03.2015).

[30] E. van Andel, "Heat exchanger and method for manufacturing the same," European Patent EP0 714 500 B1, 1998.

[31] J. P. Bonestroo, "Calculation model of fine-wire heat exchanger," master's thesis, Twente University, Enschede, Netherlands, 2012.

[32] Air Preheater, "Envelope for a plate type heat exchanger," U.S. Patent US19 590 792 193, 1959.

[33] B. Berthome, F. Chauvet, S. Moreau, S. T. Valeo, H. Robidou, and Y. Yamamoto, "Heat exchanger and method for producing a heat exchange element for such a heat exchanger," French Patent FR20 060 008 235, 2006.

[34] A. Kumra, N. Rawal, and P. Samui, "Prediction of Heat Transfer Rate of a Wire-on-Tube Type Heat Exchanger: An Artificial Intelligence Approach," *Procedia Engineering*, vol. 64, pp. 74–83, 2013, http://dx.doi.org/10.1016/j.proeng.2013.09.078.

[35] T.-H. Lee, J.-Y. Yun, J.-S. Lee, J.-J. Park, and K.-S. Lee, "Determination of airside heat transfer coefficient on wire-on-tube type heat exchanger," *International Journal of Heat and Mass Transfer*, vol. 44, no. 9, pp. 1767–1776, 2001, http://dx.doi.org/10.1016/S0017-9310(00)00201-5.

[36] E. van Andel and E. van Andel, "Heat exchanger and applications thereof," U.S. Patent US7 963 067 B2, 2006.

[37] R. Balzer, "Wärmetauschvorrichtung für einen Wärmeaustausch zwischen Medien und Webstruktur," German Patent DE102 006 022 629 A1, 2006.

[38] J. Dong, J. Chen, Z. Chen, and Y. Zhou, "Air-side thermal hydraulic performance of offset strip fin aluminum heat exchangers," *Applied Thermal Engineering*, vol. 27, no. 2-3, pp. 306–313, 2007, http://dx.doi.org/10.1016/j.applthermaleng.2006.08.005.

[39] O. P. Bergelin, A. P. Colburn, and H. L. Hull, *Heat Transfer and Pressure Drop During Viscous Flow Across Unbaffled Tube Banks*. Newark, Delaware: University of Delaware. Engineering Experiment Station. Bulletin, 1950, vol. Bulletin No. 2.

[40] B. N. Rajani, A. Kandasamy, and S. Majumdas, "Numerical simulation of laminar flow past a circular cylinder," *Applied Mathematical Modelling*, vol. 33, no. 3, pp. 1228–1247, 2009, https://doi.org/10.1016/j.apm.2008.01.017.

[41] Verein Deutscher Ingenieure, *VDI-Wärmeatlas*, 9th ed. Berlin & Heidelberg, Germany: Springer-Verlag, 2002.

[42] D. Sucker and H. Brauer, "Stationärer Stoff- und Wärmeübergang an stationär quer angeströmten Zylindern," *Wärme- und Stoffübertragung*, vol. 9, 1976, http://dx.doi.org/10.1007/BF01465599.

[43] G. H. Jirka, *Einführung in die Hydromechanik*. Karlsruhe, Germany: Univ.-Verlag Karlsruhe, 2007, http://dx.doi.org/10.5445/KSP/1000007165.

[44] M. Coutanceau and R. Bouard, "Experimental determination of the main features of the viscous flow in the wake of a circular cylinder in uniform translation. Part 1. Steady flow," *Journal of Fluid Mechanics*, vol. 79, no. 02, p. 231, 1977, http://dx.doi.org/10.1017/S0022112077000135.

[45] N. Sahiti, "Thermal and Fluid Dynamic Performance of Pin Fin Heat Transfer Surfaces," PhD Thesis, Friedrich-Alexander Universität, Erlangen-Nürnberg, 2006, https://opus4.kobv.de/opus4-fau/frontdoor/index/index/docId/242 (visited on 05.11.2019).

[46] V. Gnielinski, "Gleichungen zur Berechnung des Wärmeübergangs in querdurchströmten einzelnen Rohrreihen und Rohrbündeln," *Forschung im Ingenieurwesen A*, vol. 44, no. 1, pp. 15–25, 1978, http://dx.doi.org/10.1007/BF02560750.

[47] H. N. Fairchild and C. P. Welch, "Convection heat transfer and pressure drop of air flowing across in-line tube banks at close back spacings," in *ASME Annual Meeting*, ASME, Ed., New York, NY, U.S., 1961.

[48] D. Bacellar, V. Aute, Z. Huang, and R. Radermacher, "Airside friction and heat transfer characteristics for staggered tube bundle in cross-flow configuration with diameters from 0.5mm to 2.0mm," *International Journal of Heat and Mass Transfer*, vol. 98, pp. 448–454, 2016, http://dx.doi.org/10.1016/j.ijheatmasstransfer.2016.02.072.

[49] D. Bacellar, V. C. Aute, and R. Radermacher, "Airside Performance Correlations and Optimal Heat Pump Heat Exchanger Designs Based on 0.5mm-2mm Finless Round Tube Bundles," in *International Refrigeration and Air Conditioning Conference, 2016*, Purdue University, 2016, http://docs.lib.purdue.edu/iracc/1611 (visited on 04.11.2019).

[50] D. Bacellar, "CFD-Based Correlation Development For Air Side Performance Of Finned And Finless Tube Heat Exchangers With Small Diameter Tubes," in *International Refrigeration and Air Conditioning Conference, 2014*, Purdue University, 2014, http://docs.lib.purdue.edu/iracc/1410 (visited on 15.09.2018).

[51] R. Radermacher, D. Bacellar, V. Aute, Z. Huang, Y. Hwang, J. Ling, J. Muehlbauer, J. Tancabel, O. Abdelaziz, and M. Zhang, "Miniaturized

Air-to-Refrigerant Heat Exchangers," Center for Environmental Energy Engineering Department of Mechanical Engineering, University of Maryland, Maryland, US, 2017, http://dx.doi.org/10.2172/1358252.

[52] P. G. LaHaye, F. J. Neugebauer, and R. K. Sakhuja, "A Generalized Prediction of Heat Transfer Surfaces," *Journal of Heat Transfer*, vol. 96, no. 4, p. 511, 1974, http://dx.doi.org/10.1115/1.3450237.

[53] R. L. Webb, "Goodness factor comparisons," in *HEDH Multimedia*. Begell House, 2014, http://hedhme.com/content_map/?link_id=17260&article_id=302 (visited on 05.11.2019).

[54] R. L. Webb and N.-H. Kim, *Principle of Enhanced Heat Transfer*. New York, NY, U.S.: Taylor & Francis, 1994.

[55] J. G. Soland, "Performance ranking of plate-finned heat exchanger surfaces." Dissertation, Massachusetts Institute of Technology, Cambridge, 1975, http://hdl.handle.net/10945/20982 (visited on 20.10.2019).

[56] T. A. Cowell, "Comparison of Compact Heat Transfer Surfaces," *Journal of Heat Transfer*, vol. 112:2, 1990. [Online]. Available: http://www.osti.gov/scitech/biblio/6018589 (visited on 04.11.2019).

[57] N. Sahiti, F. Durst, and A. Dewan, "Strategy for selection of elements for heat transfer enhancement," *International Journal of Heat and Mass Transfer*, vol. 49, no. 19-20, pp. 3392–3400, 2006, http://dx.doi.org/10.1016/j.ijheatmasstransfer.2006.03.011.

[58] Q. Li, G. Flamant, X. Yuan, P. Neveu, and L. Luo, "Compact heat exchangers: A review and future applications for a new generation of high temperature solar receivers," *Renewable and Sustainable Energy Reviews*, vol. 15, no. 9, pp. 4855–4875, 2011, http://dx.doi.org/10.1016/j.rser.2011.07.066.

[59] J. E. Marthinuss, "Air Cooled Compact Heat Exchanger Design For Electronics Cooling," 2004. [Online]. Available: https://www.electronics-cooling.com/2004/02/air-cooled-compact-heat-exchanger-design-for-electronics-cooling/ (visited on 20.10.2019).

[60] P. Korhonen and J. Wallenius, "Visualization in the Multiple Objective Decision-Making Framework," in *Multiobjective Optimization. Lecture Notes in Computer Science*, J. Branke, K. Deb, K. Miettinen, and R. Słowiński, Eds. Berlin & Heidelberg, Germany: Springer-Verlag, 2008, https://doi.org/10.1007/978-3-540-88908-3_8.

[61] K. Miettinen and M. M. Mäkelä, "On scalarizing functions in multiobjective optimization," *OR Spectrum*, vol. 24, no. 2, pp. 193–213, 2001. [Online]. Available: https://link.springer.com/content/pdf/10.1007%2Fs00291-001-0092-9.pdf (visited on 20.10.2019).

[62] M.-H. Kim and C. W. Bullard, "Air-side thermal hydraulic performance of multi-louvered fin aluminum heat exchangers," *International Journal of Refrigeration*, vol. 25, no. 3, pp. 390–400, 2002, http://dx.doi.org/10.1016/S0140-7007(01)00025-1.

[63] R. M. Manglik and A. E. Bergles, "Heat transfer and pressure drop correlations for the rectangular offset strip fin compact heat exchanger," *Experimental Thermal and Fluid Science*, vol. 10, no. 2, pp. 171–180, 1995, http://dx.doi.org/10.1016/0894-1777(94)00096-Q.

[64] J. Dong, J. Chen, Z. Chen, W. Zhang, and Y. Zhou, "Heat transfer and pressure drop correlations for the multi-louvered fin compact heat exchangers," *Energy Conversion and Management*, vol. 48, no. 5, pp. 1506–1515, 2007, http://dx.doi.org/10.1016/j.enconman.2006.11.023.

[65] S. P. Mahulikar and H. Herwig, "Fluid friction in incompressible laminar convection: Reynolds' analogy revisited for variable fluid proper-

ties," *The European Physical Journal B*, vol. 62, no. 1, pp. 77–86, 2008, http://dx.doi.org/10.1140/epjb/e2008-00115-0.

[66] Z. S. Spakovszky and R. Moore, "Notes on Thermodynamics and Propulsion," 1999. [Online]. Available: https://web.mit.edu/16.unified/www/FALL/thermodynamics/notes/node122.html (visited on 20.10.2019).

[67] P. von Böckh and T. Wetzel, *Heat Transfer*. Berlin, Heidelberg: Springer-Verlag, 2012. [Online]. Available: http://link.springer.com/10.1007/978-3-642-19183-1 (visited on 04.11.2019).

[68] R. K. Shah and London, A. L., *Laminar flow forced convection in ducts: A source book for compact heat exchanger analytical data*, ser. Advances in heat transfer : Supplement. New York. U.S.: Academic Press, 1978, vol. 1.

[69] I. B. Celik, U. Ghia, Roache, Patrick J., Freitas, Christopher J., H. Coleman, and P. E. Raad, "Procedure for Estimation and Reporting of Uncertainty Due to Discretization in CFD Applications," *Journal of Fluids Engineering*, vol. 130, no. 7, pp. 078 001 (1–4), 2008, http://dx.doi.org/10.1115/1.2960953.

[70] B. Zohuri, *Compact Heat Exchangers: Selection, Application, Design and Evaluation*, 1st ed. Cham, Switzerland: Springer International Publishing, 2017, http://dx.doi.org/10.1007/978-3-319-29835-1.

[71] H. Herwig and B. Schmandt, "Drag with external and pressure drop with internal flows: A new and unifying look at losses in the flow field based on the second law of thermodynamics," *Fluid Dynamics Research*, vol. 45, no. 5, 2013, http://dx.doi.org/10.1088/0169-5983/45/5/055507.

[72] H. Herwig, “Determination of Conduit Component Loss Coefficients Based on the Second Law of Thermodynamics,” in *23rd. Int. Symp. on Transport Phenomena*, Auckland, New Zealand, 2012.

[73] Kays, W. M. and London, A. L., *Compact Heat Exchangers*, 3rd ed. University of Michigan, U.S.: Krieger Publishing Company, 1984.

[74] H. Kang, “Evaluation of Fin Efficiency and Heat Transfer Coefficient for Fined Tube Heat Exchange,” in *International Refrigeration and Air Conditioning Conference*, Purdue University, 2012, http://docs.lib.purdue.edu/iracc/1338 (visited on 29.03.18).

[75] Normenausschuß Heiz- und Raumlufttechnik, “Wärmeaustauscher - Messungen und Meßgenauigkeit bei der Leistungsbestimmung, Norm, EN 306 : 1997,” Beuth Verlag GmbH, Berlin, Germany, 1997.

[76] S. J. Petroski, “An investigation of the performance of confined, saw-tooth shaped wire-on-tube condensers,” Air Conditioning and Refrigeration Center, Urbana, IL, U.S., 1999. [Online]. Available: https://www.ideals.illinois.edu/handle/2142/11901 (visited on 04.11.2019).

[77] M. Niemeyer, “Planung, Auslegung und Aufbau eines Prüfstands zur Charakterisierung von kompakten Wärmeübertragerstrukturen, basierend auf Gewebe zur Oberflächenvergrößerung,” master’s thesis, Fraunhofer Institute for Solar Energy Systems and Technische Universität Berlin, Berlin, 2015.

[78] A. Sauter, “ProX™ 400 Production 3D Printer,” 2018. [Online]. Available: https://arnd-sauter.de/prox-400/ (visited on 04.11.2019).

[79] R. Rezaey, F. Loosmann, S. Chandra, and C. Tropea, “Conduction Heat Transfer Investigation of Laser Sintered Heat Exchangers,” in *Proceedings of The Canadian Society for Mechanical Engineering International Congress*, Toronto, Canada, 2014.

[80] L. Schnabel, F. Roell, K. Hattler, T. Studnitzky, E. Laurenz, and S. Kaina, "Energieeffiziente Wärmeübertragung durch 3D-Metallgewebestrukturen (EffiMet): Gemeinsamer Abschlussbericht: 10.2314/GBV:835139093," TIB - Technische Informationsbibliothek Universitätsbibliothek Hannover, 2015. [Online]. Available: https://www.tib.eu/suchen/id/TIBKAT:835139093/ (visited on 05.11.2019).

[81] Normenausschuss Technische Grundlagen, "Guide to the Expression of Uncertainty in Measurement, Norm, DIN V ENV 13005," Beuth Verlag GmbH, Berlin, Germany, 1999.

[82] C.-S. Tsou, "NSGA2: Elitist Non-dominated Sorting Genetic Algorithm based on R," 2013. [Online]. Available: https://www.rdocumentation.org/packages/mco/versions/1.0-15.1/topics/nsga2 (visited on 05.11.2019).

[83] Y. Yang and Y. Li, "General prediction of the thermal hydraulic performance for plate-fin heat exchanger with offset strip fins," *International Journal of Heat and Mass Transfer*, vol. 78, pp. 860–870, 2014, http://dx.doi.org/10.1016/j.ijheatmasstransfer.2014.07.060.

[84] J. Dong, J. Chen, Z. Chen, Y. Zhou, and W. Zhang, "Heat transfer and pressure drop correlations for the wavy fin and flat tube heat exchangers," *Applied Thermal Engineering*, vol. 27, no. 11-12, pp. 2066–2073, 2007, http://dx.doi.org/10.1016/j.applthermaleng.2006.11.012.

[85] J. Dong, L. Su, Q. Chen, and W. Xu, "Experimental study on thermal–hydraulic performance of a wavy fin-and-flat tube aluminum heat exchanger," *Applied Thermal Engineering*, vol. 51, no. 1-2, pp. 32–39, 2013, http://dx.doi.org/10.1016/j.applthermaleng.2012.09.018.

[86] M. Khoshvaght Aliabadi, F. Hormozi, and E. Hosseini Rad, "New correlations for wavy plate-fin heat exchangers: Different working fluids," *International Journal of Numerical Methods for Heat & Fluid Flow*,

vol. 24, no. 5, pp. 1086–1108, 2014, http://dx.doi.org/10.1108/HFF-09-2012-0195.

[87] G. Cicala, L. Cirillo, A. Diana, O. Manca, and S. Nardini, "Experimental Evaluation of Fluid Dynamic and Thermal Behaviors in Compact Heat Exchanger with Aluminum Foam," *Energy Procedia*, vol. 101, pp. 1103–1110, 2016, http://dx.doi.org/10.1016/j.egypro.2016.11.150.

[88] P. Böckh and T. Wetzel, *Wärmeübertragung: Grundlagen und Praxis*, 7th ed., ser. Lehrbuch. Berlin, Germany: Springer Vieweg, 2017.

[89] I. H. Bell and E. A. Groll, "Air-side particulate fouling of microchannel heat exchangers: Experimental comparison of air-side pressure drop and heat transfer with plate-fin heat exchanger," *Applied Thermal Engineering*, vol. 31, no. 5, pp. 742–749, 2011, https://doi.org/10.1016/j.applthermaleng.2010.10.019.

Conference Contributions and Publications

[BFS17] Richard Balzer, Hannes Fugmann, and Lena Schnabel. Wire Cloth Micro Heat Exchanger with High Pressure Stability. In H. Krüssmann, editor, *Compact Heat Exchangers: Designs, Materials and Applications*. PP PUBLICO Publications, 2017. http://publica.fraunhofer.de/documents/N-525497.html (visited on 05.11.2019).

[FDS16] Hannes Fugmann, Paolo Di Lauro, and Lena Schnabel. Heat Transfer Surface Area Enlargement by Usage of Metal Textile Structures – Development, Potential and Evaluation. In *International Textile Conference*, 2016. http://publica.fraunhofer.de/documents/N-458875.html (visited on 04.11.2019).

[FDSS18] Hannes Fugmann, Paolo Di Lauro, Aniket Sawant, and Lena Schnabel. Development of Heat Transfer Surface Area Enhancements: A Test Facility for New Heat Exchanger Designs. *Energies*, 11(5):1322, 2018. http://dx.doi.org/10.3390/en11051322.

[FGS19] Hannes Fugmann, Sebastian Gamisch, and Lena Schnabel. Efficiency of Micro Pin Fin Heat Exchangers with Non-Uniform Temperature Profile of Ambient Fluid. *to be sumitted to Energies*, 2019.

[FLS17] Hannes Fugmann, Eric Laurenz, and Lena Schnabel. Wire Structure Heat Exchangers—New Designs for Efficient Heat Transfer.

Energies, 10(9):1341, 2017. http://dx.doi.org/10.3390/en10091341.

[FLS19] Hannes Fugmann, Eric Laurenz, and Lena Schnabel. Multi-Dimensional Performance Evaluation of Heat Exchanger Surface Enhancements. *Energies*, 12(7):1406, 2019. http://dx.doi.org/10.3390/en12071406.

[FMS+19] Hannes Fugmann, Sebastian Martens, Lena Schnabel, Carsten Mehring, Richard Balzer, and Martin Brenner. Performance Evaluation of Wire Cloth Micro Heat Exchangers. *to be sumitted to Energies*, 2019.

[FNT+15] Hannes Fugmann, Björn Nienborg, Gregor Trommler, Antoine Dalibard, and Lena Schnabel. Performance Evaluation of Air-Based Heat Rejection Systems. *Energies*, 8(2):714–741, 2015. http://dx.doi.org/10.3390/en8020714.

[FOS17] Hannes Fugmann, Thore Oltersdorf, and Lena Schnabel. Metal Wire Structures as Heat Transfer Surface Area Enlargement – Design Study and Potential Analysis for Air-to-Water Heat Pumps. *12th IEA Heat Pump Conference 2017, Rotterdam*, 2017. http://hpc2017.org/wp-content/uploads/2017/05/0.4.8.1-Metal-Wire-Structures-as-Heat-Transfer-Surface-Area-Enlargement.pdf (visited on 08.10.2019).

[FSD16] Hannes Fugmann, Lena Schnabel, and Paolo Di Lauro. Performance Evaluation of Heat Transfer Surface Area Enlargement by Usage of Metal Wire Structures, Presentation. In *4. International Symposium on Innvative Materials for Processes in Energy Systems*, Taormina, Italy, 2016.

[FSF19] Hannes Fugmann, Lena Schnabel, and Bettina Frohnapfel. Heat Transfer and Pressure Drop Correlations for Laminar Flow in an

In-line and Staggered Array of Circular Cylinders. *Numerical Heat Transfer, Part A: Applications*, 2019. http://dx.doi.org/10.1080/10407782.2018.1562741.

[FTNS15] Hannes Fugmann, Ahmed Junaid Tahir, Björn Nienborg, and Lena Schnabel. Gas-Flüssig-Wärmeübertrager aus fluidführenden Gewebematten. In *DKV-Tagungsbericht*, Dresden, Germany, 2015. http://publica.fraunhofer.de/documents/N-382844.html (visted on 17.02.2016).

[FTNS16] Hannes Fugmann, Ahmed Junaid Tahir, Björn Nienborg, and Lena Schnabel. Drahtgewebebasierte Wärmeübertrager: Entwicklung und Bewertung. *KI Kälte-Luft-Klimatechnik*, 6-7, 2016.

[FTS15] Hannes Fugmann, Ahmed Junaid Tahir, and Lena Schnabel. Woven Wire Gas-To-Liquid Heat Exchanger. In *World Congress on Mechanical, Chemical and Material Engineering*, Ottawa, Ontario, Canada, 2015. Avestia Publishing, International ASET Inc. http://avestia.com/MCM2015_Proceedings/files/papers/HTFF314.pdf (visited on 04.11.2019).

[Fug18] Hannes Fugmann. MinWaterCSP Project: Deliverables WP4 on Wire Structures, 2018. https://www.minwatercsp.eu/ (visited on 04.11.2019).

[Min18] MinWaterCSP Project. Cooling Systems: Wire structure heat transfer surfaces, 2018. https://www.minwatercsp.eu/technologies/cooling-systems/ (visited on 04.11.2019).

[NFSS13] Björn Nienborg, Hannes Fugmann, Lena Schnabel, and Peter Schossig. Performance figures for the analysis of heat rejection systems. In *5th International Conference Solar Air-conditioning*, Bad Krozingen, Germany, 2013.

[SLF+14] Lena Schnabel, Eric Laurenz, Hannes Fugmann, Steffen Kaina, and Thomas Studnitzky. Wärmeübertragungsvorrichtung und deren Verwendung, German Patent DE102014208955, 2014.

[UGF+18] Turkan Ucok Erkek, Ali Gungor, Hannes Fugmann, Alexander Morgenstern, and Constanze Bongs. Performance Evaluation of a Desiccant Coated Heat Exchanger with Two Different Desiccant Materials. *Applied Thermal Engineering*, 143:701–710, 2018. http://dx.doi.org/10.1016/j.applthermaleng.2018.06.012.

The conference contributions and publications [FNT+15, FTNS16, NFSS13, FTNS15, FSD16, FMS+19] are related to performance evaluation or wire structure heat exchanger development, but are not mentioned in the thesis. For the sake of completeness they have been added in the list above.

Supervised Students' Theses

[Alt18] Mareike Altenberend. *Entwicklung eines Versuchsstandes zur Charakterisierung von Drahtstrukturwärmeübertragern bei gasseitigem Partikelfouling*. master's thesis, Fraunhofer Institute for Solar Energy Systems and Universität Stuttgart, Stuttgart, 2018.

[Asa19] Nasir Asadov. *Simulation and Measurement of Different Geometries and Materials for Heat Exchangers in Decentralized Compact Ventilation Systems with Heat Recovery*. master's thesis, Fraunhofer Institute for Solar Energy Systems and Albert-Ludwigs-Universität Freiburg, Freiburg, 2019.

[Car18] Danny Alejandro Carvajal Puche. *Improvement of a Test Facility for Performing the Thermo-hydraulic Characterization of Compact Heat Transfer Enhancement Surfaces*. master's thesis, Fraunhofer Institute for Solar Energy Systems and Hochschule Offenburg, Offenburg, 2018.

[Mad16] Paula Camilla Madariaga Escobar. *Experimenteller Vergleich des Druckverlusts und der Wärmeübertragung einer Drahtstruktur mit einer Lamellenstruktur zur Oberflächenvergrößerung eines Wärmeübertragers*. bachelor's thesis, Fraunhofer Institute for Solar Energy Systems and Hochschule für Angewandte Wissenschaften Hamburg, Hamburg, 2016.

[Rin17] Juan Pablo Rincon Duarte. *Characterization of a Novel Heat Exchanger Design with Woven Metallic Wire Structure*. master's the-

sis, Fraunhofer Institute for Solar Energy Systems and Technische Universität Berlin, Berlin, 2017.

[Saw16] Aniket Sawant. *Numerical Simulation and Experimental Characterization of Heat Transfer and Flow within Metal Wire Heat Exchanger Structures*. master's thesis, Fraunhofer Institute for Solar Energy Systems and Hochschule Offenburg, Offenburg, 2016.

[Tah15] Ahmed Junaid Tahir. *Numerical Simulation and Experimentation of Woven Wire Gas to Liquid Heat Exchangers*. master's thesis, Fraunhofer Institute for Solar Energy Systems and Technische Universität München, München, 2015.

Nomenclature

Reynolds and Nusselt numbers

SYMBOL	SI UNIT	DESCRIPTION
Re_{st}	–	Reynolds number based on v_{st} and d_{st}
$Re_{st,d}$	–	Reynolds number based on v_{st} and specified d
$Re_{st,ma}$	–	Reynolds number based on v_{st} and specified d_{ma}
$Re_{st,mi}$	–	Reynolds number based on v_{st} and specified d_{mi}
Re_{water}	–	Reynolds number based on v_{water} and d_{water}
Nu_{st}	–	Nusselt number based on h_{st} and d_{st}
Nu_{water}	–	Nusselt number based on h_{water} and d_{water}
Nu_{air}	–	Nusselt number based on h_{air}, d_{st} and $k_{air,st}$
$Nu_{air,d}$	–	Nusselt number based on h_{air} and specified d
Nu_{st,y^*}	–	Nusselt number based on h_{st} and d_{st} for a non-dimensional flow length y^*
$Nu_{st,local,y^*}$	–	local Nusselt number based on h_{st} and d_{st} at the non-dimensional flow length y^* position

Latin letters – Upper case

SYMBOL	SI UNIT	DESCRIPTION
A_{HTS}	m^2	heat transfer surface area of primary and secondary surface on the air side
$A_{HTS,water}$	m^2	heat transfer surface area on the water side
A_{st}	m^2	heat transfer surface area of secondary structure surface on the air side
A_{wall}	m^2	heat transfer surface area on the wall
$A_{in,st}$	m^2	free-flow area at the inlet of the structure volume
A_{in}	m^2	free-flow area at the channel before the heat exchanger
A_p	m^2	heat transfer surface area of primary surface on the air side
Br	–	Brinkman number (see Eq. (3.5))
C	–	auxiliary coefficients
F	–	correction factor for flow configuration
G_{st}	kg/s	core structure mass velocity
H_{st}	m	height of structure
K_c	–	contraction loss coefficient
K_e	–	exit loss coefficient
L_{st}	m	length of structure
L^*_{hy}	–	non-dimensional hydraulic entrance length (see Eq. (A.25))
L^*_{th}	–	non-dimensional thermal entrance length (see Eq. (4.6))
Pr_{air}	–	Prandtl number
P_{diss}	W	dissipated power based on Δp_{st} and $\dot{V}_{air,st}$

$\dot{Q}$	W	heat transfer rate
$\dot{Q}_{\mathrm{HX}}$	W	heat transfer rate within the heat exchanger
T	K	temperature
$T_{\mathrm{air,in}}$	K	inlet air temperature at heat exchanger
U	$\mathrm{W/(m^2\,K)}$	overall heat transfer coefficient
$U_{\mathrm{air,eff}}$	$\mathrm{W/(m^2\,K)}$	effective heat transfer coefficient on the air side including heat conduction through fins
V	$\mathrm{m^3}$	volume
V_{st}	$\mathrm{m^3}$	available volume for structure between tubes or plates
$V_{\mathrm{st,mat}}$	$\mathrm{m^3}$	volume of solid part of structure without the air volume
$\dot{V}$	$\mathrm{m^3/s}$	volume flow rate
$\dot{V}_{\mathrm{air,st}}$	$\mathrm{m^3/s}$	volume flow rate based on $\rho_{\mathrm{air,st}}$ and $\dot{m}_{\mathrm{air}}$
W	m	width

Latin letters – Lower case

SYMBOL	SI UNIT	DESCRIPTION
a	–	non-dimensional lateral wire or fin distance based on d_{st} and l_{lateral}
b	–	non-dimensional longitudinal wire distance based on d_{st} and $l_{\mathrm{longitudinal}}$
c	–	non-dimensional height of structure based on d_{st} and H_{st}
c_{d}	–	drag coefficient
c_p	$\mathrm{J/(kg\,K)}$	specific heat capacity
$c_{p,\mathrm{air}}$	$\mathrm{J/(kg\,K)}$	specific heat capacity of air

$c_{p,\text{water}}$	$\mathrm{J/(kg\,K)}$	specific heat capacity of water
d	m	characteristic diameter
d_{st}	m	characteristic diameter for structure (equals d_{wire} for wire structure)
d_{water}	m	characteristic diameter for water side (equals d_{tube} for round tubes)
f_{st}	–	Fanning friction factor based on Δp_{HX}, L_{st}, d_{st}, v_{st}, and corrected with K_c and K_e
h_{st}	$\mathrm{W/(m^2\,K)}$	air side convective heat transfer coefficient based on secondary structure surface A_{st} only
h_{air}	$\mathrm{W/(m^2\,K)}$	air side convective heat transfer coefficient based on secondary surface A_{st} and primary surface A_{p}
j	–	Colburn factor $h\mathrm{Pr}^{2/3}/(G_{\text{st}}c_p)$
k	$\mathrm{W/(m\,K)}$	thermal conductivity
k_{wall}	$\mathrm{W/(m\,K)}$	thermal conductivity of the wall material
k_{st}	$\mathrm{W/(m\,K)}$	thermal conductivity of solid material used for structure
$k_{\text{air,st}}$	$\mathrm{W/(m\,K)}$	mean thermal conductivity of air within the structure
l	m	half the fin length; used for fin efficiency calculation (see Eq. (2.26))
l_{lateral}	m	lateral distance (pitch) of wires or fins
$l_{\text{longitudinal}}$	m	longitudinal distance of wires
m		auxiliary variable used for fin efficiency calculation (see Eq. (2.26))
m_{st}	kg	mass of the structure
$\dot{m}_{\text{air}}$	kg/s	mass flow rate of air
n_{wires}	–	number of wire rows

n_{tubes}	–	number of tubes
ntu	–	number of transfer units (see Eq. (2.23))
p	Pa	pressure
p_{mesh}	–	order of convergence
r_{mesh}	–	grid refinement ratio
s	m	tube pitch
$\mathbf{u}$	m/s	velocity vector field
u_{c}	variable	combined uncertainty
v_{st}	m/s	superficial structure air velocity based on $A_{\text{in,st}}$ and $\rho_{\text{air,st}}$
v_{water}	m/s	water velocity based on $A_{\text{in,tube}}$ and ρ_{water}
$v_{\text{air,in}}$	m/s	air velocity based on A_{in} and $\rho_{\text{air,in}}$
y^*	–	non-dimensional flow length based on y, d_{st}, and b

Greek letters – Upper case

SYMBOL	SI UNIT	DESCRIPTION
Θ	–	feasibility set
ΔT	K	temperature difference
ΔT_{water}	K	temperature difference between the water inlet and outlet
ΔT_{air}	K	temperature difference between the air inlet and outlet
ΔT_{log}	K	logarithmic temperature difference between two domains
ΔT_{m}	K	mean temperature difference between two domains
Δp_{HX}	Pa	pressure drop associated with a heat exchanger

Δp_{st}	Pa	pressure drop within the core structure
Δp_{in}	Pa	pressure drop at the core entrance
Δp_{out}	Pa	pressure rise at the core exit

Greek letters – Lower case

SYMBOL	SI UNIT	DESCRIPTION
α	–	auxiliary coefficient (see Eq. (A.13))
β	m^2/m^3	heat transfer surface area density based on A_{HTS} and V_{st} (see Eq. (3.2))
β_{st}	m^2/m^3	heat transfer surface area density based on A_{st} and V_{st}
δ_{wall}	m	wall thickness
θ	–	feasible decision
ϵ	–	dimensional efficiency (see Tab. 3.2)
ϵ^*	–	non-dimensional efficiency (see Tab. 3.3)
ϵ_{air}	–	air-side effectiveness (see Eq. (2.24))
κ	–	product of m and l; used for fin efficiency calculation (see Eq. (2.28))
μ	Pa s	dynamic viscosity
ν	m^2/s	kinematic viscosity
$\nu_{air,st}$	m^2/s	mean kinematic air viscosity within the structure
ρ	kg/m^3	density
$\rho_{air,st}$	kg/m^3	mean air density within the structure
$\rho_{air,in}$	kg/m^3	air density at the inlet of the heat exchanger
$\rho_{air,out}$	kg/m^3	air density at the outlet of the heat exchanger
ρ_{water}	kg/m^3	mean water density within the tube
ρ_{st}	kg/m^3	density of solid material used for structure

φ_{st}	–	porosity of structure based on $V_{st,mat}$ and V_{st} (see Eq. (3.3))
η_{fin}	–	fin efficiency
$\eta_{fin,uT}$	–	fin efficiency based on uniform temperature profile of ambient fluid
$\eta_{fin,nuT}$	–	fin efficiency based on non-uniform temperature profile of ambient fluid (see Eq. (4.18))
$\eta_{fin,sim}$	–	fin efficiency based on 3D simulation results
η_0	–	extended surface efficiency
σ	–	ratio of core structure to heat exchanger free-flow area
$\chi_{wall,st}$	–	ratio of thermal conductivity of the tube wall k_{wall} versus the structure k_{st}
$\chi_{st,air}$	–	ratio of thermal conductivity of the structure k_{st} versus the air $k_{air,st}$

Mathematical operators

SYMBOL	DESCRIPTION
$\partial(\dots)$	partial derivative
$(\dots)\cdot\nabla$	convective operator
$\nabla\cdot(\dots)$	divergence operator
$\nabla(\dots)$	gradient
$\Delta(\dots)$	Laplace operator

Abbreviations

SYMBOL	DESCRIPTION
1D	one-dimensional
2D	two-dimensional
3D	three-dimensional
AS	assumption
CAD	computer-aided design
eff	effective
GCI	grid convergence index
HTS	heat transfer surface
HVAC	heating, cooling and air-conditioning
HX	heat exchanger
HXelm	heat exchanger element
in	inlet
m	mean
nuT	non-uniform temperature profile
out	outlet
saplt	sample plate
st	structure
TS	testing structure

List of Figures

List of Tables

A Appendix

A.1 Performance Evaluation

A.1.1 Transformation from Dimensional to Non-Dimensional Key Figures

Assuming Equation (3.1) holds for the heat transfer rate, then the volume-specific heat transfer rate can be expressed as

$$\frac{\dot{Q}}{V_{\mathrm{st}}} = \underbrace{\frac{v_{\mathrm{st}}^2 k_{\mathrm{air,st}} \Delta T_{\mathrm{m}}}{\nu_{\mathrm{air,st}}^2}}_{\text{driving}} \epsilon_V \underbrace{\frac{\nu_{\mathrm{air,st}}^2}{v_{\mathrm{st}}^2 k_{\mathrm{air,st}}}}_{\epsilon_V^*} . \tag{A.1}$$

The first term on the right hand side is a driving parameter, equal for comparable heat exchangers based on the restrictions R1 to R5, for constant structure frontal area. The second term represents the non-dimensional volume efficiency ϵ_V^*. Similarly, the mass-specific heat transfer rate can be expressed as

$$\frac{\dot{Q}}{m_{\mathrm{st}}} = \underbrace{\frac{v_{\mathrm{st}}^2 k_{\mathrm{air,st}} \Delta T_{\mathrm{m}}}{\rho_{\mathrm{air,st}} \nu_{\mathrm{air,st}}^2}}_{\text{driving}} \epsilon_M \underbrace{\frac{\rho_{\mathrm{air,st}} \nu_{\mathrm{air,st}}^2}{v_{\mathrm{st}}^2 k_{\mathrm{air,st}}}}_{\epsilon_M^*} . \tag{A.2}$$

The non-dimensional mass efficiency ϵ_M^* is the variable term on the right side of the equation.

A.1.2 Exemplary Heat Transfer Surface Enhancements

Two surface enhancements are used exemplarily in Section 3.2.3 besides the wire structures. They are presented here. The information is based on [FLS19].

Louvered Fins

The louvered fin geometry and performance correlation are taken from Kim et al. [62]. The geometry is shown in Figure A.1; the detailed definitions of parameter values are given in Table A.1.

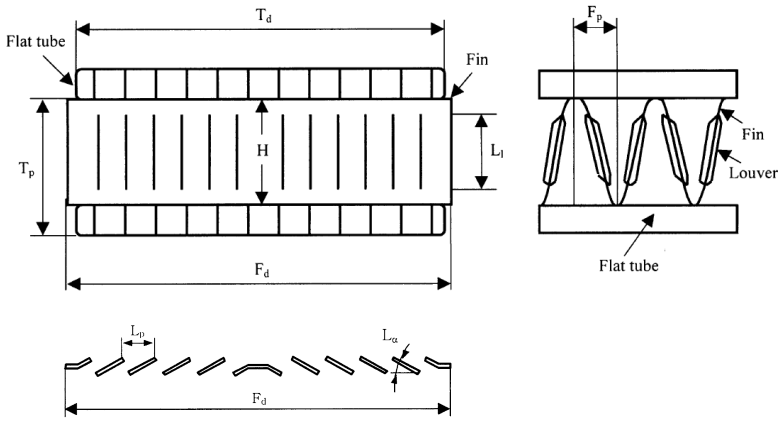

Figure A.1: Definition of geometrical parameters for a multi-louvered fin heat exchanger; based on [62] and [FLS19].

Offset Strip Fins

The offset strip fin geometry and performance correlation are taken from Manglik et al. [63]. The geometry is shown in Figure A.2; the detailed definitions of parameter values are given in Table A.2.

Parameter definition in [62]	**Parameter definition in this Study**	**Dimension**	**Value**
F_p	$l_{lateral}$	mm	2.29
L_p	$l_{longitudinal}$	mm	4.76
δ_f	d_{st}	µm	152
F_d	L_{st}	mm	48
H	H_{st}	mm	10
L_l	-	mm	9
L_α	-	°	28
T_p	-	mm	12

Table A.1: Geometrical Parameters of the louvered fin heat exchanger used in Chapter 3.2.3 with nomenclature from [62] and nomenclature used within this study; based on [FLS19].

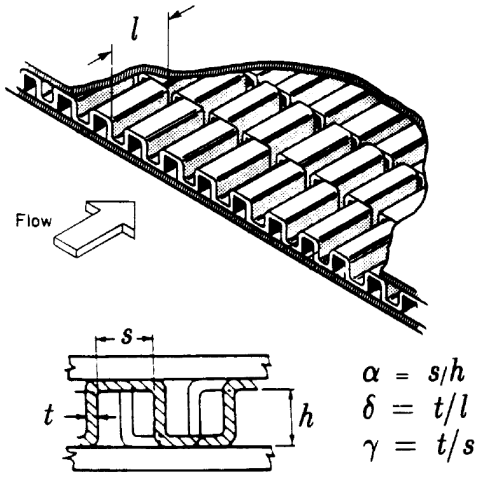

Figure A.2: Definition of geometrical parameters for an offset strip fin heat exchanger; based on [63] and [FLS19].

Parameter definition in [63]	**Parameter definition in this Study**	**Dimension**	**Value**
$s+t$	l_{lateral}	mm	1.9
l	$l_{\text{longitudinal}}$	mm	1.01
t	d_{st}	µm	152
$h+t$	H_{st}	mm	10

Table A.2: Geometrical Parameters of the offset strip fin heat exchanger used in Chapter 3.2.3 with nomenclature from [63] and nomenclature used within this study; based on [FLS19].

A.1.3 Combined Performance Evaluation

An extension of Section 3.2.2 is discussed next with the statement of a single-objective optimization problem based on the three-objective problem related to energy, volume, and mass. “A simple but effective scalarizing [or transformation] procedure is to define the product of the dimensionless key figures with weighting factors. The combined efficiency ϵ_{C} is thus defined as

$$\epsilon_{\mathrm{C}}^{*} = \epsilon_{\mathrm{E}}^{*\,w_{\mathrm{E}}} \epsilon_{\mathrm{V}}^{*\,w_{\mathrm{V}}} \epsilon_{\mathrm{M}}^{*\,w_{\mathrm{M}}}. \tag{A.3}$$

The weighting factors w_{E}, w_{V}, and w_{M} fulfil:

$$w_{\mathrm{E}} + w_{\mathrm{V}} + w_{\mathrm{M}} = 1 \tag{A.4}$$

and

$$0 \leq w \leq 1 \text{ for all } w \in \{w_{\mathrm{E}}, w_{\mathrm{V}}, w_{M}\}. \tag{A.5}$$

Based on the last column in Table 3.3, the combined efficiency ϵ_{C} can be written as

$$\epsilon_{\mathrm{C}}^{*} = \epsilon_{\mathrm{V}}^{*} \left(\frac{\mathrm{Re}_{\mathrm{st}}}{2\mathrm{f}_{\mathrm{st}}} \right)^{w_{\mathrm{E}}} \left(\frac{\rho_{\mathrm{air}}}{\rho_{\mathrm{st}}(1-\varphi_{\mathrm{st}})} \right)^{w_{\mathrm{M}}}. \tag{A.6}$$

The combined efficiency ϵ_{C} in Equation (A.3) allows comparing different frontal structure areas and modified Reynolds numbers $\mathrm{Re}_{\mathrm{st,ma}}$ in the same way as the energy, volume, and mass efficiencies do. Two heat exchangers, HX1 and HX2, have the same combined specific heat transfer rate if and only

if the efficiency ϵ_C^* shows the following relationship with the Reynolds number $\mathrm{Re}_{st,ma}$:

$$\left(\frac{\dot{Q}}{P_{diss}^{w_E} V_{st}^{w_V} m_{st}^{w_M}}\right)_{HX1} = \left(\frac{\dot{Q}}{P_{diss}^{w_E} V_{st}^{w_V} m_{st}^{w_M}}\right)_{HX2}$$
$$\Leftrightarrow \epsilon_{C,HX1}^* = \left(\frac{\epsilon_C^*}{\mathrm{Re}_{st,ma}^{2(w_E - w_V - w_M)}}\right)_{HX2} \mathrm{Re}_{st,ma,HX1}^{2(w_E - w_V - w_M)} \tag{A.7}$$

The quantity $\dot{Q}/P_{diss}^{w_E} V_{st}^{w_V} m_{st}^{w_M}$ has the dimension $\left(\mathrm{W/m^3}\right)^{w_V} (\mathrm{W/kg})^{w_M}$" [FLS19]. "The combined ϵ_C efficiency is given in Figure A.3. Two different sets of weighting factors were used exemplarily. The first set emphasizes the importance of the energy efficiency: With $w_E = 0.8$, $w_V = 0.1$, and $w_M = 0.1$, a change in energy efficiency by a factor ζ could be compensated by a change in volume efficiency by a factor ζ^{-8} (keeping the mass efficiency equal). This weighting yields a superior performance for the pin fins up to a Reynolds number of $\mathrm{Re}_{st,ma} = 1600$, compared to $\mathrm{Re}_{st,ma} = 550$ for the energy efficiency only (cf. Figure 3.5). The second set reduces the importance of the energy efficiency further on to $w_E = 0.6$, $w_V = 0.2$, and $w_M = 0.2$. In Figure A.3 (bottom) the louvered fins show now the lowest performance for Reynolds numbers up to $\mathrm{Re}_{st,ma} = 2000$, compared to $\mathrm{Re}_{st,ma} = 550$ for the energy efficiency only (cf. Figure 3.5). These two weighing sets can serve as an example of an abundance of possible and reasonable weighting sets dependent on the application" [FLS19].

The method of single-objective performance evaluations presented here, will be used for the wire structure heat exchangers on Appendix A.4.

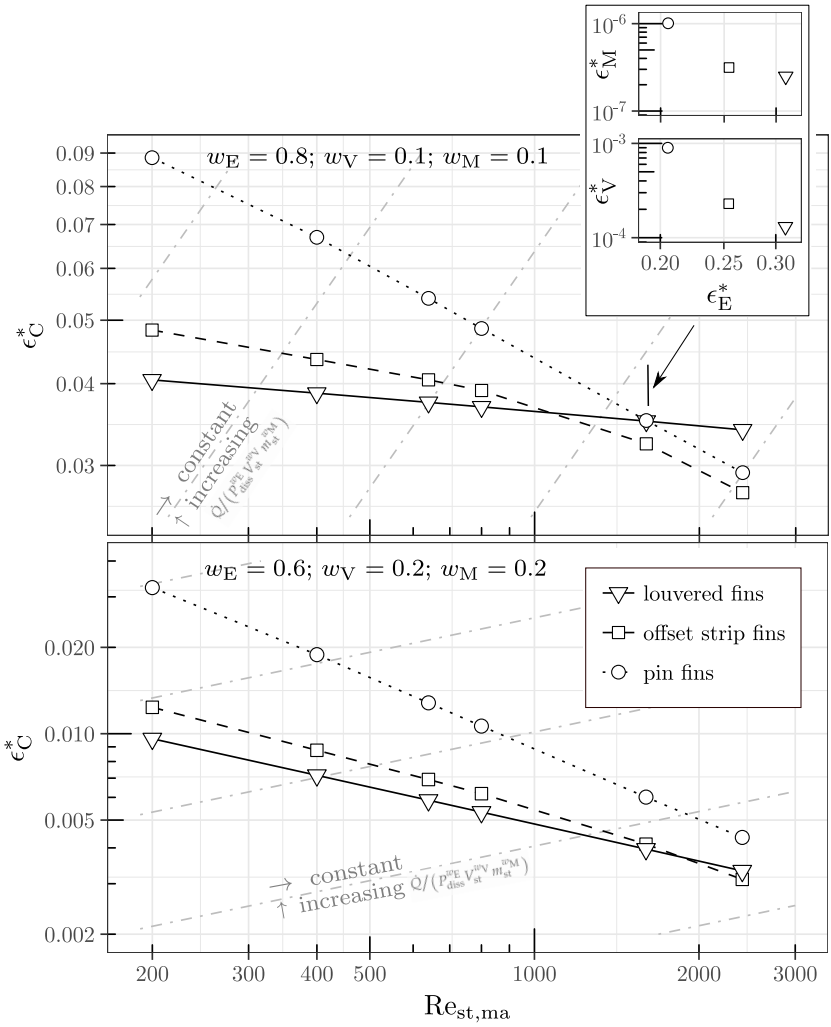

Figure A.3: Combined efficiency ϵ^*_C versus Reynolds number $Re_{st,ma}$ for different enhancements; grey dash-dot lines represent combinations of ϵ^*_C and $Re_{st,ma}$ with equal $\dot{Q}/(p^{w_E}_{diss} V^{w_V}_{st} m^{w_M}_{st})$; for $Re_{st,ma} = 1600$, the data points are additionally shown in an ϵ^*_E-ϵ^*_V and ϵ^*_E-ϵ^*_M diagram similar to Figure 3.8; based on [FLS19].

A.2 Fin Efficiency

The following two sections are based on [FGS19] and related to Section 4.5.

A.2.1 Fin Efficiency for Non-Constant Temperature Profiles

"The ordinary differential equation system (4.12) to (4.14) together with Equation (4.15) can be written in the interval $0 \leq \theta \leq 1$ in non-dimensional form by

$$\frac{\partial^2 \tilde{T}_{\text{fin}}}{\partial \theta^2} - \kappa^2 \left(\tilde{T}_{\text{fin}} - \exp(K_1 \theta) - K_1 \theta \exp(-K_1) \right) = 0, \tag{A.8}$$

$$\tilde{T}_{\text{fin}}(0) = 1, \tag{A.9}$$

$$\frac{\partial \tilde{T}_{\text{fin}}}{\partial \theta}(1) = 0. \tag{A.10}$$

With the transformation of the form

$$\tilde{T}_{\text{fin}}(\theta) = \frac{T_{\text{fin}}(\theta l) + K_2 K_3}{T_{\text{wall}} + K_2 K_3}, \tag{A.11}$$

the solution to the non-dimensional ordinary differential equation system (A.8) to (A.10) is

$$\tilde{T}_{\text{fin}}(\theta) = K_1 \theta e^{-K_1} + \frac{\kappa^2 e^{-K_1 \theta}}{-K_1^2 + \kappa^2} + \alpha_1 e^{-\kappa \theta} + \alpha_2 e^{\kappa \theta} \tag{A.12}$$

with

$$\alpha_1 = \frac{K_1^2 e^{-K_1 + \kappa} \left(K_1 + \kappa e^{K_1 + \kappa} \right)}{\kappa \left(K_1^2 - \kappa^2 \right) \left(e^{2\kappa} + 1 \right)}, \tag{A.13}$$

$$\alpha_2 = \frac{K_1^2 e^{-K_1} \left(\kappa e^{K_1} - K_1 e^{\kappa} \right)}{\kappa \left(K_1^2 - \kappa^2 \right) \left(e^{2\kappa} + 1 \right)}. \tag{A.14}$$

Some wire temperature courses according to Equation (A.12) are shown in Figure A.4 based on the parameter κ.

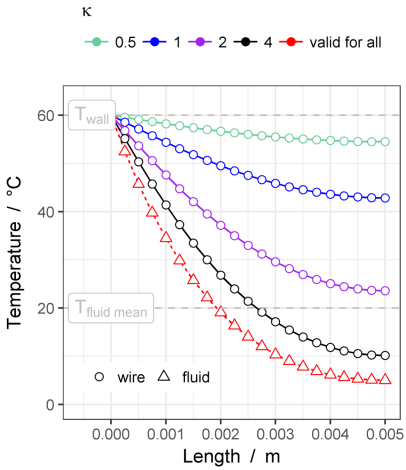

Figure A.4: Fluid temperature course and wire temperature courses along the length of the fin for an exemplaric wall temperature and mean fluid temperature for different values of κ and fixed $K_1 = 2$; based on [FGS19].

The fin efficiency can be expressed as:

$$\eta_{\text{fin,nuT}} = -\frac{1}{m^2} \frac{\frac{\partial \tilde{T}_{\text{fin}}}{\partial \theta}(0)}{\int_0^l \tilde{T}_{\text{fin}}(\zeta) - \tilde{T}_{\text{fluid},\infty,\text{mean}}(\zeta)\, d\zeta}. \tag{A.15}$$

Based on

$$\frac{\partial \tilde{T}_{\text{fin}}}{\partial \theta}(0) = K_1 e^{-K_1} - \frac{K_1 \kappa^2}{-K_1^2 + \kappa^2} - \alpha_1 \kappa + \alpha_2 \kappa \tag{A.16}$$

it follows, that

$$\eta_{\text{fin,nuT}} = -\frac{1}{\kappa^2} \frac{K_1 e^{-K_1} - \frac{K_1 \kappa^2}{\kappa^2 - K_1^2} - \alpha_1 \kappa + \alpha_2 \kappa}{1 - e^{-K_1}\left(\frac{K_1}{2} - \frac{1}{K_1}\right) - \frac{1}{K_1})}. \tag{A.17}$$

The behaviour of η_{fin} from Equation (A.17) for $K_1 \to \infty$ is as follows:

- $\eta_{\text{fin,nuT}} \to \frac{\alpha_1 - \alpha_2}{\kappa}$,
- $\alpha_1 \to \frac{e^{2\kappa}}{e^{2\kappa}+1}$,
- $\alpha_2 \to \frac{1}{e^{2\kappa}+1}$.

Thus, it holds $\eta_{\text{fin,nuT}} \to \frac{\tanh(\kappa)}{\kappa} = \eta_{\text{fin,uT}}$ (cf. Equation (2.25))" [FGS19]. Equation (A.17) is transferred to the main part of this thesis via Equation (4.18).

A.2.2 2D Model of Heat Conduction for Pin Fins

"The 2D energy equations for a fin and a fluid (air) side temperature distribution are given in [74]. The 2D plane is spanned by the flow direction and the pin fin direction. The energy equations in [74] can be transformed in a non-dimensional form by

$$\frac{\partial^2 \tilde{T}_{\text{fin}}}{\partial \theta^2} - \kappa^2 \left(\tilde{T}_{\text{fin}} - \tilde{T}_{\text{fluid}} \right) = 0, \tag{A.18}$$

$$\frac{\partial \tilde{T}_{\text{fluid}}}{\partial \zeta} - \text{ntu}_{\text{fluid}} \left(\tilde{T}_{\text{fin}} - \tilde{T}_{\text{fluid}} \right) = 0, \tag{A.19}$$

with $0 \leq \theta \leq 1$ and $0 \leq \zeta \leq 1$ and $\text{ntu}_{\text{fluid}} = \frac{h_{\text{air}} A_{\text{ATS}}}{\dot{m}_{\text{air}} c_{p,\text{air}}}$. The boundary conditions are given in Figure A.5. From the basic ansatz

$$\dot{m}_{\text{air}} c_{p,\text{air}} \left(\tilde{T}_{\text{fluid,in}} - \tilde{T}_{\text{fluid,out}} \right) = h_{\text{air}} A_{\text{ATS}} \eta_{\text{fin}} \frac{\tilde{T}_{\text{fluid,in}} - \tilde{T}_{\text{fluid,out}}}{\log \left(\frac{\tilde{T}_{\text{fluid,in}} - \tilde{T}_{\text{fin,base}}}{\tilde{T}_{\text{fluid,out}} - \tilde{T}_{\text{fin,base}}} \right)}, \tag{A.20}$$

it follows

$$\eta_{\text{fin}} = \frac{\log(1 - \epsilon_{\text{fluid}})}{\text{ntu}_{\text{fluid}}}. \tag{A.21}$$

The fluid side effectiveness ϵ_{fluid} is given by the temperature field $\tilde{T}_{\text{fluid}}$ and it is solely dependent on κ and $\text{ntu}_{\text{fluid}}$, through a non-explicitly given Function F" [FGS19]:

$$\epsilon_{\text{fluid}} = \int_0^1 \tilde{T}_{\text{fluid}}(\theta, \zeta = 1)\, d\theta = F(\kappa, \text{ntu}_{\text{fluid}}). \tag{A.22}$$

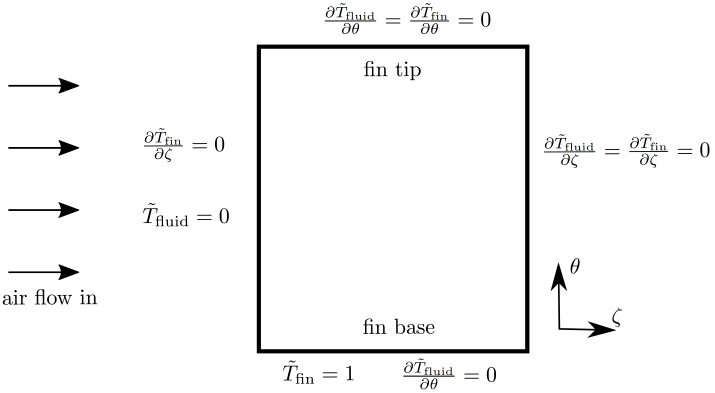

Figure A.5: Boundary conditions for energy equations A.18; based on [FGS19].

A.3 Correlation

A.3.1 Dependencies

The dependencies of the Nusselt number, the friction factor, and the extended surface efficiency on operating and geometry conditions are given in Table A.3.

Parameter	Dependency	Source	Comment
$\mathrm{Nu}_{\mathrm{air}}$	$\mathrm{Re}_{\mathrm{st}}$, $\mathrm{Pr}_{\mathrm{air}}$, T_w/T_m, geometry	[88, ch. 3], [41, p. 523]	T in Kelvin; influence of T_w/T_m for gases is usually small
f_{st}	$\mathrm{Re}_{\mathrm{st}}$, geometry	[11, ch. 6]	Risk of confusion between Darcy and Fanning friction factor
η_0	$\mathrm{Re}_{\mathrm{st}}$, $\mathrm{Pr}_{\mathrm{air}}$, $\chi_{\mathrm{st,air}}$, geometry	[11, p. 289]	Simplified assumptions on geometry are used

Table A.3: Dependencies; based on [FLS19].

A.3.2 Definition of Correlation for Fanning Friction Factor

For the friction factor the same procedure is followed as for the Nusselt number in Section 4.2.3. The non-dimensional hydraulic entrance length L^*_{hy}, and the global and local friction factors f_{st,y^*}, $f_{\mathrm{st,local},y^*}$, respectively, are given by

$$f_{\mathrm{st},y^*} = f_{\mathrm{st},\infty} + \frac{C_{1,f}}{C_{2,f}(y^*-1)}\left(1 - y^{*-C_{2,f}}\right), \tag{A.23}$$

$$f_{\mathrm{st,local}y^*} = f_{\mathrm{st},\infty} + C_{1,f}y^{*-(C_{2,f}+1)}, \tag{A.24}$$

$$L^*_{\mathrm{hy}} = \left(\frac{f_{\mathrm{st},\infty}\,\epsilon}{C_{1,f}(1-\epsilon)}\right)^{\frac{-1}{C_{2,f}+1}}. \tag{A.25}$$

A.3.3 Correlation for Staggered Arrangement

For the staggered arrangement, the coefficients of the correlations for $\mathrm{Nu}_{\mathrm{st}}$ and f_{st} are given in Table A.4. The related correlation errors are shown in Table A.5.

Coefficients	Equations
$\mathrm{Nu}_{\mathrm{st},\infty}$	$\mathrm{Nu}_{\mathrm{st},\infty} = \tilde{A}_{\mathrm{Nu}} + 0.021\mathrm{Re}_{\mathrm{st}}^{\tilde{B}_{\mathrm{Nu}}}$
	$\tilde{A}_{\mathrm{Nu}} = 0.91 + \frac{2.57}{b} + \frac{2.2 - 0.78a}{\exp(b)}$
	$\tilde{B}_{\mathrm{Nu}} = 0.598 + 0.065\frac{a}{b} - 0.393\left(\frac{a}{b}\right)^{0.5}$
$f_{\mathrm{st},\infty}$	$f_{\mathrm{st},\infty} = \exp(\tilde{A}_f + \tilde{B}_f \log(\mathrm{Re}_{\mathrm{st}}))$
	$\tilde{A}_f = 1.28 + 0.62\frac{b}{a} + \frac{4.31 - 2.05a^{0.5}}{b} - 0.015a - 2.06\log(b)$
	$\tilde{B}_f = -\frac{1.43}{b} + \frac{2.65}{ab} + 0.078\frac{a}{b^2} - 0.297 - b0.23^a - 0.025a$
$C_{1,\mathrm{Nu}}$	$C_{1,\mathrm{Nu}} = \begin{cases} \tilde{A}_{1,\mathrm{Nu}} & \text{if } \mathrm{Re}_{\mathrm{st}}^{0.9} a^{2.4} b^{-1.2} > 240 \\ 0 & \text{if } \mathrm{Re}_{\mathrm{st}}^{0.9} a^{2.4} b^{-1.2} \leq 240 \end{cases}$
	$\tilde{A}_{1,\mathrm{Nu}} = 0.22 + 0.16\mathrm{Re}_{\mathrm{st}} + \frac{0.89}{b} + 0.02ab + 1.45 \times 10^{-5}\mathrm{Re}_{\mathrm{st}}^3$ $- 0.35b - 0.0021\mathrm{Re}_{\mathrm{st}}^2 - 0.2\mathrm{Nu}_{\mathrm{st},\infty}^2$
$C_{1,f}$	$C_{1,f} = \begin{cases} \tilde{A}_{1,f} & \text{if } \mathrm{Re}_{\mathrm{st}}^{0.9} a^{2.2} b^{-1.1} > 255 \\ 0 & \text{if } \mathrm{Re}_{\mathrm{st}}^{0.9} a^{2.2} b^{-1.1} \leq 255 \end{cases}$
	$\tilde{A}_{1,f} = f_{\mathrm{st},\infty}\Bigg(0.15\mathrm{Re}_{\mathrm{st}}^{0.5} - \frac{4.97}{a} - 0.46$ $+ \frac{0.017a(0.87 + \mathrm{Re}_{\mathrm{st}})^{0.5}(13.85\log(a))^{0.5}}{b}\Bigg)$
$C_{2,\mathrm{Nu}}$	$C_{2,\mathrm{Nu}} = \frac{1.20}{1 + \tilde{A}_{2,\mathrm{Nu}}}$
	$\tilde{A}_{2,\mathrm{Nu}} = 3.070 \times 10^{-4}\ \mathrm{Re}_{\mathrm{st}}^{0.886} a^{2.719} b^{-0.928}$
$C_{2,f}$	$C_{2,f} = \frac{1.01}{1 + \tilde{A}_{2,f}}$
	$\tilde{A}_{2,f} = 3.286 \times 10^{-6}\ \mathrm{Re}_{\mathrm{st}}^{1.448} a^{3.842} b^{-1.260}$

Table A.4: Predicted correlation for coefficients of $\mathrm{Nu}_{\mathrm{st}}$ and f_{st} for staggered wire structure based on Equation (4.4) and (A.23). Correlation is valid for: $3 \leq a \leq 12$, $1.3 \leq b \leq 8$, $3 \leq \mathrm{Re}_{\mathrm{st}} \leq 60$; based on [FSF19].

		relative residual error $3 \leq a \leq 12$		**relative residual error** $5 \leq a \leq 12$	
		$< 5\%$	$< 10\%$	$< 5\%$	$< 10\%$
$\mathrm{Nu}_{\mathrm{st},\infty}$	$n_{\mathrm{wires}} > L^*_{\mathrm{th}}$	67	90	70	88
$f_{\mathrm{st},\infty}$	$n_{\mathrm{wires}} > L^*_{\mathrm{hy}}$	71	89	80	95
$\mathrm{Nu}_{\mathrm{st},y^*}$	$n_{\mathrm{wires}} > 2$	68	92	73	91
$\mathrm{Nu}_{\mathrm{st},y^*}$	$n_{\mathrm{wires}} > 5$	68	91	74	90
f_{st,y^*}	$n_{\mathrm{wires}} > 2$	68	87	78	95
f_{st,y^*}	$n_{\mathrm{wires}} > 5$	69	88	79	95

Table A.5: Percentage of correlated data which satisfy a relative residual error below 5% and 10% for $\mathrm{Nu}_{\mathrm{st},\infty}$, $f_{\mathrm{st},\infty}$, $\mathrm{Nu}_{\mathrm{st},y^*}$, and f_{st,y^*} in staggered wire arrangement. The percentage is specified for different number of wire rows. Correlation is valid for: $3 \leq a \leq 12$, $1.3 \leq b \leq 8$, $3 \leq \mathrm{Re}_{\mathrm{st}} \leq 60$; based on [FSF19].

A.4 Combined Performance Evaluation of Wire Structures

Based on Equation A.3, the combined efficiency ϵ_C^* is calculated for a broad selection of feasible decisions within Θ_{V1} (cf. Table 6.1). Different combinations of weighting factors w_E, w_V, and w_M are shown in Figure A.6 to Figure A.8.

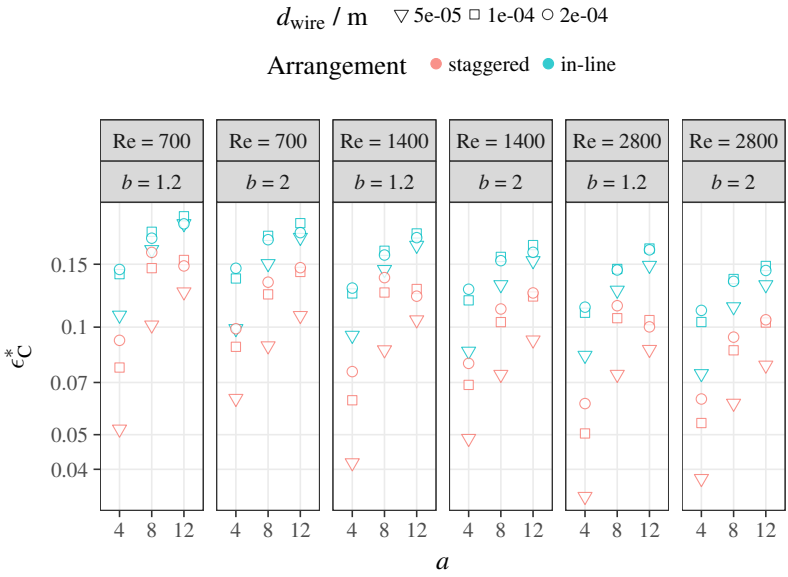

Figure A.6: Combined efficiency for broad selection of feasible decisions from Θ_{V1} with $Re_{st,ma}$ from 700 to 2800. Weighting factors are: $w_E = 0.8$, $w_V = 0.2$, $w_M = 0.0$.

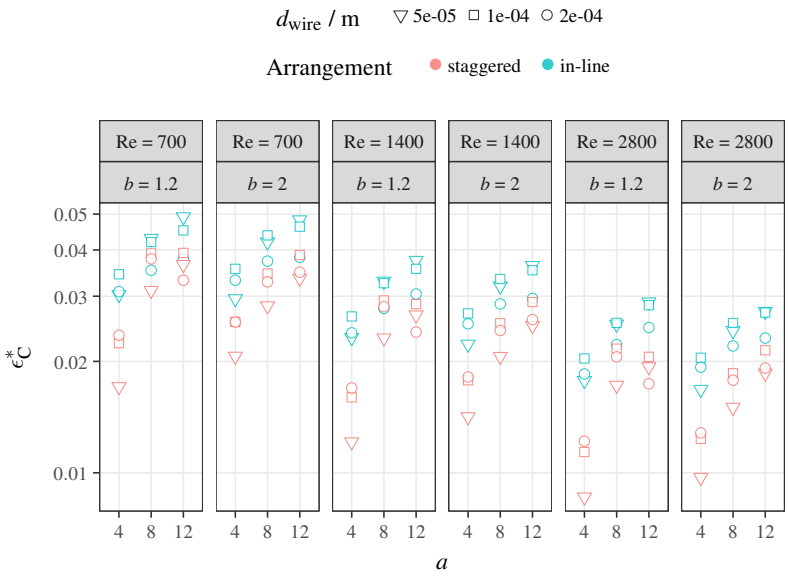

(a) $w_E = 0.8$, $w_V = 0$, $w_M = 0.2$

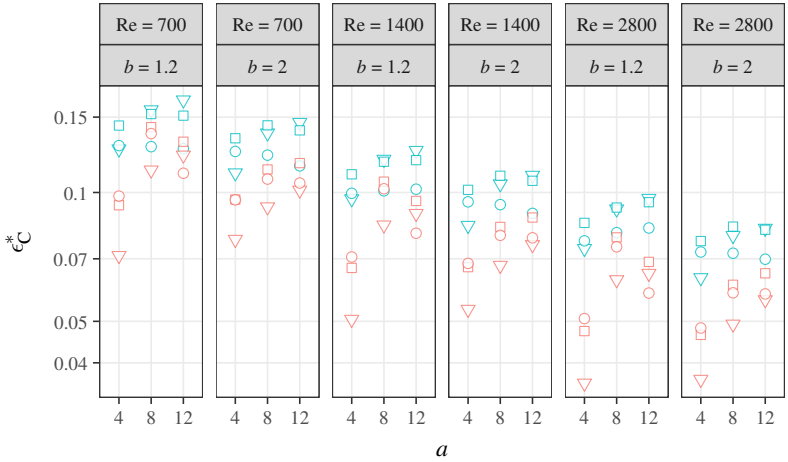

(b) $w_E = 0.8$, $w_V = 0.2$, $w_M = 0.0$

Figure A.7: Combined efficiency for broad selection of feasible decisions from Θ_{V1} with $Re_{st,ma}$ from 700 to 2800.

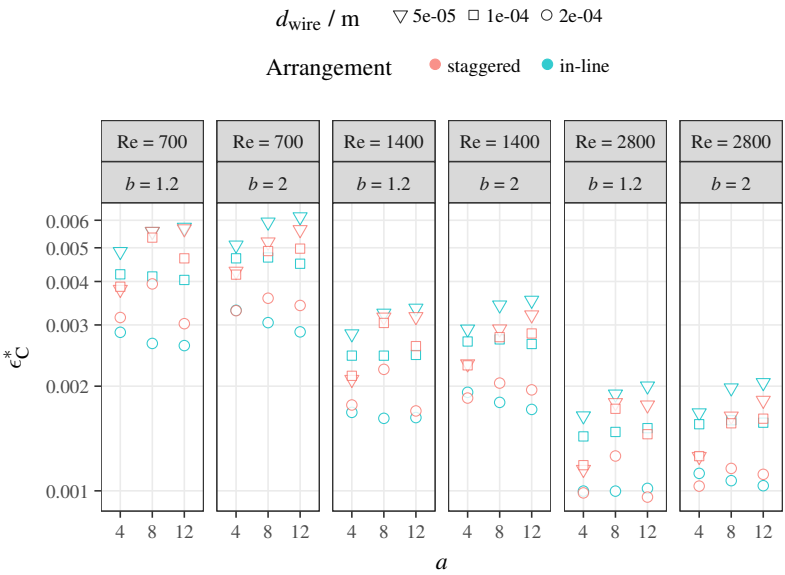

(a) $w_E = 0.6$, $w_V = 0$, $w_M = 0.4$

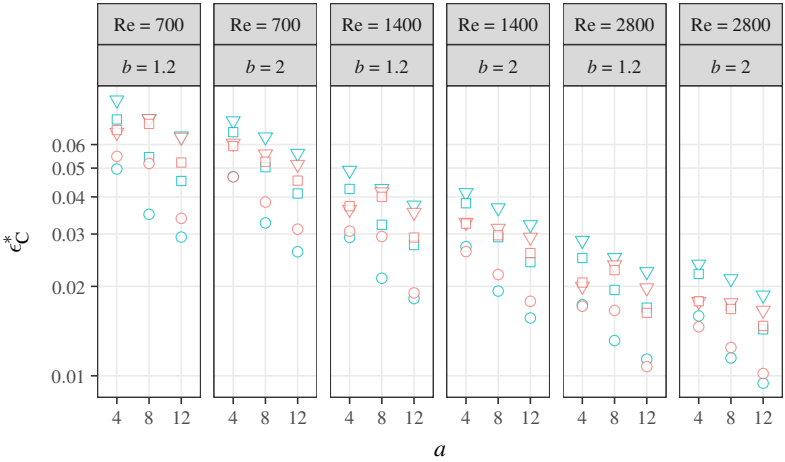

(b) $w_E = 0.6$, $w_V = 0.4$, $w_M = 0.0$

Figure A.8: Combined efficiency for broad selection of feasible decisions from Θ_{V1} with $\text{Re}_{\text{st,ma}}$ from 700 to 2800.

A.5 Comparison to Classical Heat Transfer Enhancement

A.5.1 Feasibility Sets

The feasibility sets of the rectangular channels, the louvered fins, the metal foams, and the wire structures used in Section 6.2.2 are shown in Table A.6 to Table A.8. The rectangular channel width and height are l_{lateral} and H_{st}, respecively (this corresponds to $2b$ and $2a$ in [11, p. 476]). The louvered fin geometry [62] is given in Figure A.1 with a transfer of parameter definitions in Table A.1.

Parameter	Θ
d_{ma}	10 mm
H_{st}	10 mm
$\chi_{\text{st,air}}$	11673
$\rho_{\text{air,st}}/\rho_{\text{st}}$	0.00013
Pr	0.71

Table A.6: Common parameters of the feasibility sets Θ_{channels}, Θ_{louvers}, Θ_{wires}, and Θ_{foams}.

Parameter	Θ_{channels}	Θ_{foams}
d_{st}	$50\,\mu\text{m} \leq d_{\text{st}} \leq 200\,\mu\text{m}$	-
l_{lateral}	$0.5\,\text{mm} \leq l_{\text{lateral}} \leq 3\,\text{mm}$	-
ppi	-	10-30

Table A.7: Additional paramters for the feasibility sets Θ_{channels} for rectangular channels and Θ_{foams} for metal foams.

Parameter	$\Theta_{\text{lou}v\text{ers}}$	Θ_{wires}
d_{st}	$100\,\mu\text{m} \leq d_{\text{st}} \leq 120\,\mu\text{m}$	$50\,\mu\text{m} \leq d_{\text{st}} \leq 300\,\mu\text{m}$
l_{lateral}	$1\,\text{mm} \leq l_{\text{lateral}} \leq 1.4\,\text{mm}$	ad_{st}
a	-	$4 \leq a \leq 12$
$l_{\text{longitudinal}}$	$1.5\,\text{mm} \leq l_{\text{longitudinal}} \leq 1.7\,\text{mm}$	bd_{st}
b	-	$1.2 \leq b \leq 4$
L_{st}	$16\,\text{mm} \leq l_{\text{longitudinal}} \leq 24\,\text{mm}$	$n_{\text{wires}}bd_{\text{st}}$
n_{wires}	-	100
L_{l}	$6\,\text{mm} \leq L_{\text{l}} \leq 7\,\text{mm}$	-
L_{α}	$15° \leq L_{\alpha} \leq 29°$	-
T_{p}	$1.2d_{\text{ma}}$	-
Arrangement	-	in-line and staggered

Table A.8: Additional paramters for the feasibility sets $\Theta_{\text{lou}v\text{ers}}$ for louvered fins and Θ_{wires} for wire structures.

A.5.2 Further Performance Evaluation

In Figure A.9, the mass efficiency has been bounded by a lower limit. This limit is given by a linear function with $\epsilon^*_M > 2 \times 10^{-6} \left(1 - \frac{\epsilon^*_E}{0.6}\right)$ such that all geometries, that do not fulfil this inequality, are not feasible. Especially the louvered fin design is not capable to satisfy this requirement.

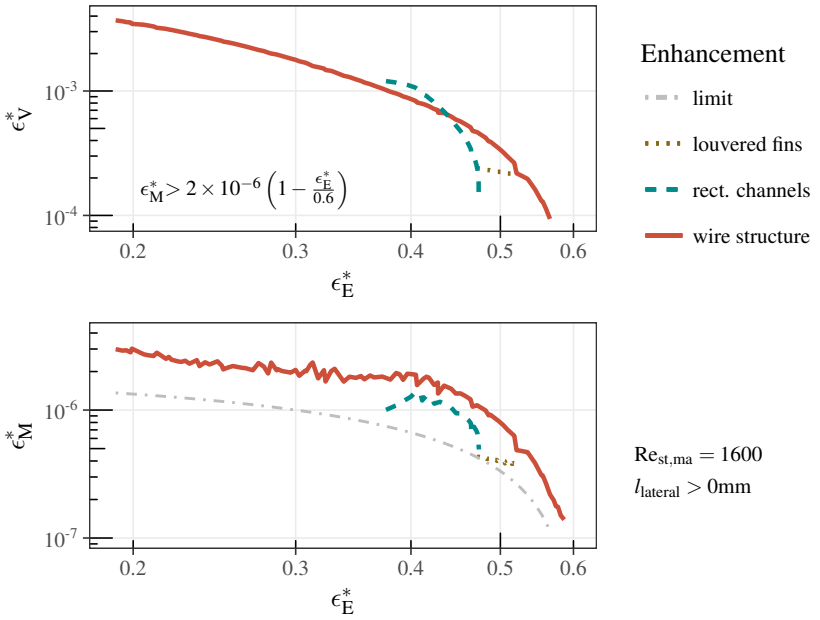

Figure A.9: Relationship between energy, volume and mass efficiency in terms of ϵ^*_E-ϵ^*_V Pareto optimal sets of louvered fins, rectangular channels, and wire structures based on the feasibility sets $\Theta_{louvers}$, $\Theta_{channels}$, and Θ_{wires}, respectively; with an additional limitation on mass efficiency, represented by the grey dash-dotted line.

In Figure A.10, the Reynolds number is set to $\mathrm{Re}_{\mathrm{st,ma}} = 4500$ and the lateral fin distance is bounded by $l_{\mathrm{lateral}} > 1\,\mathrm{mm}$. In terms of optimized combinations of ϵ^*_{E} and ϵ^*_{V} the louvered fins are favourable for all combinations.

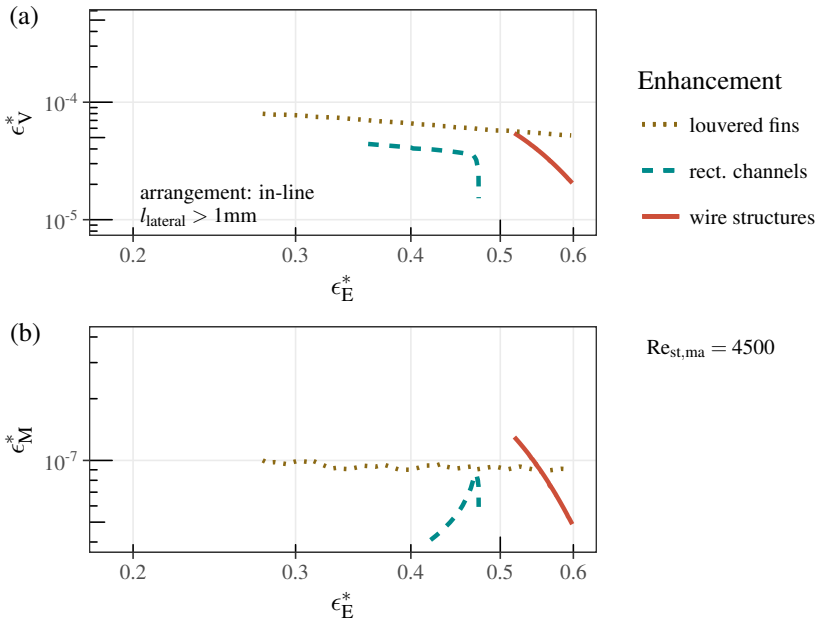

Figure A.10: Relationship between energy, volume and mass efficiency in terms of ϵ^*_{E}-ϵ^*_{V} Pareto optimal sets of louvered fins, rectangular channels, and wire structures based on the feasibility sets $\Theta_{\mathrm{louvers}}$, $\Theta_{\mathrm{channels}}$, and Θ_{wires}, respectively; with an additional limitation on lateral fin distance $l_{\mathrm{lateral}} > 1\,\mathrm{mm}$.

A.6 Cost Analysis

A.6.1 Raw Material Costs versus Stock Exchange Price

The stock exchange price averaged over one year (period 3.12.17 - 3.12.18) are given in Table A.9.

Material	Averaged price in Euro/tonne	Minimum (52 weeks) in Euro/tonne	Maximum (52 weeks) in Euro/tonne
Copper	6580	5073	6457
aluminum	1800	1699	2235

Table A.9: Stock exchange prices of aluminum and copper; based on [Fug18].

The raw price of copper is about 3.6 times as high as that of aluminum.

A.6.2 Wire Production

The factor price of drawn wires in relation to the price of the raw material depending on the wire diameter are given in Table A.10.

Wire diameter / mm	Aluminum	Copper
0.053	50	4.2
0.1	40	3.6
0.2	13	1.5

Table A.10: Factor price raw material to wire (related to mass); based on [Fug18].

The wire is considerably more expensive than the raw material. The costs for wire production increase with decreasing wire diameter. The price increase for aluminum is significantly higher than for copper. Further costs arise from the processing of the wire into wire cloth (wire fabric). The price of the finished textile fabric is approx. 2-6 times higher than the price of the wire. This

factor depends on the quantity produced. For larger quantities, the factor is reduced because the one-off costs incurred by loading and adjusting the weaving machine are spread over a larger quantity.

The production costs of metal sheets are hardly dependent on the material for aluminum or copper. The prices for the finished metal sheet are about a factor of 1.2 to the cost of the raw material [Fug18].

A.7 Particle Fouling Analysis

One concern for the use of wire structures as heat exchanger enhancement is a possible particle fouling on the air-side, that might be larger than for known heat transfer enhancements (e.g. corrugated metal sheets). In [Alt18] a test facility for particle fouling on a heat exchanger is described. This test facility was used to analyze particle fouling on the Wire Structure I heat exchanger from Section 5.2.2. The test facility is shown schematically in Figure A.11

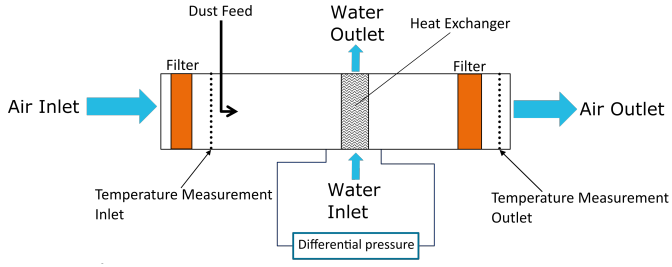

Figure A.11: Schematic view on the dust feeding in the channel before the heat exchanger and main sensor and filter positions; based on [Alt18].

Arizona Test Dust and gypsum has been fed into the air channel before the heat exchanger. Similar to Bell and Groll [89] a significant change in pressure drop could not be detected during dust feeding on the wire structure heat exchanger. The pressure drop is in fact slightly decreasing for the fouled heat exchanger. This phenomenon is described in [89] as well. However, the decrease in pressure drop is accompanied by a decrease in heat transfer. Bell and Groll describe the phenomenon as follows: “For the Arizona Road Test Dust, the particulate matter coats all the enhanced surfaces of the heat exchanger, particularly the stagnation regions. The thermal conductivity of the Arizona Road Test Dust is lower than that of the fin material, resulting in a significant decrease in heat transfer. The relatively thin film of particulate matter results in an insignificant increase in air-side pressure drop due to a negligible blockage of the frontal area”[89]. This assessment can be followed.

The fouling with gypsum is less pronounced than with Arizona Test Dust. However the behaviour is the same. The frontal area experiences a high fouling rate in the stagnation and wake region; with increasing depth in air flow direction the fouling rate decreases. Figure A.12 and Figure A.13 show the fouling on the frontal face.

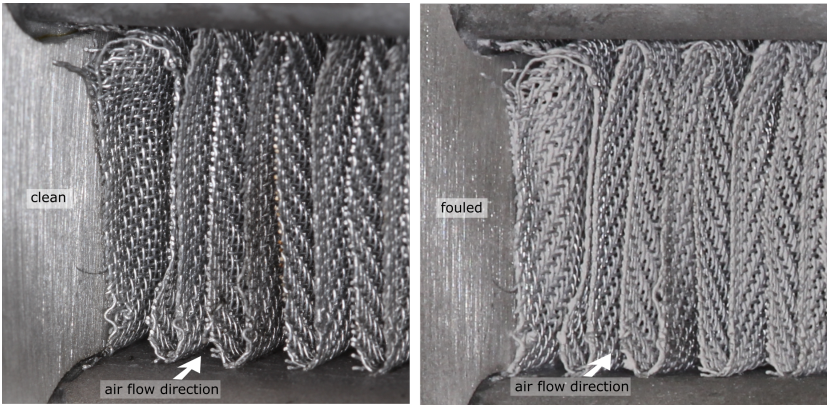

Figure A.12: Dust feeding with gypsum on Wire Structure I; clean wire structure (left) and fouled structure (right) in direct comparison; based on [Fug18].

Figure A.14 shows the fouling on the outlet. There is no blocking of channels visible. Therefore a change in pressure drop is not expected from the visual assessment.

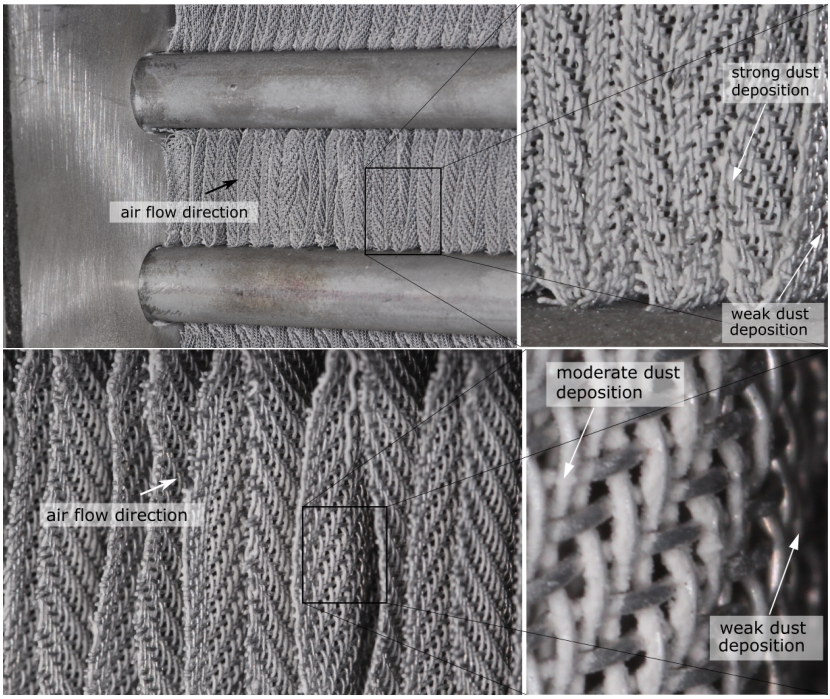

Figure A.13: View on the frontal face of the heat exchanger Wire Structure I after dust feeding (gypsum); based on [Fug18].

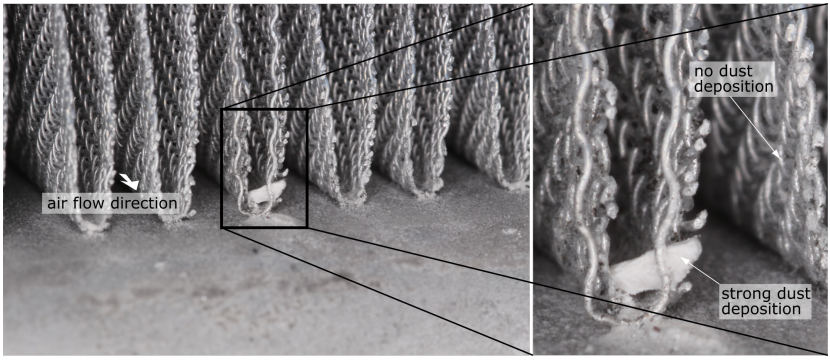

Figure A.14: View on the outlet face of the heat exchanger Wire Structure I after dust feeding (gypsum); based on [Fug18].

Acknowledgements

I would like to take the opportunity to express my sincere thanks to **Lena Schnabel**. Without her guidance and persistent help this dissertation would not have been possible. A discussion with Lena allows to see alternatives in situations where every door seems to be locked.

I would especially like to thank professor **Bettina Frohnapfel** for supervising this thesis. She helped me to concentrate on the major questions and to analyze the appearing phenomena with the necessary depth. Her positive way, made every trip to Karlsruhe an enrichment.

My work on wire structures was linked to several projects within the division Thermal Systems and Buildings at Fraunhofer ISE. I was lucky enough to join a team of fantastic colleagues and to learn from each of them over the last 6 years.

When it comes to experimental work, **Paolo di Lauro** is the person you need to talk to. Paolo does not do things half-heartedly, he is fascinated by details and the persistence he worked with thousands of small wires is incredible. Within the MinWaterCSP project he was my major support. Thank you Paolo.

Together with **Alexander Morgenstern**, I worked on open sorption technology in the project Optimat. His advise regarding air conditioning for and operation of test facilities was brilliant. Thank you Alex.

Eric Laurenz laid the foundation of wire structure development in the project Effimet. His analytical capability is incredible and our discussions on a fair performance evaluation contributed significantly to the comprehensive evaluation method within this thesis. Thank you Eric.

Gerrit Füldner is the guy with the long-standing experience in our office. He generates one idea after another. Not only in the project Harvest could I benefit from his general competence but as well in every day business. Thank you Gerrit.

With **Sebastian Gamisch** I shared not only my office but as well the development of new applications for wire structure heat exchangers in the project Thermogewebe. Those 15 minutes we spent once or twice a week talking on simulation models, experimental results, and data evaluation in front of his or my computer screen, are concealed in every page of this thesis. Thank you Sebastian.

Björn Nienborg supported me within my first project SolaRück at Fraunhofer ISE on performance evaluation of cooling towers. We never had and probably never will have a single talk that just lasts the time planned. There are too many things that need to be discussed. Thank you Björn.

I especially thank my students **Ahmed Junaid Tahir, Aniket Sawant, Juan Pablo Rincon Duarte, Paula Camilla Madariaga Escobar, Danny Alejandro Carvajal Puche, Mareike Altenberend and Nasir Asadov**. All of them were highly motivated students, working independently on the project's objectives and writing excellent theses. Parts of their work are used within my thesis.

I also thank my collegues **Alexander Warlo, Andreas Velte, Rahel Volmer** and **Peter Schossig** and the entire division TSB for the innumerable discussions on technological and social reality and future.

I am also grateful to my industrial partners. **Richard Balzer** from Spörl oHG and **Albert Zapke** from Enexio made it possible to have large-scale wire structure heat exchangers in our hands.

A very special thank you to my friend **Johannes Dietrich** for his invaluable advice and feedback on my research and for helping me with the proofreading of this thesis.

I would like to express my deepest gratitude to my **Mom, Dad** and my **parents-in-law** for always believing in me and supporting me and my family in every conceivable way. And to my son **Arved** for retrieving me from my working space to the social world. And finally to my wife **Svenja**. She has been by my side throughout my entire academic career. When I start trying to solve a problem with mathematical analysis, she has already solved it with her empathy and laughter. This dissertation would not have been possible without my family's warm love, continued patience, and endless support.